Investigation of the Lithium Ion Mobility in Cyclic Model Compounds and their Ion Conducting Properties

Dissertation

zur Erlangung des Grades
„Doktor der Naturwissenschaften”
im Promotionsfach Chemie

dem Fachbereich Chemie, Pharmazie und Geowissenschaften
der Johannes Gutenberg-Universität Mainz

vorgelegt von

Jörg Thielen
geboren in Zell a.d. Mosel

Mainz, 2011

Die vorliegende Arbeit wurde in der Zeit
von Juni 2008 bis Juni 2011
am Max-Planck-Institut für Polymerforschung in Mainz
unter der Anleitung von Prof. … angefertigt.

Dekan:

1. Berichterstatter:

2. Berichterstatter:

Mündliche Prüfung: 27. 07. 2011

Meinen Eltern

'I read somewhere... how important it is in life

not necessarily to be strong… but to feel strong.'

- Into the wild -

Abstract

Efficient energy storage and conversion is playing a key role in overcoming the present and future challenges in energy supply. Batteries provide portable, electrochemical storage of green energy sources and potentially allow for a reduction of the dependence on fossil fuels, which is of great importance with respect to the issue of global warming. In view of both, energy density and energy drain, rechargeable lithium ion batteries outperform other present accumulator systems. However, despite great efforts over the last decades, the ideal electrolyte in terms of key characteristics such as capacity, cycle life, and most important reliable safety, has not yet been identified.

Steps ahead in lithium ion battery technology require a fundamental understanding of lithium ion transport, salt association, and ion solvation within the electrolyte. Indeed, well-defined model compounds allow for systematic studies of molecular ion transport. Thus, in the present work, based on the concept of '*immobilizing'* ion solvents, three main series with a cyclotriphosphazene (CTP), hexaphenylbenzene (HBP), and tetramethyl-cyclotetrasiloxane (TMS) scaffold were prepared. Lithium ion solvents, among others ethylene carbonate (EC), which has proven to fulfill together with propylene carbonate safety and market concerns in commercial lithium ion batteries, were attached to the different cores via alkyl spacers of variable length.

All model compounds were fully characterized, pure and thermally stable up to at least 235 °C, covering the requested broad range of glass transition temperatures from -78.1 °C up to +6.2 °C. While the CTP models tend to rearrange at elevated temperatures over time, which questions the general stability of alkoxide related (poly)phosphazenes, both, the HPB and CTP based models show no evidence of core stacking. In particular the CTP derivatives represent good solvents for various lithium salts, exhibiting no significant differences in the ionic conductivity σ_{dc} and thus indicating comparable salt dissociation and rather independent motion of cations and ions.

In general, temperature-dependent bulk ionic conductivities investigated via impedance spectroscopy follow a *William-Landel-Ferry* (*WLF*) type behavior. Modifications of the alkyl spacer length were shown to influence ionic conductivities only in combination to changes in glass transition temperatures. Though the glass transition temperatures of the blends are low, their conductivities are only in the range of typical polymer electrolytes. The highest σ_{dc} obtained at ambient temperatures was 6.0 x 10^{-6} S·cm^{-1}, strongly suggesting a rather tight coordination of the lithium ions to the solvating 2-oxo-1,3-dioxolane moieties, supported by the increased σ_{dc} values for the oligo(ethylene oxide) based analogues.

Further insights into the mechanism of lithium ion dynamics were derived from ^{7}Li and ^{13}C Solid- State NMR investigations. While localized ion motion was probed by i.e. ^{7}Li spin-lattice relaxation measurements with apparent activation energies E_a of 20 to 40 kJ/mol, long-range macroscopic transport was monitored by Pulsed-Field Gradient (PFG) NMR, providing an E_a of 61 kJ/mol. The latter is in good agreement with the values determined from bulk conductivity data, indicating the major contribution of ion transport was only

detected by PFG NMR. However, the µm-diffusion is rather slow, emphasizing the strong lithium coordination to the carbonyl oxygens, which hampers sufficient ion conductivities and suggests exploring *'softer'* solvating moieties in future electrolytes.

Zusammenfassung

Die effiziente Speicherung und Umwandlung von Energie spielt eine Schlüsselrolle in der zukünftigen Energieversorgung. Batterien bieten die Möglichkeit, ökologisch gewonnenen Strom in mobiler Form elektrochemisch zu speichern. Dies eröffnet die Chance, die Abhängigkeit von fossilen Energieträgern, deren Verwendung eng mit dem Problem der globalen Erwärmung verknüpft ist, zu reduzieren. In Bezug auf Energiedichte und Leistungsabgabe übertreffen Lithiumionen-Akkumulatoren die Leistungsfähigkeit herkömmlicher Batterien. Dennoch konnte trotz ausgiebiger Forschung der ideale Elektrolyt hinsichtlich entscheidender Batterieparameter wie Energiedichte, Lebensdauer und insbesondere Betriebssicherheit noch nicht gefunden werden.

Entscheidende Fortschritte setzen daher ein grundlegenderes Verständnis des Ionentransportes sowie der Assoziation bzw. Solvatation des Salzes im Elektrolyten voraus. Für systematische Untersuchungen auf molekularer Ebene empfehlen sich klar definierte Modellsubstanzen. Basierend auf dem Konzept der *‚Immobilisierung‘* von Ionensolvenzien wurden in der vorliegenden Arbeit drei Modellserien mit Zyklotriphosphazen- (CTP), Hexaphenylbenzol- (HPB) bzw. Tetramethylcyclotetrasiloxan- (TMS)-Kernen hergestellt. Die für den Ionentransport verantwortlichen Seitengruppen, u.a. Ethylenkarbonat (EC), das sich in Kombination mit Propylenkarbonat als Elektrolyt in kommerziellen Batterien bewährt hat, werden über Alkyl-Spacer unterschiedlicher Länge an die Grundgerüste angebunden.

Alle Modellsubstanzen wurden vollständig charakterisiert, sind bis mindestens 235 °C thermisch stabil und decken den gewünschten breiten Bereich an Glastemperaturen ab (–78.1 °C bis +6.2 °C). Während bei erhöhten Temperaturen für die CTP-basierten Substanzen mit der Zeit Umlagerungen zu beobachten sind, was die generelle Stabilität von Alkoxy(poly)phosphazenen zur Diskussion stellt, zeigen weder die CTP- noch HPB-basierten Modelle Anzeichen einer Stapelordnung. Speziell die CTP-Derivate sind gute Solvenzien für verschiedenste Lithiumsalze ohne signifikante Unterschiede in der Ionenleitfähigkeit, was auf vergleichbare Salzdissoziation sowie eine eher unabhängige Kationen- und Anionen-Bewegung hinweist.

Generell folgt die mittels Impedanz-Spektroskopie bestimmte temperaturabhängige Leitfähigkeit der Modellelektrolyte dem *William-Landel-Ferry* (*WLF*) Verhalten, wobei Veränderungen der Spacer-Länge die Leitfähigkeit nur beeinflussen sofern dies Einfluss auf die Glastemperatur hat. Obwohl letztere eher gering sind, bewegen sich die Leitfähigkeiten im Bereich typischer Polymerelektrolyte. Die höchste bei Raumtemperatur gemessene Leitfähigkeit erreicht 6.0×10^{-6} S·cm^{-1}, was auf eine zu starke Koordination zwischen den Lithiumionen und den zyklischen Karbonat-Einheiten hinweist. Unterstützt wird dies durch die im Vergleich höheren Leitfähigkeiten der ethylenoxid-funktionalisierten Modelle.

Weitere Erkenntnisse über die Ionendynamik wurden aus ^{7}Li und ^{13}C Festkörper-NMR Messungen abgeleitet. Während die Untersuchung lokaler Ionenbewegungen mit u.a. ^{7}Li Spin-Gitter-Relaxationsmessungen scheinbare Aktivierungsenergien (E_a) von 20 bis 40 kJ/mol liefert, ist weitreichender Transport nur mittels Feldgradienten-NMR (PFG-NMR) zu beobachten. Die hier erhaltene E_a von 61 kJ/mol liegt im Bereich der aus den

Leitfähigkeitsdaten bestimmten und deutet an, dass der Hauptbeitrag zum eigentlichen Ionentransport nur durch PFG-NMR detektierbar ist. Jedoch ist die µm-Diffusion eher langsam, was die angesprochene potentiell zu enge Koordination der Lithiumionen unterstreicht. Dadurch wird eine ausreichende Ionendynamik erschwert und eine Untersuchung von potentiell ‚weicheren' Solvenzien auf ihre Eignung als zukünftige Elektrolyten angedeutet.

Contents

CHAPTER I

CHAPTER II

CHAPTER III

CHAPTER IV

CHAPTER V

CHAPTER VI

CHAPTER VII

Appendix

CHAPTER I

1. Introduction

The expected depletion of the worldwide reserves of non-renewable fuels in combination with a continuously increasing demand for oil is a scenario, which will end up in serious problems in the upcoming decades.[1.1]* So far no alternatives based on green energy sources are able to replace the current combustion engines. Besides the fact that the dependence on foreign oil and gas creates dependence of the economy on political changes and unrests, the fulminate ascent of CO_2 emissions over the last decades associated with combustion of oil resulted in an observable rise in global temperature, which is expected to cause serious climate changes in the future.[1.1][1.2] To combust oil '*just*' for transportation is incidentally not the first choice of utilization due to the importance of oil for the chemical industry as basis for manifold products including pharmaceuticals. Thus, in order to deal with these problems, in particular the severe issue of global warming, renewable energies have to be used in a much higher extent than it is presently the case.[1.1] A distinct reduction of carbon dioxide emissions is thereby closely related to the replacement of internal combustion engine automobiles by electric, zero emission vehicles. Consequently, efficient energy storage and conversion plays a key role in overcoming the present and future challenges in energy supply, since most of the green energy sources such as solar radiation, wind or waves are fluctuating in power over time and space.[1.3] Energy produced in stationary power plants based on these resources has to be made portable in order to be able to compete with fossil fuels. Batteries provide this portability and can convert chemically stored energy on demand to electrical energy - highly efficient and without gaseous exhaust. Thus, reliable accumulators with long cycle life, high power and energy density constitute a major contribution for redemption of fossil fuels on the basis of green energy sources.

---

* Remark: References are listed after each chapter.

Several German car manufacturers and suppliers have recognized this enormous future market of '*electro mobility*' and accordingly invest more and more in research & development on lithium ion batteries for automotive applications, as for example *SB LiMotive*, a joint company between *BOSCH* and *Samsung*, or *Li-tec,* the counterpart from *Evonik* and *Daimler AG*, respectively. The main goal of these programs is to solve the various problems of current battery technologies in order to establish a broad distribution of lithium ion batteries in electric vehicles.

An overview over lithium ion battery technology will be given to classify this work.

1.1 Rechargeable Lithium Ion Batteries [1.2][1.4]

Batteries, by definition, store chemical energy and on demand convert them into electrical power. In contrast to a *primary battery cell,* the electrochemical reactions in a *secondary battery* are reversible through an electric current from an exterior power source flowing in the opposite direction than in the state of discharge. This process reverses the cell reaction and recharges the device.

1.1.1 General Considerations - Why Lithium?

Lithium is the lightest metal with a molecular weight of M = 6.94 g/mol (specific gravity $\rho = 0.53\ \text{g·cm}^{-3}$) bearing the highest electrochemical standard potential (-3.04 V versus

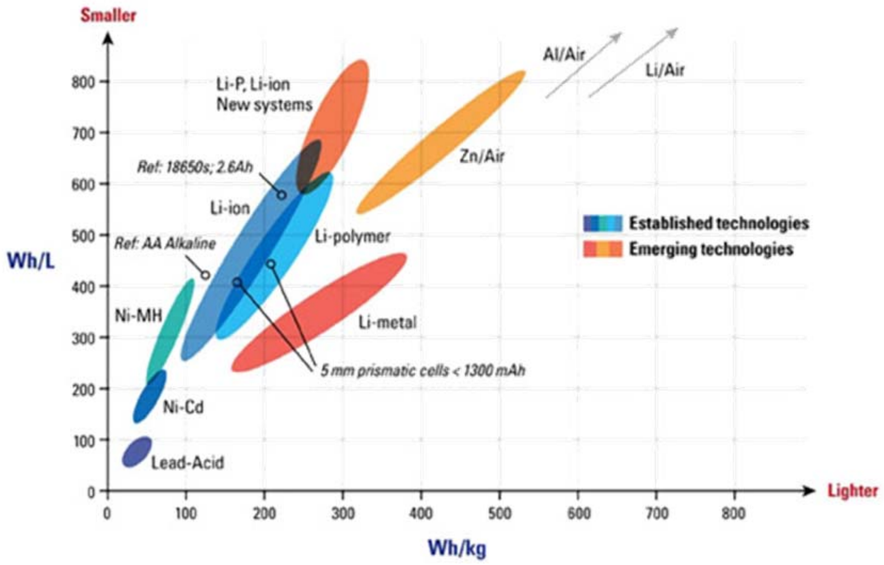

Figure 1.1. Energy storage capability of common rechargeable battery systems (a specific energy of 100 Wh/kg means that a 1 kg battery of this type is able to power a 200 W consumer for 0.5 h). Reproduced from ref. [1.6].

standard hydrogen electrode) of all elements and therefore qualifies optimal for high energy density batteries.[1.5] The development of rechargeable lithium ion batteries can be considered as a milestone for the internal power supply of the tremendously increasing amount of mobile and portable electric and electronic devices.[1.4]

The significant higher energy density both per volume and weight in comparison to other common secondary batteries such as lead acid or nickel-metal hydride renders the lithium ion based accumulators the current battery of choice for mobile applications and is expected to dominate the hybrid vehicle application sector.[1.2] This is graphically illustrated in Figure 1.1.

1.1.2 Construction and Safety Issues

In lithium ion batteries lithium ions are solvated by an organic solvent and diffuse freely between the anode and cathode, which are physically isolated by a separator membrane.[1.7][1.8] Most commonly used components are a graphite anode, a cathode formed by a lithium metal oxide (e.g. $LiCoO_2$) and blends of highly polar carbonates such as ethylene carbonate (EC), propylene carbonate (PC), diethyl carbonate (DEC), or dimethyl carbonate (DMC) with lithium hexafluorophosphate ($LiPF_6$) functioning as electrolyte.[1.9] Figure 1.2 shows a schematic illustration of a common *'rocking chair'* battery.[1.10]

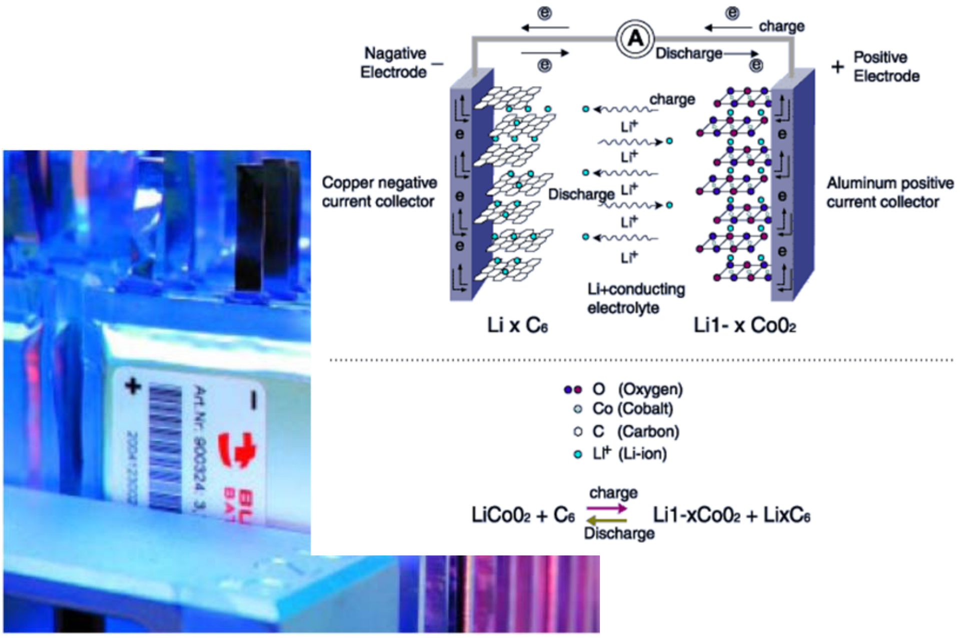

Figure 1.2. Picture and scheme of a common *'rocking chair'* battery.[1.11][1.12]

In case of charging or discharging, the lithium ions are shuttled reversibly between the lithium carbon and the lithium metal oxide intercalation compounds comprising the electrodes. The application of insertion materials instead of metallic lithium as negative electrode substantially reduced the severe problem of dendrite growth.[1.13] The electrolyte serves as transport medium for the lithium ions and is required to be chemically, thermally and electrochemically stable under regular operating conditions.

In case of small battery packages, electrolytes based on polar carbonates have proven to fulfill safety and market concerns in terms of high ionic conductivity at ambient temperatures (in the order of 10^{-3} $S \cdot cm^{-1}$) combined with high boiling and low melting point as well as safe performance over a wide temperature range.[1.14] However, the usage of organic liquids in rather large batteries necessary for electric vehicles poses potential safety hazards. Referring to an operating cell voltage of ~ 4 V for common rechargeable lithium ion batteries and high oxidation potentials of the metal oxide cathodes, decomposition of the liquid electrolyte is a potential failure concerning long-time stability, cycle life and safety. Despite graphite/$LiCoO_2$ based batteries operate beyond the thermodynamic stability window of common electrolytes, they are kinetically stable. A*d hoc* reductive decomposition of the electrolyte, in more detail the ethylene carbonate additive, results in the formation of a passivating film at the negative electrode.[1.15] These surface films are known as *Solid-Electrolyte-Interphases* (*SEI*) and are in an ideal case electronic insulators, which hinder further electrolyte reduction.[1.16] The *SEI* composition and exact nature is still controversially debated, its formation, however, irreversibly consumes both electrolyte and charge carriers, leading to a capacity loss. Furthermore, in case of unexpected events such as accidental overcharging, the system exceeds the oxidative limit. As a consequence, no protective film is formed at the cathode side and the electrolyte oxidation proceeds.[1.1] This process eventuates in not only a loss in capacity, but also in safety hazards due to the high flammability and the present vapor pressure of the organic liquid itself as well as the developing gaseous degradation products. In addition, due to abrupt leakage when mechanical forces are applied (e.g. in car accidents) or overheating as a course of sudden and uncontrolled discharge (‘*short circuits*’ e.g. due to dendrite growth), the *thermal runaway* may also cause ignition or in the last resort even explosion of the battery.[1.17] Therefore, to use the electrolytes safely, technical measures such as hermetic metal encasements or relief valves are necessary, which lead to a decrease in the effective energy density of the battery and do not provide the flexible, shape-effective requirements dictated by the progressing electronic miniaturization.[1.5]

Owing to these serious drawbacks, which reveal the limitations of *state-of-the-art* batteries, new approaches of alternative electrode and electrolyte materials are currently under development, particularly in due consideration of the critical secondary battery parameters such as high specific energy and power, robust cycle life, short charge time, negligible loss of performance by self-discharge, low cost and finally reliable safety.[1.1]

From the electrode side, combinations of cathode and anodes working in the stability window of common electrolytes are attractive to improve safety. However, replacing for example graphite by a 1.5 V $Li_4Ti_5O_{12}$ anode and $LiCoO_2$ by a 3.5 V $LiFePO_4$ cathode,[1.18] the outcome is a battery with a lower voltage level.[1.19][1.20] Nevertheless, $LiFePO_4$ is found already in commercial batteries since it has some advantages over $LiCoO_2$ including less toxicity, reasonable high capacity, lower costs and finally due to the strength of the P-O-bonds a higher intrinsic stability. Yet, the reduced operating voltage restricts the usage in high voltage applications.

For the electrolyte side, innovative chemistry is still required, not only to make high voltage cathodes accessible, but also to solve the safety issues discussed above.

1.1.3 Types of Electrolytes

In principle, an electrolyte should satisfy the following criteria:[1.3][1.21]

- High lithium ion conductivities ($\sigma_{Li+} > 10^{-3}$ S·cm^{-1}) and chemical stability over the temperature range of battery operation (usually from -20 °C up to +60 °C).[1.22]
- Large energy separation between LUMO and HOMO equivalent to a broad ‘*window*’ in which the electrolyte is electrochemically stable.
- High electronic resistivity ($\sigma_e < 10^{-10}$ S·cm^{-1}).
- High transference numbers: Optimal $\sigma_{Li+}/\sigma_{total} \approx 1$.

- Retention of good electrode/electrolyte interfacial contact and chemical stability with respect to the electrodes. This includes fast and stable *SEI* formation.
- Fire resistance.
- Low toxicity.
- Low cost.

Many pathways exist for designing electrolytes exhibiting improved properties. In case of liquid (cyclic carbonate) based electrolytes, which are reasonably good solvents for lithium salts,[1.23] the embedding of electrolyte additives is an economic and effective method to overcome certain problems. Among others there are additives to build up stable *SEI* layers, cathode protection agents, redox-shuttles to protect from overcharge and *thermal runaway*, fire-retardants and finally alternative lithium salts or $LiPF_6$ salt stabilizers, respectively.[1.24][1.25] Especially the salt stabilizer are rather substantial, since $LiPF_6$ can undergo autocatalytic decomposition into LiF and PF_5, which subsequently reacts with cyclic carbonates above 60 °C.[1.26]

P. V. Wright's discovery in 1973, showing that alkali metal salt complexes of poly-(ethylene oxide) (PEO) show substantial ionic conductivity,[1.27] was the starting point for manifold approaches in order to substitute the potentially hazardous liquid electrolytes by solvent-free ion conducting polymer electrolytes. Following main routes of *'salt-in'* polymer electrolytes were explored:[1.22][1.28]

(i) Dry solid (polymer) electrolytes (*SPE*s):[1.29]

- Polymer electrolytes consisting of a lithium salt, e.g. LiTFSI, dissolved in an amorphous polymer; typically polyether-based, where a special separator is not necessary. Conductivities $\leq 1 \times 10^{-4}$ S·cm^{-1} at ambient temperatures. Ion migration is believed to occur mainly through continuous change of coordination sites and is scaled by temperature dependent segmental motion of the complexing segments. Accordingly, notable conductivities are solely observed above the glass transition temperature of the polymer host. Therefore, attention focuses on *'low-T_g'* polymer materials showing poor mechanical stability.[1.30] Thus, in dual-phase polymers two polymer blocks are linked in order to combine the mechanical stability of one block with the conducting characteristics of the other one in a single material.[1.31] In '*single-ion*' conductors the anion function is additionally fixed to the polymer.[1.32] The apparent level of conductivity is generally lower compared to '*salt-in*' systems described before,[1.28][1.33] which also accounts for inorganic solid lithium ion conducting materials such as $Li_2S + GeS_2 + GeO_2$ glasses.[1.34][1.35] The latter have a wide electrochemical window, but show poor electrode/electrolyte interface properties, limiting their current application to thin-film batteries.[1.36]

(ii) Gel polymer electrolytes:[1.37]

- *Hybrid electrolyte systems* involve a (cross-linked) polymer matrix, e.g. PAN (poly(acrylonitrile)) or PVdF (poly(vinylidene fluoride)), swollen by common liquid carbonate based electrolytes. These systems show high conductivities ($> \sim 1\ S \cdot cm^{-1}$ at ambient temperature) whereas the polymer itself does not act as lithium ion solvent.[1.37] The trapped liquid prevents abrupt leakage; however, safety issues related to liquid cyclic carbonate electrolytes are not avoided and mechanical properties have to be improved.

(iii) Composite polymer electrolytes:[1.21][1.38]

- Mixed ceramic-polymer electrolytes: Enhancement of lithium ion conductivity through incorporation of inert, nanoparticulate ceramic fillers (~ 10 wt%) is considered to be due to a reduction of the polymer host crystallinity (for PEO[1.39]) and surface or grain-boundary conductivity, respectively. '*Soggy sand*' electrolytes, obtained by heterogeneous doping of non-aqueous salt solutions with oxide particles, e.g. mesoporous SiO_2 or TiO_2, were studied by *Maier et al.*, addressing the increase in ionic conductivity upon formation of an oxide particle network.[1.40]

(iv) Ionic liquids (IL):[1.41][1.42]

- Low temperature molten salts (e.g. combination of an imidazole-type cation and a bis(trifluormethanesulfone)imide (TFSI) anion)[1.43] offer several advantages compared to common carbonate based liquid electrolytes: Higher oxidation potential (~ 5.3 V vs. Li^+/Li^0), non-flammability, lower vapor pressure, better thermal stability, and higher lithium solubility. However, one drawback is the poor stability at voltages below 1.1 V due to electrochemically deprotonation of the imidazolium-based cations,[1.44] restricting the usage of low voltage graphite anodes without adding EC as *SEI* formation agent.

In summary, despite great efforts and testing of various compounds as replacements, the ideal electrolyte providing ionic conductivities better than 1×10^{-3} S·cm^{-1} in the temperature range from -20 °C to +60 °C accompanied by mechanical, thermal, and electrochemical stability, has not yet been identified.

Steps ahead in lithium ion battery technology can only be achieved by a breakthrough in electrolyte and electrode materials.[1.1] Improving ionic conductivities requires a better understanding of the fundamentals of ion dissociation and transport within the electrolyte,[1.5] which is the focus of this work.

1.2 Motivation and Aim

Previous studies in our institute based on the general approach of '*immobilizing*' ion solvents revealed that tethering the structural element of EC to a poly(meth)acrylate backbone yielded rather high ionic conductivities, despite the comparably high glass transition temperatures (T_g).[1.45] The latter did not serve as reference temperature for the conductivity in the corresponding modified *William-Landel-Ferry* (*WLF*) plot, suggesting that the ion mobility is controlled by side chain relaxation modes rather than by segmental motion of the polymer backbone.

With respect to these results, which are indicating that the ion mobility is decoupled from the other membrane relevant properties of the polymer, the presented work aims at the synthesis of suitable model compounds in order to study the influence of both, glass transition temperatures and spacer length on the ionic conductivity in more detail.

Indeed, well-defined model compounds allow for reliable analysis of molecular ion transport governed by the complex interplay of numerous parameters within an electrolyte, such as viscosity, salt dissociation, ion-solvent interaction or ion association, hence affecting the bulk conductivity.

Therefore, the model compounds are studied considering following aspects:

- Structure, purity, and stability.
- Thermal properties.
- Ionic conductivity via dielectric impedance spectroscopy.
- Analysis of the ion dynamics by multinuclear Solid-State and PFG NMR studies dependent on spacer length and core.

It is anticipated, that this study provides suggestions for further optimization directions and detailed insights into possible ion conducting mechanisms. The latter is fundamental not only for tailored improvement of current electrolytes, but also for potentially low-cost secondary batteries of high voltage, capacity, and rate-capability, in strong demand for an expected future mass market of electric transport and hence reduction of CO_2 emissions.

1.3 Bibliography

[1.1] Scrosati, B.; Garche, J. *J. Power Sources* **2010**, 195, 2421.

[1.2] Winter, M.; Brodd, R. *J. Chem. Rev.* **2004**, 104, 4245.

[1.3] Goodenough, J. B.; Kim, Y. *Chem. Mater.* **2010**, 22, 587.

[1.4] Scrosati, B. *JEC Battery Newsletters* **1993**, 6, 44.

[1.5] Tarascon, J.-M.; Armand M. *Nature* **2001**, 414, 359.

[1.6] Internet presence, ICCNexergy™.

[1.7] Schalkwijk, van, W.; Scrosati, B. (Eds.), *Advances in Lithium-Ion Batteries* **2002**, Kluwer Academic/Plenum, New York.

[1.8] Zhang, S. S. *J. Power Sources* **2007**, 164, 351.

[1.9] Xu, K. *Chem. Rev.* **2004**, 104, 4303.

[1.10] (a) Lazzari, M.; Scrosati, B. *J. Electrochem. Soc.* **1980**, 127, 773.

(b) Armand, M. in: *Materials for Advanced Batteries*, Eds. D. W. Murphy, J. Broadhead and B. C. H. Steele, Plenum Press, New York, **1980**, 145.

[1.11] Internet presence, GastonNarada*Int*.

[1.12] Fraunhofer ISIT*, Annual Report* **2004**, p. 69.

[1.13] Dolle, M.; Sannier, L.; Beaudoin, B.; Trentin, M.; Tarascon, J.-M. *Electrochem. Solid-State Lett.* **2002**, 5, A286.

[1.14] Tsutsumi, H.; Sumisyoshi, Y.; Onimura, K.; Oishi, T. *Solid State Ionics* **2003**, 160, 131.

[1.15] Yazami, R. *Electrochim. Acta* **1999**, 45, 87.

[1.16] Verma, P.; Maire, P.; Novak, P. *Electrochimica Acta* **2010**, 55, 6332.

[1.17] Vogdanis, L.; Martens, B.; Uchtmann, H.; Hensel, F.; Heitz, W. *Macromolekul. Chem.* **1990**, 191, 465.

[1.18] P. Kubiak, P.; Geserick, J; Hüsing, N.; Wohlfahrt-Meherens, M. *J. Power Sources* **2008**, 175, 510.

[1.19] Paghi, A. K.; Nanjundaswama, K. S.; Masquellier, C.; Okada, S.; Goodenough, J. B. *J. Electrochem. Soc.* **1997**, 144, 1609.

[1.20] Reale, P.; Panero, S.; Scrosati, B.; Garche, J.; Wohlfahrt-Meherens, M.; Wachtler, M. *J. Electrochem. Soc*. **2004**, 151, 12.

[1.21] Scrosati, B.; Vincent, C. A. *MRS Bulletin* **2000**, 3, 28.

[1.22] Meyer, W. H. *Adv. Mater.* **1998**, 6, 10.

[1.23] Xu, K. *Chem. Rev.* **2004**, 104, 4303.

[1.24] Chen, Z.; Qin, Y.; Amine, K. *Electrochim. Acta* **2009**, 54, 5605.

[1.25] Zhang, S. S. *J. Power Sources* **2006***,* 162, 1379.

[1.26] Sloop, S. E.; Pugh, J. K.; Wang, S.; Kerr, J. B.; Kinoshita, K. *Electrochim. Solid-State Lett.* **2001**, 4, A42.

[1.26] Fenton, D. E.; Parker, J. M.; Wright, P. V. *Polymer* **1973**, 14, 589.

[1.28] Wright, P. V. *MRS Bulletin* **2002**, 597.

[1.29] F.M. Gray in *Solid Polymer Electrolytes*, VCH, Weinheim, **1991**.

[1.30] Angell, C. A.; Liu, C.; Sanchez, E. *Nature* **1993**, 362, 137.

[1.31] Ichino, T.; Takeshita, Y.; Rutt, J. S.; Nishi, S. *Polymer Network Blends* **1995**, 5, 21.

[1.32] Sadoway, D. R.; Huang, B.; Trapa, P. E.; Soo, P. P.; Bannerjee, P.; Mayes, A. M. *J. Power Sources* **2001**, 97, 621.

[1.33] Christie, A. M., Lilley, S. J.; Staunton, E.; Andreev, Y. G.; Bruce, P. G. *Nature* **2005**, vol. 43, 50.

[1.34] Adachi, G.-Y.; Imanaka, N.; Aono, H. *Adv. Mater.* **1996**, 8, 127.

[1.35] Kim, Y.; Saienga, J.; Martin, S. W. *J. Phys. Chem. B* **2006**, 110, 16318.

[1.36] Bates, J. D.; Dudney, N. J.; Neudecker, B.; Ueda, A.; Evans, C. K. *Solid State Ionics* **2000**, 135, 33.

[1.37] Lee, S.-Y.; Meyer, W. H.; Wegner, G. *Macromolecules* **1997**, 30, 2092.

[1.38] Stephan, A. M.; Nahm, K. S. *Polymer* **2006**, 47, 5952.

[1.39] Kumar, B.; Scanlon, L. G.; Marsh, R.; Mason, R.; Higgins, R.; Baldwin, R. *Electrochim. Acta* **2001**, 46, 1515.

[1.40] Bhattacharyya, A. J.; Maier, J.; Bock, R.; Lange, F. F. *Solid State Ionics* **2006**, 177, 2565.

[1.41] Webber, A.; Blombergen, G. E. in *Advances in Li-Ion Batteries*, van Schalkwijk, W.; Scrosati, B., Eds.; Kluwer Academic/Plenum Publishers: New York, **2002**; Ch. 6.

[1.42] (a) Garcia, B.; Lavallee, S.; Peron, G.; Michot, C.; Armand, M. *Electrochim. Acta* **2004**, 49, 4583. (b) Wang, Y.; Zaghib, K.; Guerfi, A.; Bazito, F. F. C.; Torresi, R. M.; Dahn, J. R. *Electrochim. Acta* **2007**, 52, 6346.

[1.43] Fernicola, A.; Scrosati, B.; Ohno, H. *Ionics* **2006**, 12, 95.

[1.44] Fuller, J.; Carlin, R. T.; Osteryoung, R. A. *J. Electrochem. Soc.* **1997**, 144, 3881.

[1.45] Britz, J.; Meyer, W. H.; Wegner, G. *Macromolecules* **2007**, 40, 7558.

CHAPTER II

2. Synthesis

Two main series of well-defined model compounds were chosen with the objective to cover a preferably broad range of glass transition temperatures. One series is based on the relatively flexible cyclotriphosphazene (CTP) core, while polyphosphazene itself, well-known for low glass transition temperatures,[2.1-2.3] was not considered. Notably, the build-up of cyclic carbonates from an alkenole functionalized polyphosphazene via epoxidation with metachloroperoxybenzoic acid potentially lead to degradation and chain cleavage due to the rather harsh and oxidative reaction conditions. Indeed, degradation and rearrangement of a variety of different functionalized polyphosphazenes is well documented.[2.1][2.3-2.5]

The second series is based on the rather stiff hexaphenylbenzene (HPB) core, possibly allowing self-assembly and local packing.[2.6] In both cases, the tethered cyclic carbonate (2-oxo-1,3-dioxolane) groups serve as ion solvating moieties. The spacer length between the cyclic carbonate moieties and the different cores as well as the position of the cyclic carbonate was varied, mainly to reveal the impact of the local mobility of the solvating units on the performance as lithium ion conductor. This will be discussed in Chapter IV and V.

2.1 Cyclotriphosphazene based Model Compounds

2.1.1 Why Cyclotriphosphazenes and not the Polymer Analogues?

Polyphosphazenes have been reported with a spectrum of potential applications such as fire retardants, biomedical materials or polymer electrolytes for solid lithium ion batteries.[2.1] For the latter, the low glass transition temperature of polyphosphazenes in relation to other common polymers allows for higher ion mobilities and closely related for potentially higher conductivities.

Polymer electrolytes based on polyphosphazenes were first introduced with the synthesis of MEEP by *Austin* and *Allcock* in 1984,[2.7] where MEEP stands for poly-[bis(methoxyethoxyethoxy)phosphazene]. Its characteristics are the very low glass transition of -83 °C, its complete amorphicity, and the high amount of etheric oxygens equivalent to a high number of possible cation coordination sides per polymer repeat unit. Consequently, the ionic conductivity of MEEP blended with lithium triflate gave values in the range of 2.7×10^{-5} $S{\cdot}cm^{-1}$ at ambient temperature,[2.8] which are three orders of magnitude higher compared to a similar PEO system, but nevertheless still insufficient for battery applications. Based on the assumed conducting mechanism in MEEP, denoted as *'hand-to-hand transfer'* of cations between different etheric coordination sites triggered by the internal mobility,[2.1] extensive studies have been made to improve the ionic conductivity as well as the physical properties. The latter is important since MEEP becomes viscous at elevated temperatures, making a separator necessary in order to prevent short circuits in battery operating conditions. Varying the length of the oligo(ethylene oxide) side groups,[2.9] introducing non-coordinative alkoxide side groups to increase the chain flexibility,[2.10] modifying the side groups itself in terms of crown ethers, branched side chains or cyclic carbonates, respectively, and/plus lowering the polyphosphazene chain length are among the investigated pathways to identify the optimum material in terms of internal mobility, ionic conductivity and mechanical properties, respectively.[2.11][2.12]

More recent approaches focus on alternative phosphazene architectures such as polyphosphazenes with cyclotriphosphazene side groups, polymers featuring tri-star geometry or cross-linked cyclotriphosphazenes.[2.13][2.14] In this way ionic conductivities of about 6×10^{-5} $S{\cdot}cm^{-1}$ at room temperature could be achieved, which are among the highest values obtained for unplasticized polymers.

Previous studies in our group based on our general approach of '*immobilizing*' ion solvents revealed that tethering the structural element of EC to poly(meth)acrylate backbones results in rather surprising high ionic conductivities, despite the comparably high glass transition temperatures up to 50 °C for Poly(2-oxo-[1,3]-dioxolan-4-yl)methacrylate (PDOA) (Figure 2.1 and compare Chapter 1.2).[2.15] Therefore, a polyphosphazene analogue is a promising counterpart in order to study in detail the influence of the glass transition temperature on ionic conductivity.

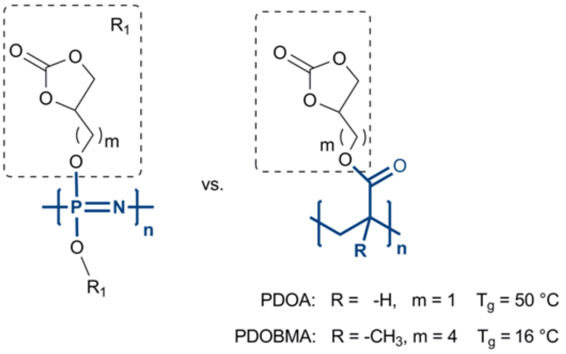

Figure 2.1. Synthesized polymethacrylates and targeted polyorganophosphazene analogue.[2.15]

Starting point of the polyphosphazene synthesis route was the straightforward one-pot in situ synthesis of polydichlorophosphazene (PDCP) after *Wang et al.* (Scheme 2.1).[2.16] Compared to former methods this modification avoids isolation of the highly versatile phosphoranimine monomer by variable temperature vacuum distillation,[2.17][2.18] which is often the main factor for low product yields. Furthermore the utilization of PCl_3 in the monomer synthesis, initially prepared by reaction of PCl_5 with $LiN(SiMe_3)_2$ or $N(SiMe_3)_3$, circumvents instant and concurrent polymerization due to the presence of PCl_5, a well-known initiator for the polymerization of $Cl_3P{=}NSiMe_3$. Besides, no $ClN(SiMe_3)_2$ side product is developed, which also inhibits polymerization.

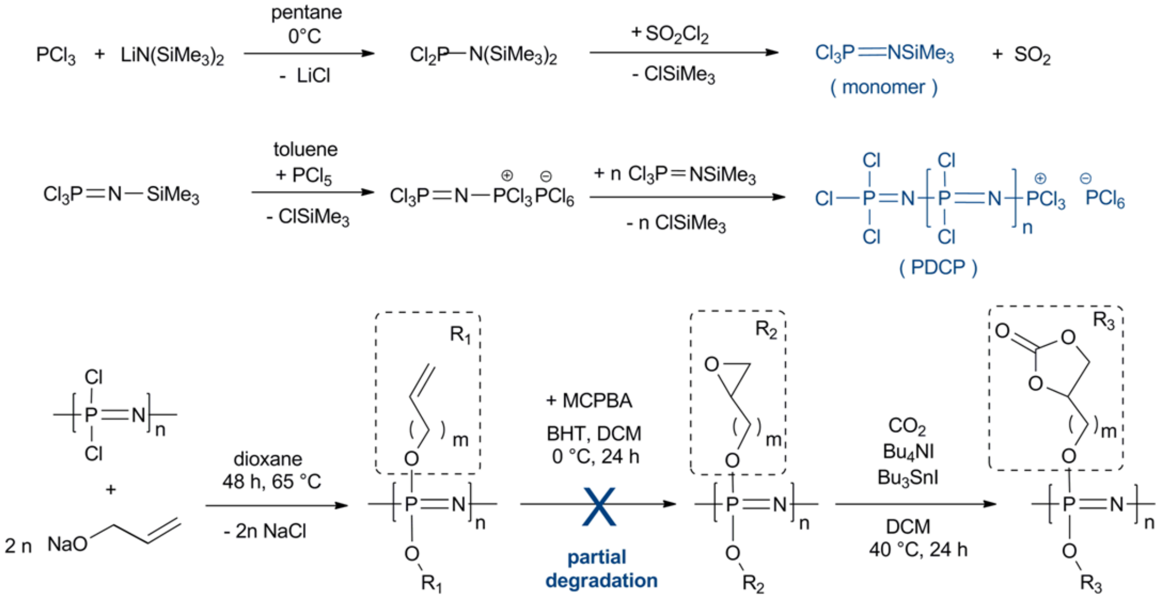

Scheme 2.1. Synthesis of polydichlorophosphazene and reaction pathway to access a cyclic carbonate functionalized polyorganophosphazene.

In order to gain access to polyphosphazenes with tethered 2-oxo-1,3-dioxolane groups an incorporation of the respective side group by macromolecular substitution was limited:

Apart from the reduced solubility of the highly polar alkoxide of 4-(4-hydroxybutyl)-1,3-dioxolan-2-one in polar solvents such as DMF or DMSO, which moderates the reaction rate, the cyclic carbonate group is sensitive against strong bases, e.g. sodium hydride. Consequently, a pathway via secondary reactions on hexen-1-ol and decen-1-ol functionalized PDCP was chosen. While obtaining the former was at first appearance un-problematic (sharp singlet at -8.20 ppm in ^{31}P NMR; signals at +18 ppm and +4 ppm are assigned to the trimeric and tetrameric cyclophosphazene side products), the critical next step, epoxidation of the terminal carbon-carbon double bond, lead to significant chain cleavage and degradation, evident through additional signals between +5 and –5 ppm in the respective ^{31}P NMR spectrum (Figure 2.2(b)).

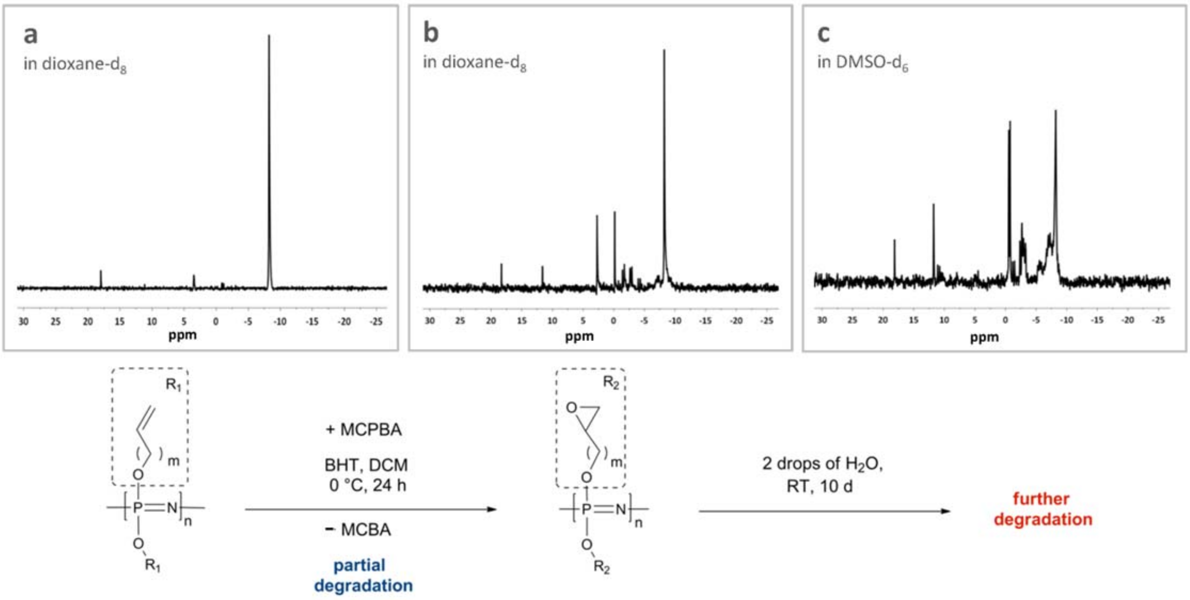

Figure 2.2. ^{31}P NMR spectra of 5-hexen-1-ol functionalized polyorgano-phosphazene: (**a**) before and (**b**) after exposure to MCPBA respectively; (**c**) after stirring 10 days in contact with H_2O.

Stirring the obtained mixture (Figure 2.2(b),(c)) in DMSO-d_6 together with a small amount of water lead to further degradation, monitored by increase of the signals around 0 ppm at expense of the main polymer signal at -8.20 ppm. The peaks around 0 ppm are commonly attributed to phosphoric esters or free phosphoric acid (compare Scheme 2.2).

In addition to bond cleavage in consequence of the harsh reaction conditions, a percentage of defects below the detection limit of NMR due to incomplete substitution of the main chain may also be a reason for the observed degradation and crosslinking. This is supported by the fact that subsequent addition of steric undemanding sodium methoxide has a positive effect on the temporal stability of hexen-1-ol functionalized polyphosphazene. *Rehahn et al.* even postulated that full substitution for the polymer analogue reaction involving PDCP is not possible.[2.19]

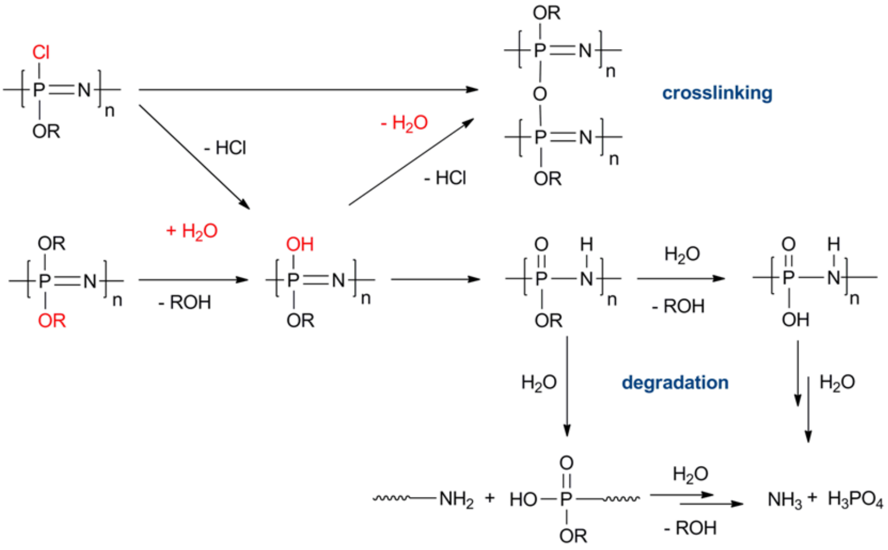

Scheme 2.2. Possible hydrolytic pathway of polyorganophosphazenes leading to crosslinking and degradation.[2.1]

Furthermore, the hexen-1-ol functionality itself may be an inappropriate side group being sensitive against moisture (Scheme 2.2), since apart from the references mentioned earlier, which document degradation of various polyphosphazenes monitored by decrease in molecular weight, even for aryloxy based substituents degradation is reported.[2.20] With respect to these facts our objective to perform a reliable study on the ion dynamics within an electrolyte based on a poly-organophosphazene is not promising due to the doubtful long-time (temperature) stability and possibly varying composition and properties. In case of hexachloro-cyclotriphosphazene, however, full substitution is feasible, so that the cyclic trimer was chosen as well-defined '*low*-T_g' model scaffold providing the basis for a reliable study.

2.1.2 Synthesis of CTP based Model Compounds

The synthetic route employed to prepare 2-oxo-1,3-dioxolane substituted model compounds based on CTP comprises a three step reaction (Scheme 2.3):

First, $N_3P_3Cl_6$ is reacted under inert conditions with the appropriate sodium alkoxide of ω-hexen-1-ol (***1***), ω-decen-1-ol (***4***) or ω-tetradecen-1-ol (***7***), respectively. Not commercially available 13-tetradecen-1-ol (***10***) was prepared by protecting 10-bromodecan-1-ol with 3,4-dihydro-2*H*-puran in presence of *p*-toluenesulfonic acid monohydrate yielding 2-(8-bromodecyloxy)-tetrahydro-2H-puran.[2.21] This compound is refluxed afterwards with an excess of allylmagnesium chloride in THF followed by cleaving the -OTHP-protecting group with p-toluenesulfonic acid in methanol, leading to the requested 13-tetradecen-1-ol.[2.22] After distillation and drying over mole sieve (4 Å), the sodium alkoxide of 13-tetradecen-1-ol was reacted with $N_3P_3Cl_6$.

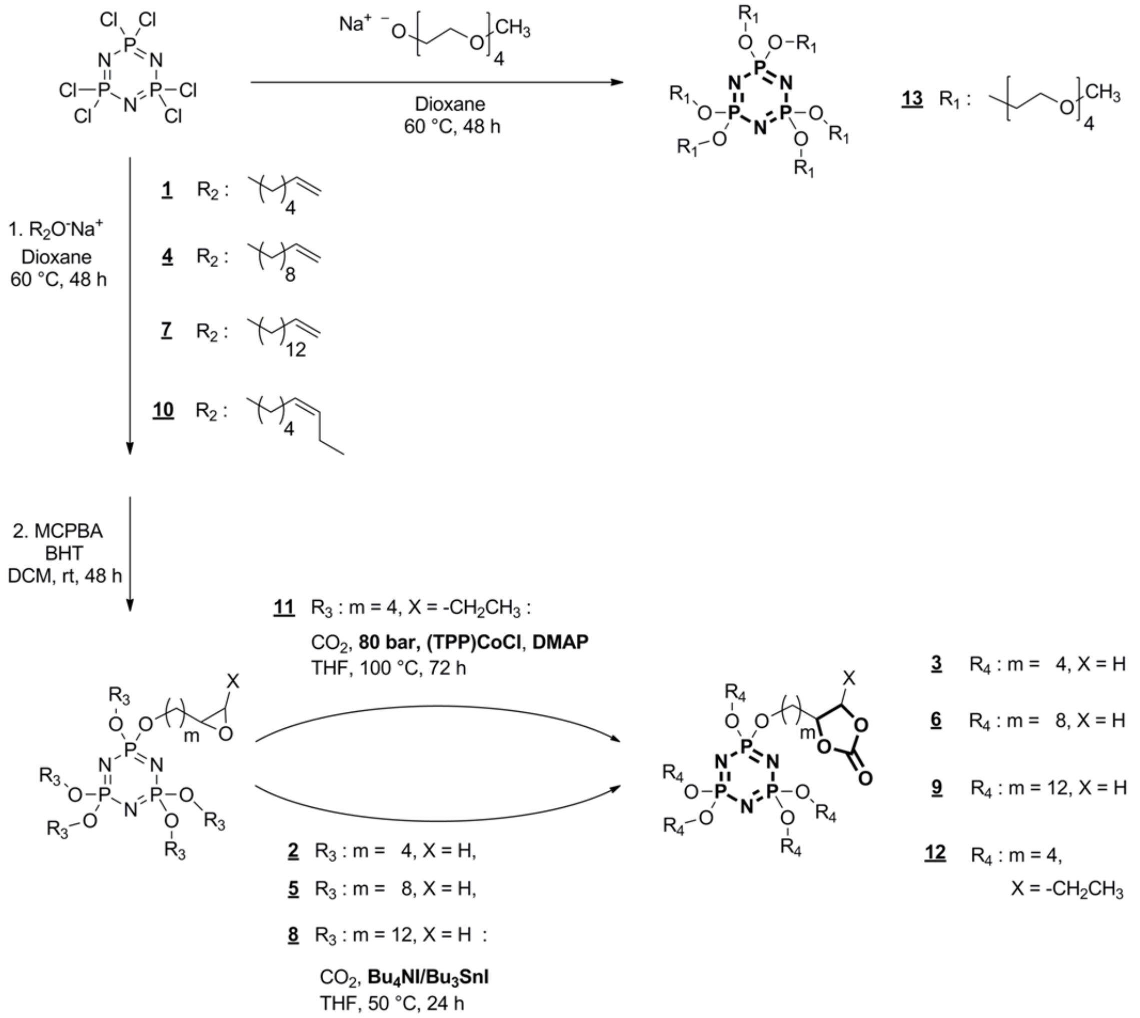

Scheme 2.3. Synthesis of cyclic carbonate and oligo(ethylene oxide) functionalized model compounds based on a CTP core.

Second, epoxidation of the carbon-carbon double bonds was conducted with 3-chloroperoxybenzoic acid (MCPBA) in dichloromethane to yield ***2***, ***5***, ***8***, and ***11***. The mechanism of epoxidation in an indifferent solvent (‘*Prilezhaev reaction*’)[2.59] follows a concerted pathway, proven by retention of the *cis*-configuration for compound ***10*** (Scheme 2.4). Per acids are strongly polarized, resulting in a positive partial charge at one of the per-oxygen, which renders an electrophilic addition to an alkene feasible. In the so-called ‘*butterfly transition state*’ the bonds to the electrophilic oxygen of the per-acid are tied and the hydrogen is transferred.

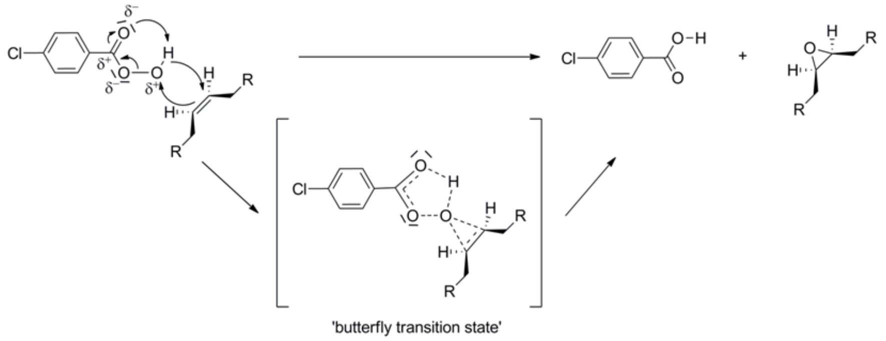

Scheme 2.4. Mechanism of -C=C-bond epoxidation with MCPBA.

The P=N-double bond is hardly affected by MCPBA, since the electron density compared to the C=C-double bond is not high enough, e.g. due the *-I-effect* of the attached alkoxide side groups. In general, epoxidation of a P=N-double bond with MCPBA is possible, if electron donating side groups are attached to the phosphorus and/or the nitrogen.[2.23] However, in the present case it is crucial to use equimolar rather than catalytic amounts of the antioxidant 2,6-di-tert-butyl-4-methylphenol (BHT)

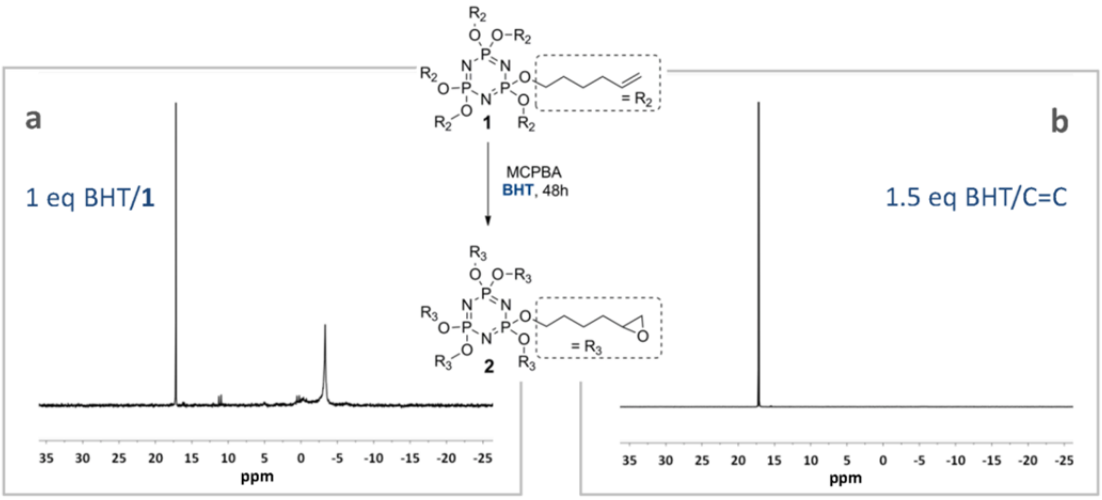

Figure 2.3. ^{31}P NMR spectra applying different amounts of antioxidant BHT (**a**) 1 eq. BHT per mole ***1*** (**b**) 1.5 eq. BHT per -C=CH.

with respect to the amount of MCPBA in order to prevent serious degradation of the CTP core (Figure 2.3).[2.24] BHT functions as scavenger for the radicals present in the reaction due to temperature induced homolytic cleavage of the peroxides.

In the final third step **2**, **5**, and **8** are converted into hexakis-(4-(4-butoxy)-1,3-dioxolan-2-one)-cyclotriphosphazene (**3**), hexakis-(4-(8-octoxy)-1,3-dioxolan-2-one)-cyclotriphosphazene (**6**) and hexakis-(4-(12-dodecyloxy)-1,3-dioxolan-2-one)-cyclotriphosphazene (**9**) by transition metal catalyzed insertion of CO_2 into the epoxide ring.[2.25] The mechanism is outlined in Scheme 2.5.[2.26] In case of *Matsuda et al.* the combination of tributyltin iodide/tetrabutyl phosphonium iodide corresponds to the catalyst A^+X^-.

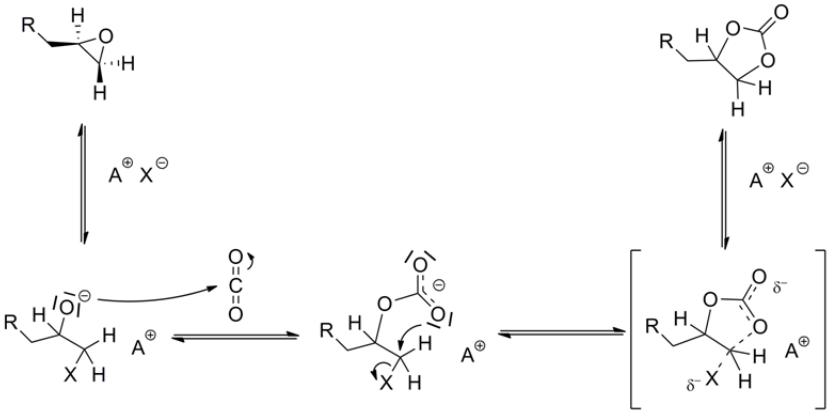

Scheme 2.5. Mechanism of transition metal catalyzed CO_2 insertion into an epoxide ring.[2.26]

It is believed that the iodide in Bu_4PI is transferred to the tin and plays an active role in the catalytic oxirane ring opening. Separately, neither Bu_3SnI nor Bu_4PI shows any catalytic activity. In cases of the compounds **2**, **5**, and **8** even tetrabutylammonium iodide in combination with Bu_3SnI exhibits a sufficient catalytic activity to reach full conversion.

The CO_2 insertion into the internal *cis*-epoxide **11** using tributyltin iodide/tetrabutylammonium iodide as catalyst system, however, was not exceeding 80% of conversion as evidenced by ^1H NMR, despite a higher reaction temperature of 100 °C compared to the terminal epoxides and an applied CO_2 partial pressure of 95 bar. Alternatively, lithium bromide applied in combination with n-methyl pyrrolidone under similar reaction conditions also resulted in a partial conversion of about 90%,[2.27] while a rather rare full conversion of CO_2 insertion into the internal epoxide was achieved in an autoclave applying a highly efficient catalyst system as reported by *Paddock et al.*. The system consists of 2 mol% chlorocobalt tetraphenylporphyrin ((TPP)Co^{III}Cl) and 4 mol% dimethylaminopyridine (DMAP).[2.28-2.30] Commercially available Co^{II}-tetraphenylporphyrin in combination with DMAP was not sufficient due to the limited catalytic activity compared to the oxidized and more electrophilic (TPP)Co^{III}Cl/DMAP complex. The *turnover number* (TON, moles of carbonate produced per mole of catalyst) and the *turn over frequency* (TOF, moles of carbonate per mole of catalyst per hour) for the Co^{III} system are reported to be 30 or 50 times larger respectively ($TON_{TPPCo/DMAP} = 36$ vs. $TON_{(TPP)CoCl/DMAP} = 1102$ and $TOF_{TPPCo/DMAP} = 16$ vs. $TOF_{(TPP)CoCl/DMAP} = 826$).[2.30] The obtained product *cis*:*trans* ratio out of the reaction of ***11*** in the presence of (TPP)Co^{III}Cl/DMAP applying 100 °C and a CO_2 partial pressure of 80 bar amounts to 94:6, supporting the proposed mechanistic pathway from *Paddock et al.*, which suggests retention of the configuration due to double inversion of the stereochemistry at the attacked carbon. The proposed mechanism is shown in Scheme 2.6.[2.30]

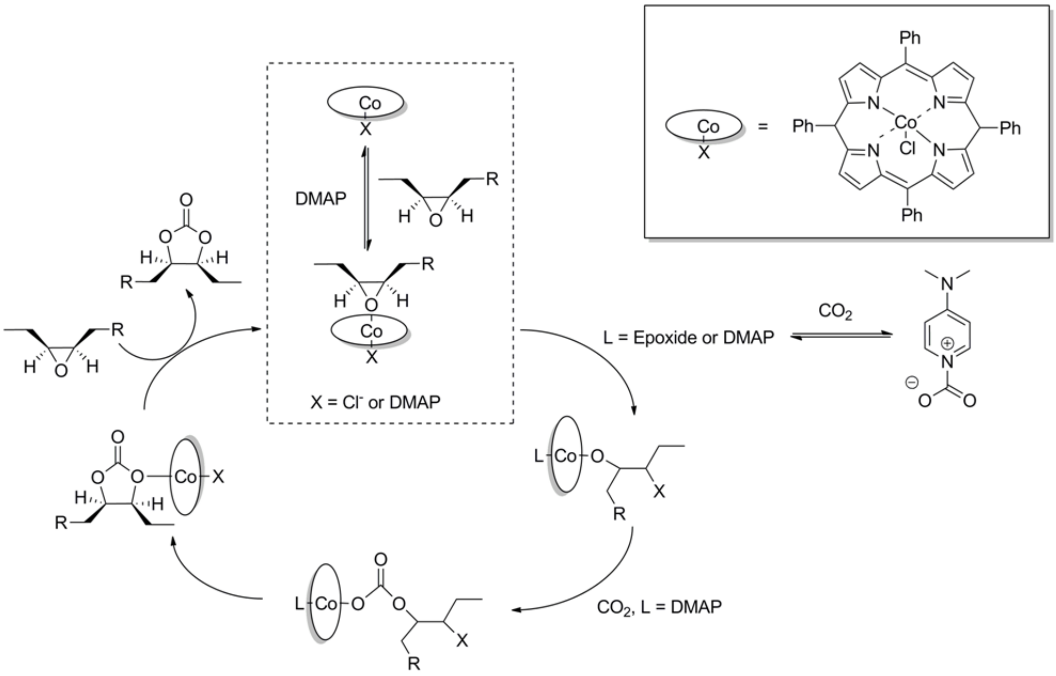

Scheme 2.6. Proposed mechanism for the coupling of CO_2 and epoxides by a Lewis acid/DMAP catalyst system.[2.30]

Starting step is the activation of the epoxide via binding to a coordinately unsaturated lewis acid metal center. Nucleophilic ring-opening results in a metal alkoxide intermediate. DMAP as nucleophilic co-catalyst is required to promote the ring opening of the (TPP)Co^{III}Cl-activated epoxide. In addition, DMAP is supposed to play an important role in facilitating the insertion of CO_2 into the ring-opened intermediate via activation of the carbon dioxide as shown in Scheme 2.6.[2.30] However, too much lewis base is supposed to saturate the free metal binding sites of (TPP)Co^{III}Cl, thereby inhibiting the coordination of the metal center to the epoxide. Notably, two equivalents of co-catalyst were found to be very effective also in this work.[2.31]

In contrast, the degree of stereospecificity for the catalyst system Bu_4NI/Bu_3SnI is lower. Mainly inversion of the configuration occurred, since the observed product *cis*:*trans* ratio applying these conditions to ***11*** was 20:80 (Figure 2.4), consistent to the mechanism shown in Scheme 2.5.

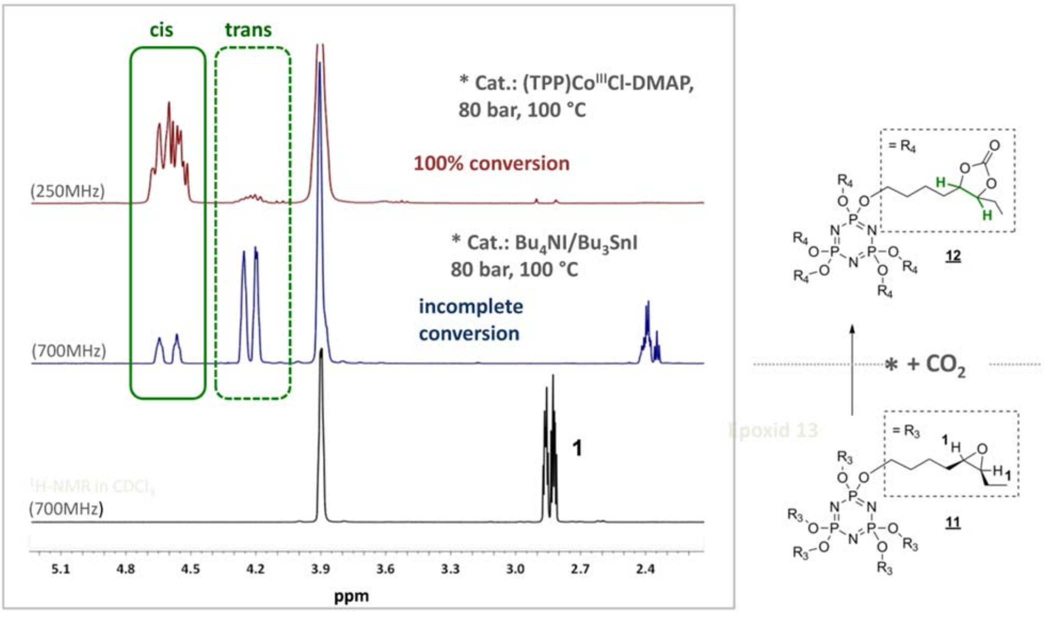

all spectra measured in $CDCl_3$

Figure 2.4. ^{1}H NMR spectra of the CO_2 insertion step dependent on the applied catalyst system.

CTP based model compounds with alternative side groups containing less oxygen atoms, e.g. lactone side groups, were not accessible starting from the epoxy functionalized substances ***2*** and ***5***. Full conversion was either not achieved following a modified procedure applying 1-morpholino-2-trimethylsilyl acetylene and $BF_3{\cdot}OEt_2$,[32] or the reaction conditions were too harsh in terms of the elevated temperature, as e.g. for the reaction of the epoxides ***2*** and ***5*** with diethylmalonate.[33] Consequently, significant degradation of the phosphazene ring was observed, notable by several peaks around 0 ppm in the corresponding ^{31}P NMR spectra. Also the attempt of designing a lactone end group by the exposure of bromoacetic acide and benzoyl peroxide to ***1*** did not lead to the desired product.[2.34]

Following the *Pearson concept*,[2.35] *'softer'* solvating moieties based for example on sulfur are expected to interact less strongly with lithium ions in comparison to the cyclic carbonate units and potentially allow for faster ion mobility. However, attempts to synthesize a cyclic dithiocarbonate starting from epoxide functionalized CTP ***2*** gave only incomplete conversion for the tested catalysts. *Pural MG 30*, a hydrotalcite, and CS_2 interacting with ***2*** showed no conversion,[2.36] while LiBr or LiI in combination with CS_2 and THF as solvent gave maximum conversions of about 80%, with a slightly better performance for LiI.[2.37] Nevertheless, in all cases the reactions were accompanied by slightly degradation of the cyclotriphosphazene ring. Regarding the limited adequacy of imperfect defined model compounds for reliable analysis of molecular ion dynamics, these compounds have not been considered for further investigations.

Finally, an oligo(ethylene oxide) functionalized phosphazene reference ***13*** was prepared simply by reacting $N_3P_3Cl_6$ with the appropriate alkoxide of tetraethyleneglycol monomethyl ether, since EO based electrolytes are well-known for substantial ionic conductivities and remarkable low glass transition temperatures of less than -65 °C.[2.38] Accordingly, ***13*** should help to classify the ionic conductivity of the cyclic carbonate model compounds.

2.2 Hexaphenylbenzene based Model Compounds

2.2.1 General Remarks

Research on lithium ion conducting (polymer) electrolytes focuses to a great extent either on materials exhibiting already a preferably low glass transition temperature and consequently a high intrinsic mobility, or on increasing the flexibility of certain electrolytes via doping with small molecules (compare Chapter I). However, a different approach utilizing self-assembly or preorganization respectively to increase conductivity may be considered. This idea was applied to proton conductors by preparing hexakis(*p*-phosphonato-phenyl)benzene (*p*-6PA-HPB) in the group of *K. Muellen*.[2.6] The *p*-6PA-HPB molecules self-assemble into columnar structures and form an *'inverse-proton-conducting'* cable, since the main structural element is based on an insulating core surrounded by the phosphonic acid groups. The high degree of organization which makes out transport pathways as well as the high concentration of phosphonic acid groups plus the amphoteric character enable proton conductivity through the crystalline material.[2.6] Based on these investigations, HPB was chosen as core for a second main series of model compounds in order to investigate, if the described concept may be transferred also to lithium ion conductors.

2.2.2 Synthesis of HPB based Model Compounds

The synthesis of the key compound (Scheme 2.7) for all HPB models begins with a palladium-catalyzed ethynl-aryl coupling of 4-bromanisol and trimethylsilyl acetylene according to the method of *Sonogashira-Hagihara*,[2.39][2.40] one of the most popular procedures for alkynylation of aryl or alkenylhalids since the application of copper(I) iodide greatly accelerates the cross-coupling reaction and makes a performance at room temperature possible.

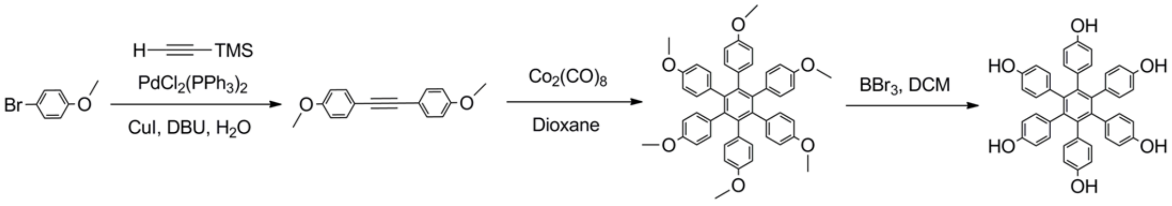

14

Scheme 2.7. Synthesis of hexakis-(4-hydroxyphenyl)-benzene.[2.48]

This observation is also known from the *Stephens-Castro* coupling of copper acetylides and phenyl halides[2.41] and a great advantage compared to earlier studies on this topic by *Heck*[2.42] and *Cassar*,[2.43] whose procedure applying a phosphane-palladium catalyst in combination with an appropriate base required generally higher temperatures. The exact mechanism of the copper-cocatalyzed *Sonogashira-Hagihara* coupling is unknown, but the coupling reaction is believed to take place as shown in Scheme 2.8.[2.44]

The '*palladium catalyst cycle*' begins with a fast oxidative addition of the aryl halide to the initial palladium(0) complex. The next step connects with the cycle of the copper co-catalyst: A rate-determining trans-metalation from the copper-acetylide formed by dehydrogenation generates a $R_1Pd(-C\equiv C-R)(PPh_3)_2$ species. Since the employed amines are generally not basic enough to deprotonate the alkyne, a π-alkyne complex, which makes the alkyne proton more acidic, is supposed to be involved in the copper cycle. In the palladium catalyzed main cycle *trans/cis* isomerization followed by reductive elimination with regeneration of the catalyst gives finally the coupled alkyne. It should be mentioned that one of the main drawbacks of *Sonogashira-Hagihara* cross-coupling is a possible generation of the homo-coupled products of the terminal alkyne, eminently problematic if the terminal alkyne is difficult to obtain.

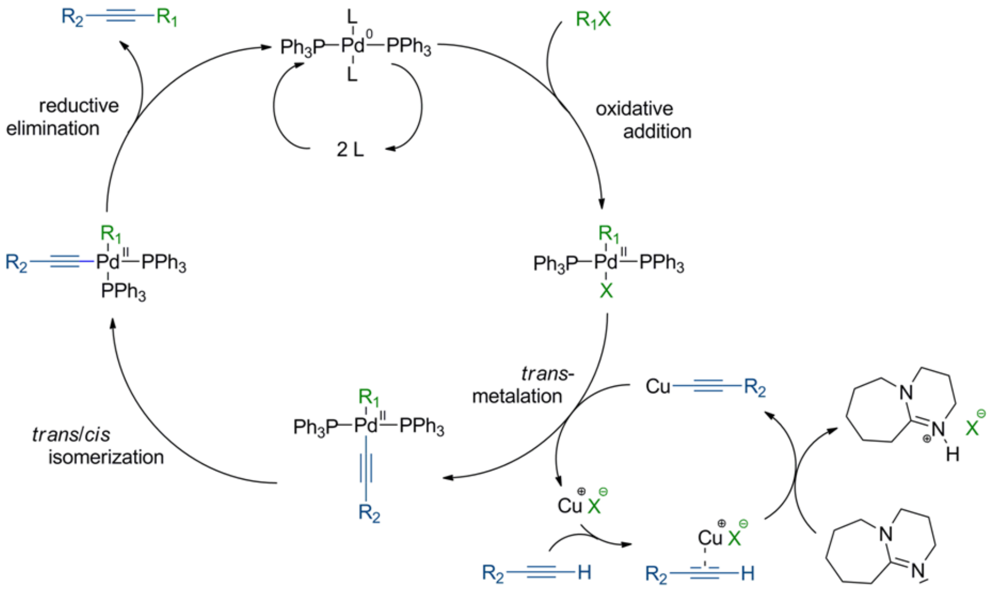

Scheme 2.8. Mechanism of the copper-cocatalyzed *Sonogashira-Hagihara* cross-coupling reaction.[2.45]

The obtained bis(4-methoxyphenyl)acetylene, a so-called *tolane*, was then cyclo-trimerized under the catalytic action of dicobalt octacarbonyl. The mechanism of the [2+2+2] cyclotrimerization shown in Scheme 2.9 is an abbreviated version of the *Knox-Pauson-Spicer* mechanism.[2.46] In a first step [$Co_2(CO)_8$] reacts with an acetylene derivative to [(alkyne)$Co_2(CO)_6$], containing a bridging acetylene ligand. The conversion of this complex to the cobalt-cyclopentadiene ***C*** is believed to occur through a dissociative process via ***A***, which rapidly adds another alkyne (***B***).[2.47] A Diels-Alder like addition of another alkyne to the cyclopentadiene ***C*** is followed by a reductive elimination of the desired arene.

Deprotection of the obtained hexakis-(4-methoxyphenyl)-benzene with boron tri-bromide yielded hexakis-(4-hydroxyphenyl)-benzene (***14***) (Scheme 2.7).[2.48]

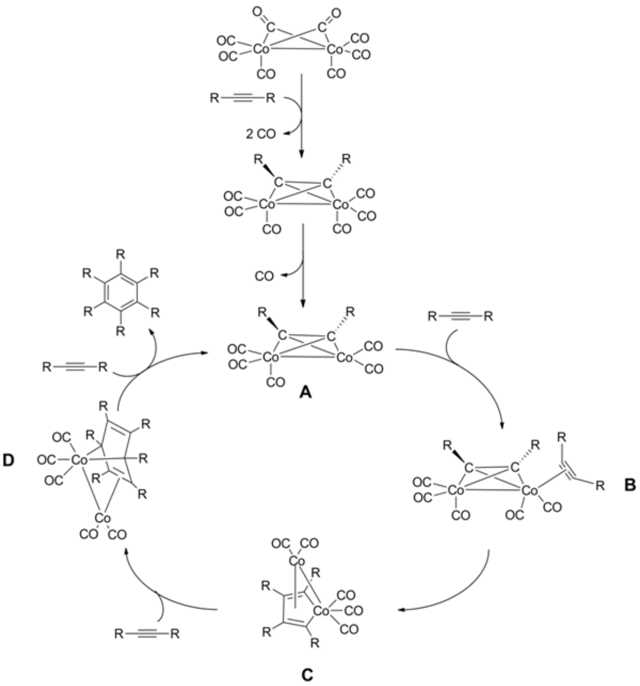

Scheme 2.9. Proposed mechanism of a cobalt-catalyzed cyclotrimerization.[2.46]

Based on the latter as scaffold, the HPB models were built up as followed (Scheme 2.10):

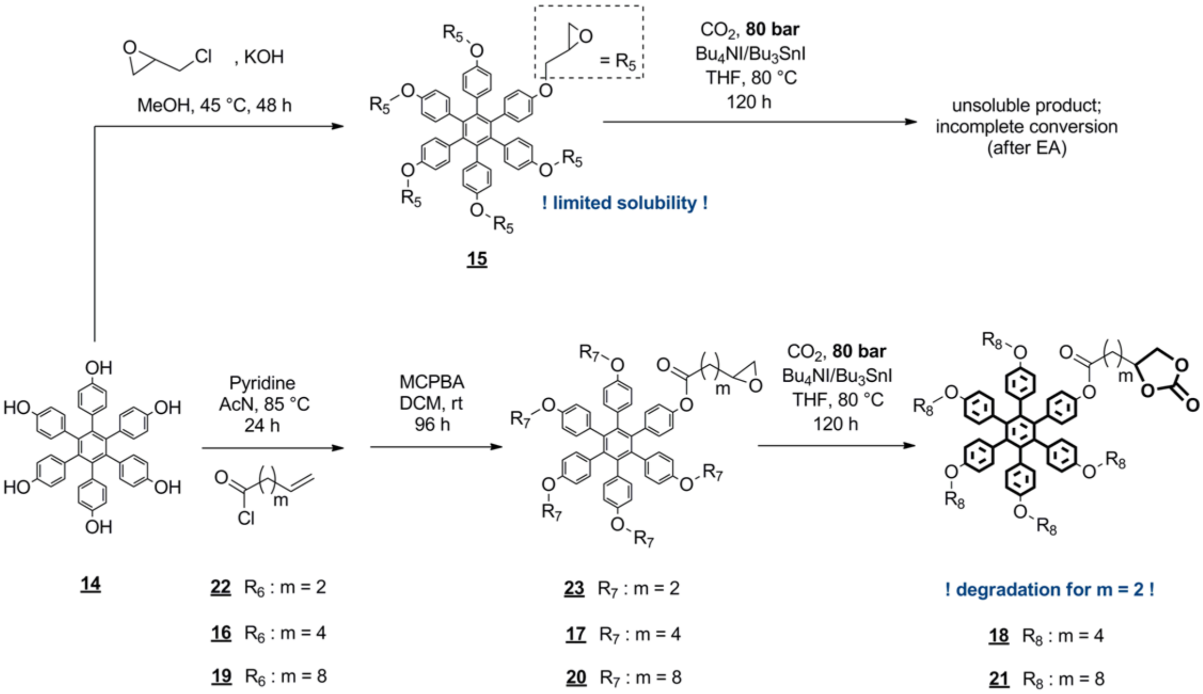

Scheme 2.10. Synthesis of cyclic carbonate functionalized model compounds based on a HPB core.

Hexakis-(4-(hept-4-enoate)-phenyl)-benzene (***16***) and hexakis-(4-(undec-10-enoate)-phenyl)-benzene (***19***) were synthesized via esterification of 6-heptenoyl chloride and 10-undecenoyl chloride respectively with hexakis-(4-hydroxyphenyl)-benzene in the presence of pyridine. The *Einhorn modification* of the *Schotten-Baumann* reaction holds the advantage of preventing possible alkaline hydrolysis of the ester due to the absence of aqueous potassium hydroxide as HCl scavenger and moreover the highly reactive pyridinium intermediate accelerates the rate-determining step of alcohol addition.

The build-up of the cyclic carbonate side group followed a similar way described above for the CTP model compounds. Nevertheless, it is essential that the esterification is performed prior to epoxidation, since otherwise the basic reaction conditions of the esterification lead to epoxide ring opening and subsequent formation of *trans*-1,2-dioles. For both epoxides, ***17*** and ***20***, complete transition metal catalyzed CO_2 insertion was only successful at a CO_2 partial pressure of about 80 bar at a temperature of at least 80 °C. A specific reason for the need of high CO_2 partial pressures in this particular case is unknown. Potentially, the overall reduced polarity and solubility of ***17*** and ***20*** in comparison to the cyclotriphosphazenes results in less effective interactions with the chosen catalyst system and makes higher CO_2 partial pressures necessary.

Due to the adequate accessibility of hexakis-(4-hydroxyphenyl)-benzene more elaborate pathways via cyclotrimerization of cyclic carbonate-functionalized tolanes were not chosen.

Attempts to synthesize a HPB based model compound with a shorter alkyl spacer in order to allow for a higher stacking probability of the HPB moieties proved difficult due to limited solubility. Since the resulting product ***15*** from the reaction of hexakis-(4-hydroxyphenyl)-benzene and epichlorhydrin was hardly soluble in any common solvent, for the subsequent pressurized CO_2 insertion only a limited degree of conversion (≈ 67%, verified by elemental analysis) was achieved.[2.49] This also applies for the reaction pathway starting from hexakis-(4-hydroxyphenyl)-benzene and 4-pentenoyl-chloride. As a consequence of the limited solubility of ***23***, either full conversion was not achieved under the approved conditions, or degradation took place when more harsh temperatures and a higher partial CO_2 pressure were applied.

Similarly, as for the CTP based model compounds an oligo(ethylene oxide) functionalized HPB reference ***26*** was synthesized in order to classify the ionic conductivities of the other cyclic carbonate based HPB model compounds (Scheme 2.11).[2.50]

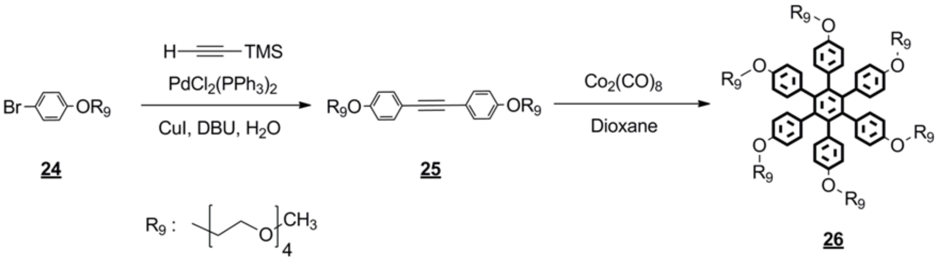

Scheme 2.11. Synthesis of an oligo(ethylene oxide) functionalized model compound based on a HPB core.[2.50]

Thus, a *Sonogashira* reaction of 1-(2-(2-(2-(2-methoxyethoxy)-ethoxy)ethoxy)ethoxy)-4-bromobenzene to ***25*** and subsequent cyclotrimerization lead to Hexakis-(4-(2-(2-(2-(2-methoxyethoxy)ethoxy)ethoxy)ethoxy)-phenyl)-benzene (***26***), bearing the same amount of oxygen atoms per side group than the cyclic carbonate equivalents.

2.3 Tetramethylcyclotetrasiloxane based Model Compounds

In addition to the HPB and CTP based model compounds two tetramethylcyclotetrasiloxane (TMS) based model compounds have been synthesized for further comparison (Scheme 2.12).

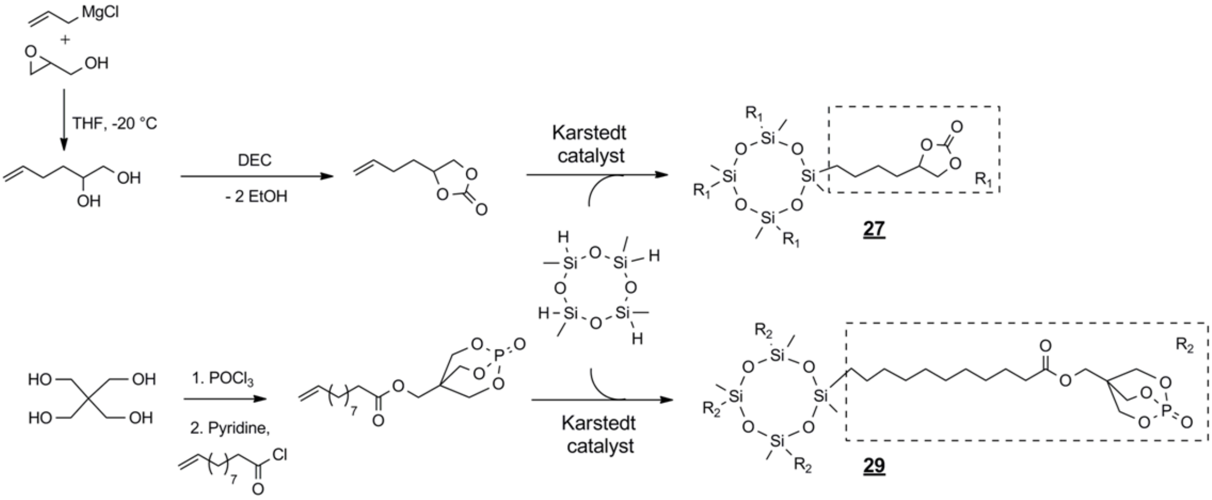

Scheme 2.12. Synthesis route for the tetramethylcyclotetrasiloxane based model compounds.[2.51-2.53]

By means of Platinum(0)-1,3-divinyl-1,1,3,3-tetramethyl-disiloxane (also known as *Karstedt's catalyst*) catalyzed hydrosilylation specific silicon-carbon bonds can be prepared.[2.54] Formally, a -Si-H-functionality is added to an -C=C- or -C≡C-bond following a modified *Chalk-Harrod* mechanism.[2.55][2.56] Thus, in the present case, the cyclic carbonate functionality is attached to tetramethylcyclotetrasiloxane by applying 4-(buten-3-yl)-1,3-dioxolan-2-one together with *Karstedt's catalyst* in toluene. In addition, 1-oxo-4-methoxy-2,6,7-trioxa-1-phospha-bicyclo[2.2.2]octane was implemented as side group. The bicyclic phosphate group benefits on the one side from its excellent heat resistance, rendering it promising for application as flame-retardant constituent, and on the other side can improve the material properties due to its plasticizing effect.[2.57] Alkaline catalyzed ring opening polymerization of ***29*** lead to an insoluble resin and was not considered further.[2.58]

2.4 Summary

An overview on the series of model compounds which have been successfully synthesized gives Scheme 2.13:

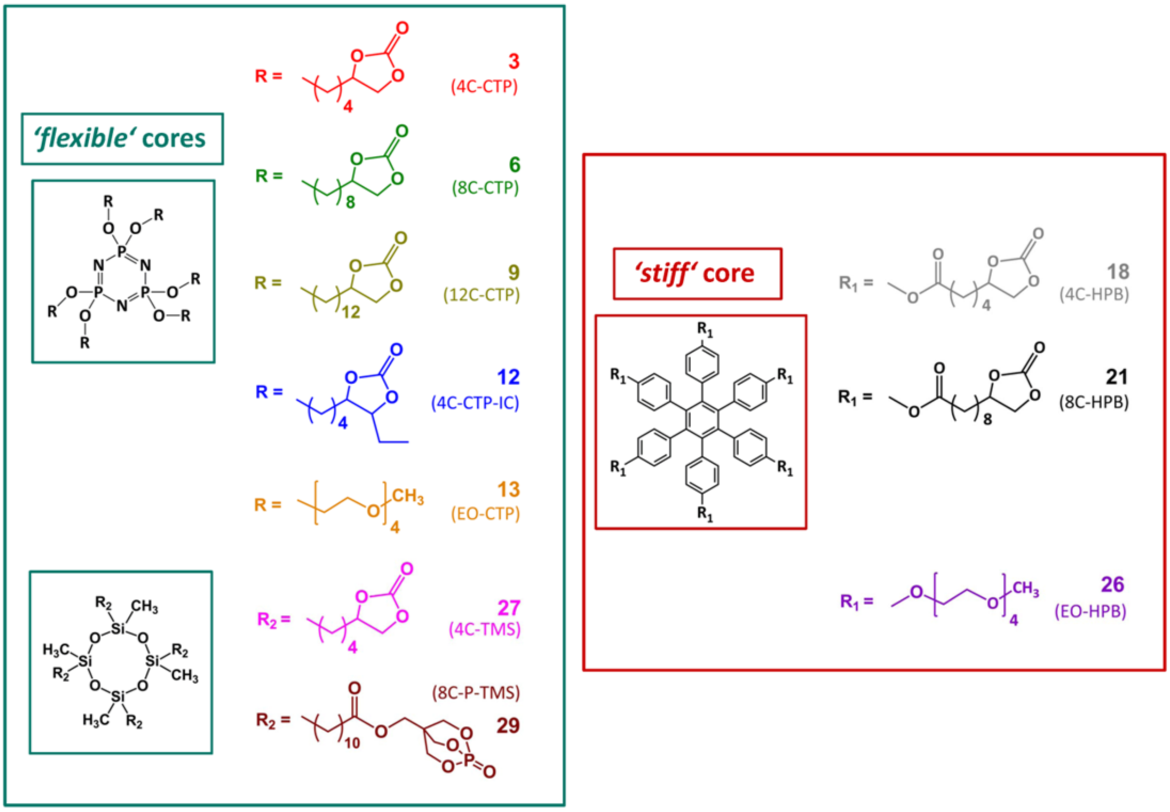

Scheme 2.13. Overview on the relevant HPB, CTP and TMS based model compounds.

2.5 Bibliography

[2.1] Allcock, H. R. in *Chemistry and Applications of Polyphosphazenes*, H.R. Allcock, Wiley-Interscience, New York, **2003**, pp. 528.

[2.2] Kaskhedikar, N.; Burjanadze, M.; Karatas, Y.; Wiemhöfer, H.-D. *Solid State Ionics* **2006**, 177, 3129.

[2.3] Tada, Y.; Sato, M.; Takeno, N. *Macromol. Chem. Phys.* **1994**, 195, 1923.

[2.4] Andrianov, A. K.; Marin, A.; Peterson, P. *Macromolecules* **2005**, 38, 7972.

[2.5] DeCollibus, D.P.; Marin, A.; Andrianov, A. K. *Biomacromolecules* **2010**, 11, 2033.

[2.6] Jimenez-Garcia, L.; Kaltbeitzel, A.; Pisula, W.; Gutmann, J. S.; Klapper. M.; Muellen, K. *Angew. Chem. Int. Ed.* **2009**, 48, 9951.

[2.7] Blonsky, P. M.; Shriver, D. F.; Austin, P.; Allcock, H. R. *J. Am. Chem. Soc.* **1984**, 106, 6854.

[2.8] Blonsky, P. M.; Shriver, D. F.; Austin, P.; Allcock, H. R. *Polym. Mater. Sci. Eng.* **1985**, 53, 118.

[2.9] Allcock, H. R.; Kuharcik, S. E.; Reed, C. S.; Napierala, M. E. *Macromolecules* **1996**, 29, 3384.

[2.10] Allcock, H. R.; Napierala, M. E.; Cameron, C. G.; O'Connor, S. J. M. *Macromolecules* **1996**, 29, 1951.

[2.11] Allcock, H. R.; O'Connor, S. J. M.; Olmeijer, D. L.; Napierala, M. E.; Cameron, C. G. *Macromolecules* **1996**, 29, 7544.

[2.12] Tada, Y.; Sato, M.; Takeno, N. *Macromol. Chem. Phys.* **1994**, 195, 1923.

[2.13] Allcock, H. R.; Sunderland, N. J.; Ravikaran, R.; Nelson, J. M. *Macromolecules* **1998**, 31, 8026.

[2.14] Kaskhedikar, N.; Burjanadze, M.; Karatas, Y.; Wiemhoefer, H.-D. *Solid State Ionics* **2006**, 177, 3129.

[2.15] Britz, J.; Meyer, W. H.; Wegner, G. *Macromolecules* **2007**, 40, 21.

[2.16] Wang, B. *Macromolecules* **2005**, 38, 643.

[2.17] Wang, B.; Rivard, E.; Manners, I. *Inorg. Chem.* **2002**, 41, 1690.

[2.18] Honeyman, C. H.; Manners, I.; Morrissey, C. T.; Allcock, H. R. J. *J. Am. Chem. Soc.* **1995**, 117, 7035.

[2.19] M. Rehahn et al. *New Polyphosphazene-based Polyeletrolytes*, *Makromolekulares Kolloquium* **2008**, Freiburg, Germany.

[2.20] Andrianov, A. K.; Marin, A.; Chen, J. *Biomacromolecules* **2006**, 7, 394.

[2.21] Gebauer, J.; Blechert, S. *J. Org. Chem.* **2006**, 71, No 5, 2021.

[2.22] Zou, Y.; Millar, J. G. *Tetrahedron Letters* **2010**, 51, 1336.

[2.23] Bauer, S.; Marinetti, A.; Richard, L.; Mathey, F. *Angew. Chemie Int. Ed.* **1990**, 29, 1166.

[2.24] Fantin, G.; Medici, A.; Fogagnolo, M.; Pedrini, P.; Gleria, M. *Eur. Polym. J.* **1993**, 29, 1571.

[2.25] Baba, A.; Nozaki, T.; Matsuda, H. *Bull. Chem. Soc. Jpn.* **1987**, 60, 1552.

[2.26] Kossev, K.; Koseva, N.; Troev, K. *J. Molecular Catalysis A* **2003**, 194, 29.

[2.27] Ochiai, B.; Hatano, Y.; Endo, T. *J. Polymer Chem. Part A* **2009**, 47, 3170.

[2.28] Sugimoto, H.; Kuroda, K. *Macromolecules* **2008**, 41, 312.

[2.29] Sakurai, T.; Yamamoto, K.; Naito, H.; Nakamoto, N. *Bull. Chem. Soc. Jpn.* **1976**, 49, 3042.

[2.30] Paddock, R. L.; Hiyama, Y.; McKay, J. M.; Nguyen, S. T. *Tetrahedron Letters* **2004**, 45, 2023.

[2.31] Paddock, L. P.; Nguyen, S. T. *Chem. Commun.* **2004**, 1622.

[2.32] Movassaghi, M.; Jacobsen, E. N. *J. Am. Chem. Soc.* **2002**, 124, 2456.

[2.33] Bonsignore, S.; Dalcanale, E.; Martinengo, T. *Synth. Commun.* **1988**, 18, 2241.

[2.34] Nakano, T.; Kayama, M.; Nagai, Y. *Bull. Chem. Soc. Jpn*. **1987**, 60, 1049.

[2.35] Pearson, R. G. *J. Am. Chem. Soc.* **1963**, 85, 22, 3533.

[2.36] Maggi, R.; Malmassari, C.; Oro, C.; Pela, R.; Sartori. G.; Soldi, L. *Synthesis* **2008**, No. 1, 0053.

[2.37] Kihara, N.; Nakawaki, Y.; Ende, T. *J. Org. Chem.* **1995**, 60, 473.

[2.38] Allcock, H. R.; Ravikiran, R.; O'Connor, S. J. M. *Macromolecules* **1997**, *30*, 3184.

[2.39] Tohda, Y.; Sonogashira, K.; Hagihara, N. J. C. S. *Chem. Commun*. **1975**, 2, 54.

[2.40] Takashi, S.; Kuroyama, Y.; Sonogashira, K.; Hagihara, N. *Synthesis* **1980**, 9, 627.

[2.41] Stephens, R. D.; Castro, C. E. *J. Org. Chem.* **1963**, 28, 2163.

[2.42] Diek, H. A.; Heck, F. R. *J. Organomet. Chem.* **1975**, 93, 259.

[2.43] Cassar, L. *J. Organomet. Chem.* **1975**, 93, 259.

[2.44] Chinchilla R., Najera C. *Chem Rev.* **2007**, 107, 874.

[2.45] Nicolaou, K. C.; Bulger, P. G.; Sarlah, D. *Angewandte Chemie* **2005**, 117, 4516.

[2.46] Baxter, R. J.; Knox, G. R.; Moir, J. H.; Pauson, P. L.; Spicer, M. D. *Organometallics* **1999**, 18, 206.

[2.47] Baxter, R. J.; Knox, G. R.; Pauson, P. L.; Spicer, M. D. *Organometallics* **1999**, 18, 197.

[2.48] Kobayashi, K.; Shirasaka, T.; Sato, A.; Horn, E.; Furukawa, N. *Angew. Chemie Int. Ed.* **1999***,* 38, 23, 3483.

[2.49] Regla, I.; Luviano-Jardón, A.; Demare, P.; Hong, E.; Torres-Gavilán, A.; López-Munguía, A.; Castillo, E. *Tetrahedron: Asymmetry* **2008**, 19, 2439.

[2.50] Lu, Y.; Suzuki, T.; Zhang, W.; Moore, J. S.; Marinas, B. J. *Chem. Mater.* **2007**, 19, 3194.

[2.51] Zhu, Z.; Einset, A. G.; Yang, C.-Y.; Chen, W.-X.; Wnek, G. E. *Macromolecules* **1994**, 27, 15, 4076.

[2.52] McNeill, A. h.; Thomas, E. J. *Tetrahedron Letters* **1993**, 34, 1669.

[2.53] Xie, F.; Wang, Y.-Z.; Yang, B.; Liu, Y. *Macromolecular Materials and Engineering* **2006**, 291, 247.

[2.54] Marciniec, B. *Comprehensive Handbook on Hydrosilation*, Pergamon Press, New York, **1992**.

[2.55] Chalk, A. J.; Harrod. J. F. *J. Am. Chem. Soc.* **1965**, 87, 16.

[2.56] Faglioni, F.; Blanco, M.; Goddard, W. A.; Saunders, D. *J. Phys. Chem. B* **2002**, 106, 1714.

[2.57] Onchi, Y.; Takashi, I.; *United States Patent*, US 6,794,528 B2, **2004**.

[2.58] Suh, H.; Lee, Y. S. *Electrochimica Acta* **2004**, 50, 311.

[2.59] Becker, H. G. O. *Organikum*, Weinheim: Wiley-VCH, **2004**.

CHAPTER III

3. Characterization

Beside the structural clarification of all derivatives by ^{1}H, ^{13}C or ^{31}P solution-state NMR, the compounds were analyzed by elemental analysis and MALDI mass spectrometry respectively (see experimental part for further details), where the thermal behavior is of particular interest concerning the ionic conductivity of the blends with appropriate lithium salts.

3.1 NMR Spectroscopy

All model compounds show good solubility in common organic solvents such as THF, DCM, dioxane, DMSO or DMF. Solubility in THF increases with increasing side chain length. Characterization after purification either by column chromatography or precipitation with subsequent drying in vacuum by ^{1}H, ^{13}C, and ^{31}P solution-state NMR spectroscopy revealed well-defined, fully functionalized and pure products. Figure 3.1 shows representative ^{1}H and ^{31}P NMR spectra of hexakis-(4-(8-octoxy)-1,3-dioxolan-2-one)-cyclotriphosphazene ***6*** and hexakis-(4-(9-(2-oxo-1,3-dioxolan-4-yl)nonanoate)-phenyl)-benzene ***21***.

Similar to all CTP based model compounds, the ^{31}P NMR of ***6*** exhibits a sharp singlet, in this case at $\delta = +17.22$ ppm, proving that equivalent phosphorus atoms exist in the CTP core in agreement with a fully substituted phosphazene ring. The ^{1}H NMR spectra confirm the chemical structure. Characteristic for all model compounds bearing 2-oxo-1,3-dioxolane units are the signals of the tertiary cyclic carbonate proton (9), appearing at around $\delta = +4.6$ ppm, and the secondary methylene protons (10) within the cyclic carbonate ring. The latter show up at around $\delta = +4.0$ ppm and $\delta = +4.5$ ppm, respectively. Also typical for the cyclotriphosphazenes derivatives is the signal of the protons at the α-carbon to the alkoxide group (1) at around $\delta = +3.8$ ppm, slightly dependent on the alkyl side chain length. The hexaphenylbenzene species are identified based on the doublets of the aromatic protons (11) and (12) at circa δ = +6.6 ppm and δ = +6.8 ppm, as well as the methylene protons in α-position to the ester linkage at δ = +2.4 ppm.

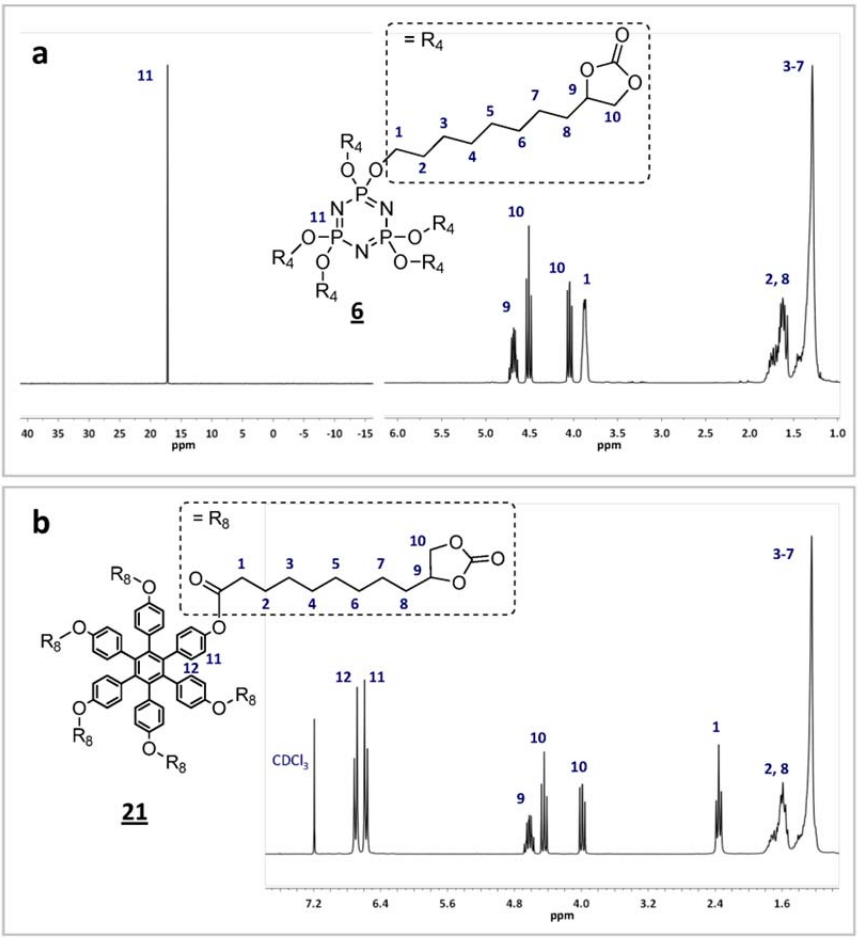

Figure 3.1. (**a**) ^{31}P NMR (left) and ^{1}H NMR spectra (right) of CTP model compound ***6***. (**b**) ^{1}H NMR spectra of HPB model compound ***21*** (see Figure 2.13 for sample numbering).

3.2 Thermal Properties

3.2.1 Thermal Gravimetric Analysis - TGA

Investigations on the thermal stability where performed at a heating rate of 10 K·min^{-1} under N_2 atmosphere by measuring the thermo gravimetric weight loss. The onset of degradation/decomposition was set at the temperature, where a distinct weight loss (about 1%) was observed. All model compounds were stable up to at least 235 °C when investigated by TGA under N_2 applying a heating rate of 10 K·min^{-1} (Figure 3.2).

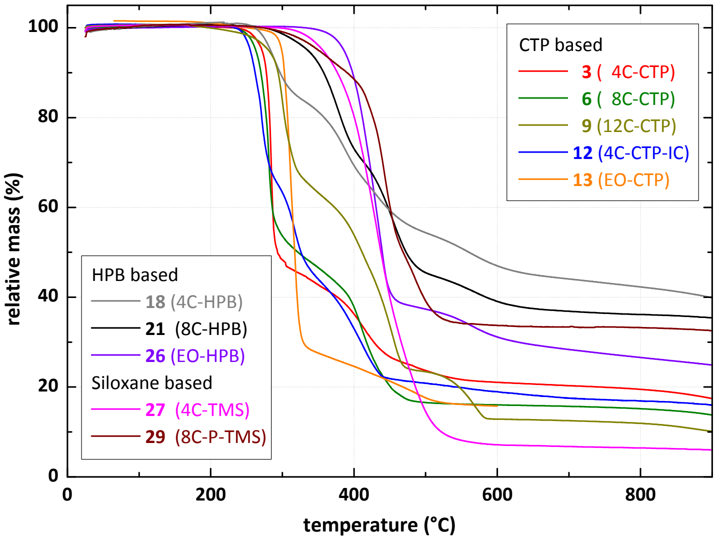

Figure 3.2. TGA traces of the pure model compounds under N_2 at a constant heating rate of 10 K·min^{-1} (see Figure 2.13 for sample numbering).

Decomposition in case of the CTP model compounds bearing cyclic carbonate units starts between 236 °C for ***9*** and 253.8 °C for ***3***, whereas the oligo(ethylene oxide) functionalized equivalent ***13*** is even stable up to 284.5 °C, indicating that the cyclic carbonate decomposes most likely prior to the cyclotriphosphazene ring. Model compounds based on HPB cores bearing cyclic carbonate moieties (***18*** and ***21***) appear to be slightly more stable compared to the CTP derivatives. Similar to the CTP analogues, the oligo(ethylene oxide) functionalized HPB model compound ***26*** is less sensitive to heat.

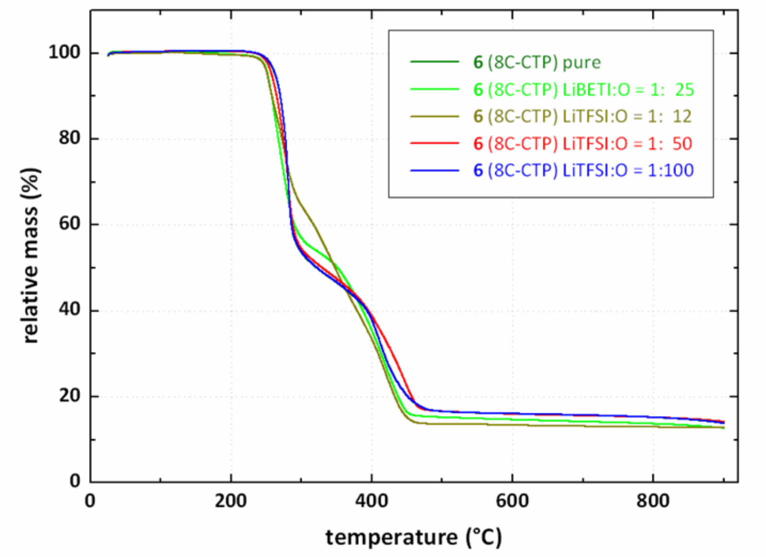

Figure 3.3(a). TGA traces of the model compounds blended with several lithium salts in various Li:O ratios at a constant heating rate of 10 K·min^{-1} (see Figure 2.13 for sample numbering).

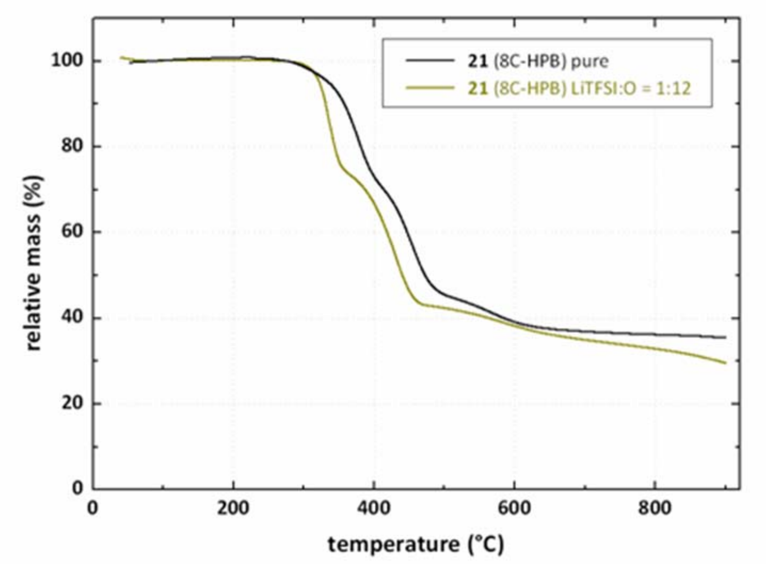

Figure 3.3(b). TGA traces of the model compounds blended with several lithium salts in various Li:O ratios at a constant heating rate of 10 K·min^{-1} (see Figure 2.13 for sample numbering).

For the siloxane compounds a thermal stability up to 324.5 °C was observed, which gives a hint that the cyclotriphosphazene ring is less sensitive to heat than the tetramethylcyclotetrasiloxane scaffold. The thermal stability of the model compounds blended with diverse lithium salts (e.g. LiTFSI, LiBETI or LiBOB) in various concentrations is comparable to those of the respective pure compounds. Selected TGA traces are shown in Figure 3.3(a) (previous page) and 3.3(b).

3.2.2 Thermal Rearrangement of CTP based Model Compounds

In case of the CTP based model compounds, over time, in particular, after extensive heating at elevated temperatures (> 100 °C), additional ^{31}P NMR peaks develop. At first sight, degradation in terms of destruction of the phosphazene ring was expected, however, the TGA results indicate that at this temperature no weight loss occurs. Furthermore, correlated 2D-^{31}P-^{31}P-Correlated NMR spectroscopy revealed that all three novel multipletts at around +15, +7 and 0 ppm, which are not present in the initial sample, show strong ^{2}J and ^{4}J coupling (Figure 3.4). The splitting pattern in each case is a doublet of doublets due to the coupling of the particular phosphorus nucleus with the remaining two magnetic non-equivalent phosphorus nuclei within the cycle.

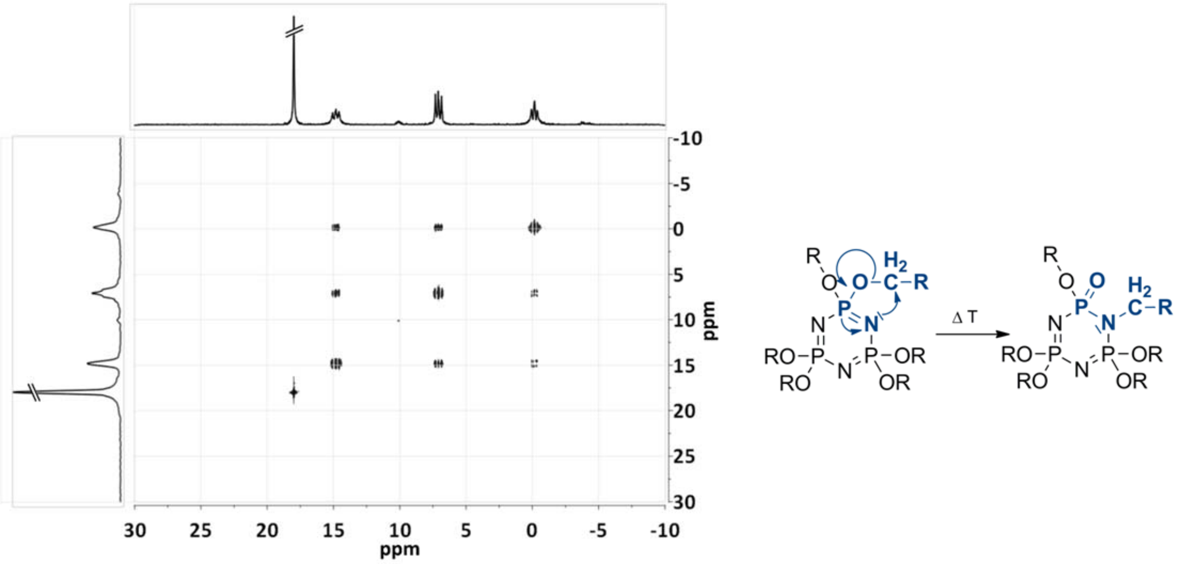

Figure 3.4. ^{31}P-^{31}P-COSY NMR of model compound ***6*** after heating for 72 h at 100 °C in DMSO and proposed mechanism for the thermal induced rearrangement of the cyclotriphosphazene side groups.

Thus, the COSY NMR data indicate that the CTP core remains intact, while the substitution pattern may be a matter of the samples thermal history. The rearrangement is assumed to follow the proposed intra-molecular mechanism shown in Figure 3.4, involving an attack of the nitrogen atom on the α-carbon of the alkoxy group.[3.1] The 2D-^{31}P-^{31}P-Cosy NMR spectrum of thermally treated hexakis(methoxy)cyclotriphosphazene shows an identical splitting pattern described above for ***6***. In addition, the newly developed peak in the ^{13}C NMR spectrum at +25 ppm can be assigned to the =N-CH_3-carbon, which supports the proposed mechanism. The extent of thermal rearrangement after conductivity measurement amounts in general to less than 5% of all phosphorus according to integration of the regarding ^{31}P NMR peaks, indicating that eventual further rearrangements can be excluded. In addition, a full rearrangement of $[N{=}P(OR)_2]_3$ to $[RN\text{-}P({=}O)OR]_3$ rather results in two and not, as observed, three new signals due to the change of the planar geometry of the phosphazene ring system to a boat-like ring structure of the phosphazane, known for the rearrangement of $[N{=}P(OMe)_2]_3$.[3.2]

3.2.3 Differential Scanning Calorimetry - DSC

Differential scanning calorimetry (DSC) was used to study thermally induced phase transitions of the model compounds. Considering the general measurement procedure the probe is sealed in an alumina pan and heated following a distinct annealing program together with a reference, typically an empty alumina pan, which shows no transitions in the regarding temperature range. Any phase transition, e.g. first order (melting, crystallization) or second order (glass transition), results in a heat flux difference necessary to maintain sample and reference pan at the same temperature. The difference in heat flux is monitored and plotted versus the temperature, while second heating profiles were compared. The first inflection point of the curve, where the second derivative is equal to zero, defines the glass transition temperature. From the difference between the extrapolated linear regime of the curve before and after the glass transition, the change in heat capacity Δc_p can be determined.

Figure 3.5 shows thermograms of all HPB and CTP based model compounds. In case of CTP based model compounds apparent glass transitions (T_g) were observed, except for ***9*** bearing the longest alkyl-spacer (12 methylene groups). Model compound ***9*** shows instead a sharp melting transition at 70.5 °C, most likely due to melting of crystallized alkyl side chains, which is supported by sharp reflections in the X-ray diffractogram at RT between 2Θ = 18° and 2Θ = 24°. According to this, the CTP model compound ***6*** bearing an alkyl spacer with 8 methylene groups is at the boundary to crystallization since solidification of ***6*** at room temperature is kinetically hindered and may take up to several weeks or batch-dependent never even happens after months, although characterization by multinuclear NMR spectroscopy, mass spectroscopy and FTIR reveals no differences between the batches. The crystalline sample ***6*** shows an endothermic melting transition at +33 °C plus an exothermic recrystallization transition starting at ‑18 °C (not shown). In contrast, viscous ***6*** exhibits a glass transition at -35.2 °C. Its potential liquid crystal behavior was not further studied.[3.3]

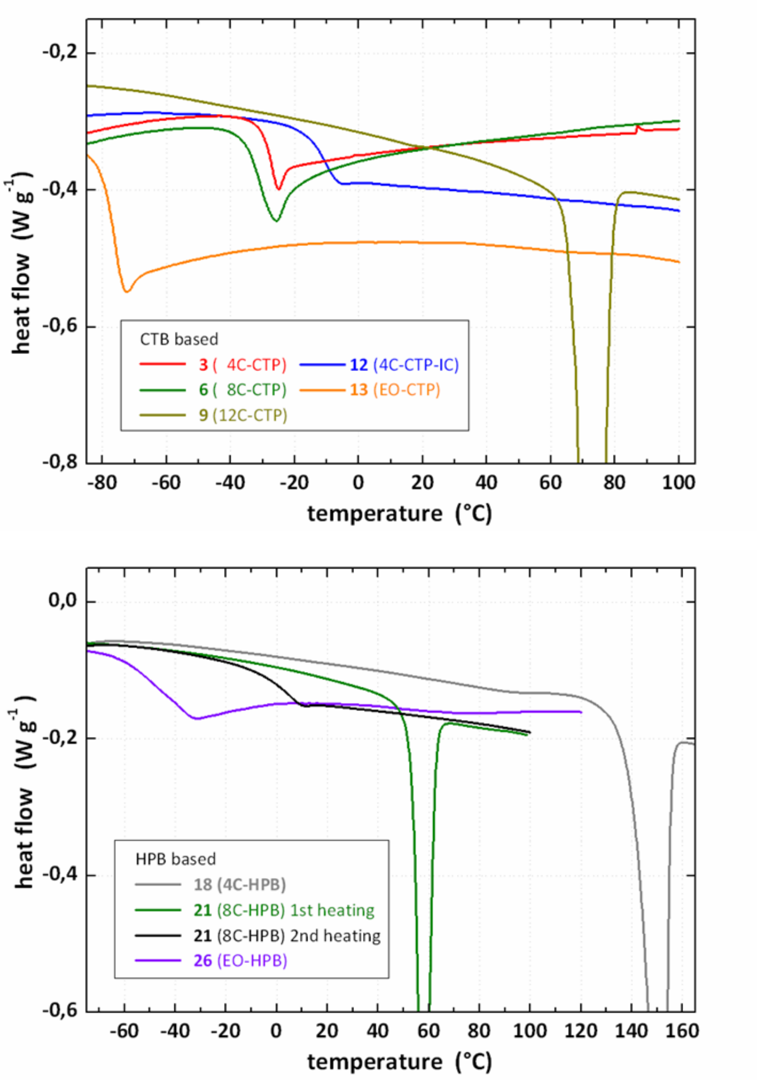

Figure 3.5. DSC traces (second heating) of the pure CTP model compounds (upper graph) and the pure HPB model compounds (lower graph) under N_2 at a constant heating rate of 10 K·min^{-1} (see Figure 2.13 for sample numbering).

The thermal behavior of the HPB based derivatives is more difficult to address since the thermal transitions are very much kinetically controlled. While pure ***18*** shows a sharp, reproducible melting transition at 150.8 °C, the equivalent model compound ***21*** bearing a longer alkyl spacer depicts a melting peak at 58 °C in the first heating scan; subsequent heating and cooling scans exhibit a glass transition at 3.5 °C, where even prolonged annealing for several hours at 15 °C did not lead to partial crystallization. Thus, longer alkyl chains hamper a possible ordering of the HPB cores due to their enhanced local mobility revealed by inhibited crystallization of ***21***. In summary, the glass transitions of the model compound series cover as desired a broad temperature range from -78.1 °C for the EO based CTP derivative up to +3.5 °C for the HPB based cyclic carbonate model compound ***21***. The T_g of pure CTP based ***3*** is -28.9 °C. An increase of the side chain length may induce a greater *free volume*; hence the onset of segmental motion and the glass transition is shifted to lower temperatures. Consequently, compound ***6*** exhibits a slightly lower T_g as compared to compound ***3***.

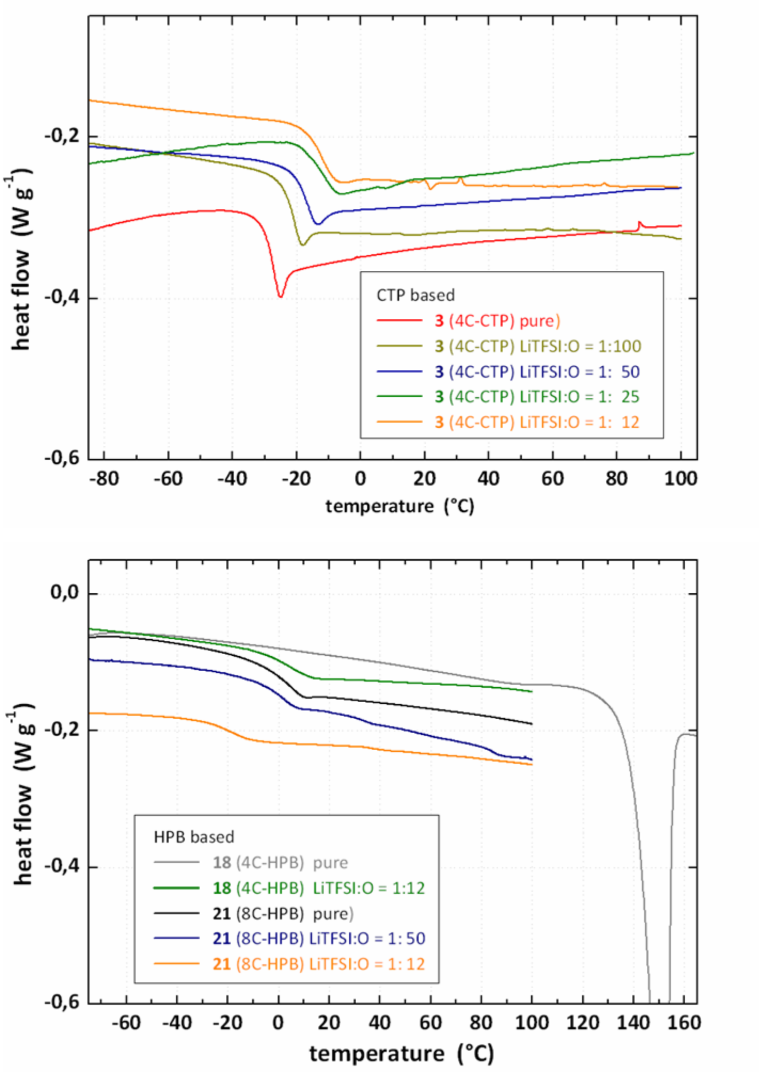

Figure 3.6. DSC traces (second heating) of the CTP (upper graph) and HPB (lower graph) model compounds blended with LiTFSI under N_2 at a constant heating rate of 10 K·min^{-1} (see Figure 2.13 for sample numbering).

The T_g of ***12*** with the internal 2-oxo-1,3-dioxolane group is higher, probably because the mobility of the side chain is decreased compared to ***3*** and ***6***.

The addition of LiTFSI to CTP based model compounds increases the glass transition temperatures with increasing lithium salt concentration due to cation complexation and ion-dipole interactions (Figure 3.6). In contrast, the glass transition temperature of the HPB based substance ***21*** decreases slightly (+2.3 °C) upon addition of LiTFSI in ratio

Li:O = 1:50 and lowers even more in case of Li:O = 1:12 (-18.0 °C). Unlike, the blend of ***18*** with LiTFSI does not show a melting peak as pure ***18*** does, but instead a glass transition well below the melting point of pure ***18***. In both cases the lithium salt is supposed to interfere interactions between the HPB cores. As a consequence, the system dynamics are increasing and a phase transition at lower temperature is observed. Other applied salts such as $LiClO_4$ and LiBOB did not yield a homogeneous mixture in combination with ***21***, so that no plasticizing effect was observed.

The oligo(ethylene oxide) functionalized materials ***13*** and ***26*** exhibit lower glass transition temperatures than the cyclic carbonate analogues, e.g. due to higher mobility of the oligo(ethylene oxide) side groups and their weaker electrostatic interactions compared to the model compounds bearing the more polar 2-oxo-1,3-dioxolane functionalities. Addition of LiTFSI to ***13*** and ***26*** increases the glass transition temperatures similar to the other CTP models.

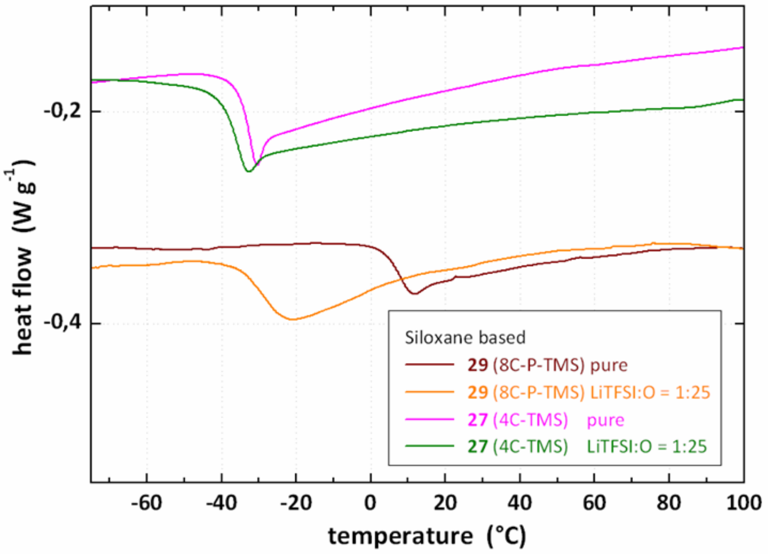

Figure 3.7. DSC traces (second heating) of the siloxane based model compounds blended with LiTFSI under N_2 at a constant heating rate of 10 K·min^{-1} (see Figure 2.13 for sample numbering).

Derivatives ***27*** and ***29*** (Figure 3.7), which are based on a tetramethylcyclotetrasiloxane core show glass transition temperatures in the range of the CTP and HPB based series. This allows for further discussions on the influence of the scaffold by comparing the ionic conductivity values (Chapter IV).

In general, the results above raise the question after the detailed nature of the observed glass transitions, exhibiting a change in heat capacity Δc_p of 0.5 ±0.2 J·g^{-1}·K^{-1}, which is comparable with reported values of polymer analogues as for example poly[bis(methoxyethoxyethoxyethoxy)phosphazene] (MEEEP) ($\Delta c_{p,\mathrm{MEEEP}}$ = 0.85 vs. $\Delta c_{p,\mathbf{13}+\mathrm{LiTFSI}}$ = 0.72-0.87).[3.4] However, while in case of the CTP based models both, core and side chains, are rather flexible and may be involved in the glass transition, for the HPB based ones the core is rather stiff and merely the onset of the side chain motion appears to fit the relatively low glass transition temperatures of the blends. In either cases a thorough analysis of the nature of the glass transition and its influence on the molecular basis of lithium ion transport by Solid-State NMR was investigated and will be discussed in Chapter V.

Notably, all blends utilized in the further work have been investigated in the amorphous state, which was confirmed based on X-Ray diffraction data.

3.3 Summary

All selected model compounds are pure and structural fully characterized. They show a sufficient thermal stability up to at least 235 °C in pure state as well as blended with various lithium salts, where the CTP models undergo a thermal rearrangement to a small percentage. The glass transitions cover a broad temperature range as intended, starting from -78.1 °C for the pure oligo(ethylene oxide) functionalized CTP up to +3.5 °C for the pure HPB based model compound featured by an alkyl chain of eight methylene groups between core and the lithium solvating groups. Tables 3.1 and 3.2 give an overview over the thermal properties of the respective model compounds.

3.4 Bibliography

[3.1] Doughty, S. W.; Fitzsimmons, B. W.; Reynolds, C. A. *J. Chem. Soc., Dalton Trans.* **1997**, 367.

[3.2] Thomas, B.; Paasch, S.; Böhme, U. *Z. Anorg. Allg. Chem.* **2005**, 631, 85.

[3.3] Pugh, C.; Percec, V. *J. Mater. Chem.* **1991**, 1(5), 765.

[3.4] Landry, C. J. T.; Ferrar, W. T.; Teegarden, D. M.; Coltrain, B. K. *Macromolecules* **1993**, 26, 35.

Model Compound^a	T_g (°C)	T_d (°C)	T_m (°C)	Δc_p (J $g^{-1}K^{-1}$)	ΔH_m (J g^{-1})
3 - *pure*	-28.9	253.8	-	0.47	-
LiTFSI:O = 1: 12	-12.7	nm	-	0.42	-
LiTFSI:O = 1: 25	-13.4	nm	-	0.44	-
LiTFSI:O = 1: 50	-18.4	nm	-	0.38	-
LiTFSI:O = 1:100	-22.2	nm	-	0.43	-
LiBOB:O= 1: 25	- 7.9	nm	-	0.41	-
$LiClO_4$:O= 1: 50	-22.9	nm	-	0.40	-
9 - *pure*	-	236.0	70.5	-	53.8
LiTFSI:O = 1: 25	-24.4	nm	-	-	-
12 - *pure*	-16.6	246.2	-	0.51	-
LiTFSI:O = 1: 50	-12.1	244.0	-	0.49	-

Model Compound^a	T_g (°C)	T_d (°C)	T_m (°C)	Δc_p (J $g^{-1}K^{-1}$)	ΔH_m (J g^{-1})
6 – *pure **	-35.2	247.7	-	0.59	-
LiTFSI:O = 1: 12	-24.5	234.7	-	0.46	-
LiTFSI:O = 1: 25	-32.5	nm	-	0.51	-
LiTFSI:O = 1: 50	-34.1	246.3	-	0.55	-
LiTFSI:O = 1:100	-32.5	248.7	-	0.43	-
LiBOB:O = 1: 25	-25.9	nm	-	0.51	-
$LiClO_4$:O = 1: 25	-24.5	nm	-	0.51	-
LiBETI:O = 1: 25	-30.2	236.5	-	0.46	-
13 - *pure*	-78.1	284.5	-	1.28	-
LiTFSI:O = 1: 12	-48.2	nm	-	0.72	-
LiTFSI:O = 1: 25	-61.4	nm	-	0.87	-
LiTFSI:O = 1: 50	-61.6	nm	-	0.87	-

T_g = glass transition (DSC); T_m = melting transition; T_d = onset of weight loss / degradation after TGA; Δc_p = change in heat capacity; ΔH_m = melting enthalpy; nm = not measured; * non-crystalline, see text; phase transition observed from 2nd heating in DSC.

Table 3.1. Thermal transitions and thermodynamic parameters of the CTP based model compounds including the respective blends (see Figure 2.13 for sample numbering).

Model Compound^a	T_g (°C)	T_d (°C)	T_m (°C)	Δc_p (J $g^{-1}K^{-1}$)	ΔH_m (J g^{-1})
18 - *pure*	-	268.8	150.8	-	46.7
LiTFSI:O = 1: 12	24.7	258.1	-	0.24	-
21 - *pure*	3.5	295.5	-	0.31	-
LiTFSI:O = 1: 12	-18.0	289.3	-	0.37	-
LiTFSI:O = 1: 25	-10.2	nm	-	0.41	-
LiTFSI:O = 1: 50	2.3	nm	-	0.37	-
$LiClO_4$:O= 1: 12	4.1	nm	-	0.45	-
LiBOB:O = 1: 12	9.7	nm	-	0.41	-

Model Compound^a	T_g (°C)	T_d (°C)	T_m (°C)	Δc_p (J $g^{-1}K^{-1}$)	ΔH_m (J g^{-1})
26 - *pure*	-47.4	360.7	-	0.58	-
LiTFSI:O = 1: 18	-22.9	324.4	-	0.48	-
LiTFSI:O = 1: 37	-37.4	358.2	-	0.59	-
LiTFSI:O = 1: 50	-39.2	342.4	-	0.60	-
$LiClO_4$:O = 1: 37	-32.7	267.5	-	0.75	-
LiBOB:O = 1: 37	-36.1	285.9	-	0.63	-
27 - *pure*	-34,3	324.5	-	0.41	-
LiTFSI:O = 1: 25	-37.7	-	-	0.42	-
29 - *pure*	6,2	302.5	-	0.27	-
LiTFSI:O = 1: 25	-29,5	-	-	0.39	-

T_g = glass transition (DSC); T_m = melting transition; T_d = onset of weight loss / degradation after TGA; Δc_p = change in heat capacity; ΔH_m = melting enthalpy; nm = not measured; phase transition observed from 2nd heating in DSC.

Table 3.2. Thermal transitions and thermodynamic parameters of the HPB and TMS based model compounds including the respective blends with lithium salts (see Figure 2.13 for sample numbering).

CHAPTER IV

4. Lithium Ion Conductivity

Conductivity is the result of charge carrier transport and is closely connected to diffusion, since the diffusion coefficient describes the transport of matter. In contrast to electronic conductivity, charge transport in ionic conductors is related to the migration of ions, which is of great importance for e.g. electrochemical energy storage. Various types of (polymer) electrolytes in which ion transport is taken place have been introduced earlier (chapter I). In order to determine the ionic conductivity either direct (DC) or alternating current (AC) methods can be applied.[4.1-4.3] However, in case of DC measurements, active (*non-blocking*) electrodes are necessary, which subsequently deliver charge carriers into the electrolyte and whose interphase to the electrolytes therefore has to be permeable for the respective ions. In practice, problems related to the reversibility of the active electrodes in the desired temperature window arise. Thus, the DC conductivities are frequently derived from AC conductivities via extrapolation to zero frequency. Indeed, dielectric spectroscopy constitutes the most common method to determine AC ionic conductivities of organic electrolytes, which will be explained in detail in the upcoming paragraphs.[4.2]

4.1 Dielectric Spectroscopy [4.1-4.3]

The basic principle of dielectric spectroscopy is rather simple: A system consisting of a (polymer) dielectric probe placed between two inert (*blocking*) electrodes of a capacitor is exposed to a sinusoidal voltage ($V(\omega, t) = V_0 \sin(\omega\, t)$). In order to relate the current reply of the system ($I(\omega, t) = I_0 \sin(\omega\, t + \theta)$) to the applied voltage two parameters are necessary: One represents the motion of present ions into the direction of the oppositely charged electrodes. This is equal to the ratio of the voltage and current maxima V_{max}/I_{max} or in other words the resistance R. The other is the phase shift θ between voltage and current. The combination of these two parameters gives the impedance Z of the system, corresponding to the total response of the material on the alternating field. Generally, the magnitude of the impedance $|Z| = V_{max}/I_{max}$ and the phase shift θ are dependent on the frequency f.

Thus, in a typical AC experiment the impedance of the system or the cell respectively is measured as a function of the frequency f of the applied signal over a wide frequency range.

4.1.1. Determination of DC Conductivity via Complex Impedance [4.1][4.3]

Dealing with AC circuits mathematically, the regarding parameters are expressed in complex numbers. The general expressions for current and voltage are

$$V(\omega, t) = V_0 \exp(i(\omega t + \varphi_v)) \qquad \textbf{eq. 4.1}$$

$$I(\omega, t) = I_0 \ \exp(i(\omega t + \varphi_I)) \qquad \textbf{eq. 4.2}$$

with $V(t)$ and $I(t)$ the time-dependent amplitudes of voltage and current, t the time, $\omega = 2\pi f$ the angular frequency and φ_I or φ_v respectively the phase difference between current and voltage.

In case of a linear behavior of the sample cell, the complex impedance amounts to:

$$Z \ = \frac{V_0}{I_0} \exp(i\theta) = \ |Z| \exp(i\theta) = Z' - i\, Z'' \quad with \quad \theta = \varphi_V - \varphi_I \, . \qquad \textbf{eq. 4.3}$$

So, the complex impedance is no longer time-dependent, but real and imaginary part of the impedance as well as the phase shift are a function of the frequency.

In the equivalent circuit shown in Figure 4.1 (center) the total impedance of the parallel-connected resistance R and capacitance C can be calculated from the sum of the reciprocal impedances, the so-called complex admittances Y of each element

$$\frac{1}{Z} = Y_R + \ Y_C \ = \frac{1}{Z_R} + \frac{1}{Z_C} \ . \qquad \textbf{eq. 4.4}$$

Since a sinusoidal voltage applied to a resistor is at all time in phase with the current, the frequency-independent impedance

$$Z_R = R \, . \qquad \textbf{eq. 4.5}$$

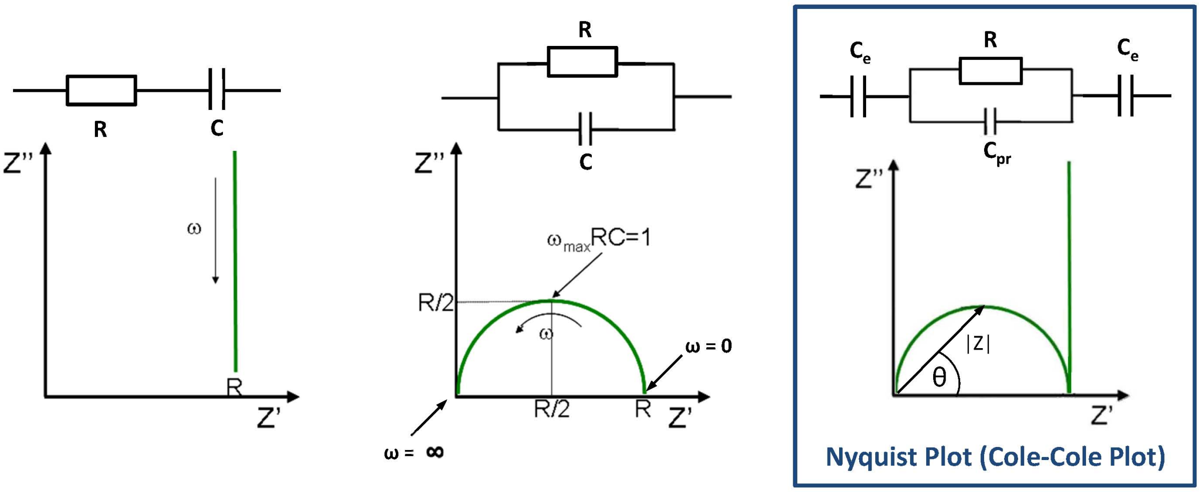

Figure 4.1. Complex impedance plots for a resistor R and a capacitance C in row (left), in parallel (center) and for an equivalent circuit including the capacitance of the electrodes C_e (right).

By contrast, in case of a capacitance the voltage lags $\theta = -\pi/2$ behind the current, so the magnitude of the impedance is frequency-dependent and can be written as

$$Z_C = \frac{1}{i\omega C} \ . \qquad \textbf{eq. 4.6}$$

Applying eq. 4.6 and 4.5 to eq. 4.4 results in the following expression for the complex impedance:

$$Z = \frac{1}{{}^1\!/_R + i\omega C} = \frac{R}{1+(i\omega C)^2} - i\,\frac{\omega R^2 C}{1+(\omega RC)^2}\,, \qquad \textbf{eq. 4.7}$$

including the formulas for the real and the imaginary part

$$Z' = \frac{R}{1+(\omega RC)^2} \quad \text{and} \quad Z'' = -\frac{\omega R^2 C}{1+(\omega RC)^2}\,. \qquad \textbf{eq. 4.8}$$

According to this derivation, the graphical illustration of the complex impedance is based on plotting the imaginary part $-Z''$versus the real part Z'. This is commonly known as *Nyquist* or *Cole-Cole* plot.

The behavior shown in Figure 4.1 (center) is due to two extreme cases:

1. $\omega \longrightarrow 0 \ : Z' \longrightarrow R\,, \quad Z'' \longrightarrow 0\,.$
2. $\omega \longrightarrow \infty : Z' \longrightarrow 0\,, \quad Z'' \longrightarrow 0\,.$

Thus, a parallel combination of a resistor and a capacitor gives rise to a semicircle in the complex impedance plane with two roots at $(0|0)$ and $(R|0)$. Out of the latter the DC conductivity at a certain temperature can be determined, since this measuring point is equal to a direct DC measurement.

In the simplest case of a cell consisting of an electrolyte with only one mobile species sandwiched between two blocking electrodes, assuming that the mobile species in the electrolyte does not take part in any electrode reactions, the electrode polarization delivers an additional part to the impedance. The migrating lithium ions cause a resistance R (*bulk resistance*), while the dielectric polarization of the sample results in a capacitance C_{pr} (*bulk polarization*). Alternating accumulation and depletion of lithium ions at each electrode induces the build-up of equal and opposite electronic charges on the electrodes. Accordingly, each electrode is somehow similar to a parallel-plate capacitor. This is expressed by the capacitances C_e connected in series as shown in the equivalent circuit (Figure 4.1, right). Then the total impedance Z_{total} amounts to

$$Z_{total} = Z + 2\, Z_{electrode}\,, \qquad \textbf{eq. 4.9}$$

where $Z_{electrode}$ is given by

$$2\, Z_{electrode} = \frac{1}{i\,\omega\, C_e}\,. \qquad \textbf{eq. 4.10}$$

Plugging in eq. 4.10 and eq. 4.7 in eq. 4.9,

$$Z_{total} = \frac{R}{1+(\omega\, R\, C_{pr})} - i\left[\frac{\omega\, R^2\, C_{pr}}{1+(\omega\, R\, C_{pr})^2} + \frac{1}{\omega C_e}\right] \qquad \textbf{eq. 4.11}$$

arises as a result.

In general is $C_e \gg C_{pr}$. Thus, the contribution of the electrode capacitance in eq. 4.11 at higher frequencies is negligible, while the impedance of the bulk resistance R and the bulk polarization C_{pr} are of comparable magnitude and contribute significantly to Z_{total}. As a consequence, the equivalent circuit can be reduced in good approximation to a parallel combination of R and C_{pr}. In the complex impedance plot one obtains a half-circle. At low frequencies is $1/\omega C_{pr} \gg R$ and hence C_{pr} contributes insignificantly to the total impedance. Therefore, the equivalent circuit reduces in this case to a series of a resistor R and a capacity C_e, appearing as a parallel to the Z'' axis in the complex impedance plot. Because of deviations from this ideal behavior due to e.g. non-ideal electrodes, inhomogeneities, ion trapping or ion-ion interactions, the actually observed *Cole-Cole* plots of the complex impedance are not showing a perfect parallel to the Z'' axis and also no root at $(R|0)$. In case of a real data set as shown for the cyclotriphosphazene ***6*** in Figure 4.2, the root has to be extrapolated for $\omega \longrightarrow 0$ in order to obtain the value for R. Since, as already mentioned, the resistance R represents ion migration, the total DC ion conductivity σ_{dc} of the electrolyte is accessible:

$$\frac{1}{R}\frac{d}{A} = \sigma_{cation} + \sigma_{anion} = \sigma_{dc} \,. \qquad \textbf{eq. 4.12}$$

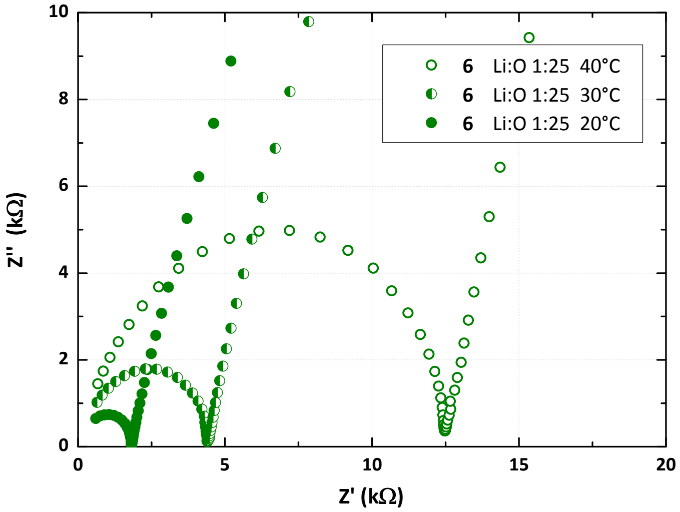

Figure 4.2. *Cole-Cole* plot of the complex impedance for model compound ***6*** at different temperatures.

Additionally, in case that R and ω_{max} are known (Figure 4.1), from the relationship including the maximum Z'' value

$$R\omega_{max}C_{pr} = 1 \,, \qquad \textbf{eq. 4.13}$$

the capacitance of the sample electrolyte can be calculated assuming a nearly ideal behavior, equivalent to an almost perfect half-circle. On that condition, the dielectric constant of the electrolyte ε_{pr} is also accessible:

$$C_{pr} = \varepsilon_{pr}\varepsilon_0 \frac{A}{d} \,, \qquad \textbf{eq. 4.14}$$

with A the electrode area, d the distance between the electrodes, and ε_0 the permittivity of the vacuum.

4.1.2 DC Ion Conductivity out of AC Ion Conductivity by Extrapolation

A convenient way to determine the DC ion conductivity, which was applied in general to the data in this work, is via utilizing the AC ion conductivity σ'. Plotting σ' for various temperatures versus the frequency ω leads to curves that basically could be divided into three areas (Figure 4.3):

At low frequencies ($\omega \longrightarrow 0$) the electrode polarization gains influence, causing a decrease in σ' (area I). At higher frequencies ($\omega \longrightarrow \infty$) σ' increases due to relaxation phenomena within the electrolyte (area III). However, in a characteristic range of medium frequencies (area II), σ' remains constant. Extrapolating this distinct plateau value to $\omega = 0$ yields the DC ion conductivity σ_{dc}.

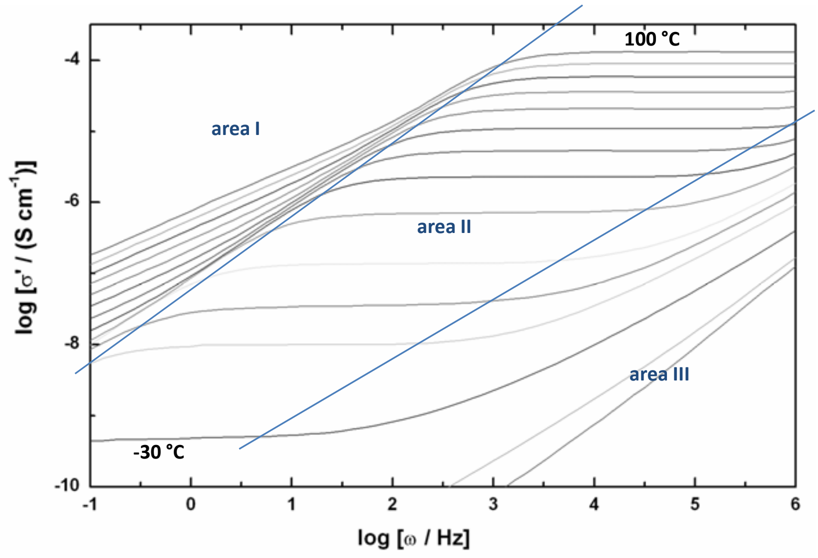

Figure 4.3. Alternating current ionic conductivity σ' of model compound ***6*** blended with LiTFSI (Li:O = 1:25); measured for various temperatures in dependence of the frequency ω for temperatures between -30 °C and +100 °C in 10 °C intervals (*Bode plot*).

Verification of the legitimacy of this extrapolation and the origin of σ' will be discussed in the following paragraph.

4.1.3 Evaluation of the Complex Dielectric Constant [4.3][4.4][4.11]

Referring to eq. 4.11 the capacitance C_{pr} of the electrolyte is entering the imaginary and the real part of the total impedance. Following eq. 4.14 the probe can be treated as capacitor with the real dielectric constant ε_{pr} as characteristic quantity. The real part ε' describes the stored energy within the system, whereas dissipative processes, among others ion migration and relaxation events, contribute to the imaginary part ε''. The complex dielectric function ε^* can then be written as

$$\varepsilon^* = \varepsilon' - i\,\varepsilon'' , \qquad \textbf{eq. 4.15}$$

with $\varepsilon' = \varepsilon_{pr}$ and ε'' qualifying the dielectric loss.

Combining eq. 4.14 and 4.15 yields the complex impedance $C^*$of a capacitor filled with an electrolyte:

$$C^* = \varepsilon_0 \, \varepsilon^* \frac{d}{A} = \varepsilon^* \, C_0 \, . \qquad \textbf{eq. 4.16}$$

C_0 is equal to the capacitance of an '*empty*' capacitor.

At the same time, as a consequence of the applied sinusoidal voltage $V(\omega, t) = V_0 \exp(i\omega t)$ during the measurement, a current $I(t)$

$$I(t) = \frac{dQ}{dt} = \frac{d[C^* \, V(t)]}{dt} \qquad \textbf{eq. 4.17}$$

flows through the probe, with dQ/dt the transported charge per infinitesimal time interval dt. Plugging in eq. 4.15 and eq. 4.16 in eq. 4.17 one obtains:

$$I(t) = (i\omega\varepsilon' + \omega\varepsilon'') \, C_0 \, V(t) = i\varepsilon^* w \, C_0 V(t) \, . \qquad \textbf{eq. 4.18}$$

The impedance of the capacitor is already given by eq. 4.7 and so results an additional expression for $I(t)$:

$$I(t) = \frac{V(t)}{Z} = \left(\frac{1}{R} + i\omega C\right) V(t) \, . \qquad \textbf{eq. 4.19}$$

Equaling eq. 4.18 and eq. 4.19 provides the formula for the real and the imaginary part of the dielectric constant:

$$\varepsilon' = \frac{C}{C_0} \qquad \textbf{eq. 4.20}$$

$$\varepsilon'' = \frac{1}{\omega \, R \, C_0} \, . \qquad \textbf{eq. 4.21}$$

As mentioned earlier, the imaginary part contains two parts that can be assigned to ion migration or ionic conductivity respectively, as well as to relaxation processes. These contributions are well represented by a parallel connection of two resistors R_{cond} and R_{rel}, whereas just R_{rel} depends on the frequency. Thus, ε'' can be separated as follows:

$$\varepsilon'' = \varepsilon''_{cond} + \varepsilon''_{rel} = \frac{1}{R_{cond}\omega C_o} + \frac{1}{R_{rel}\omega C_0} \, . \qquad \textbf{eq. 4.22}$$

The reciprocal of R_0 is equivalent to the so-called absolute DC ion conductivity (compare eq. 4.12). With the knowledge of this and with regard to eq. 4.15 one obtains an expression for ε'' including the specific ionic conductivity σ', which was mentioned above:

$$\varepsilon'' = \varepsilon''_{cond} + \varepsilon''_{rel} = \frac{\sigma'}{\omega\varepsilon_0} + \frac{1}{R_{rel}\omega C_0}\,. \qquad \textbf{eq. 4.23}$$

Rearranging eq. 4.23 results in

$$\sigma' = \varepsilon''\omega\varepsilon_0 - \frac{\varepsilon_0}{R_{rel}C_0}\,. \qquad \textbf{eq. 4.24}$$

For frequencies triggering relaxation phenomena just to a nominal extent, the second term in eq. 4.24 becomes negligible. In this frequency range ε'' is proportional to ω^{-1} and consequently $\varepsilon''\omega\varepsilon_0$ is constant. Therefore σ' attains also a constant value, which is based on the DC resistance of the probe and can be related to the plateau within the *Bode* plot shown in Figure 4.3 (area II). Thus, despite of electrode polarization influences, the extrapolation of the plateau for $\omega \longrightarrow 0$ described in paragraph 4.1.2 is permitted and the interpretation of the y-intercept as σ_{dc} is legitimated.[4.3]

Besides, at higher frequencies ε''_{rel} contributes significantly to σ', explaining the increase of the plateau value in area III, illustrated qualitatively in Figure 4.3.

4.1.4 Geometry of the Impedance Cell

The consistence of most model electrolytes was of a highly viscous, honey-like or resinous nature, respectively. Owing to this, the samples were prepared between two blocking electrodes using Teflon or fiberglass spacers as illustrated in Figure 4.4 (right).

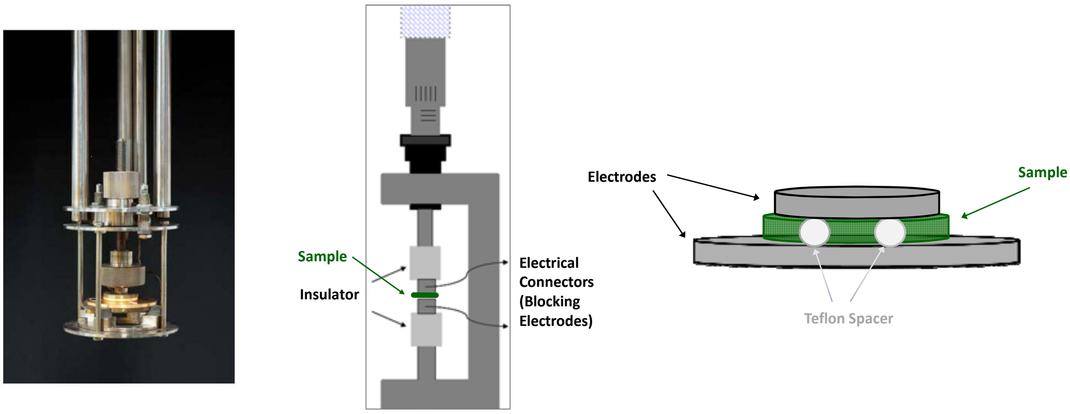

Figure 4.4. Probe mounting and illustration of sample preparation.

The spacers fulfill the task of keeping an equidistant sample thickness between round polished stainless steel or platinum electrodes over the measurement time. The smaller upper electrode (ø = 5 mm) defines the electrode area of 19.63 mm^2, while the probe thickness is equal to the diameter of the spacers, in these cases 0.1 mm. In general, this setup provided reliable results with good reproducibility, despite possible errors related to the viscous nature of the samples such as edge effects, thickness fluctuations as a consequence of changes in the clamping pressure, and/or due to the small electrode distance comparatively high relative errors in measuring the same.

An ionic conductivity measurement with a self-made cell consisting of two electrodes in a U-section Teflon tray (d = 5 mm) was not feasible due to the relatively high sample demand per measurement.

For AC measurements, the mounting of the probe is assembled into a chamber, which is temperature controlled by a cryostat (accuracy ±0.2 K) under nitrogen and connected to a dielectric converter in order to analyze the response of the system.

4.1.5 Transference Numbers [4.5]

In case of *'salt-in'* polymer electrolytes, both, cations and anions, may contribute to the total ionic conductivity. Therefore it is important to determine the proportion of the current which is carried by each species, especially the lithium ions. This proportion is ideally given by the transport number t

$$t = \frac{\sigma_n}{\sigma_{total}} \qquad \textbf{eq. 4.25}$$

for any mobile species, where $\sigma_{total} = \sigma_1 + \sigma_2 + \cdots + \sigma_n + \cdots$. In a first approximation the electronic conductivity of the electrolyte is assumed to be negligible. Thus, for a binary electrolyte in which the salt dissociates in two single species, the *electric transport number*, i.e for the cations, is defined as follows:

$$t_+ = \frac{i_+}{i_+ + i_-} = \frac{i_+}{i_{total}}, \qquad \textbf{eq. 4.26}$$

where i_+ and i_- are the partial currents carried by cations or rather anions.[4.5]

However, in a polymer electrolyte containing the salt M^+A^- there are several potential equilibria involving associated ion species such as M_2A^+ or A_2^-. As a result, just the net flux of charges carried by the positively charged species moving into the cathode direction can be measured experimentally.

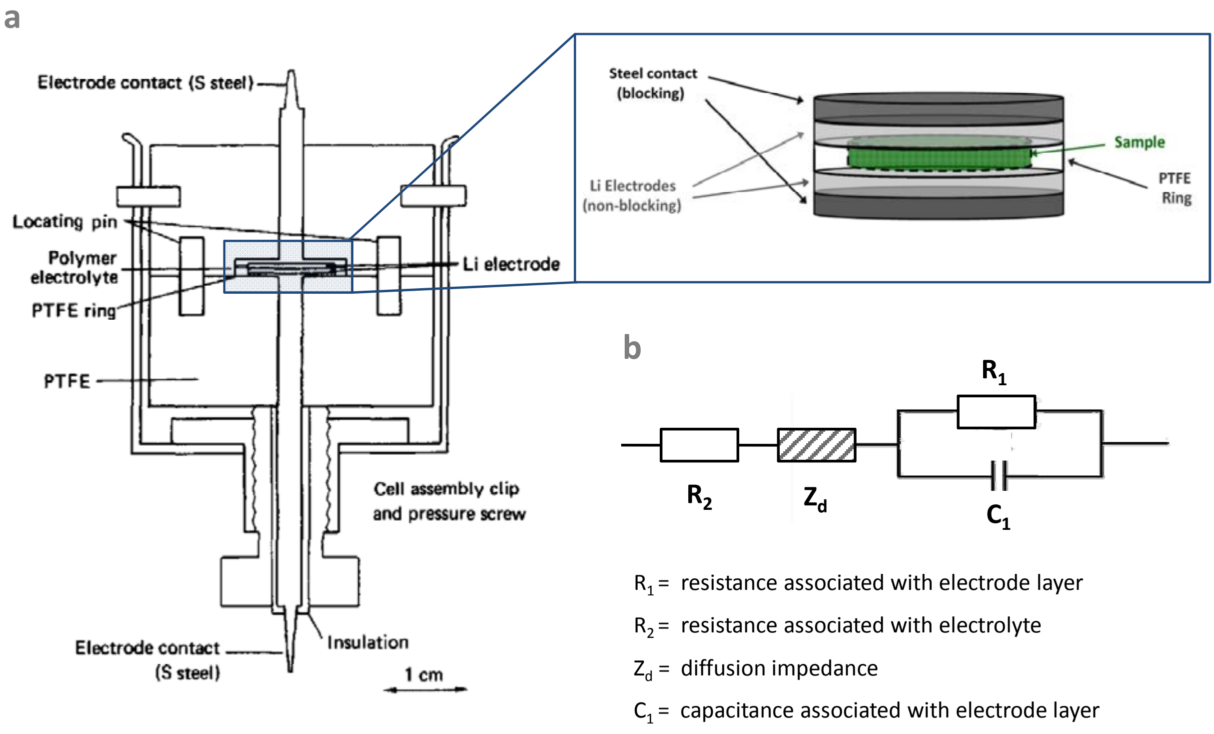

R_1 = resistance associated with electrode layer
R_2 = resistance associated with electrolyte
Z_d = diffusion impedance
C_1 = capacitance associated with electrode layer

Figure 4.5. (**a**) Cross-section of cell assembly for transference numbers measurement (modified illustration from *Bruce et al.* [4.5]).
(**b**) Appropriate equivalent circuit.

This quantity is expressed by the *transference number* T_+.[4.6] Several methods have been developed in order to measure T_+. DC methods after *Blonsky et al.*[4.7] or *Tubandt*[4.8] apply a DC current to a cell consisting of a solid electrolyte placed between two non-blocking electrodes with respect to the cation (Li/LiX in a polymer matrix/Li). In particular, the procedure after *Tubandt* is difficult to apply to polymer electrolytes. In this case the electrolyte is required to be maintained in several thin sections, which is crucial, because a defined flow of current causes mass transport due to Faraday's law and hence weight variations in the cathode and anode section, allowing for the calculation of cation transport numbers.

In close collaboration with *Prof. P. G. Bruce* (*University of St. Andrews*, Scotland) transference numbers of selected model compound electrolytes were measured following an approved technique combining DC and AC electrical polarizations, which was actually developed in his laboratory:

After determining the AC impedance of a symmetrical cell of the form Li-metal|LiTFSI model compound blend|Li-metal assembled as shown in Figure 4.5, a small DC bias of

10 mV is used for polarization and the response of the cell is monitored until a steady-state current is set. The decrease in current is thereby influenced by the following processes:

- Build-up of a concentration gradient affecting the ion motion and finally stopping the net motion of anionic species.
- Growth of passivating layers at the electrodes. This effect is observable by changes in the complex-plane plot of the AC impedance monitored during the DC polarization.

It can be shown that in case of small side effects, i.e. electrostatic ion-ion interactions, the initial and steady-state current I_0 and I_s respectively are given by

$$I_0 = \Delta V/(R_1^0 + R_2) = \Delta V/(R_1^0 + \frac{k}{\sigma}) \qquad \textbf{eq. 4.27}$$

$$I_S = \Delta V/(R_1^S + \frac{k}{T_+\sigma})\ .^{[9]} \qquad \textbf{eq. 4.28}$$

Considering the equivalent circuit shown in Figure 4.5, R_1^0 and R_1^S represent initial and steady-state resistances associated with the passivating electrode layers, whereas R_2 is related to the resistance of the electrolyte itself; T_+ displays the cationic transference number, k the cell constant and σ the DC conductivity of the electrolyte. Rearranging eq. 4.27 and plugging in the obtained value for σ into eq. 4.28 yields

$$T_+ = \frac{I_S\,(\Delta V - I_0 R_1^0)}{I_0\,(\Delta V - I_S R_1^S)}\ . \qquad \textbf{eq. 4.29}$$

In order to calculate T_+ it is essential to determine the initial and steady-state resistance via an AC impedance measurement. For the described setup applying non-blocking electrodes, the *Cole-Cole* plot of the complex impedance shows three roots at $(0|0)$, $(R_2|0)$ and $(R_2 + R_1|0)$, providing the desired values.

In general, all sample preparations and measurements were performed in an argon-filled glove box with water content lower than 2 ppm.

The author gratefully acknowledges *PhD Chuhong Zhang* for the transference numbers measurements in the laboratory of *Prof. P. G. Bruce* in St. Andrews, Scotland.

4.2 Empirical and Theoretical Description of Transport Processes [4.1][4.3][4.10-11]

4.2.1 Arrhenius and VTF behavior [4.10][4.11-4.15]

Ionic conductivity in (polymer) electrolytes is due to long-range transport of ions, whose temperature-dependent description will be reviewed in the following section.

In general, for *'salt-in'* (polymer) electrolytes the total ionic conductivity $\sigma(T)$ is dependent on the contributions of cations and anions:

$$\sigma(T) = \sigma_+ + \sigma_- \,. \qquad \textbf{eq. 4.30}$$

A simplified desription of the temperature dependent ionic conductivity is thereby illustrated by

$$\sigma(T) = \sum_i q_i n_i(T) u_i(T) \,, \qquad \textbf{eq. 4.31}$$

with $n_i(T)$ the effective number of charge carriers i per unit volume, q_i the number of charges per charge carrier, and $u_i(T)$ their mobility within the electric field.

In case of ***Arrhenius behavior***, the temperature dependent ionic conductivity $\sigma(T)$ is related to the boundary conductivity σ_0 for $T \longrightarrow \infty$:

$$\sigma(T) = \sigma_0 \exp(-\frac{E_a}{k_B\,T}) \,. \qquad \textbf{eq. 4.32}$$

In this equation E_a represents the activation energy, necessary for overcoming the energetic barrier related to the distinct transport process; k_B is the *Boltzmann*'s constant. The long-range motion of the ions through the host matrix is described herein as a sequence of thermally induced processes or '*jumps*', for each of which the activation energy E_a is required in order to reach an adjacent local and unoccupied minimum. Thus, a diffusion process which depends on the activation energy is the characteristic factor determining the ionic conductivity. This means that in case of *Arrhenius behavior* - generally for temperatures $T > T_g$ - the ionic conductivity scales with the temperature, since at higher temperatures the medial energy in the system is higher and consequently a larger percentage of ions possess the essential energy in order to change the site. This relation results in a straight line in a common logarithmic *Arrhenius plot*, displaying $\log(\sigma(T))$ plotted versus the inverse temperature.

Above T_0 the temperature dependent ion transport in liquid or amorphous electrolytes can be described via the empirically found ***Vogel-Tamman-Fulcher** (**VTF**)* equation

$$\sigma(T) = A_T \exp\left[-\frac{B}{(T-T_0)}\right] \text{ with } A_T \propto T^{-\frac{1}{2}}, \qquad \textbf{eq. 4.33}$$

where T_0 is a reference temperature also known as *critical* or *Vogel temperature*. The parameter A_T contains among other constants a temperature dependent term.[4.12] In general, *VTF behavior* assumes that the ion transport is related to a cooperative motion of molecular (chain) segments. The significance of the parameters in equation 4.33 with regard to the *VTF* model will be answered later. Interestingly, the *VTF equation* [4.13-4.15] was developed originally not to deal with ionic conductivity, but rather with the viscosity properties of super-cooled liquids. It was written as empirical relationship for the viscosity:

$$\eta(T) = C_T \exp\left[+\frac{B}{(T-T_0)}\right] \quad \text{with} \quad C_T \propto T^{\frac{1}{2}}. \qquad \textbf{eq. 4.34}$$

The correlation between viscosity, diffusion, and ionic conductivity, respectively, can be deduced from the *Stokes-Einstein equation* (eq. 4.35)

$$D_i(T) = \frac{k\,T}{6\,\pi\,r_i\eta}, \qquad \textbf{eq. 4.35}$$

with D_i the diffusion coefficient of the species i and r_i its hydrodynamic radius. Combining eq. 4.35 with equation 4.34 yields

$$D_i(T) = C \exp\left[-\frac{B}{(T-T_0)}\right]. \qquad \textbf{eq. 4.36}$$

Applying the *Nernst-Einstein equation*

$$\sigma_i(T) = \frac{c_i\,q_i^2}{k\,T} D_i\,, \qquad \textbf{eq. 4.37}$$

with c_i the concentration and q_i the charge of the ionic species i, one obtains in turn the *VTF* form for the (ionic) conductivity (eq. 4.33).

Thereby, the total ionic conductivity which can be related to diffusion ideally comprises the summed contributions of each species. Furthermore, despite the fact that eq. 4.35 is strictly valid only for diffusion of uncharged spheres in an ideal medium, in common cases also the diffusion of charged particles, hence the conductivity, follows the *VTF equation*.[4.3]

The temperature dependence of the pre-factors A_T and C_T in eq. 4.33 and eq. 4.34 is stated to be proportional to $T^{\pm 1/2}$.[4.10] However, this dependency is rather hard to verify with experimental data,[4.16] since for arbitrary chosen exponents n for T^n in between $0 \leq n \leq 1$ fitting of the data is quite equal.

4.2.2 VTF behavior and the Concept of the *Free Volume* [4.3][4.11][4.17-4.20]

An amorphous material no matter if it is a glass or a melt may be considered as an array of random, non-periodically packed molecules. In case of a polymer sample this implies a non-dense assembly of polymer chains, where the empty space between the macromolecules is called the *free volume*.[4.17]

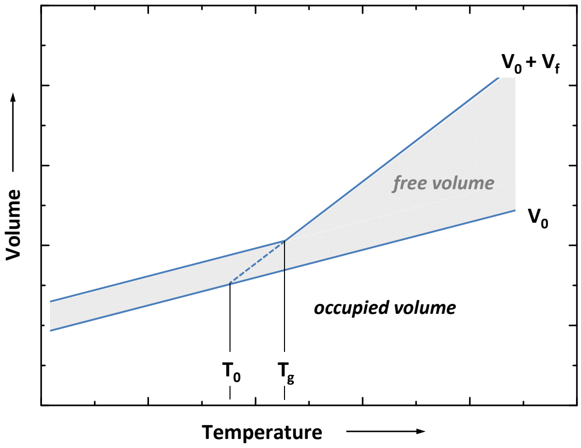

Figure 4.6. Illustration of the temperature dependency of the free and occupied volume in amorphous materials.

One can define quite generally the *specific volume* V of the material as the sum of the *Van der Waals volume* V_0 and the *free volume* V_f:

$$V = V_f + V_0 \qquad \textbf{eq. 4.38}$$

However, the temperature dependence of both terms is different: On one side, the *Van der Waals volume* of the sample increases linearly with the temperature due to thermally activated molecular vibrations, irrespective whether the sample is present in the glassy or molten state. On the other side, the *free volume* is slightly increasing up to a certain temperature, which is called the glass transition temperature T_g. At this temperature the onset of conformational changes of the (polymer) segments takes place, which is macroscopically observable as phase transition from the glassy to a rubber-like or molten state. Consequently, above T_g the *free volume* expands rapidly due to more and more rigorous molecular motions. The main part of the thermal expansion is actually assigned to the change in *free volume*, which is consistent with the observation that the transport dynamics are distinctly diminishing, if the temperature descends below the glass transition temperature.[4.11]

De facto V_f never becomes zero (Figure 4.6), since molecular motion at the glass transition temperature is already slowed down to such an extent that makes a further contraction of V_f impossible, assuming the molecular dynamics freeze, when a critical *free volume* is reached. Thus, a certain *free volume* is preserved at the glass transition temperature and rendering the system at $T < T_g$ in non-equilibrium. However, if the thermal expansion coefficient is known, the temperature whose V_f is hypothetically zero can be extrapolated. This temperature is the *critical temperature* T_0, which can be found in the *VTF equation* (eq. 4.33). As a rule of thumb, experimentally observed for a number of systems showing a glass transition, the relation $T_g - T_0 \approx 50\ K$ is valid. According to this, it is evident that different materials with comparable thermal expansion coefficients possess the same *free volume* and hence exhibit similar system dynamics at identical *reduced temperatures* $T - T_0$. By plotting the experimental data versus the *reduced temperature* $T - T_0$, the influence of the *free volume* on the ionic conductivity data becomes minor, making the comparison of discrete systems more informative.[4.11]

Empirical developments in this context have been made by several academics. While the model described above, discussing the glass transitions in terms of *free volume* falling below some critical value was introduced by *Fox and Flory*,[4.18] *Doolittle* found empirically a relation between viscosity and *free volume* for hydrocarbon liquids at '*high enough temperatures*':[4.19]

$$\eta = A \exp\left(\frac{b_0 V_0}{V_f}\right), \qquad \textbf{eq. 4.39}$$

with b_0 a constant of the order about unity.

The diffusion coefficient D_i can also be treated in terms of *free volume*. Making the assumption that diffusion occurs cooperatively as a result of ongoing redistribution of V_f and is not directly related to overcoming an energy barrier as in case of *Arrhenius* behavior, *Cohen and Turnbull* established

$$D_i = g a^* u\ exp\left(-\gamma \frac{V^*}{V_f}\right), \qquad \textbf{eq. 4.40}$$

where g is a geometrical pre-factor, a^* the approximated molecular diameter and u the thermal energy.[4.20] The latter is due to equipartition proportional to $T^{1/2}$, which explains the temperature dependence of the pre-factors A_T, C_T, and C in the equations for $\sigma(T)$, $\eta(T)$, and $D_i(T)$ (eq. 4.33, 4.34 and 4.36). γ is basically a correction factor, which considers the overlapping of the *free volume* of each single molecule; γV^* represents the molecular volume, with V^* the *critical free volume*, which is necessary for a molecule or molecular segment to undergo diffusion processes. In order to transfer eq. 4.40 into a function of temperature, the expansion of the *free volume* (eq. 4.41) has to be included:

$$V_f(T) = V_0\left(exp\left(\int_{T_0}^{T} a(T)dT\right) - 1\right). \qquad \textbf{eq. 4.41}$$

Equation 4.41 assumes a constant V_0 in the temperature range from T to T_0, where T_0 is, as stated earlier, the temperature at which V_f is extrapolated to be zero (compare Figure 4.6). If the thermal expansion coefficient $a(T)$ as well as V_0 in eq. 4.40 are replaced by their mean values $\langle a\rangle$ and $\langle V_m\rangle$ respectively, which are supposed to be valid over the range (T, T_0), the equation simplifies to

$$V_f = \langle a\rangle\langle V_m\rangle(T - T_0). \qquad \textbf{eq. 4.42}$$

Plugging in eq. 4.42 into 4.40 results in the relationship for the temperature-dependent diffusion coefficient:

$$D_i(T) = ga^*u\ exp\left(\frac{-\gamma V^*}{\langle a\rangle\langle V_m\rangle(T-T_0)}\right). \qquad \textbf{eq. 4.43}$$

Thus, *Cohen* and *Turnbull* found a relation considering the molecular fluctuations, which explains the observed correlation between viscosity and free volume discovered by *Doolittle*.

Adapting the *Nernst-Einstein* equation (eq. 4.37) to equation 4.42, one obtains the *VTF* form of the conductivity (eq. 4.32) and the following expressions for the parameters A_T and B:

$$A_T = c_i q_i^2 g a^* \frac{u}{kT} \ \text{ with } \ A_T \propto T^{1/2}, \qquad \textbf{eq. 4.44}$$

$$B = \gamma \frac{V^*}{\langle a\rangle\langle V_m\rangle}. \qquad \textbf{eq. 4.45}$$

The evaluation of the experimental data was based on the following equations with temperature constant parameters A_T:

$$\sigma(T) = \frac{A}{\sqrt{T}} \exp\left(-\frac{B}{T-T_0}\right) \quad \text{with} \quad A = \frac{c_i q_i^2}{k}\, g a^* \frac{u}{\sqrt{T}} \;, \qquad \textbf{eq. 4.46}$$

$$D_i(T) = A\sqrt{T}\, \exp\left(-\frac{B}{T-T_0}\right) \quad \text{with} \quad A = g a^* \frac{u}{\sqrt{T}} \;. \qquad \textbf{eq. 4.47}$$

Parameter $\boldsymbol{A}$ is merely a scaling factor along the y-axis when $\sigma(T)$ is plotted versus temperature. Geometrical circumstances (g) and the thermal motion of the molecules (u and a^*) via A have an impact on diffusion and conductivity as well as the charge carrier density (c_i). The latter contributes in so far to A that an increase in c_i should theoretically result in a higher conductivity. Therefore, the Li:O ratio was varied over a sufficient range (0.01 and 0.083) in order to cover the maximum value of $\sigma(T)$.

Parameter $\boldsymbol{B}$, the ratio between the critical volume (V^*) and the product of the mean value of the expansion coefficient ($\langle a \rangle$) with the mean volume ($\langle V_m \rangle$), affects the curvature of the graph. Thus, a smaller ratio leads to smaller values of B, hence a stronger bending of the curve at temperatures above T_0, which in turn results in a fastened increase of conductivity on further heating. In other words B defines how rapid the conductivity approaches the boundary value $T^{-1/2}$.

The parameter $\boldsymbol{T_0}$ is an empirical fit parameter,[4.12] but as discussed earlier, defined as the temperature at which the *free volume* theoretically becomes zero. Consequently, $log(\sigma) \longrightarrow -\infty$ for $T \longrightarrow T_0$ and in case of a temperature constant parameter A, T_0 is just causing a displacement of the curve along the x-axis.

4.2.3 The Williams-Landel-Ferry (WLF) Equation [4.3][4.10]

Equation 4.34 can be converted into the so-called ***Williams-Landel-Ferry* (*WLF*)** equation. This equation considers relaxation processes τ, which characterize glass-forming samples and corresponds to the *VTF equation* 4.33:

$$\log(a(T)) = \frac{C_1(T-T_{ref})}{C_2+T-T_{ref}} \quad \text{with} \quad a(T) = \frac{\tau(T)}{\tau(T_{ref})} \;. \qquad \textbf{eq. 4.48}$$

Thus, the *free volume theory* or the empirical *VTF* and *WLF* equation respectively are describing indepently the same issue, in particular the ionic conductivity in terms of molecular or segmental motion.[4.11]

The *shift factor* $a(T)$ in eq. 4.48 is for an amorphous polymer above T_g thereby given by the ratio of any (mechanical) relaxation at a temperature T to its value at a reference temperature T_{ref}. If one chooses for each polymer or organic glass-forming system a distinct T_{ref}, and plots $\log(a(T))$ of a measured variable ($\eta(T)$, $\sigma(T)$ or $D_i(T)$) versus $T - T_{ref}$, one obtains a universal curve, which fits well for nearly all respective systems. Often is $T_0 \cong T_g - 50\ K$ or just T_g a good choice for the value of T_{ref}.

The collapse of the data of various samples in one *WLF master curve* is an indication of a correlation between the analyzed process and the molecular or segmental motion within the investigated materials.

Since equation 4.48 is mathematically equivalent to eq. 4.33 no improvement over the *VTF* formalism in a fit to the data will be achieved.

4.3 Experimental Results

The ionic conductivity of all blends discussed in the upcoming paragraphs was measured in a cell of the geometry described under 4.1.4. The preparation of the blends itself was accomplished in a nitrogen filled glove box (moisture content $H_2O < 2$ ppm) by homogenously dissolving the respective substances together with the lithium salt in an appropriate dried solvent, usually THF. Subsequent removal of the solvent under high vacuum and temperatures between 85 °C and 120 °C at a *Schlenk line* over several days yielded the desired highly viscous electrolytes. The absence of any remaining solvent was verified by ^1H NMR spectroscopy. Afterwards, the blends were heated under inert conditions slightly above their apparent glass transitions in order to reduce their viscosity and to simplify the assembly of the electrolytes and the Teflon spacers between the electrodes.

4.3.1 Ionic Conductivity of the CTP based Model Compound Blends

The temperature dependent ionic conductivity of the CTP based model compounds blended with LiTFSI is shown in Figure 4.7(a). The measured data plotted on Arrhenius coordinates (log(σ) vs. 1000/T) exhibit a curvature, which suggests *VTF* behavior. Indeed, fitting the data according to the empirical *VTF* equation (eq. 4.46) using a nonlinear least-squares program (Origin 8.1) yielded correlations R^2 very close to unity. The fitting parameters obtained in this way are shown in the tables 4.1 till 4.3. In general, *VTF* *behavior* gives a first hint that the ionic conductivity is determined by the molecular dynamic of the cyclic carbonate substrates.

The observed ionic conductivity of the cyclic carbonate based CTP derivatives blended with LiTFSI in a molar Li:O ratio of 1:50 (in general all oxygen atoms are taken into account) ranges at 30 °C from 1.05 x 10^{-7} S·cm^{-1} for ***12*** up to 2.19 x 10^{-6} S·cm^{-1} for ***6***. The difference in ionic conductivity decreases thereby with increasing temperature.

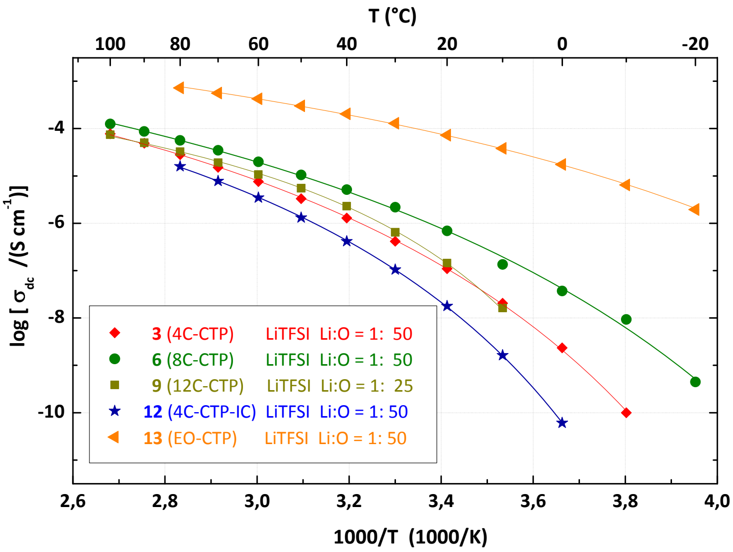

Figure 4.7(a). Arrhenius plot of the temperature dependent ionic conductivity of the CTP based model compounds blended with LiTFSI. Full lines represent VTF fits.

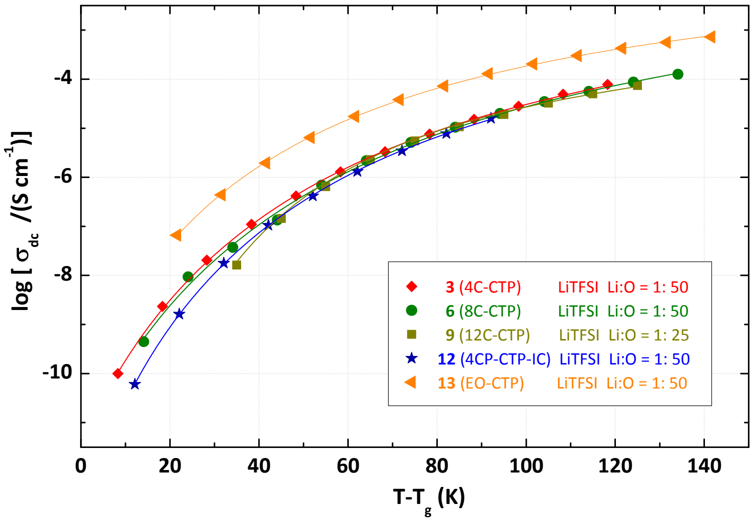

Figure 4.7(b). Ionic conductivity of the CTP based model compounds blended with LiTFSI plotted vs. the reduced temperature *T*-T_g. Full lines represent VTF fits.

In principle, a longer alkyl spacer between the cyclic carbonate moieties and the CTP core leads to a dilution of the crucial cyclic carbonate concentration within the system. However, this does not automatically result in a lower ionic conductivity, since the apparent glass transition temperature of ***6*** (8C-CTP, T_g = -34.1 °C, Li:O = 1:50) is lower than the one of ***3*** (4C-CTP, T_g = -18.4 °C, Li:O = 1:50). Thus, the mobility within the system is higher for electrolyte ***6***, overcoming the dilution effect described before and resulting in an about one order of magnitude higher conductivity compared to the blended CTP derivative bearing a shorter, four carbon alkyl spacer.

One might expect the 12C-CTP analogue ***9*** to show an even higher ionic conductivity than ***3*** or ***6***, respectively, but actually, this is not the case. The reason for this is related to the crystallization of the alkyl chains. Pure ***9*** shows a sharp melting transition at 70.5 °C and no glass transition as ***3*** and ***6*** do (compare Chapter III), while mixed with LiTFSI a very broad rather melting than glass transition starting at -24 °C and ending at +60 °C is observed. Although the blend of ***9*** is amorphous, the difference in phase behavior assumes slower dynamics. Furthermore, the dilution of the cyclic carbonates is associated with a lower dielectric constant, which, however, is crucial for a high percentage of solvated '*free*' ions. These two facts are most likely the reason for the reduced ionic conductivity in blended ***9***.

Interestingly, the CTP based model compound ***12*** with an ethyl-substituted internal cyclic carbonate exhibits an even lower conductivity as its appropriate counterpart ***3***. Obviously, the ethyl side group at the carbonate cycle does not cause a weaker interaction between the solvating moieties and the lithium ions.

The mobility μ_i of the charge carriers correlates with the glass transition temperature. Thus, if $\sigma(T)$ is plotted versus the *reduced temperature* $T - T_g$ the differences in molecular dynamics, which are closely connected to μ_i at a distinct temperature, can be eliminated, since the glass transition defines for all compounds the point at which the onset of segmental motion occurs. In other words, assuming a comparable thermal expansion coefficient $\alpha(T)$ of the *free volume* V_f for all derivatives, the ionic conductivity should then be normalized in terms of V_f. Actually, in the case of the CTP based model compounds a plot of $\log(\sigma)$ versus $T - T_g$ is resulting in the collapse of all data within the limits of error (Figure 4.7(b)), excluding the blended oligo(ethylene oxide) functionalized CTP ***13***. Regarding the cyclic carbonate models, this is consistent with the outlined remarks above. The ionic conductivity is anticipated to be based on a similar mechanism for ***3***, ***6***, ***9***, and ***12***, mainly defined by the softening of the blends or the cooperative molecular motion of the moieties, respectively. At the same time, parameters which can show an influence independently of V_f, for example the degree of salt dissociation, show a negligible effect, which is expected due to the similar chemical composition.

Just the fitted curve of compound ***13*** in Figure 4.7(b) is shifted about one order of magnitude along the y-axis. The reason for this differential behavior is not completely clear yet, but may be related to a different nature of the glass transition or to the chemical difference of the solvating moieties as a consequence of less strong interaction with the lithium ions.

Ionic Conductivity in Dependence on Salt Concentration

The discussion above was based on a fixed molar Li:O ratio of 1:50. In order to investigate the influence of the salt concentration on the ionic conductivity, the molar Li:O ratio was varied. Studied were molar Li:O concentrations of 1:12, 1:25, 1:50 and 1:100, including the optimum ratio of 1:25 for preferably high concentrations in free charge carriers referred to the literature.[4.21]

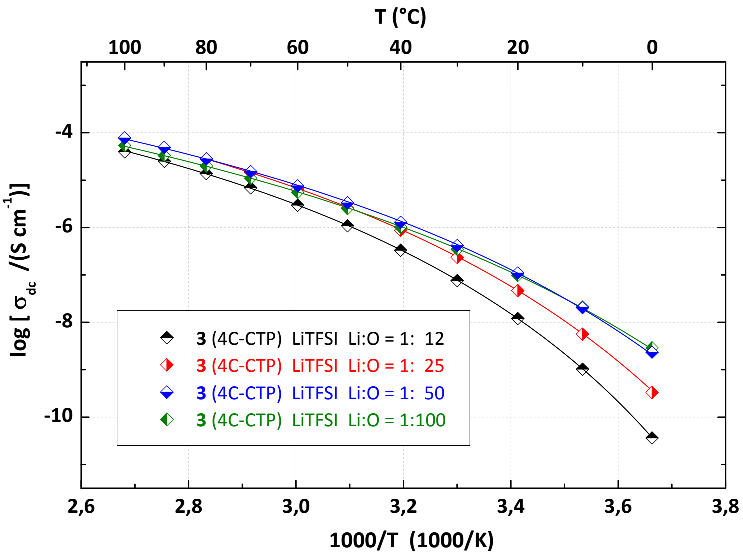

Figure 4.8. Arrhenius plot of the temperature dependent ionic conductivity of model compound ***3*** blended with LiTFSI in various molar Li:O ratios. Full lines represent VTF fits.

As shown in Figure 4.8 and Figure 4.9 the influence of c_i on the ionic conductivity of ***3*** and ***6*** at lower temperatures is significant, which most likely is due to the strong influence of c_i on the glass transition temperature. At higher temperatures the relative differences in the mobility u_i and accordingly $\sigma(T)$ lose ground due to a temperature high above the actual glass transitions. Though, for both blends, $\sigma(T)$ exhibits a maximum, while the glass transition temperatures increase with increasing salt concentration (Figure 4.10). This issue can be explained as followed: Since the ionic conductivity is proportional to the number of effective charge carriers n_i, their mobility μ_i and the electric charge q_i (eq. 4.31),[4.10] at low salt contents, the increase of charge carriers is apparently responsible for an increase in ionic conductivity. The potentially displaced counteracting effect of an increase in the glass transition temperature due to cation complexation and ion-dipole interactions may result in the observed maxima in ionic conductivity.

Due to the lower glass transition and most likely enhanced system mobility of pure compound ***6*** over ***3***, the optimum molar Li:O ratio for maximum ionic conductivity is 1:25 for ***6*** compared to 1:50 in the case of ***3***. Similar studies have been recently described for *low*-T_g (ca. -80 °C) cyclosiloxane based blends.[4.22]

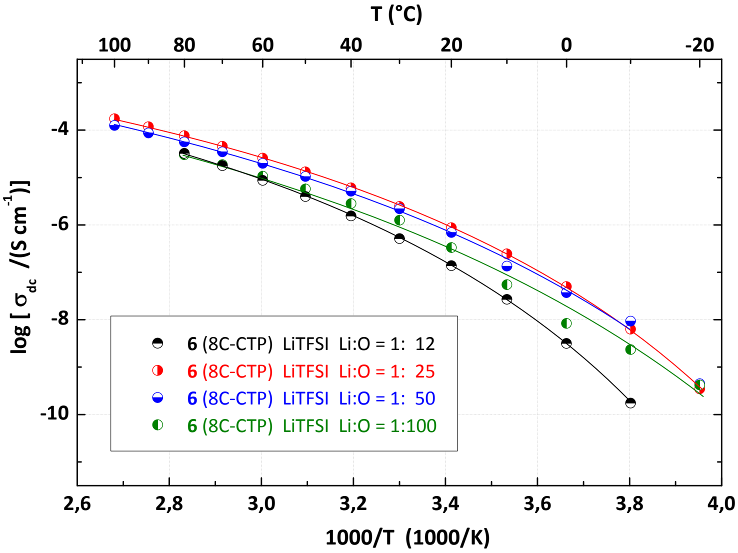

Figure 4.9. Arrhenius plot of the temperature dependent ionic conductivity of model compound ***6*** blended with LiTFSI in various molar Li:O ratios. Full lines represent VTF fits.

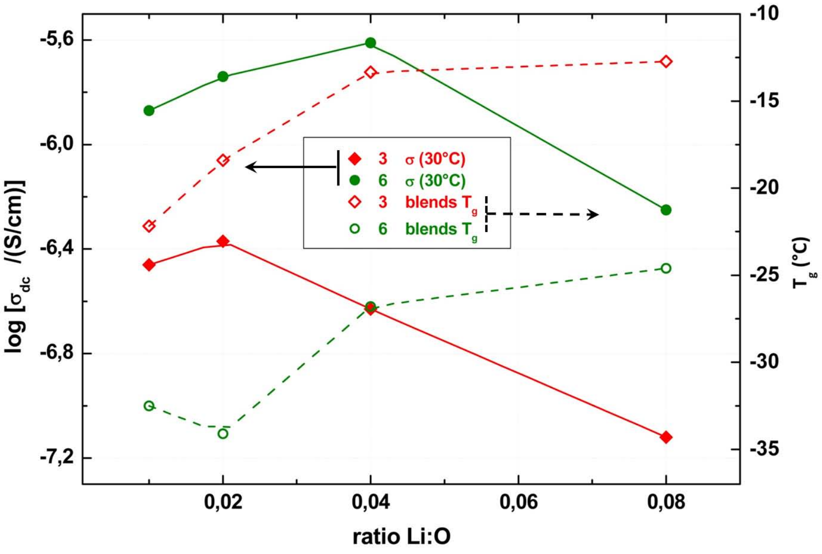

Figure 4.10. Ionic conductivity at 30 °C and related glass transition temperatures of model compounds ***3*** and ***6*** blended with LiTFSI as a function of molar ratio Li:O (see Figure 2.13 for sample numbering).

Ionic Conductivity in Dependence on Salt Type

Modification of the lithium salt had no significant influence on the ionic conductivity of the CTP based model compounds, indicating that the CTP models are suitable lithium ion solvents for various lithium salts with a similar degree of salt dissociation within the blends, irrespective of the salt dissociation constants and counterion sizes. Figure 4.11 and 4.12 display the ionic conductivity of model compounds ***3*** and ***6*** blended with LiTFSI, lithium perchlorate ($LiClO_4$), lithium bis(pentafluoroethanesulfone)imide (LiBETI) and lithium bis(oxalate)borate (LiBOB), each in a molar Li:O ratio equal to 1:25. Thereby, LiBETI has the advantage over $LiPF_6$ or LiTFSI that it reduces the decomposition of the carbonate based electrolytes and hence the amount of released free carbon dioxide during cell operation. Thus, a contribution to battery safety can be made by choosing the right salt.[4.23] So, as further example, LiBOB is thermally more stable, less toxic and less corrosive than the common $LiPF_6$. Furthermore the BOB anion is actively involved in the *SEI* formation on the anode side. The resulting stable film is protecting the graphite against carbonate cointercalation and partial exfoliation. Thus, LiBOB is the only known electrolyte salt, which allows the utilization of PC based electrolytes.[4.24]

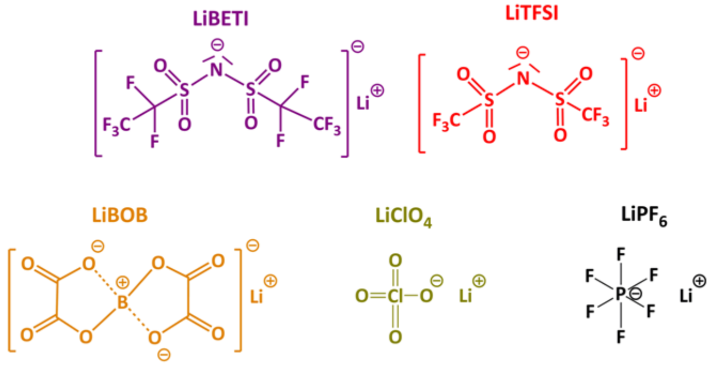

Scheme 4.1. Structure of the lithium salts used in the model compound blends.

The observed ionic conductivities in dependence on the lithium salt differ in the low temperature regime about one order of magnitude, which can be associated with variations of the glass transition temperature of the appropriate blends. The differences decrease with increasing temperature simply because the influence of T_g on the ionic conductivity decreases with increasing temperature (compare the argumentation above related to differences in salt concentration). Thus, the blend of ***6*** with $LiClO_4$ exhibits the highest T_g (-24.5 °C) but the lowest ionic conductivity (Figure 4.11). However, in case of ***3*** due to the lower molar $LiClO_4$:O ratio of 1:50 compared to 1:25 for LiTFSI and LiBOB respectively, the blend with $LiClO_4$ shows a lower T_g (-22.9 °C vs. -13.4 °C or -7.9 °C) in comparison to the other blends of ***3*** and consequently an about one order of magnitude higher ionic conductivity at temperatures below 0 °C, which is consistent with the explanations above.

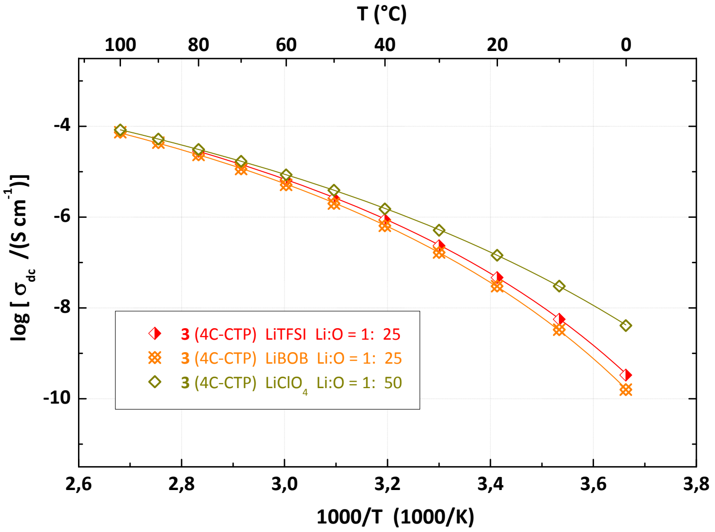

Figure 4.11. Arrhenius plot of the temperature dependent ionic conductivity of model compound ***3*** blended with different lithium salts. Full lines represent VTF fits.

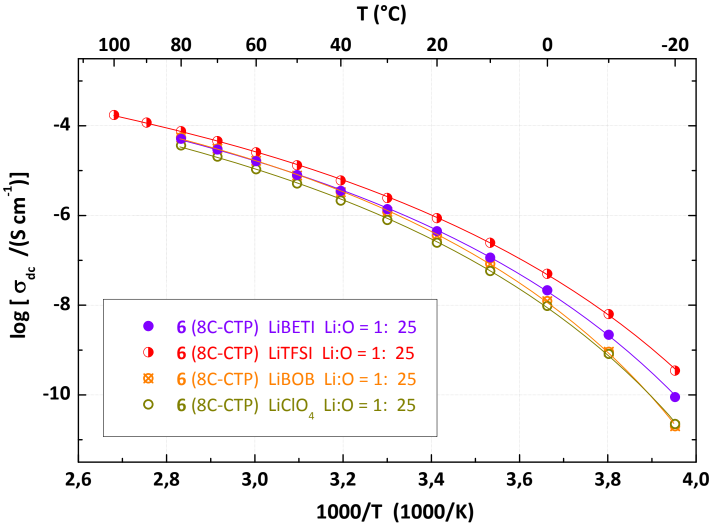

Figure 4.12. Arrhenius plot of the temperature dependent ionic conductivity of model compound ***3*** blended with different lithium salts. Full lines represent VTF fits.

It has to be mentioned at this point, that in combination with lithium hexafluorophosphate ($LiPF_6$), commonly used in commercially lithium ion batteries, an enhanced rearrangement of the CTP was observed (compare Chapter 3.2.2). Due to this circumstance and the fact that in absence of any salt stabilizers above 60 °C decomposition of $LiPF_6$ causes consecutive reactions with the cyclic carbonates (chapter I), long-time stability of the system is not provided. However, the latter is important for reliable dynamic studies via Solid-State NMR.

Regarding also the results on ionic conductivities related to the salt type for the HPB derivatives (see 4.3.2), LiTFSI was therefore the preferred choice.

4.3.2 Ionic Conductivity of the HPB based Model Compounds

The ionic conductivity of the HPB blends exhibits also *VTF* behavior and reveals similar trends than observed for the CTP model compounds (Figure 4.13).

In line with this, the ionic conductivity increases with decreasing glass transition temperatures, whereby the ionic conductivity of the oligo(ethylene oxide) functionalized HPB derivative ***26*** overcomes the performance of the cyclic carbonate analogues ***18*** and ***21***. The adequate explanations follow the outline for the CTP based blends.

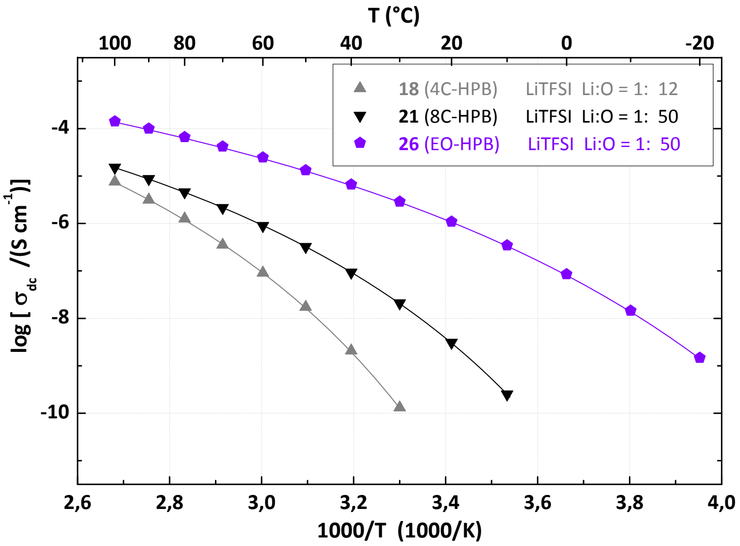

Figure 4.13(a). Arrhenius plot of the temperature dependent ionic conductivity of the HPB based model compounds blended with LiTFSI. Full lines represent VTF fits.

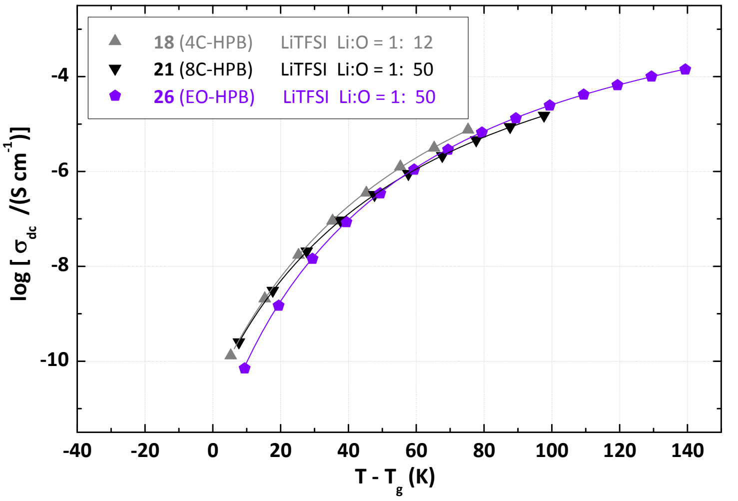

Figure 4.13(b). Ionic conductivity of the HPB-based model compounds blended with LiTFSI plotted vs. the reduced temperature T-T_g. Full lines represent VTF fits.

Ionic Conductivity in Dependence on Salt Concentration

The differences in ionic conductivity dependent on the salt concentration are for the HPB blends notably higher than for the CTP models. Even at elevated temperatures of 100 °C the difference in ionic conductivity amounts to more than one order of magnitude between the mixtures of ***21*** (8C-HPB) with LiTFSI in a molar Li:O ratio of 1:50 and 1:12, respectively (Figure 4.14). This can be assigned to the plasticizing effect of the bis(trifluoro-methanesulfone)imide anion, which results for the HPB blends in a decrease in glass transition with increasing salt content.

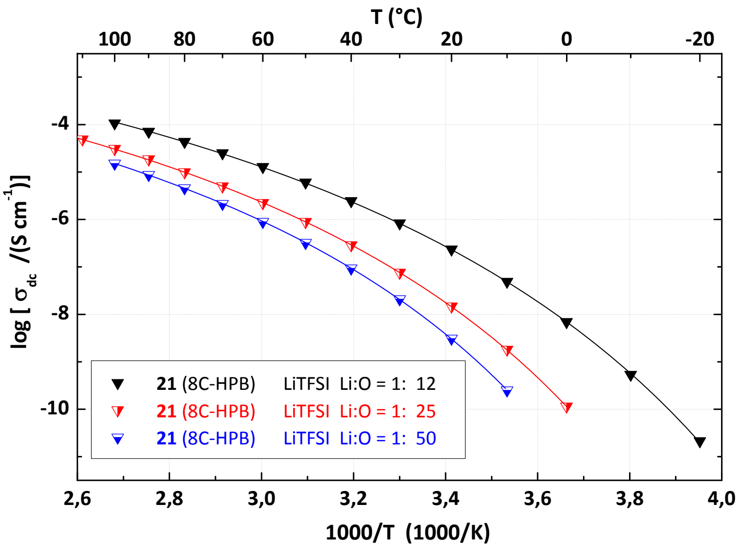

Figure 4.14. Arrhenius plot of the temperature dependent ionic conductivity of model compound ***21*** blended with LiTFSI in various molar Li:O ratios. Full lines represent VTF fits.

Consequently, there is no counteracting effect observed as for the CTP models, which states that the increasing amount of charge carriers causes a reduction of the system mobility. Actually quite the contrary is the case and hence the ionic conductivity follows the trend $\sigma(T)_{\mathbf{21},1:12} > \sigma(T)_{\mathbf{21},1:25} > \sigma(T)_{\mathbf{21},1:50}$.

Ionic Conductivity in Dependence on Salt Type

For the HPB based model compounds, blends of compound ***21*** with $LiClO_4$ or LiBOB gave no homogenous mixtures by visible inspection in contrast to the ones with LiTFSI. On the one side this can be related to the apparently lower dielectric constant of the HPB compared to the CTP models, which may explain the lower salt solubility in the HPB derivatives. On the other side it illustrates once more the well-known plasticizing effect of LiTFSI.[4.25] Based on these results, only blends of HPB model compounds with LiTFSI were chosen for Solid-State NMR dynamic studies.

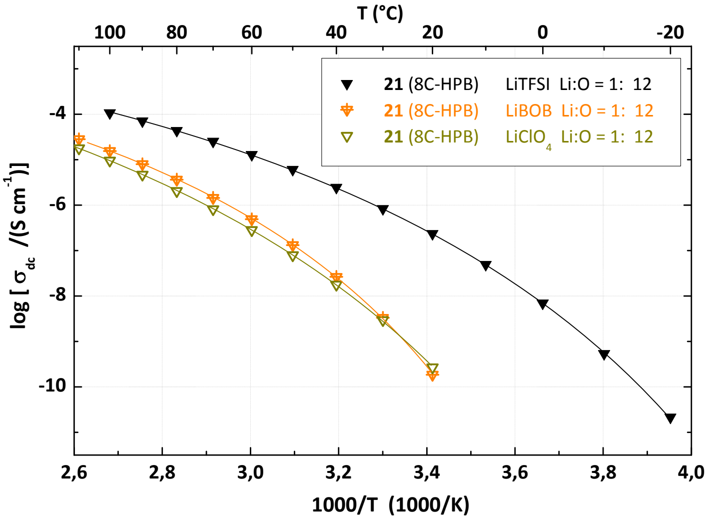

Figure 4.15. Arrhenius plot of the temperature dependent ionic conductivity of model compound ***21*** blended with different lithium salts. Full lines represent VTF fits.

4.3.3 Ionic Conductivity in Dependence of Carbonate/EO-Ratio

Since a higher ion mobility and improved salt dissociation is expected in oligo(ethylene oxide) functionalized substances as compared to cyclic carbonate functionalized models, mixtures of models ***6*** and ***13*** (Figure 4.16 (upper graph)) plus ***21*** and ***26*** respectively (Figure 4.16 (bottom graph)) were studied. For all blends the ionic conductivity values of the mixed cyclic carbonates did not exceed the values obtained for the pure oligo(ethylene oxide) model compound ***13*** or ***26***. This is in contrast to the results reported by *West et al.* for hybrid polysiloxanes bearing EO and cyclic carbonate side chains.[4.26] In this particular case, polysiloxanes containing 8.5% polar cyclic carbonate side groups showed higher ionic conductivities than the analogue polymers with either 100% oligo(ethylene oxide) or 100% cyclic carbonate based side groups.

However, for the HPB and CTP based derivatives no depression of the glass transition temperatures as a result of blending could be observed and consequently the ionic conductivity did not outperform the pure oligo(ethylene oxide) electrolytes.

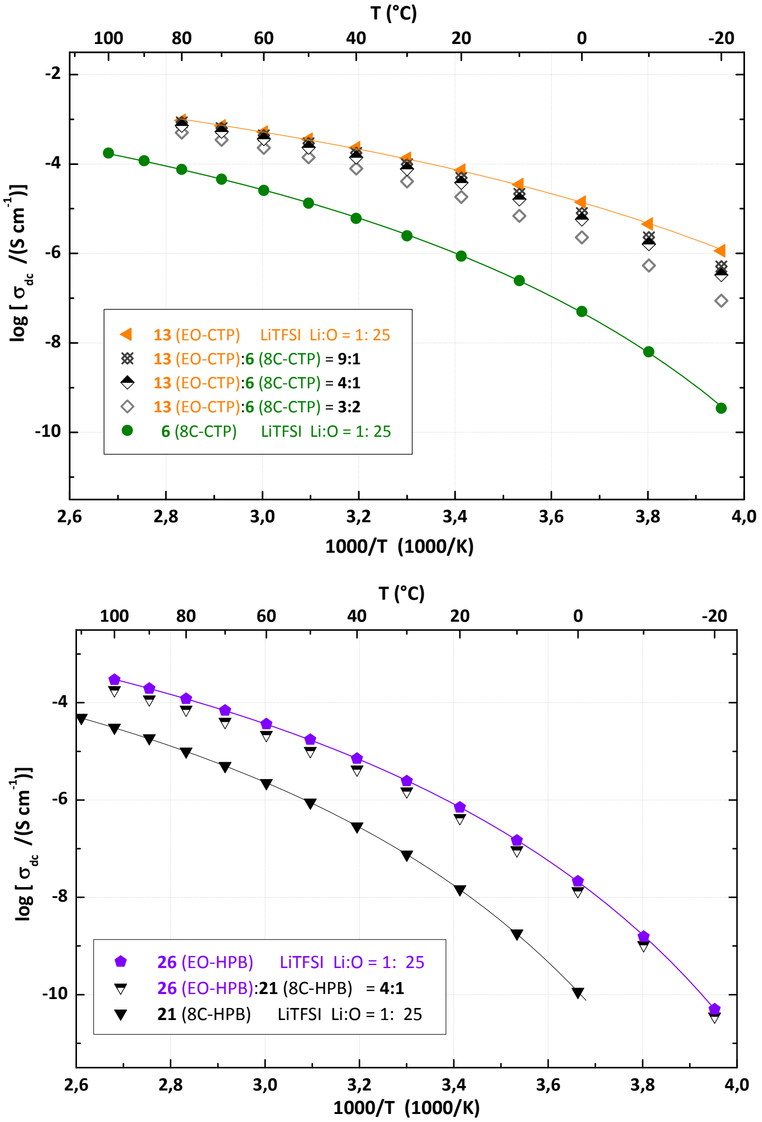

Figure 4.16. Arrhenius plot of the temperature dependent ionic conductivity of model compounds ***6*** and ***10*** (upper plot) respectively ***21*** and ***26*** (bottom plot) in different mixing ratios blended with LiTFSI (molar ratio Li:O = 1:25). (see Figure 2.13 for sample numbering). Full lines represent VTF fits.

4.3.4 Comparison of the Ionic Conductivity of the CTP and HPB based Blends

The ionic conductivities of the blended CTP and HPB based model compounds are altogether shown in Figure 4.17. In the Arrhenius representation it becomes obvious that $\log(\sigma(T))$ of the model blends does not obey a simple thermally activated hopping mechanism, since the ionic conductivity curves are no straight lines. Accordingly, the absolute conductivities across all models are the higher the lower the glass transition temperatures are.

In relation to the polymers which were studied earlier in the institute (e.g. poly(2-oxo-1,3-dioxolan-4-yl)methyl acrylate, PDOA, T_g = +50 °C),[4.27] the cyclotriphosphazene based model compound ***6*** (T_g = -34.1 °C) shows despite the much lower T_g only slightly higher ionic conductivity.

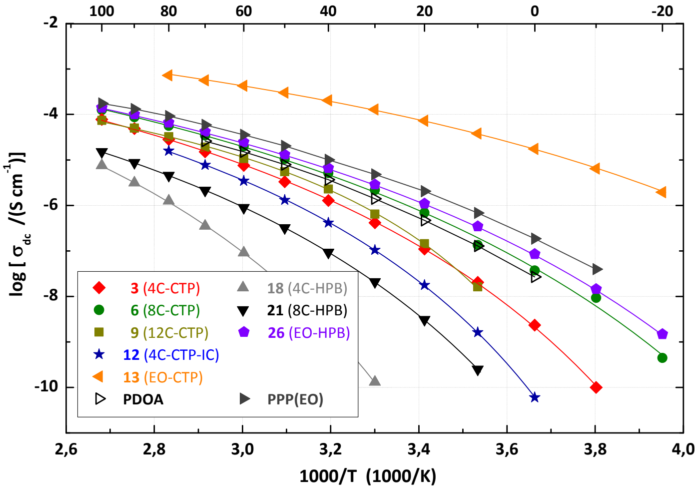

Figure 4.17. Arrhenius plot of the ionic conductivity of the various CTP and HPB based model compounds blended with LiTFSI. For all blendsthe molar ratio of Li:O is equal to 1:50; except for ***9*** (Li:O = 1:25) and ***18*** (Li:O = 1:12) (see Figure 2.13 and text below for sample numbering). Full lines represent VTF fits.

This is consistent with the fact that for PDOA the reference temperature in a *WLF* treatment is found to have values more than 100 K below the actual T_g.

Furthermore, the conductivity of the EO-functionalized HPB model blend (***26***) compares very well with poly(*p*-phenylene) bearing oligo(ethylene oxide) side chains (PPP(EO)). This is rather surprising, since PPP(EO) consists of a stiff main chain layer embedded in an amorphous matrix of EO side chain segments exhibiting a nano-phase separated structure.[4.28] However, only the EO side chains were found to contribute to the conductivity in PPP(EO) and therefore the ionic conductivity of ***26*** is in a similar range. Furthermore one might assume an organization of the HPB cores to a *'chain'* with EO side chains comparable to the described PPP(EO) picture.

WLF behavior

If not only the temperature is normalized against the glass transition temperature (compare Figure 4.7), but also the ionic conductivity $\sigma(T)$ against the value measured at the reference temperature $\sigma(T_{ref})$, a collapse of all curves in the limits of error into one

WLF master curve is observed (Figure 4.18). As reference temperature was chosen $T_g + 50K$, since for all blends T_{ref} should be in the temperature range of actually measured data. Thus, the transport of charge carriers is assumed to follow a similar mechanism for all model compound blends. Furthermore, the *free volume* as well as the molecular dynamics, which are closely related to T_g, are dominating the ion transport.

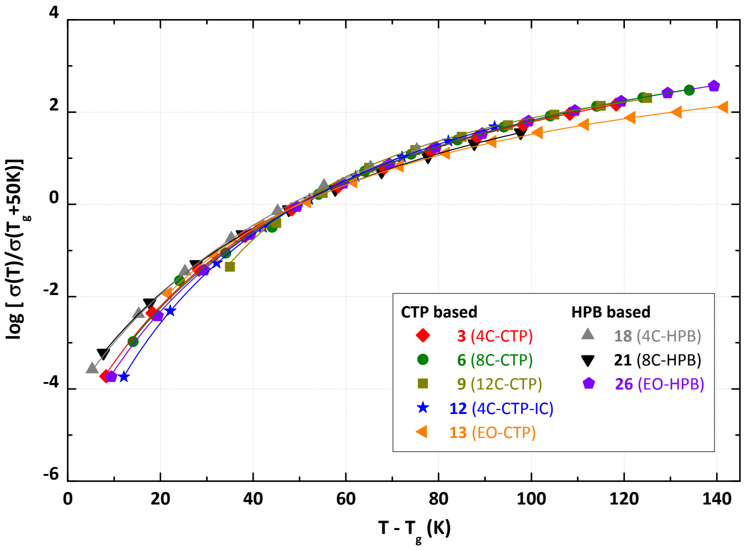

Figure 4.18. WLF plot of the shift factor log(σ(T_g)/log(σ(T_g+50K))) versus the reduced temperature *T*-T_g for the various CTP and HPB based model compounds blended with LiTFSI. For all blends the molar ratio of Li:O is equal to 1:50; except for ***9*** (Li:O = 1:25) and ***18*** (Li:O = 1:12) (see Figure 2.13 for sample numbering). Full lines represent VTF fits.

4.3.5 Tetramethylcyclotetrasiloxane based Model Compounds

The tetramethylcyclotetrasiloxane (TMS) based model compound ***27***, which bears cyclic carbonates as solvating moieties, yields ionic conductivities in the order of the CTP based analogues ***3*** and ***6***. This is a further point of reference pointing out that the core itself has no influence on the ionic conductivity, but mainly the dynamics in close relation to T_g.

However, TMS with 1-oxo-4-methoxy-2,6,7-trioxa-1-phosphabicyclo[2,2,2]octane side groups is despite the low T_g (-29.5 °C) clearly showing lower ionic conductivities than even the HPB derivative ***18*** (T_g = +24.7 °C). This behavior is attributed to the very high polarity of the bicyclic phosphate group, which may act as trap for the lithium ions, thus hampering cooperative transport. As a result, also taking the oligo(ethylene oxide) model into account, the choice of solvating moieties is crucial.

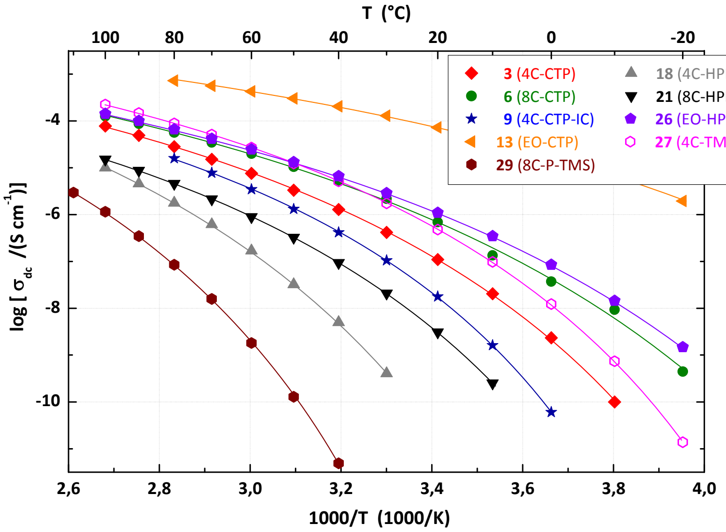

Figure 4.19(a). Arrhenius plot of the ionic conductivity of the siloxane based model compounds blended with LiTFSI in comparison to the CTP and HPB based blends. For all blends the molar ratio of Li:O is equal to 1:50; except for ***18*** (Li:O = 1:12) (see Figure 2.13 for sample numbering). Full lines represent VTF fits.

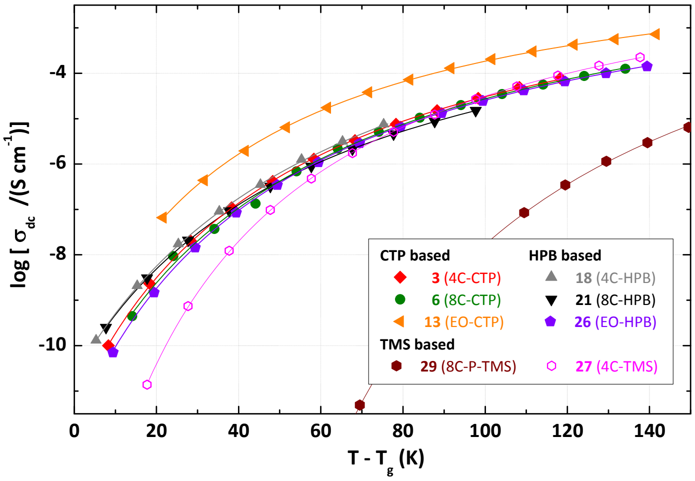

Figure 4.19(b). Ionic conductivity plotted vs. the reduced temperature of the siloxane based model compounds blended with LiTFSI in comparison to the CTP and HPB based blends. For all blends the molar ratio of Li:O is equal to 1:50; except for ***18*** (Li:O = 1:12) (see Figure 2.13 for sample numbering). Full lines represent VTF fits.

4.3.6 Best Fit Parameters

In this chapter the different fitting parameters are listed. The *VTF* fitting parameter ***A*** (compare eq. 4.46) among other factors is influenced by the charge carrier density c_i. Accordingly, $\log(A)$ decreases with increasing salt concentration for one specific model compound.

Model Compound ^{a}	T_g (°C)	*log A*	*B* (*K*)	T_0 (*K*)	R^2	T_g-T_0 (*K*)
3 - *pure*	-28.9					
LiTFSI:O = 1: 12	-12.7	0.284	524.2	217.8	0.9999	42.7
LiTFSI:O = 1: 25	-13.4	0.606	555.5	210.1	0.9999	49.7
LiTFSI:O = 1: 50	-18.4	0.444	562.9	201.8	0.9998	53.0
LiTFSI:O = 1: 100	-22.2	0.419	610.6	194.4	0.9999	56.6
LiBOB:O= 1: 25	-7.9	0.642	565.1	211.6	0.9999	53.7
$LiClO_4$:O= 1: 50	-22.9	0.842	665.5	189.8	0.9999	60.5
6 – *pure **	-35.2					
LiTFSI:O = 1: 12	-24.5	0.481	567.0	200.0	0.9999	48.7
LiTFSI:O = 1: 25	-32.5	0.486	541.5	190.8	0.9999	49.9
LiTFSI:O = 1: 50	-34.1	0.627	613.5	182.6	0.9976	56.5
LiTFSI:O = 1: 100	-32.5	0.636	688.4	176.5	0.9909	64.2
LiBOB:O = 1: 25	-25.9	0.259	495.0	202.1	0.9998	45.2
$LiClO_4$:O= 1: 25	-24.5	0.191	525.1	198.3	0.9997	50.4
LiBETI:O = 1: 25	-30.2	0.315	531.1	194.8	0.9998	48.2
9 - *pure*	70.5 (T_m)					
LiTFSI:O = 1: 25	-24.4	0.589	536.4	209.0	0.9883	39.8
12 - *pure*	-16.6					
LiTFSI:O = 1: 50	-12.1	0.167	499.2	218.5	0.9999	42.6
13 - *pure*	-78.1					
LiTFSI:O = 1: 12	-48.2	1.185	498.4	181.2	0.9999	43.8
LiTFSI:O = 1: 25	-61.4	0.678	434.3	172.4	0.9998	39.4
LiTFSI:O = 1: 50	-61.6	0.369	405.7	169.4	0.9998	42.2

T_g = glass transition (DSC); T_0 = *Vogel* temperature; * non-crystalline, see Chapter 3; A, B = *VTF* parameters; R^2 = correlation coefficient. ^{a} See experimental part or Figure 2.13 for sample numbering.

Table 4.1. Best fit VTF parameters for the CTP based model compound blends.

However, between the different derivatives no definite trend is identifiable. Here, the other variables as the geometrical factor g, or the thermal varibales a^* and μ are affected, which in combination make a useful quantification impossible.

The *VTF* parameter ***B*** covers the effect of thermal expansion on the ionic conductivity. The values of the cyclic carbonate based substances do not vary more than 20% referred to the median. The minor variations require further measurements in order to identify the extent of influence of critical molecular parameters on ***B***; e.g. determining the thermal expansion coefficient $\alpha(T)$, since the variation in spacer length may be associated with different $\alpha(T)$, which was not enforced in the scope of the present work.

Model Compound [a]	T_g (°C)	*log A*	*B* (K)	T_0 (K)	R^2	T_g-T_0 (K)
18 - *pure*	150.8 (T_m)					
LiTFSI:O = 1: 12	24.7	1.045	690.9	231.6	0.9998	66.1
21 - *pure*	3.5					
LiTFSI:O = 1: 12	-18.0	0.780	620.8	192.6	0.9999	62.6
LiTFSI:O = 1: 25	-10.2	0.411	605.7	206.7	0.9999	56.3
LiTFSI:O = 1: 50	2.3	0.152	585.5	214.3	0.9999	56.6
$LiClO_4$:O= 1: 12	4.1	1.053	783.5	209.4	0.9999	59.7
LiBOB:O = 1: 12	9.7	0.383	558.6	229.9	0.9999	33.6
26 - *pure*	-47.4					
LiTFSI:O = 1: 18	-22.9	1.003	571.7	196.4	0.9999	53.9
LiTFSI:O = 1: 37	-37.4	0.645	578.8	184.3	0.9999	51.5
LiTFSI:O = 1: 50	-39.2	0.442	573.0	182.0	0.9999	51.7
$LiClO_4$:O = 1: 37	-32.7	0.223	512.7	193.3	0.9999	47.2
LiBOB:O = 1: 37	-36.1	0.655	530.6	188.8	0.9999	48.3
27 - *pure*	-34.3					
LiTFSI:O = 1: 25	-37.7	0.685	520.9	202.6	0.9999	32.9
29 - *pure*	6.2					
LiTFSI:O = 1: 25	-29.5	1.363	767.9	245.9	0.9998	2.3

T_g = glass transition (DSC); T_0 = *Vogel* temperature; A, B = *VTF* parameters; R^2 = correlation coefficient.

[a] See experimental part or Figure 2.13 for sample numbering.

Table 4.2. Best fit VTF parameters for the HPB based model compound blends.

T_0 relates to T_g and lies 40 °C - 60 °C below the values of T_g. If *WLF* behavior holds, the fitting parameter C_2 is equal to $T_g - T_0$, which applies in the limits of error for all models (Table 4.3). The variation in the difference between T_0 and T_g is thereby only to a limited extent assigned to the fitting, since a minimal change in T_0 results in reduced R^2.

Model Compound [a]	T_g (°C)	*log A*	*B* (K)	T_0 (K)	T_g-T_0 (K)	C_2 (K)	C_1	R^2
3 *- pure*	-28.9							
LiTFSI:O = 1: 50	-18.4	0.444	562.9	201.8	53.0	51.77	24.17	0.9998
6 *– pure **	-35.2							
LiTFSI:O = 1: 50	-34.1	0.627	613.5	182.6	56.5	54.95	24.67	0.9975
9 *- pure*	70.5 (T_m)							
LiTFSI:O = 1: 25	-24.4	0.589	536.4	209.0	39.8	45.04	26.51	0.9998
12 *- pure*	-16.6							
LiTFSI:O = 1: 50	-12.1	0.167	499.2	218.5	42.6	41.69	26.81	0.9999
13 *- pure*	-78.1							
LiTFSI:O = 1: 50	-61.6	0.369	405.7	169.4	42.2	40.22	21.93	0.9998
18 *- pure*	-							
LiTFSI:O = 1: 12	24.7	1.045	690.9	231.6	66.1	65.40	23.76	0.9997
21 *- pure*	3.5							
LiTFSI:O = 1: 50	2.3	0.152	585.5	214.3	56.6	59.99	21.73	0.9999
26 *- pure*	-47.4							
LiTFSI:O = 1: 50	-39.2	0.442	573.0	182.0	51.7	50.60	25.06	0.9999
27 *- pure*	-34.3							
LiTFSI:O = 1: 25	-37.7	0.685	520.9	202.6	32.9	31.90	36.40	0.9999
29 *- pure*	6.2							
LiTFSI:O = 1: 25	-29.5	1.363	767.9	245.9	2.3	-	-	-

T_g = glass transition (DSC) was used as T_{ref} for the WLF fitting. T_0 = *Vogel* temperature; * non-crystalline, see Chapter 3; A, B = VTF parameters; R^2 = correlation coefficient. [a] See experimental part or Figure 2.13 for sample numbering.

Table 4.3. Best fit WLF and VTF parameters for selected HPB and CTP based model compound blends.

4.3.7 Transference Numbers

Transference numbers were measured for the CTP based models ***3*** and ***6***, but not for HPB derivatives, mainly because preparation of the extremely viscous, resinous HPB mixtures within the assembly described in Figure 4.5 was not possible in an appropriate way.

Figure 4.20 shows the *Cole-Cole* plot of model compound ***3*** blended with LiTFSI in a molar Li:O ratio equal to 1:25 before and after 50 h exposure to an applied direct voltage of 10 mV in the cell assembly. The roots are equivalent to the resistances and do not show a substantial change over time, indicating stable blends versus non-blocking lithium electrodes under the applied measurement conditions.

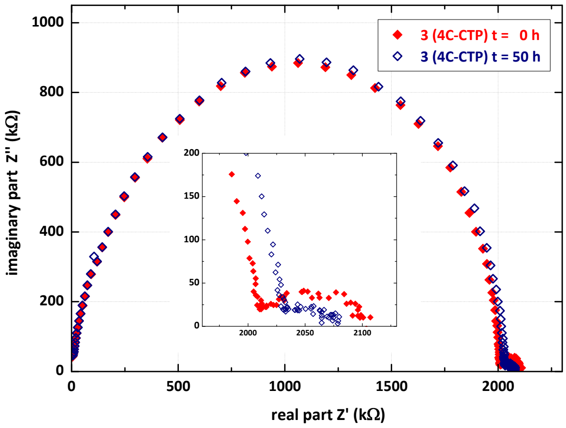

Figure 4.20. Complex-plane plot of the imaginary and real part of the AC impedance of a Li|model compound blend ***3*** |Li cell at 30 °C with an applied potential difference of 10 mV and an molar LiTFSI:O ratio equal to 1:25.

For blend ***3*** a steady-state current was reached at 30 °C after applying a DC voltage of 10 mV for around 30 hours. The lithium transference number was then determined after eq. 4.29 to be 0.58 (Figure 4.21(a)). For ***6*** the steady-state current was reached in a shorter timer of around 10 h and the transference number amounts to a slightly higher value of 0.75 (Figure 4.21(b)).

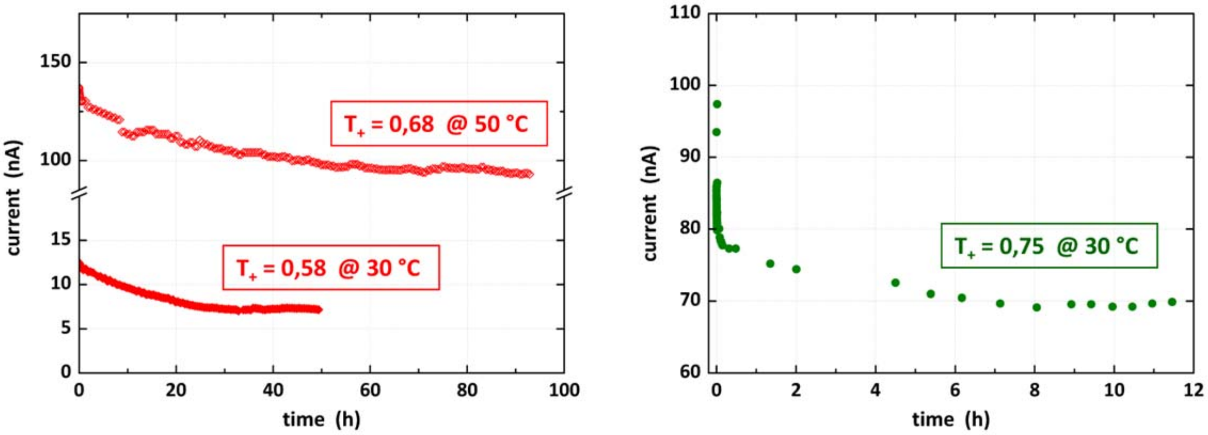

(a) ***3*** (4C-CTP) LiTFSI:O = 1:25

(b) ***6*** (8C-CTP) LiTFSI:O = 1:25

Figure 4.21. Variation of the current with time during polarization of a Li|model compound blend (***3*** or ***6***) |Li cell at various temperatures with an applied potential difference of 10 mV.

In general, these values are surprisingly high compared to the values which are typically determined for polymer electrolytes, e.g. by *Bruce et al.* applying the same method to the system Li|PEO:$LiCF_3SO_3$ (Li:O=1:9)|Li at 90 °C.[4.5] Here T_+ was found to be 0.46. The elevated values in the present case suggest differences in the translational mobility of Li^+ respectively $TFSI^-$ with increased cation diffusion.

However, the temperature dependence of the transference numbers, showing a trend to higher T_+ at higher temperatures, is not yet explained.

4.4 Bibliography

[4.1] P.G. Bruce in: *Polymer Electrolytes Reviews*, Eds. J.R. MacCallum, C. A. Vincent, Elsevier, London and New York, **1987**.

[4.2] MacDonald, J. R. *Impedance Spectroscopy*, Wiley, New York, **1987**.

[4.3] M. Schuster, Dissertation, University of Mainz, **2002**.

[4.4] N. G. McGrum, B. E. Read, G. Williams: *Anelastic and dielectric effects in polymeric solids*, Ch. 7.2, Wiley, London, **1987**.

[4.5] Evans, J.; Vincent, C. A.; Bruce, P. G. *Polymer* **1987**, Vol. 28, 2324.

[4.6] Spiro, M. in *Techniques of Chemistry*, Vol. I, Part IIA, (Eds. A. Weissberger and B. W. Rossiter), Wiley, New York, **1971**.

[4.7] Blonsky, P. M.; Shriver, D.; Austin. P.; Allcock, H. R. *Solid State Ionics* **1986**, 18/19, 258.

[4.8] Leveque, M.; Le Nest, J. F.; Gandini, A.; Cheradame, H. *Makromol. Chem. Rapid Commun.* **1983**, 4, 497.

[4.9] Bruce, P. G.; Vincent, C. A. J. *Electroanal. Chem. Interfacial Electrochem.* **1987**, 1, 225.

[4.10] M. A. Ratner in: *Polymer Electrolyte Reviews*, Ed. J. R. MacCallum, C. A. Vincent, Elsevier, London and New York, **1987**.

[4.11] G. Scharfenberger, Dissertation, University of Mainz, **2003**.

[4.12] Schuster, M.; Kreuer, K. D.; Andersen, H. T.; Maier, J. *Macromolecules* **2007**, 40, 598.

[4.13] Vogel, H. *Phys. Z.* **1921**, 22, 645.

[4.14] Tamman, G.; Hesse, W. *Z. Anorg. Allg. Chem.* **1926**, 156, 245.

[4.15] Fulcher, G. S. *J. Amer. Ceram. Soc.* **1925**, 8, 339.

[4.16] Claridge, T. D. W.; *Tetrahedron Organic Chemistry Series*, Volume 19: High-Resolution NMR Techniques in Organic Chemistry, Pergamon: Amsterdam, **1999**.

[4.17] Cowie, J. M. G. in *Chemie und Physik der synthetischen Polymere*, Vieweg, Braunschweig, **1997**.

[4.18] Fox, F. G.; Flory, P. J. *J. Am. Chem. Soc.* **1948**, 70, 2384.

[4.19] Doolittle, A. K. *J. Appl. Phys.* **1951**, 22, 1471.

[4.20] Cohen, M. H.; Turnbull, D. *J. Chem. Phys.* **1959**, 31, 1164.

[4.21] Meyer, W. H. *Adv. Mater.* **1998**, 10, 439.

[4.22] Zhang, Z.; Lyons, L. J.; Jin, J. J.; Amine, K.; West, R. *Chem. Mater.* **2005**, 17, 5646.

[4.23] Morita, M., Oral Presentation #840, *Proceedings 15th International Meeting on Lithium Ion Batteries*, Montreal, Canada, July **2010**.

[4.24] a. Täubert, C.; Fleischhammer, M.; Wohlfahrt-Mehrens, M.; Wietelmann, U.; Buhrmester, T. *J. Electrochem. Soc.* **2010**, 157, A721 (and references therein).

b. Panitz, J.-C.; Wietelmann, U.; Wachtler, M.; Ströbele, S.; Wohlfahrt-Mehrens, M. *J. Power Sources* **2006**, 153, 396.

c. Yang, L.; Furczon, M. M.; Xiao, A.; Lucht, B. L.; Zhang, Z.; Abraham, D. P. *J. Power Sources* **2010**, 195, 1698.

[4.25] Armand, M.; Gorecki, W.; Andreani, R.; Scrosati, B. *Second International Symposium on Polymer Electrolytes*, Elsevier Applied Science **1989***,* 91.

[4.26] Zhang, Z.; Lyons, L. J.; West, Ryan.; Amine, K.; West, Robert *Silicon Chemistry* **2005**, *3*, 259.

[4.27] Britz, J.; Meyer, W. H.; Wegner, G. *Macromolecules* **2007**, 40, 7558.

[4.28] Lauter, U.; Meyer, W. H.; Wegner, G. *Macromolecules* **1997**, 33, 2092.

CHAPTER V

5. Solid-State NMR Investigations

A short overview over the theoretical background of Solid-State NMR in general and the basics of the applied methods will be given in the following paragraphs.

5.1 Theoretical Background [5.1-5.6]

In principle, in solid-state there are important differences compared to common solution-state NMR. Most obvious are the observed broader resonances in powder samples resulting from the anisotropy of the chemical shift (*CSA*), heteronuclear and/or homonuclear dipolar couplings, and quadrupolar interactions. In order to deal with these effects, several basic techniques are required:

Magic Angle Spinning (MAS) [5.1-5.6]

If one inclines the principal axis frame of a single crystal in such a way that its z-axis and the direction of the outer magnetic field form an angle of $\theta = 54.74°$, called the *magic angle* (Figure 5.2), the term

$$(3cos^2\theta - 1)\,, \qquad \textbf{eq. 5.1}$$

which is comprised in the formula for the altered resonance frequencies due to dipolar and quadrupolar coupling, becomes zero. In other words, dipolar and first-order quadrupolar couplings are averaged out. Consequently, isotropic chemical shielding should be observed. However, single crystalline modifications are hard to obtain for all samples, especially for polymers. Accordingly, in low ordered materials the anisotropic interactions do not necessarily coincide and the magic angle condition is not fulfilled for all interactions. This problem can be solved, if the sample is additionally spun at an axis inclined at the magic angle to the outer magnetic field; a technique called *Magic Angle Spinning* (*MAS*).[5.4][5.5] In this case the orientation of the interaction tensors within the sample are averaged, and if the reorientation is fast relative to the chemical anisotropy, all principal axis frames are aligned parallel along the magic angle direction. Looking down the space diagonal in Figure 5.1, the x-, y- and z-coordinate appear symmetric. Thus, the nucleus experiences in one single rotation the average of the effective chemical shift, equal to the isotropic chemical shift δ_{iso}.

Figure 5.1. The space diagonal of a cube makes an angle of 54.74° with the z-axis. Rapid spinning around this axis removes the dipolar interactions. Reproduced from ref. [5.6].

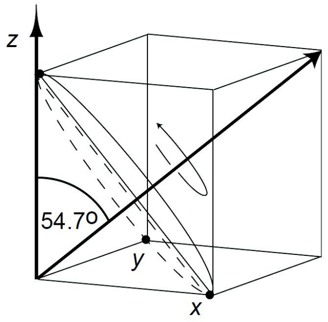

The spinning speed should be fast, particularly two times faster than the anisotropy expressed in Hertz. Otherwise incomplete averaging of the *CSA* results in lines at frequency distances of integer multiples of the spinning speed apart from the isotropic central line. These peaks are named '*spinning sidebands*'.

Decoupling [5.1-5.3][5.6]

Heteronuclear dipolar coupling also broadens the resonance lines. As a result, the peak height decreases since the absolute intensity remains constant, while the signal to noise ratio decreases.[5.3] The reason for this is assigned to through space interactions between the nuclear magnetic moment of an abundant and a rare spin, labeled by convention *I* respectively *S.* In solution, the fast reorientations mostly average these interactions out, but in solid-state this is generally not the case. The Hamiltonian

$$H_{1S} = -d(3cos^2\theta - 1)I_zS_z \qquad \textbf{eq. 5.2}$$

represents the strength of the heteronuclear dipolar coupling, with the dipolar coupling constant d being equal to

$$d = \left(\frac{\mu_0}{4\pi}\right)\frac{h\gamma_I\gamma_S}{r_{IS}^3}\,.^{[4.6]} \qquad \textbf{eq. 5.3}$$

In eq. 5.2 and 5.3, γ_I or γ_S stand for the gyromagnetic ratio of the *I* and *S* spins, I_z and I_s are the z-components of the angular momentum operators, r_{IS} describes the internuclear distance, and μ_o is the permeability of the free space. According to eq. 5.3 the magnitude of the coupling is proportional to the product of the gyromagnetic ratios, inversely dependent on the cube of the internuclear distance and shows an orientation dependency of $(3cos^2\theta - 1)$. As a consequence, one way to remove dipolar coupling is the previously described *Magic Angle Spinning*.

Another way is *continuous-wave* (*CW*) spin decoupling.[5.53] By applying a constant irradiation with the frequency of the nuclei whose influence should be eliminated, most often the one of the protons (high natural abundance and high δ), the spin of the protons is changing continuously from the '*spin-up'* to the '*spin-down'* state. Hence, the heteronuclear coupled nuclei only see the average orientation, which is in total zero.

In case of homonuclear dipolar coupling, *CW* decoupling is not applicable due to the identical resonance frequency of the coupling nuclei. Here equation 5.2 modifies insofar that just spin operators I enter the respective Hamiltonian. Those cannot be manipulated independently. Nevertheless, with the help of multipulse sequences known as *WAHUHA*[5.7] or *Lee-Goldburg*[5.8] the coupling effect can be eliminated.

Furthermore, at times *MAS* is not sufficient to remove dipolar coupling, multi pulse decoupling, i.e. two-phase modulation (TPPM), which was employed in the present work, is advantageous.[5.9] The sequence consists of consecutive pulses of around 165° with an alternating phase $(\pm\,\phi/2)$. The exact pulse length has to be optimized for each sample.

Cross Polarization (CP) [5.1-5.3][5.6]

In order to overcome the drawbacks of direct low-γ nuclei detection, such as low natural abundance, low spin polarization, and low signal intensity, *cross polarization* (*CP*) is an important technique to enhance the signal intensity by transferring magnetization from abundant (commonly ^{1}H) to the interesting rare nuclei (i.e. ^{13}C or ^{15}N).[5.6] The basis for the *CP* signal enhancement is the tendency of the magnetization to flow from highly polarized to low polarized nuclei mediated by heteronuclear coupling.[5.6] However, at high magnetic fields the heteronuclear magnetization transfer in form of '*flip-flop*' transitions (two alike spins, one flips up, one down) is not energy-conserving. Therefore, the magnetization exchange can be induced by applying external r.f. fields, as in the

Hartman-Hahn method (Figure 5.2). Here, a simultaneous application of two r.f. fields, one in resonance with the abundant, one with the rare spins, enables the independent rotation of both.[5.6]

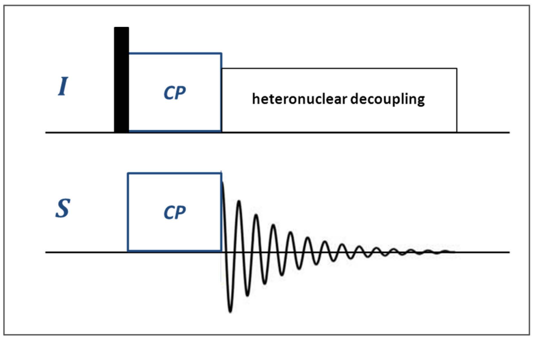

Figure 5.2. Schematic CP pulse sequence for the detection of ^{13}C (*S*) by magnetization transfer from protons (*I*).

Tuning the r.f. field strengths in such a way that the *I* and *S* spin nutation frequencies are equal results in a dipolar contact between the two spin systems, which mediates the magnetization transfer.

A further advantage of *CP* is the fact that the rather long relaxation, characterizing the low abundant nuclei, can be circumvented since the repetition rate is determined by the magnetic source, here the protons, which usually have considerably shorter relaxation times.

5.2 Applied Solid-State NMR Methods [5.1-5.2][5.10-5.15]

Solid-State NMR is a powerful tool to investigate local ion dynamics within *'salt-in'* (polymer) electrolytes and provides insights into the molecular mechanism of ionic transport. Indeed, profound understanding of the latter is crucial in order to give directions for potential improvements of current (polymer) electrolytes (compare Chapter I).

In particular, the relative contributions of cations or anions to the overall measured DC conductivity and the impact of side group solvating moieties is of interest, where the latter is potentially related to segmental motions of the polymer and the corresponding temperature dependence.[5.11] By multinuclear Solid-State NMR the motional process and ion diffusion of different constituents can be probed independently on different time and length scales.

The NMR techniques outlined in Figure 5.3 are capable to measure motional parameters such as the jump rates of cations and anions (in this work $^7Li^+$ or ^{19}F (in TFSI$^-$) respectively) over a wide frequency range starting in the *sub-Hz regime* (less than one jump per second, *SAE*) and ending in the *GHz-regime* (more than one million jumps per second, *SLR* in the laboratory frame).[5.12]

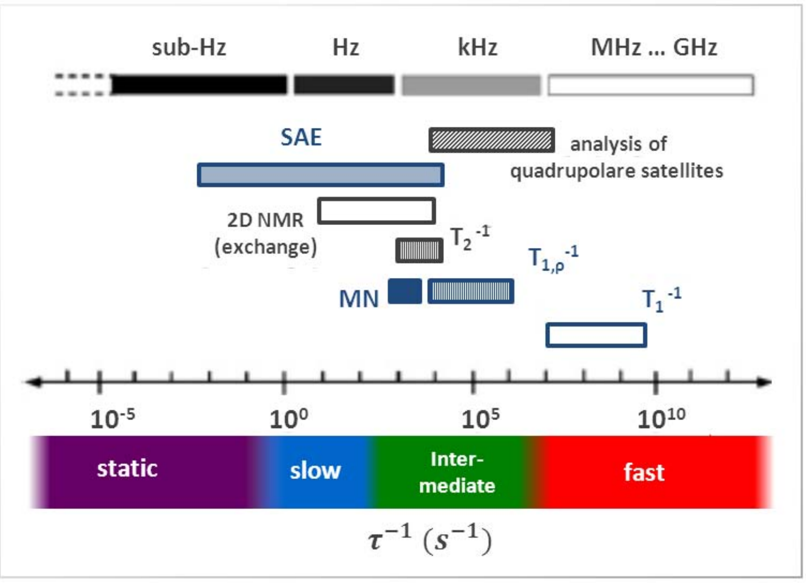

Figure 5.3. Different NMR techniques and the corresponding timescales on which motional parameters such as the jump rate τ^{-1}can be probed. The dynamic range covers about ten order of magnitude. T_1^{-1}: NMR spin-lattice relaxation (SLR) rate in the laboratory frame; $T_{1\rho}^{-1}$: NMR SLR rate probed in the rotating frame of reference; T_{1D}^{-1}: dipolar NMR SLR; T_2^{-1}: NMR spin-spin relaxation rate; MN: motional narrowing (e.g. temperature-dependent line width analysis); SAE: spin-alignment echo. Modified Figure from ref. [5.12].

In this work, spin-lattice relaxation (*SLR*) in both, laboratory (T_1) and rotating frame of reference ($T_{1\rho}$), temperature dependent motional narrowing (*MN*) of the static line width, stimulated ^{7}Li echoes via spin-alignment echo technique (*SAE*), and finally pulsed-field gradient (*PFG*) NMR are applied to study the lithium ion dynamics therein.

The methods are described in the following subchapters.

5.2.1 Microscopic Methods

Spin-Lattice Relaxation (SLR) Measurements [5.1][5.13-5.15]

Spin-lattice relaxation (*SLR*) measurements in the laboratory frame (static co-ordinate system, T_1) as well as in the rotating frame ($T_{1,\rho}$) provide information on the lithium ion motion via temporal fluctuations of the local fields, which are induced primarily by the motion of particles.

SLR in the Laboratory Frame - T_1 [5.1][5.13-5.15]

Spin-lattice relaxation in the laboratory reference frame describes the recovery of the *longitudinal* magnetization into the equilibrium state. In case of the ***inversion recovery*** method a 180° radio-frequency (r.f.) pulse inverts the equilibrium $+z$-magnetization into the -z-direction. This can be explained if one considers the setup consisting of a sample placed in a strong, external magnetic field B_0, whereby the sample itself is surrounded by a coil perpendicular to the z-direction of B_0. The coil enables the application of a pulsed alternating field B_1 with a frequency ω in the r.f. regime. This field is made time-independent by choosing a coordinate system rotating with the same frequency ω along the direction of B_0. The result is a reduced field along the z-axis, which adds vectorially with the field B_1 to a stationary effective magnetic field B_{eff}. If then ω is equal to the Larmor precession frequency ω_L, the z-component of B_{eff} vanishes and so the equilibrium magnetization M_0 in z-direction will be tilted. The length t_p of the applied r.f. pulse determines the magnitude of the rotation or flip angle β, which is equal to ωt_p. The subsequent precession of the rotated magnetization in the xy-plane of the laboratory reference frame induces a detectable voltage in the coil, which is known as the *free induction decay* (*FID*). Coming back to the inversion recovery experiment, the relaxation of the magnetization $M_z(t)$ along the z-axis after the π-pulse is monitored in terms of incremented delay times τ. At short τ the change in magnetization is minor and thus, the 90° reading pulse, which rotates the current magnetization into the $+y$-direction, leads to a negative line in the corresponding spectrum. With increasing delay times, relaxation proceeds and thus the magnetization diminishes first to zero accompanied by a decrease of the negative line and finally increases along +z. In the latter case the 90° pulse onto -y leads to positive lines in the spectrum, which reach at sufficiently long τ a maximum value.[5.1][5.13]

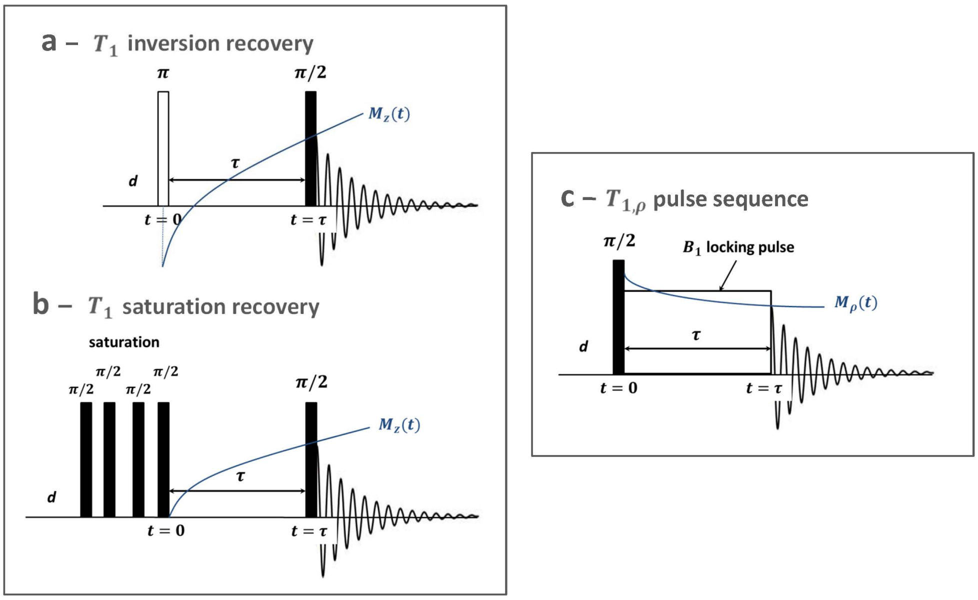

Figure 5.4. Pulse sequence of a T_1 (**a**) inversion and (**b**) saturation recovery experiment plus (**c**) principle of a $T_{1,\rho}$ experiment.

The ***saturation recovery*** method utilizes the same effect described above. The major difference is that the longitudinal magnetization is destroyed by a 90° pulse train. Consequently, at a relaxation delay close to zero no signal is obtained since the magnetization along the z-axis is zero. With increasing τ the z-magnetization recovers, where a maximum in intensity is observed after a delay equal to 5 times T_1. The corresponding pulse programs are outlined in Figure 5.4.

The recovery of $M(t)$ follows in the simplest case an exponential given by

$$M_z(t)/M_0 = 1 - \exp(-t/T_1)\,, \qquad \textbf{eq. 5.4}$$

with the spin-lattice relaxation rate $1/T_1$.[5.15] Relaxation occurs due to fluctuating fields, which are a result of temperature induced motion of the nuclei.[5.15] These fields are either of dipolar (correlation in between adjacent nuclei) or of quadrupolar nature (local *EFG*) and can be described by a correlation function $G(t)$. *Bloembergen*, *Purcell* and *Pound* introduced the following equation for $G(t)$

$$G(t) = G(0)\, exp\,(-|t|/\tau_c), \qquad \textbf{eq. 5.5}$$

where τ_c is the characteristic correlation time and $G(0)$ the correlation function at the time $t = 0$.[5.42] The *SLR* rate $1/T_1$ is proportional to the Fourrier transform of eq. 5.5, namely the spectral density function $J(\omega)$, which is given by

$$J(\omega) = G(0)\,\frac{2\tau_c}{1+(\omega\tau_c)^2} \propto {}^{1}\!/_{T_1}\,. \qquad \textbf{eq. 5.6}$$

[5.14]

The temperature dependence of τ_c often follows an Arrhenius relation and spin-lattice relaxation becomes effective, when $J(\omega)$ has elements at the Larmor frequency ω_L. Furthermore, eq. 5.5 reveals that $J(\omega)$ passes through a maximum and so also $T_1^{-1}(T)$, when plotted versus $1/T$, providing that the rates are solely induced by diffusion. The temperature possessing the maximum relaxation rate $T_1^{-1}(T)$ is thereby determined by the condition $\omega_L \tau_c \approx 1$.[5.13]

The characteristic behavior of T_1^{-1} is sketched in Figure 5.5. In this representation at temperatures above (*high-T flank,* $\omega_L \tau_c \ll 1$) and below (*low-T flank,* $\omega_L \tau_c \gg 1$) the rate maximum, the slope gives the activation energy E_a for long- and short-range diffusion, respectively.[5.12]

Figure 5.5. Characteristic behavior of ^{7}Li NMR spin-lattice relaxation rates T_1^{-1} plotted vs. 1000/T. Modified Figure from ref. [5.12].

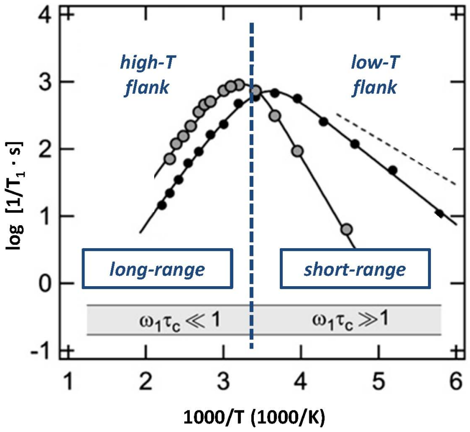

Standard *BPP* behavior of T_1^{-1} for uncorrelated motion lead to symmetric rate peaks for each Larmor frequency, whereas the *SLR* rate shows no ω_L-dependence at temperatures above the rate maximum.[5.42] In the *low-T flank* T_1^{-1} is proportional to ω_L^{-2}. However, deviations from the *BPP* prediction are often found in real solid materials. This results in asymmetric rate peaks exhibiting a reduced absolute slope in the low temperature regime and a ω_L dependence obeying $T_1^{-1} \propto \omega_L^{\alpha}$ with $\alpha \leq 2$.[5.12] Correlation effects in terms of structural disorder or Coulomb interactions are assumed to influence the slope.[5.16] Asymmetric rate peaks are also anticipated if the activation energies for long- and short-range diffusion tend to be different. In this case the *high-T flank* leads to E_a's comparable with those obtained from DC conductivity data.[5.12]

SLR in the Rotating Frame - $T_{1,\rho}$ [5.13-5.14]

Spin-lattice relaxation probed in the rotating instead of laboratory frame provides $T_{1,\rho}$.[5.14] The pulse sequence in this case consists of a $\pi/2$ pulse, which tilts the magnetization into the xy-plane. Afterwards, a locking pulse keeps the magnetization parallel to B_1 in the rotating frame. The magnetization M_ρ relaxes during the looking pulse τ and the value $M_\rho(\tau)$ can be measured by the *FID* at the end of the pulse. Out of the decreasing signal with increasing length of the locking pulse, $T_{1,\rho}$ is accessible. Since B_1 is in general much smaller than B_0, considerable longer correlation times are accessible in comparison to the experiments in the laboratory frame.

In case of *SLR* referred to the rotating frame and the alternating field B_1, the rate $T_{1,\rho}^{-1}$ follows the relation

$$T_{1,\rho}^{-1} \propto J(2\omega_1) \text{ with } \omega_1 = \gamma B_1 \,. \qquad \textbf{eq. 5.7}$$

Here, the rate maximum of $T_{1,\rho}^{-1}$ occurs, when $\omega_1 \tau_c \approx 0.5$, which explains the possible investigation of longer correlation times.

Spin-Alignment Echo (SAE) NMR - T_{SAE} [5.14][5.17-5.18]

Spin-alignment echo (*SAE*) spectroscopy on deuterons was originally established by *Spiess et al.* and proved to be a successful tool to investigate deuteron dynamics and to provide detailed information about the type of nuclear motion.[5.19-5.21] Not all that long ago, static *SAE* NMR spectroscopy was also applied to quadrupolar nuclei: *Böhmer et al.* studied ultraslow lithium dynamics (*jump rates* smaller than 10^4 s^{-1}) in lithium phosphates and recently even amorphous samples where investigated.[5.22] In principle, *SAE* NMR takes advantage of the interactions between the nuclear quadrupole moment of the nucleus and a non-vanishing *electric field gradient* (*EFG*) tensor at its site.[5.17] These interactions define the angular quadrupole frequency ω_Q, which changes upon ion motion. Consequently, labeling of the ions and thus probing the lithium ion dynamics via the time dependence of ω_Q is possible. Thereby, the time evolution of ^{7}Li spins in a non-rotating sample is given by the first-order quadrupolar Hamiltonian[5.23]

$$\hat{H}_Q = \frac{1}{\sqrt{6}}\, \omega_Q\, \hat{T}_{20} \,, \qquad \textbf{eq. 5.8}$$

with the spherical tensor operator

$$\hat{T}_{20} = \frac{1}{\sqrt{6}}\left[\,3\,\hat{I}_Z^2 - \hat{I}\big(\hat{I}+1\big)\right] \qquad \textbf{eq. 5.9}$$

and the quadrupole precession frequency in the rotating frame

$$\omega_Q/2\pi = \frac{1}{4}\,C_Q(3\cos^2\Theta - 1 - \eta\,\sin^2\Theta\cos\,(2\Phi))\,,\ C_Q = \frac{e^2qQ}{h}\,.^{[5.17]} \qquad \textbf{eq. 5.10}$$

C_Q is thereby the quadrupolar coupling constant for a spin-3/2 nuclei, with e the charge of the proton, h Planck's constant, eq the principal component of the electric field gradient tensor, and Q the electric quadrupole moment of the nucleus. The angles Θ and Φ specify the orientation of the *EFG* tensor at the nucleus site with respect to the external magnetic field. $\hat{I}_Z$ and $\hat{I}$ represent the nuclear spin operators, while η denotes the asymmetry parameter.[5.17] The latter alters the angular Zeeman frequency ω_0 in terms of $\omega_0 \pm \omega_Q$. If a '*jumping*' ion visits on its diffusion pathway sites with non-equivalent *EFG*, a change of the angular frequency ω_Q occurs, allowing for ion dynamic monitoring.[5.17]

The spin alignment technique renders measurements of two-time single-particle correlation function S_2, yielding information about dynamic as well as geometric parameters.[5.17] The method employed in this work is the so-called *Jeener-Broekaert* (*JB*) pulse sequence,[5.24] which was applied to spin-3/2 nuclei e.g. ^{9}Be by *Tang and Wu* [5.25][5.26] and ^{7}Li by *Böhmer et al.*.[5.22] The sequence is constructed as follows:

$$(90°)_x - t_p - (45°)_y - t_m - (45°)_\phi - t - aquisition\,.$$

The phase ϕ of the third pulse is thereby arbitrary.[5.17] Ideally, starting from thermal equilibrium $\hat{I}_Z$, the first two pulses, separated by a preparation time t_p, generate a longitudinal pure quadrupole spin-alignment.[5.17] However, in order to prevent unwanted coherences, i.e. of dipolar order,[5.26] and to decrease the effect of pulse imperfections, proper phase cycling is essential.[5.27] Furthermore, t_p has to be shorter than the spin-spin relaxation time T_2. In this work, if not stated otherwise, t_p was chosen to be 15 µs.[5.17] The final third pulse of the sequence, also called *reading pulse*, transforms the quadrupole spin-alignment back into a detectable transverse magnetization, which leads to an echo.[5.17] The amplitude of this echo is maximal in case the three pulses are chosen to be 90°, 45°, and again 45°.

Then, S_2 can be expressed by eq. 5.11:

$$\mathrm{S}_2\left(t_p, t_m, t\right) = \frac{9}{20}\langle\sin\left[\omega_Q(t_m = 0)t_p\right]\sin\left[\omega_Q(t_m)t\right]\rangle\,. \qquad \textbf{eq. 5.11}$$

Here, the $\langle\ldots\rangle$ brackets reflect the powder average and t the acquisition time.[5.18] For fixed t_p the decay of the stimulate echo amplitude $S_2\left(t_p, t_m\right)$ as a function of the mixing time t_m, which is varied from a few microseconds up to several seconds, is due to two classes of processes: First, actual '*hopping*' of lithium ions, and second, quadrupolar spin-lattice relaxations and/or spin diffusion.[5.17] The former renders direct measurement of the correlation time τ feasible, since the decay of $S_2(t_p, t_m)$ with increasing t_m is directly dependent on '*hopping*' ions and consequently on different frequencies ω_Q. Usually the decay shows a stretched exponential behavior:

$$S_2\left(t_p, t_m\right) \propto e^{\left[-\left(\frac{t_m}{\tau_{echo}(t_p)}\right)^{\gamma_{echo}}\right]} \text{ with } 0 < \gamma_{echo} \leq 1\,. \qquad \textbf{eq. 5.12}$$

This is the result of a superposition of different damping factors. Besides the contribution of successful hops of lithium ions, spin-lattice relaxation and spin-diffusion give rise to additional damping effects on the echo.[5.28] Therefore, t_m has to be chosen to be smaller than T_1 in order to meet the experimental time window for the investigation of ionic motion.

5.2.2 Macroscopic Methods

Pulsed-Field Gradient (PFG) NMR [5.14][5.29-5.30]

The pulsed-field gradient (*PFG*) technique provides an effective approach to measure long-range (μm) translational diffusion. Two gradient pulses are complemented into a so-called *Hahn* spin echo pulse sequence (90°-τ-180-acquisition) as follows:

After the equilibrium magnetization is tilted perpendicular to B_0 by means of a $90°$ pulse, the spins i in different magnetic surroundings lose coherence due to precession at different rates (*dephasing*). A gradient pulse of duration δ with a magnitude $g(t)$ in z-direction, applied shortly afterwards within the first τ-period at time t, labels the z-coordinate of the spins. In other words, the spatially dependent gradient causes a phase shift $\phi_i(\tau)$ of the precessing magnetization,[5.14] which is given by

$$\phi_i(\tau) = \gamma B_0 \tau + \gamma g \int_{t_1}^{t_1+\delta} z_i(t) dt \;.^{[5.29]} \qquad \textbf{eq. 5.13}$$

The first term in eq. 5.13 is the result of the static field, the second one of the applied gradient. After a delay τ a π-pulse (*rephasing*) inverts the direction of the magnetization in the xy-plane and therewith the sign of the first gradient pulse.[5.14] If then in the time interval Δ between the two equal gradient pulses no translational diffusion along the z-axis is taking place, the second gradient pulse compensates the phase difference created during the first one. Consequently, all spins refocus and no difference in amplitude in comparison to the simple spin echo experiment is observable.[5.29] In this case damping occurs only due to T_2 (spin-spin) relaxation. However, if there is translational diffusion with respect to the z-direction, i.e. ionic transport, the echo is additionally damped, since the compensation is incomplete as a consequence of the altered magnetic surrounding, which is interacting with the spins.[5.31] The damping is thereby proportional to the displacement along the z-axis, which proceeds within the period Δ. Effects on the attenuation of the echo intensity $I(g)$ have the gradient strength g and the corres-ponding gradient duration δ together with the time intervals Δ and τ between the gradient or r.f. pulses, respectively.

However, especially in highly viscous materials such as the prepared model compounds or real solids, in which the diffusion is expected to be slow, T_2 can be very short. The latter is yet limiting the duration of the experiment and may be even too short in order to observe a distinct attenuation of the echo.[5.14] Therefore, a modified pulse sequence utilizing instead of a *Hahn* pulse sequence a *stimulated echo* (*STE*) sequence with two $\pi/2$ r.f. pulses replacing the π r.f. pulse, is preferable (Figure 5.6).[5.32] The reason behind this is related to the fact that between the second and the third 90° pulse the magnetization is stored parallel to the z-axis.[5.14] As a consequence, the magnetization is not affected by T_2 relaxation between the second and third $\pi/2$ r.f. pulse; only T_1 relaxation has an effect. Since usually, in viscous or solid samples $T_1 \gg T_2$ is valid, the available time window is enlarged. Hence, slower diffusion can be probed with the *STE* sequence. Fitting the echo damping for the same with the exponential decay function

$$I(g) \; = \; I_0 \, exp\left[-D\,\gamma^2 g^2 \delta^2 \left(\Delta - \frac{\delta}{3}\right)\right] \qquad \textbf{eq. 5.14}$$

makes the diffusion coefficient D of the investigated species accessible.[5.14][5.33] Equation 5.14 is thereby applicable if $\Delta \gg \delta$ and the diffusion process itself is random.[5.29]

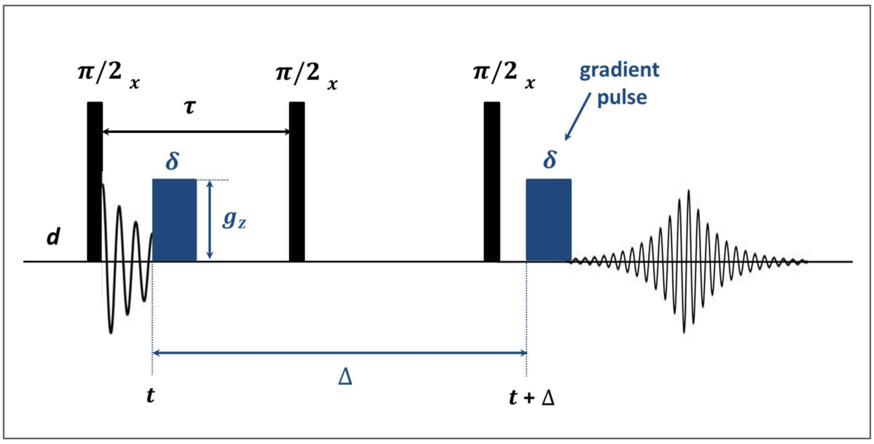

Figure 5.6. PFG pulse sequence after *Tanner* utilized in order to obtain ^{7}Li diffusion coefficients.[5.32]

5.3 Results & Discussion

5.3.1 ^{1}H, ^{13}C and ^{31}P NMR

5.3.1.1 Temperature-dependent One-Dimensional ^{1}H NMR Spectra

One-Dimensional ^{1}H MAS NMR spectra of the pure model compounds plus the corresponding blends with LiTFSI were acquired at a Bruker ASX 500 spectrometer working at a Larmor frequency $\omega_0/2\pi$ of 500.13 MHz. The air and moisture-sensitive samples were packed in a nitrogen-filled glove box into a rotor with 2.5 mm outer diameter and rotated with a spinning rate of 25 kHz. Figures 5.7 compares the temperature dependent ^{1}H MAS NMR spectra of the pure CTP based model compounds ***3*** (4C-CTP) and ***6*** (8C-CTP). Related to the glass transition temperatures T_g of -28.9 °C and -35.2 °C, respect-tively, the development of distinct signals attributed to the cyclic carbonate protons sets in ca. 40 °C above the actual T_g, whereas model compound ***6*** bearing the longer alkyl spacer in between the carbonate moieties and the CTP core shows a considerably better resolution.

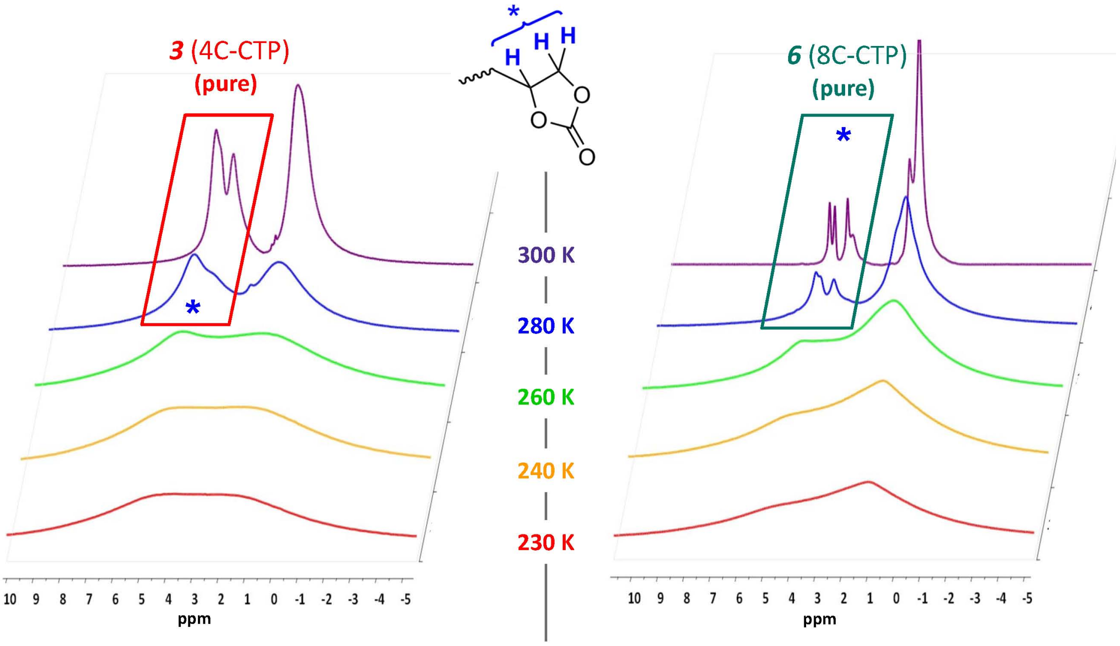

Figure 5.7. Temperature-dependent ^{1}H MAS NMR spectra (25 kHz, 500 MHz) of the pure model compounds ***3*** (left) and ***6*** (right).

Referring to the similar glass transition temperatures one might deduce a higher absolute mobility of the cyclic carbonates of pure ***6*** over ***3***. However, this does not hold for the investigated blends. First of all, if the models are blended with LiTFSI in a molar Li:O ratio of 1:25, the mobility of the cyclic carbonates at elevated temperatures is decreasing since the glass transition temperature is increased due to LiTFSI addition (compare Chapter III). This is exemplary evidenced by the stacked temperature-dependent ^{1}H MAS NMR spectra of blended and pure ***6*** shown in Figure 5.8(a). However, if the blends of ***3*** and ***6*** are directly compared to each other, there is no hint for a higher absolute mobility of the cyclic carbonate groups within one CTP based blend (Figure 5.8(b)). More precisely, the T_g of ***3*** respectively ***6*** blended with LiTFSI amounts to -13.4 °C or -32.5 °C respectively. 50 °C above T_g, for ***3*** this is at ca. 310 °C (exact: 309.8 °C) and for ***6*** at ca. 290 °C (exact: 290.7 °C), the resolution of the cyclic carbonate protons in both blends is comparable and so is the mobility in relation to the corresponding glass transition temperature.

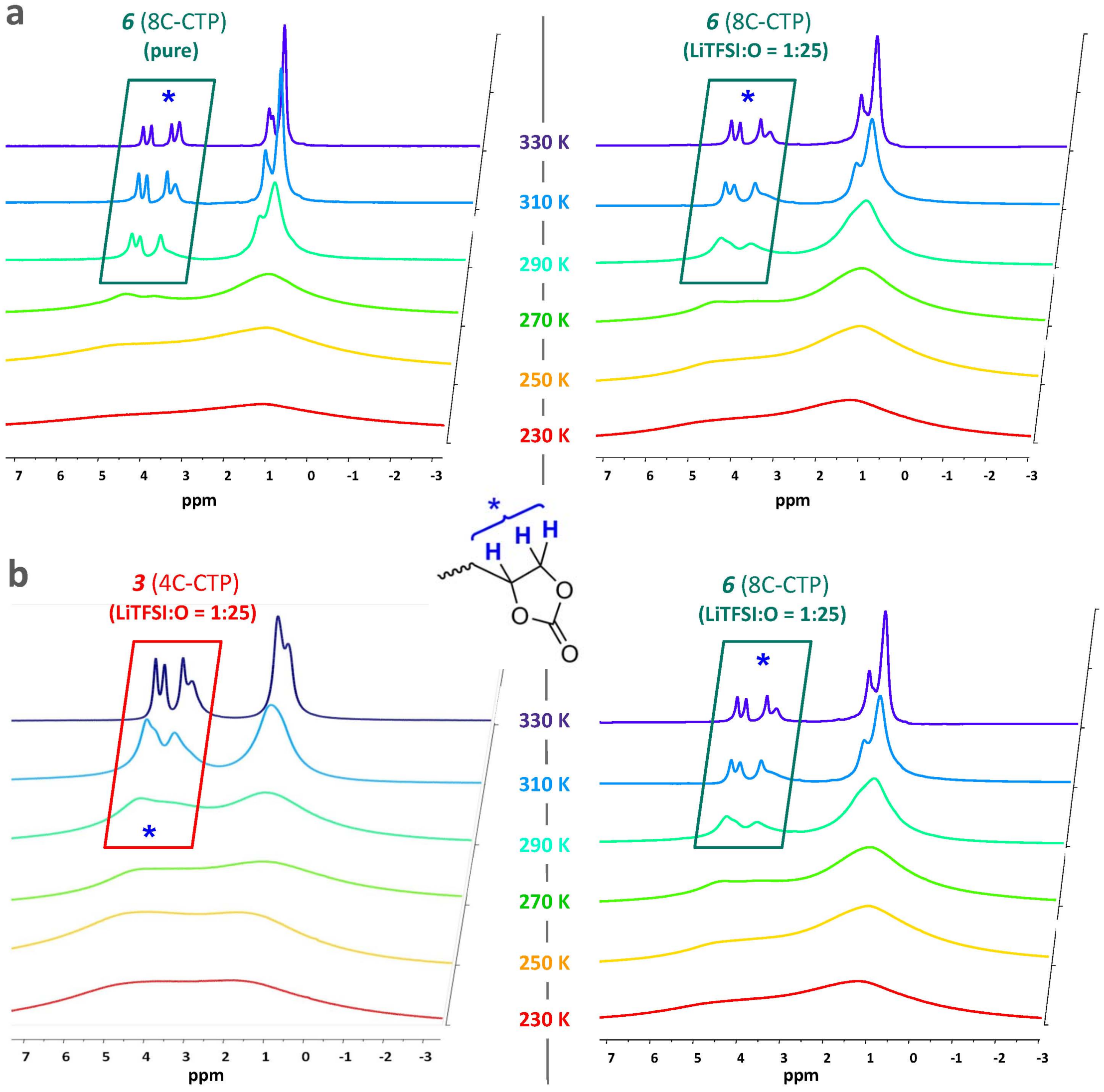

Figure 5.8. (**a**) Temperature-dependent ^{1}H MAS NMR spectra (25 kHz, 500 MHz) of ***6*** in pure state (left) and ***6*** blended with LiTFSI in a molar ratio Li:O = 1:25 (right). (**b**) Temperature-dependent ^{1}H MAS NMR spectra (25 kHz, 500 MHz) of ***3*** (left) and ***6*** (right) blended with LiTFSI in a molar ratio Li:O = 1:25.

Nevertheless, in summary, the mobility of the cyclic carbonates at a particular temperature in blended ***6*** is higher than in blended ***3***, due to the simple fact that for example at 30 °C blended ***6*** is 62.5 °C above T_g, whereas blended ***3*** just 43.4 °C. This observation is consistent with the ionic conductivity studies (compare Chapter IV), which reveal a higher ionic conductivity for model compound ***6***. The proton spectra of the respective HPB model compound ***18*** and ***21*** are not shown, since in the interesting temperature window just very broad spectra were observed.

5.3.1.2 Temperature-dependent One-Dimensional ^{13}C NMR Spectra

One-Dimensional proton-decoupled ^{13}C (CP) MAS NMR spectra of the model compounds were recorded at a Bruker ASX 500 spectrometer with a Larmor frequency of 125.76 MHz.

At temperatures below the glass transition the peak at 157.2 ppm assigned to the carbonyl carbons of the cyclic carbonates in ***3*** splits into two distinct signals (Figure 5.9): One is shifted to higher (159 ppm), one to lower ppm (156.3 ppm). This also holds for the blended model compound ***6*** (8C-CTP).[5.34]

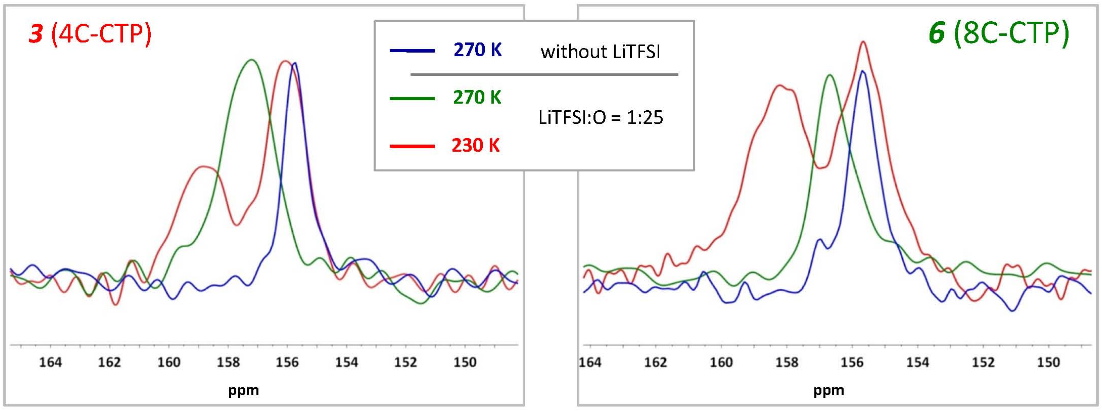

Figure 5.9. Temperature-dependent ^{13}C (CP) MAS NMR spectra of ***3*** respectively ***6*** blended with LiTFSI in a molar ratio Li:O = 1:25.

Thus, the observed glass transitions appear to be accompanied with the onset of the cyclic carbonate motion. Closely connected thereto is the motion of the lithium ions, since the splitting is assumed to be the result of *'frozen'* coordination sites of lithium ions to the C=0 group. The latter acts as electron donor and interacts with the lithium ions in terms of $Li^+ \cdots O=C$. This influences the magnetic shielding of the carbonyl carbon C_1 and results in the observed downfield shift. At temperatures above the glass transition the thermally induced onset of dynamics lead to the observation of an averaged carbonyl coordination, which results in one single peak. In order to prove the splitting not being just an artifact, ^{13}C (CP) MAS NMR spectra at different salt concentrations were measured. Deconvolution of the two signals reveals that the ratio of the two signals obviously correlates with the salt concentration (Figure 5.10): Doubling the salt concentration lead to an increase of the ratio of the downfield integral to the overall area from 20% to 40%.

Identical observations have been made for the HPB based model compound ***21*** blended with LiTFSI in a molar Li:O ratio of 1:25.

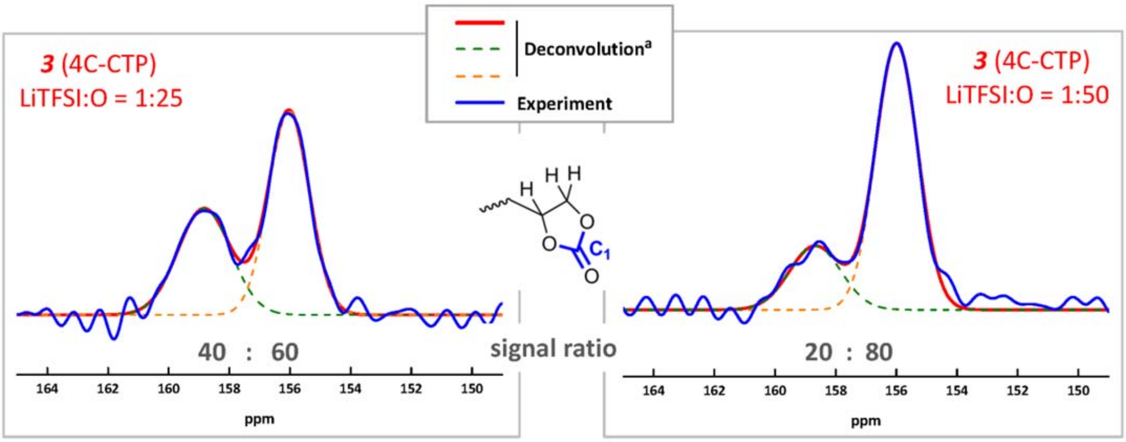

[a] Massiot, D. et al., Modelling one and two-dimensional solid-state NMR spectra, *Magn. Reson. Chem.* **2002**, 40, 70-76.

Figure 5.10. Deconvolution of the ^{13}C CP/MAS NMR peaks allocated to the carbonyl carbon C_1 of the cyclic carbonates. Measurement temperature T = 230 K. (left) LiTFSI:O = 1:25. (right) LiTFSI:O = 1:50.

However, the actual lithium ion coordination is still unclear. Therefore *density functional theory* (*DFT*) calculations were performed with the objective to assign the chemical shift of the split signals to a specific coordination. Preliminary results suggest that the difference in the chemical shift is due to the different chemical and magnetic surroundings related to a 3-fold or 4-fold coordination of the lithium ions. Peak contributions of uncoordinated cyclic carbonates due to the salt concentration cannot be excluded.

5.3.1.3 Temperature-dependent One-Dimensional ^{31}P NMR Spectra

One-Dimensional ^{31}P (CP) MAS NMR spectra of the CTP based model compounds were recorded at a Bruker ASX 500 spectrometer with a Larmor frequency of 202.46 MHz at a spinning rate of 20 kHz. Figure 5.11 shows the temperature dependent ^{31}P MAS NMR spectra of model compound ***3*** blended with LiTFSI in a molar Li:O ratio of 1:25. The line width (FWHM) decreases with temperature, while the onset of line narrowing is related to the glass transition temperature (here: -13.4 °C) and, as expected, the FWHM approaches a limit value at elevated temperatures. Comparing the ^{31}P chemical shift of the blends with the pure CTP based substances no shift change of the symmetrical peaks is observable, which indicates that the nitrogen as possible coordination site is most likely not involved in lithium ion solvation.

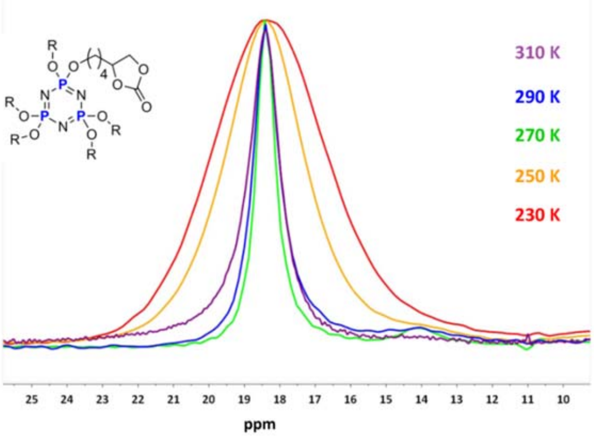

Figure 5.11. Temperature-dependent ^{31}P (CP) MAS NMR spectra of CTP based model compound ***3*** blended with LiTFSI in molar Li:O ratio of 1:25.

Notably, the fixed chemical shift over the whole temperature range indicates the absence of CTP core stacking, which is consistent with the amorphous nature of the blends.

Supplementary ^{15}N NMR measurements gave no exploitable data due to the low natural abundance.

5.3.2 ^{7}Li and ^{19}F NMR

5.3.2.1 Temperature-dependent One-Dimensional ^{7}Li Spectra

^{7}Li (spin 3/2) is a half-integer quadrupolar nucleus possessing an *electric quadrupole moment* in addition to the magnetic dipole moment all nuclei, which are observable by NMR, must have. Accordingly, in contrast to any spin-1/2 nuclei, the electric energy of the spin-3/2 nuclei depends on the orientation of the nucleus with respect to the surrounding. The main orientation-dependent term comprises the interaction of the quadrupole moment with the *electric field gradient* (*EFG*) produced by nuclei and electrons around the nucleus of interest. Since for quadrupolar nuclei magnetic and electric influences play a role on the reorientation of the nuclei, NMR experiments on the same are more complicated in comparison to spin-1/2 measurements.[5.35]

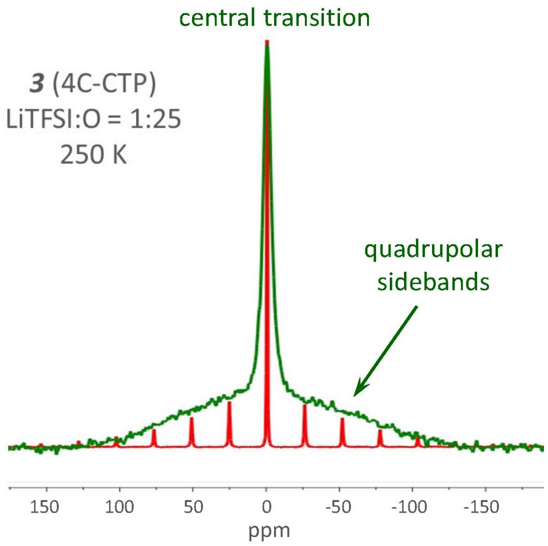

Figure 5.12. Static proton-decoupled ^{7}Li solid-echo NMR spectra of model compound ***3*** blended with LiTFSI in a molar Li:O ratio of 1:25. For comparison the respective ^{7}Li MAS NMR spectra (500 MHz, 10 kHz) are shown.

A typical low-temperature ^{7}Li spectrum obtained for the CTP based model compound blends is depicted in Figure 5.12. The static spectrum obtained by utilizing a proton-decoupled solid-echo sequence is a superposition of a narrow *Lorentzian* shaped central line and a broad *Gaussian* satellite line associated with the corresponding transitions ($^{1}/_{2} \leftrightarrow -^{1}/_{2}$, $^{1}/_{2} \leftrightarrow {}^{3}/_{2}$ and $-^{1}/_{2} \leftrightarrow -^{3}/_{2}$ respectively).[5.18] The broadening is dominated by the anisotropy of the nuclear electric quadrupolar interactions.[5.18]

The corresponding ^{7}Li MAS spectra feature the expected quadrupolar sidebands only at temperatures below the glass transition. This indicates poor dynamics since the *EFG* tensor is well-defined and consequently the lithium ions are on average in a constant environment. Above T_g the enhanced dynamics average the orientation dependence of the *EFG* completely and the sidebands vanish (Figure 5.13).

The symmetry of the static ^{7}Li NMR spectra suggests one local lithium site in the low and medium temperature range. Remarkable, at higher temperatures, the static ^{7}Li peaks become less and less symmetrical (Figure 5.14), where the development of a shoulder hints at a second mobile lithium species.[5.36] However, in the observed temperature range it was not possible to resolve separated lines. Furthermore, taking into account the discussed thermal rearrangement of the cyclotriphosphazenes at elevated temperatures (compare Chapter III) it would be in any case hard to address the line shape alteration to a second site either related to the increasing temperature and/or the accompanied structural modification.

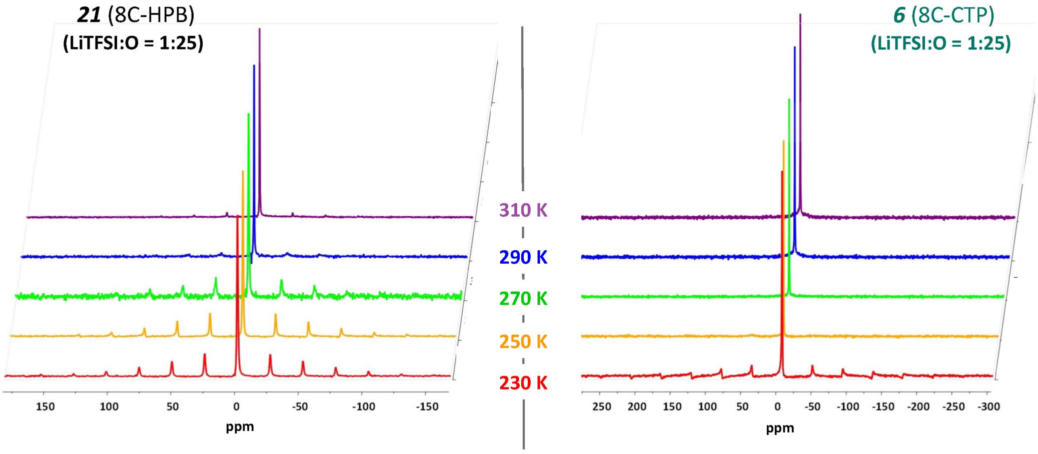

Figure 5.13. Temperature dependence of ^{7}Li MAS NMR spectra of the CTP based model ***6*** and the HPB based model ***21*** blended with LiTFSI in a molar ratio Li:O = 1:25 at temperatures between 230 K and 310 K. Spectra are recorded at a Bruker ASX 500 (spinning rate 5 kHz and 10 kHz respectively).

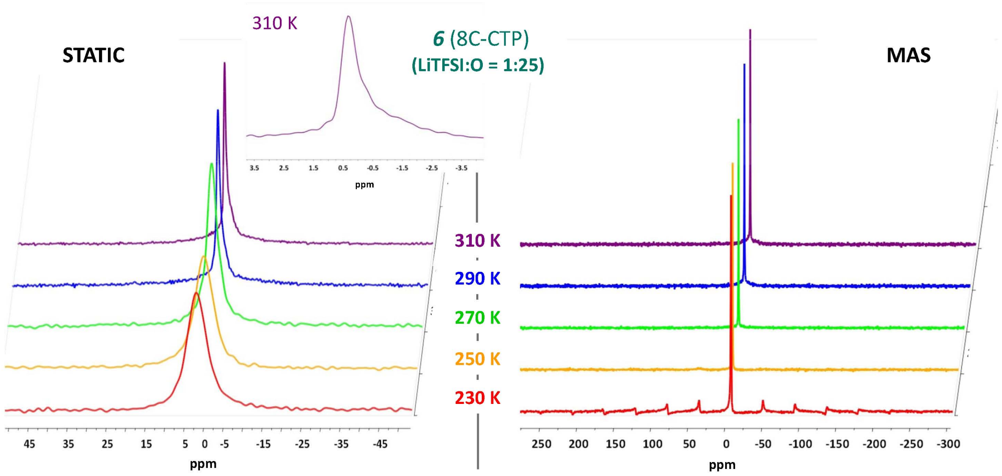

Figure 5.14. Temperature dependence of ^{7}Li MAS and static NMR spectra of the CTP based model compound ***6*** blended with LiTFSI in a molar ratio Li:O = 1:25. Spectra are recorded at a Bruker DSX 300 spectrometer (spinning rate 10 kHz).

Temperature-dependent ^{7}Li linewidth (FWHM)

The progress of the temperature-dependent static ^{7}Li NMR linewidths obtained for the various model compounds plotted versus the inverse temperature is depicted in Figure 5.15. The measurements were performed on a Bruker ASX 300 spectrometer in a 4 mm rotor and the data were taken to be the *full width at half maximum* (FWHM) of the central transition. ^{1}H decoupling technique removed the dipolar interactions between the lithium cations and the protons within the matrix. At the lowest temperature of 225 K accessible with the external cooling machine, the linewidths are almost unaffected by temperature changes, characterizing the so-called *rigid-lattice limit*, where the lithium ions are rather immobile. Hence, the observed broadened linewidths are due to increased quadrupolar and/or internuclear dipole-dipole interactions. Upon increasing the temperature, the linewidth decreases rapidly as a result of enhanced system dynamics, which induce lithium ion mobility. The onset of line narrowing is again closely related to the glass transition temperature of the blends. Accordingly, reasonable conductivity values are measured solely above T_g ($\approx T_{Onset}$), which confirms the observed *VTF* behavior of σ_{dc} (Chapter IV). Notably, the linewidths at high temperatures reach the regime of extreme narrowing ($T > T_g + 50$) due to averaged dipole-dipole interactions and electric field inhomogeneities.[5.14]

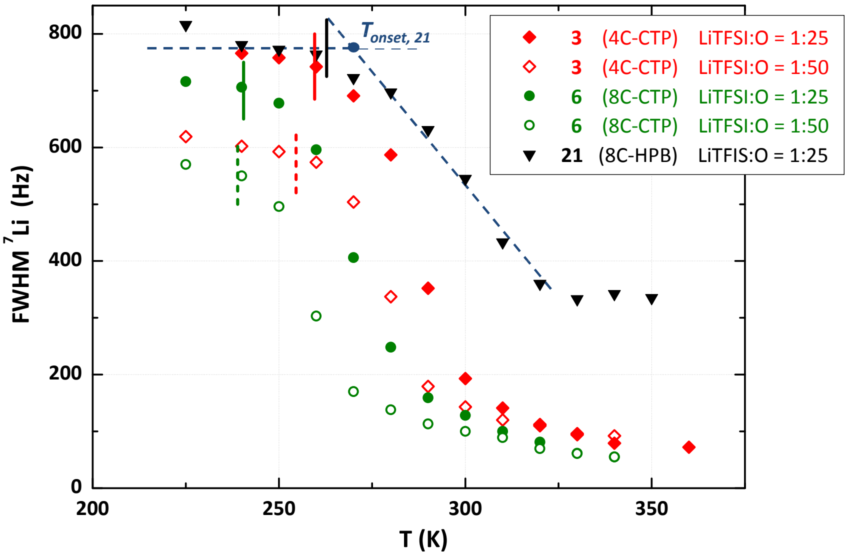

Figure 5.15. Temperature dependent free width half maximum (FWHM) of proton-decoupled static 1D ^{7}Li NMR spectra for the investigated model compound blends. Vertical lines represent glass transition temperatures (see Figure 2.13 for sample numbering).

The observed linewidths $\Delta\upsilon$ are for all model compounds in the order of several hundreds of Hertz, suggesting that the line shape is mainly sensitive to motional dynamics in the millisecond range. In other words, motional narrowing is initiated, when the rate of fluctuations $1/\tau$ of the electric field gradients and/or local magnetic fields is roughly around the order of the *rigid-lattice* linewidth Δ_0.[5.37] In the extreme cases, if $1/\tau \gg \Delta_0$, the ionic motion does not affect the lineshape, and if $1/\tau \ll \Delta_0$ at elevated temperatures, a motionally averaged spectrum results.

The onset temperature of motional narrowing allows a rough estimation of the activation energy E_a related to the process, which is responsible for the motional narrowing based on the semi-empirical equation of *Waugh* and *Fedin* (eq. 5.15):[5.38]

$$E_{a,(W.F.)}(kJ/mol) \approx 0.156 * T_{Onset}(K)\,. \qquad \textbf{eq. 5.15}$$

The activation energies obtained in this way are close to 40 kJ/mol. These values are substantially smaller than the *apparent* activation energies received out of the $log(\sigma_{dc} * T)$ versus 1000/T plots following an approach by *Roling et al.*.[5.39] Those apparent E_a's range between 76 kJ/mol and 116 kJ/mol at 30 °C (Figure 5.16). Thus, the *Waugh-Fedin* equation underestimates the activation energy of the complex motional processes in the present case, which hints at a wide distribution of correlation times.[5.40][5.41]

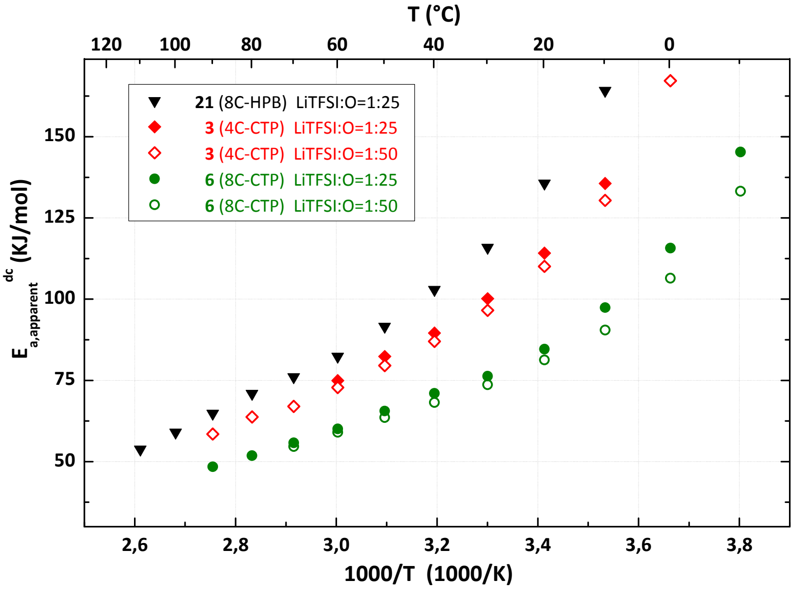

Figure 5.16. Variation of the '*apparent*' activation energies with temperature for the investigated model compounds (see Figure 2.13 for sample numbering).

Alternatively, activation energies may be extracted from motional linewidth narrowing based on the *Bloemborgen-Purcell-Pound* (*BPP*) model, yielding average correlation times τ_{LS}:[5.41-5.43]

$$\tau_{LS} = \frac{1}{2\pi\alpha\Delta\upsilon}\tan\left(\frac{\pi}{2}\,\frac{\Delta\upsilon^2 - \Delta\upsilon_\infty{}^2}{\Delta\upsilon_0{}^2}\right). \qquad \textbf{eq. 5.16}$$

In equation 5.16 $\Delta\upsilon_0$ and $\Delta\upsilon_\infty$ stand for linewidths in the limit of low (*rigid-lattice*) and high temperature, respectively. The fit parameter α is a constant often set to unity; the experimental values for $\Delta\upsilon_0$ and $\Delta\upsilon_\infty$ are listed in Table 5.1.

Model Compound [a]	T_g (°C)	T_{Onset} (°C)	$E_a(\mathrm{W.F.})$ (KJ mol^{-1})	$\Delta\upsilon_0$ (Hz)	$\Delta\upsilon_\infty$ (Hz)	$E_a(\tau_{LS})$ (KJ mol^{-1})	$E_a(\mathrm{SAE})$ (KJ mol^{-1})
3 - *pure*	-28.9	-	-	-	-	-	-
LiTFSI:O = 1: 50	-18.4	-14.8	40.3	620	90	41.7	-
LiTFSI.O = 1: 25	-13.4	-8.4	41.3	775	65	42.0	18.6
6 – *pure **	-35.2	-	-	-	-	-	-
LiTFSI:O = 1: 50	-34.1	-27.2	38.4	580	55	39.9	14.9
LiTFSI:O = 1: 25	-32.5	-26.1	38.5	720	50	40.3	15.2
21 - *pure*	3.5	-	-	-	-	-	-
LiTFSI:O = 1: 25	-10.2	-5.4	41.8	800	330	40.9	11.2

T_g = glass transition (DSC); T_{Onset} = onset temperature of line-narrowing * non-crystalline, see Chapter III; $\Delta\upsilon_0$ and $\Delta\upsilon_\infty$= linewidth in the limit of low and high temperature; E_a = activation energy; W.F. = Waugh-Fedin; τ_{LS} = correlation time extracted out of line shape analysis; SAE = Spin-alignment echo.

[a] See experimental part or Figure 2.13 for sample numbering.

Table 5.1. Comparison of the activation energies determined out of the different applied measurement techniques.

The temperature dependence of the calculated correlation times by means of equation 5.16 is sketched in Figure 5.17. For the CTP based blends an Arrhenius behavior of τ_{LS} with activation energies around 40 kJ/mol is observed and as expected, slightly higher values are obtained for an increased salt concentration.

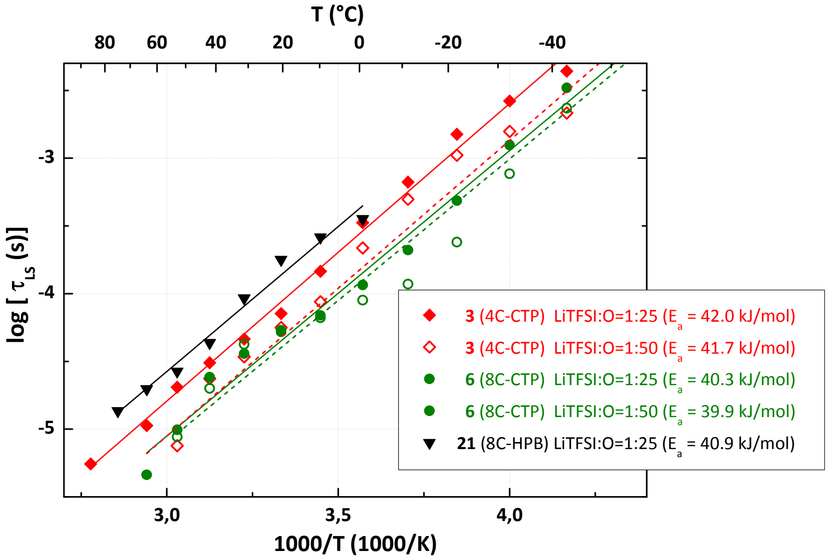

Figure 5.17. Temperature-dependent correlation times τ_{LS} calculated from the static ^{7}Li line widths data by means of eq. 5.16.

Despite the fact that based on equation 5.16 activation energies close to those obtained out of σ_{dc} data are also not accessible, similar values of E_a for all model compounds as well as the similarity in the temperature dependence of the linewidth indicate a most likely common conducting/diffusion mechanism on the microscopic scale.[5.44] Hence, the influence of the core is supposed to be minor.

Measurements utilizing ^{6}Li (I = 1), which bears the lowest quadrupolar moment of all stable isotopes - 50 times smaller compared to the one of ^{7}Li - were refrained due to the prohibitively long T_1 values of more than 150 s in a blend of ***6*** with ^{6}LiTFSI (95% ^{6}Li).

5.3.2.2 Temperature-dependent One-Dimensional ^{19}F NMR

The temperature-dependent development of the ^{19}F MAS linewidth (FWHM) for all samples is plotted in Figure 5.18. In contrast to the ^{7}Li line width no distinct onset of line narrowing closely related to the glass transition temperature is observed, suggesting independent anion mobility, whereas the influence of the CF$_3$-rotation is not fully understood. Since in the investigated temperature range the *rigid-lattice limit* was not reached, the determination of the activation energy via the calculation of τ_{LS} similar than for the ^{7}Li experiments was not possible.

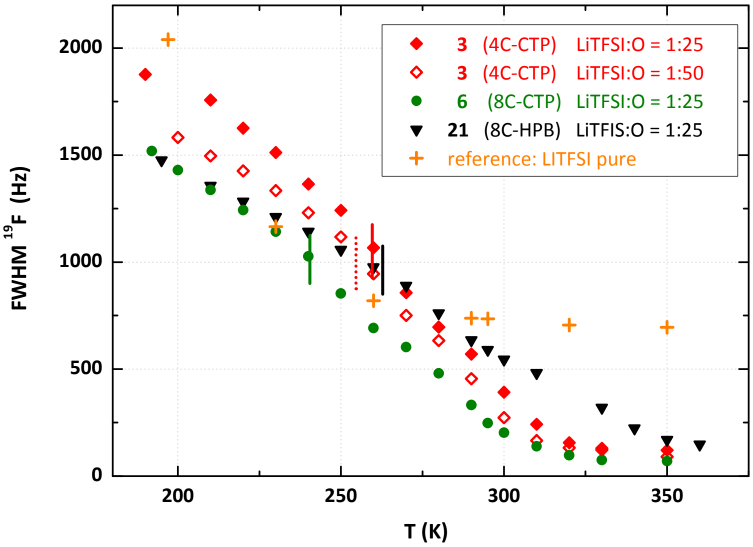

Figure 5.18. Temperature-dependent free width half maximum (FWHM) of 1D ^{19}F MAS spectra for the investigated model compound blends. Vertical lines represent glass transition temperatures.

5.3.3 NMR Spin-lattice Relaxation (SLR) Measurements

Spin-lattice relaxation measurements are very sensitive on the time modulations of the local interactions (chemical shielding, dipolar, etc.), which indirectly reflect the motion of the lithium ions on a timescale comparable to the inverse Larmor frequency.[5.45]

Laboratory Frame - T_1

In this work *SLR* times in the laboratory frame were recorded at 116.64 MHz, 194.37 MHz and 272.09 MHz, respectively, employing commercial Bruker probe heads and using the following spectrometers: Bruker DSX 300, ASX 500 and DRX 700.

The ^{7}Li *SLR* rates obtained from the frequency-dependent measurements of the hexa-phenylbenzene (***21***) or the cyclotriphosphazene based (***6***) model compound blended each with LiTFSI in a molar Li:O ratio equal to 1:25 are presented in Figure 5.19. The rates were extracted from the signal progress by a reasonable fit applying a single exponential function. Deviations from single exponential behavior due to the small quadrupole moment of ^{7}Li, which theoretically make at least a two-exponential least-squares fit necessary, were hardly detectable in this work.[5.43][5.46]

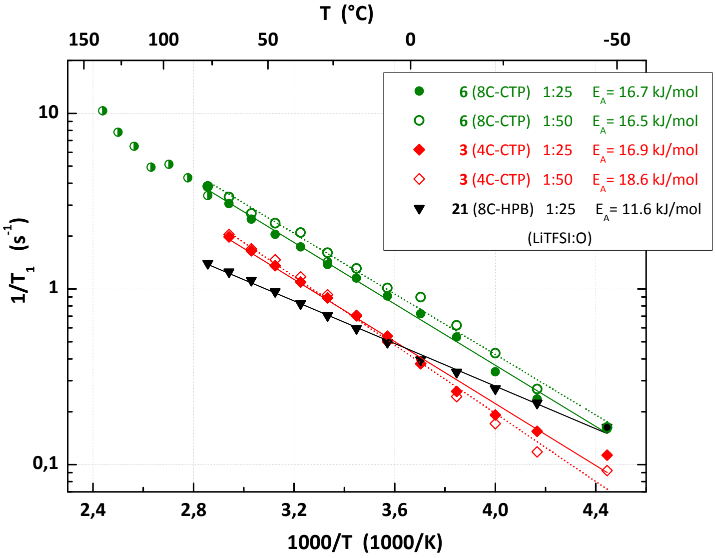

Figure 5.19. Temperature dependent static ^{7}Li spin-lattice relaxation rates T_1^{-1} as a function of 1000/T for the investigated model compounds (see Figure 2.13 for sample numbering).

T_1 decreases with increasing temperature, suggesting that the lithium ions become more and more mobile. The increase of the related SLR rate T_1^{-1} with temperature indicates that the motion is slow compared to the Larmor frequency. However, in the investigated temperature window from 225 K to 350 K no rate maxima were observed. Only the *low-T flank* (see also Chapter 5.1) of the rate peaks arise. The maxima are expected when the motional correlation time τ_c is comparable to the reciprocal Larmor frequency ω_0. Regarding the applied ω_0, the timescale for maximum τ_c should be in between 0.6 and 1.3 ns. In order to access the potential *high-T flank*, clearly higher temperatures have to be investigated ($T \gg 350\text{K}$), which, however, are in the regime of the described thermal rearrangement of the CTP based model compounds and hence not feasible. The absence of T_1 minima also hints at heterogeneous local lithium environments and a rather broad distribution of correlation times, as clearly supported by the development of a second lithium species at higher temperatures.

Initially, the validity of the *BPP* behavior was taken for granted (compare line-shape analysis), however, the observed frequency dependence of the *SLR* rate does not follow the power law

$$T_1^{-1} \propto \upsilon^{-\beta} \qquad \textbf{eq. 5.17}$$

with $\beta = 2$, as characteristic for standard *Bloembergen-Purcell-Pound* behavior and motions denoted by a single averaged correlation time.[5.42] Instead, β amounts on average to 1.1 for ***6*** and 1.6 for ***21***, respectively. Consequently, a description of the relaxation behavior and a determination of the correlation times τ_c with the help of the *BPP* model is not applicable (Figure 5.20).

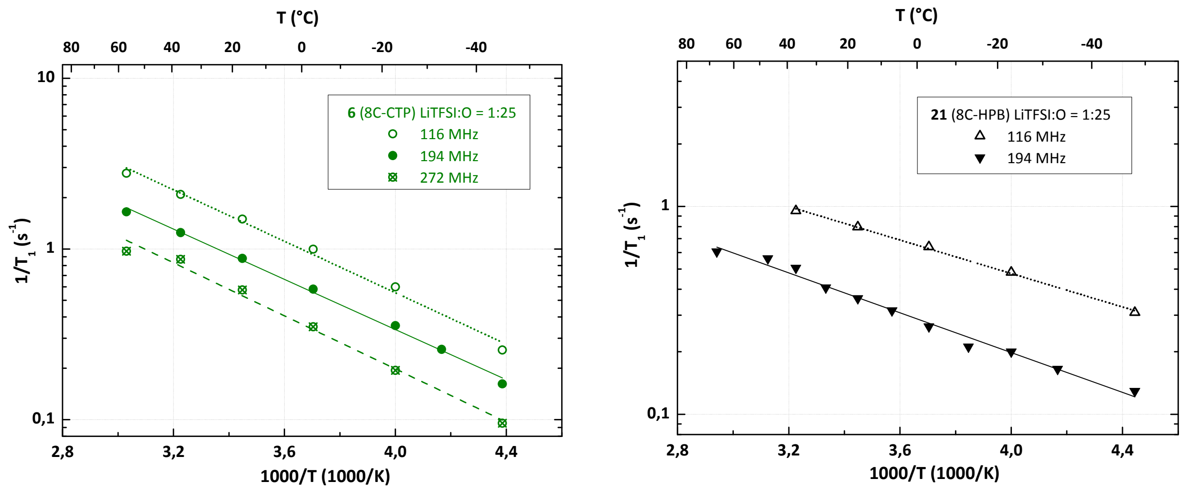

Figure 5.20. Field-dependent ^{7}Li spin-lattice relaxation rates T_1^{-1} for the investigated model compounds ***6*** (8C-CTP) and ***21*** (8C-HPB) blended with LiTFSI in a molar ratio Li:O = 1:25. Measured under MAS (see Figure 2.13 for sample numbering).

The T_1 values in the studied temperature range are smaller for the 8C-CTP than for the other model compounds. Furthermore, for lower salt concentration the T_1 values of the 8C-CTP blend are also slightly reduced, indicating higher lithium ion mobility in agreement with the ionic conductivity data (compare Chapter IV).

The linear Arrhenius behavior of the relaxation rates on the *low-T flank* for each blend suggests a thermally activated motional process with activation energies in the region of 16 kJ/mol. Those values are considerably lower in comparison to the E_a obtained by macroscopic techniques. In general, this emerges from the fact that relaxations on the *low-T flank* are sensitive to short-range and/or Coulomb-based correlation effects, i.e. strongly localized hopping with characteristic low activation energies.[5.17] On the other hand, the long-range diffusion can be probed on the *high-T flank* only, which again was not observed in the accessible temperature range.[5.17]

The relaxation of the bis(trifluoromethanesulfone)imide anion was probed via measuring the ^{19}F spin-lattice relaxation of the CF_3-group. A major part of the relaxation should be attributed to CF_3-spin rotation interaction, which can explain the high rate as well as its nearly constant value within the investigated temperature window (Figure 5.21).[5.48][5.49]

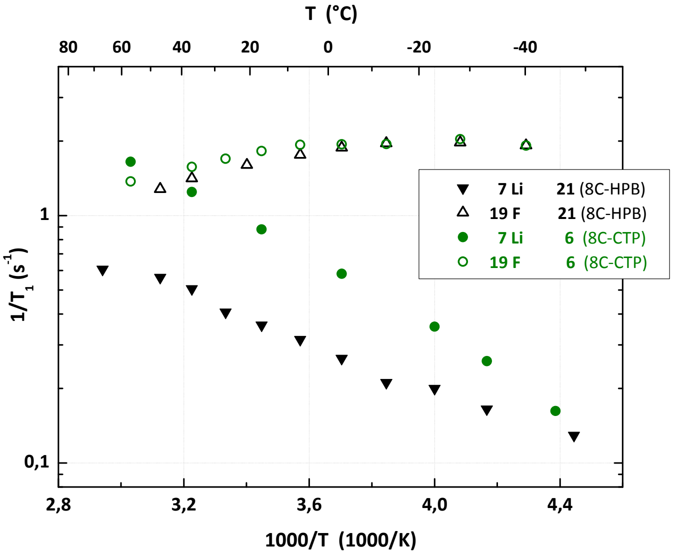

Figure 5.21. Temperature dependent ^{7}Li and ^{19}F spin-lattice relaxation rates T_1^{-1} for ***6*** and ***21*** mixed with LiTFSI in a molar ratio of Li:O = 1:25 (500 MHz, MAS, 15 kHz for ^{19}F, 5 kHz for ^{7}Li) (see Figure 2.13 for sample numbering).

Rotating Frame - $T_{1,\rho}$

Since in the laboratory frame no *SLR* rate maxima could be observed within the sample-specific temperature ranges, additional measurements in the rotating frame ($T_{1,\rho}^{-1}$) were performed in order to shift the maxima to lower temperatures. As expected and shown in Figure 5.22, the $T_{1,\rho}^{-1}$ rates are much higher than those obtained in the laboratory frame, but also in the rotating frame no clear rate peaks were observed. For the CTP based model compounds the rates reach an apparent plateau in the suggested fast regime above 1000/T equal to 3.6. If one assumes an Arrhenius behavior of the relaxation rates (Figure 5.22) activation energies are obtained, which are comparable to those obtained out of the linewidth data via the *Waugh-Fedin* relation. However, those are not in correspondence to the activation energies resulting from the DC conductivity experiments. This can be ascribed to the fact that similar to the T_1 relaxation experiment only the *low-T flank* and hence short-range motions are addressed, which in general possess lower E_a. Furthermore, perturbing quadrupolar effects of ^{7}Li possibly alter the rate behavior. Nevertheless, between -20 °C and +40 °C the highest $T_{1,\rho}^{-1}$ is assigned to the highest mobility, which is consistent with the σ_{dc} data.

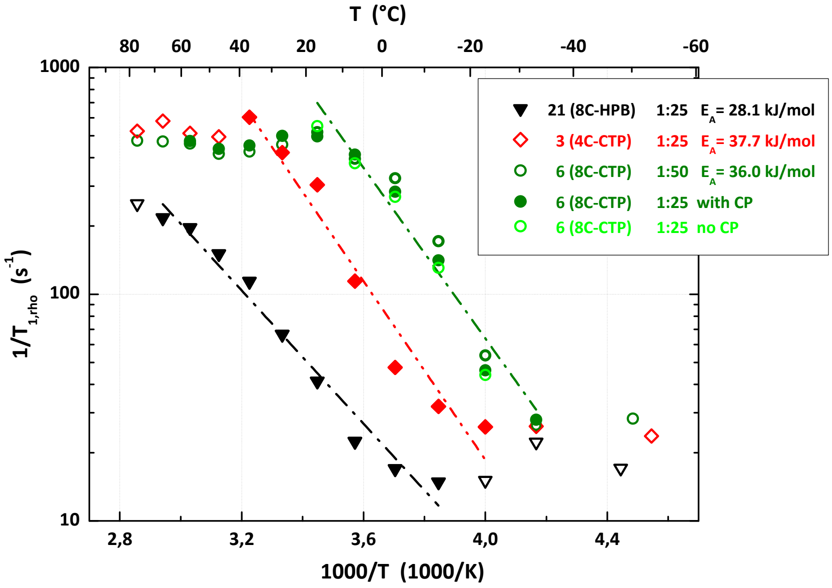

Figure 5.22. Static temperature-dependent spin-lattice relaxation rates $T_{1,rho}^{-1}$ for the investigated model compound blends plotted vs. 1000/T (see Figure 2.13 for sample numbering).

5.3.4 NMR Spin-Alignment Echo (SAE) Measurements

Spin-alignment data were obtained at a Larmor frequency $\omega_0/2\pi$ = 116.64 MHz with a Bruker DSX 300 spectrometer connected to a cryomagnet of a fixed field of 7.04 T. The decay of the two-time correlation functions $S_2(t_p, t_m)$ in dependence of mixing time t_m ($10\ \mu s \leq t_m \leq 100\ s$) for the different model compounds is shown in Figure 5.23 and 5.24. All echoes were collected at a fixed preparation time $t_p = 15\ \mu s$ in a temperature range from 220 K up to 340 K utilizing the *Jeener-Broekaert* sequence (see 5.2.1). The phase cycle was chosen in such a way that it was robust against pulse length imperfections, eliminates all unwanted coherences during t_m, and shows no sensitivity against longitudinal magnetization build-up. The recycle delay was at least 5 times T_1 and the 90° pulse length amounted to 3 µs in order to ensure a nonselective excitation of the entire spectrum.

The echo decay proceeds for all samples in one stretched exponential step over the whole investigated temperature range, while deviations were hard to detect. The normalized curves (range between 0 and 1) can be well parameterized by a *Kohlrausch-Williams-Watts* (*KWW*) function

$$S_2(t_p, t_m) = (1 - S_\infty) \exp\left[-\left(\frac{t_m}{\tau_{echo}}\right)^{\gamma_{echo}}\right] \qquad \textbf{eq. 5.18}$$

where S_∞ is the final state correlation and γ_{echo} the stretched exponential factor.[5.22]

The decay behavior of the echo amplitude allows for first statements on the geometric properties of the diffusion pathway within the sample. In case of lithium ion *'jumps'* in a crystalline material between two distinct sites, e.g. in Li_xTiS_2[5.50], the echo amplitude S_2 decays in clearly two steps, where the final state amplitude of the first decay is equal to 0.5. However, for the investigated blends the echo is not decaying in a two-step fashion, which is observed in crystalline materials if the lithium ions jump directly between two equivalent sites. In the present case, ω_Q is rather not changing and consequently the echo is only damped by relaxation processes.[5.50]

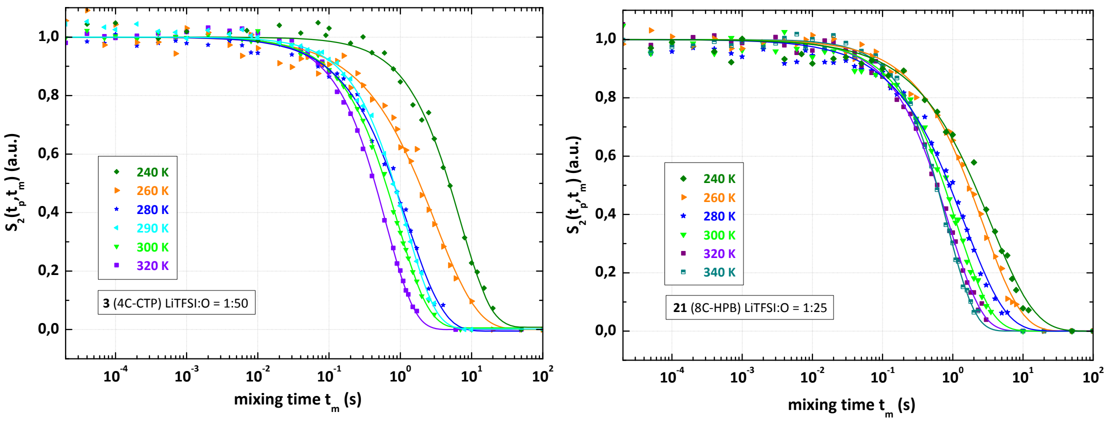

Figure 5.23. Temperature-dependent ^{7}Li spin-alignment echo signals $S_2(t_p, t_m)$ of model compound ***3*** and ***21*** blended with LiTFSI in a molar Li:O ratio of 1:50 respectively 1:25 plotted vs. the mixing time t_m. Solid lines represent *Kohlrausch-Williams-Watts* (*KWW*) fits with γ_{echo} varried between 0.5 and 1.

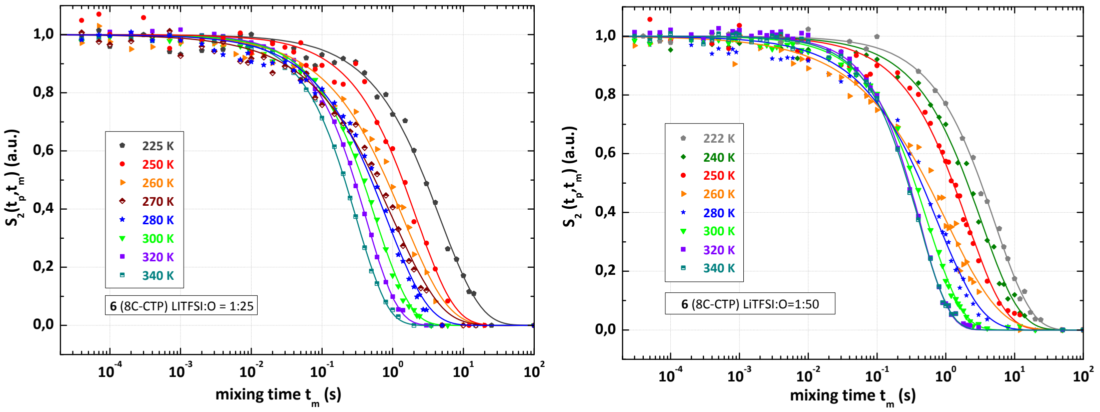

Figure 5.24. Temperature-dependent ^{7}Li spin-alignment echo signals $S_2(t_p, t_m)$ of model compound ***6*** blended with LiTFSI in a molar Li:O ratio of 1:25 (left) and 1:50 (right) plotted vs. the mixing time t_m. Solid lines represent *Kohlrausch-Williams-Watts* (*KWW*) fits with γ_{echo} varried between 0.5 and 1.

Another possible explanation for one-step decay is that the lithium ion exchange involves many electrically (theoretically infinite) nonequivalent sites *N*, which can be expected in amorphous samples. Thus, the final state amplitude S_2 is equal to 1/N and close to zero.[5.50]

Plotting the corresponding correlation times τ_{echo}, which were extracted from the *KWW* fits, versus the inverse temperature no hints for different regions could be located in the observed temperature range. τ_{echo} follows over the whole temperature range an Arrhenius relation according to

$$\tau_{echo}^{-1} \propto exp\left(-E_a/(k_B T)\right) \qquad \textbf{eq. 5.19}$$

where $k_B$is *Boltzmann*'s constant.

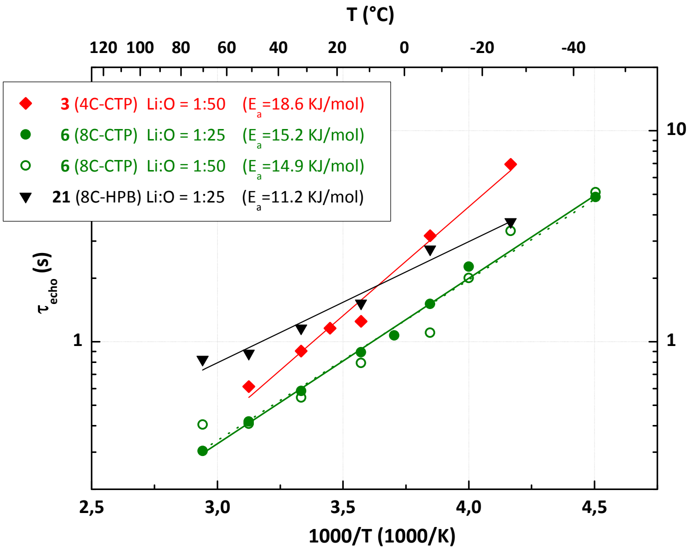

Figure 5.25. Arrhenius plot of the correlation times τ_{echo} extracted from the *KWW* fittings (Figure 5.23 and 5.24).

The obtained activation energies E_a for the blends amount to around 15 KJ/mol and the average decay rates τ_{echo}^{-1} are approximately 1 s^{-1} (Figure 5.25), presuming that the echo damping in the observed temperature range is additionally affected by weaker-than-activated processes most likely e.g. spin diffusion or quadrupolar spin-lattice relaxations, and actual long-range mass transport plays a minor role,[5.51] consistent with rather poor dynamics.

In Figure 5.28 the temperature dependence of the stretching exponents γ_{echo} is shown. At higher temperatures γ_{echo} converges to unity for all model electrolytes, while the values pass through a minimum of about 0.6 around the observed glass transition temperatures of the blends. The dependence of γ_{echo} on temperature indicates that over the investigated temperature range different lithium diffusion processes are probed.

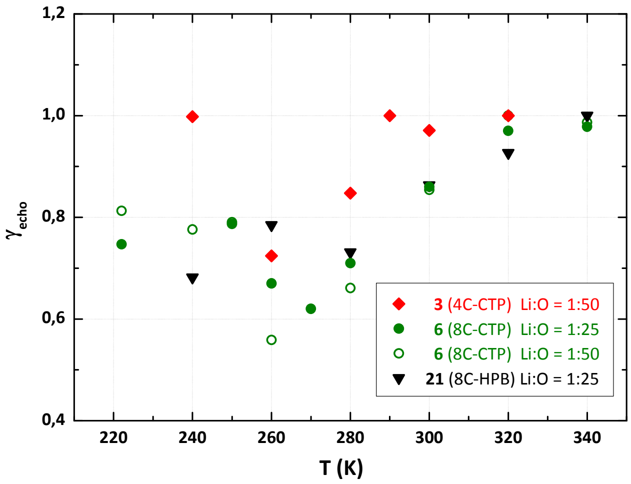

Figure 5.28. Temperature dependence of γ_{echo} values for the investigated model compound blends obtained from the S_2 decay curves recorded at $t_p = 15\ \mu s$.

5.3.5 Pulsed-Field Gradient (PFG) NMR Measurements

PFG NMR experiments were performed in close collaboration and with the help of *Prof. M. Schönhoff* at the *University of Münster*. The measurements were realized at a 400 MHz Avance NMR spectrometer from Bruker with a liquid state probe head (Bruker, Diff 30). The maximum available gradient strength in order to probe diffusion was 11.8 T·m^{-1}. The temperature was calibrated by a GMH 3710 controller with a Pt100 thermocouple (*Greisinger electronics*, Germany) and a proposed deviation in temperature of $\pm$0.25 K.[5.11] Due to the high viscosity and the limited amount of the model compound blends, a specific way of sample preparation was required. Therefore, short glass tubes with a length of about 30 mm, featuring an outer diameter slightly smaller (< 0.1 mm) than the inner diameter of a standard NMR tube, worked as '*shuttle*'. After charging the '*shuttle*' with the appropriate sample in an argon-filled glove box, it was inserted in the standard NMR tube and slide to the lower end. Subsequently, the tube was set under vacuum and sealed by fusing the glass. *Post hoc* developing bubbles within the sample were removed by centrifugation and/or heating the sample over several days.

The cyclotriphosphazene model substance ***6*** (8C-CTP) blended with LiTFSI in a molar Li:O ratio of 1:25 yielded at 70 °C a diffusion coefficient D of about 5 x 10^{-13} m^{2}·s^{-1}. The chosen gradient pulse length δ was 2 ms, the gradient step number equal to 20 and the observation time Δ was set to 350 ms. At lower temperatures the attenuation of the echo was even at an applied Δ of 1200 ms (δ = 2ms) hardly 15%, indicating a diffusion coefficient close to the lower detection limit of roughly 10^{-14} $m^2 \cdot s^{-1}$. In comparison to e.g. polysiloxane-based *'salt-in'* polymer electrolytes the value of D is three orders of magnitude lower,[5.11] which gives a further hint for the low conductivity. Since both electrolytes are at 70 °C clearly above their glass transition temperature, -32.5 °C for ***6*** and -54.6 °C for the oligo(ethylene oxide) based siloxane,[5.52] respectively, it is supposed that the electrostatic interactions between the carbonyl oxygen and the lithium ion are too vigorous and thus a drawback for high translational diffusion.

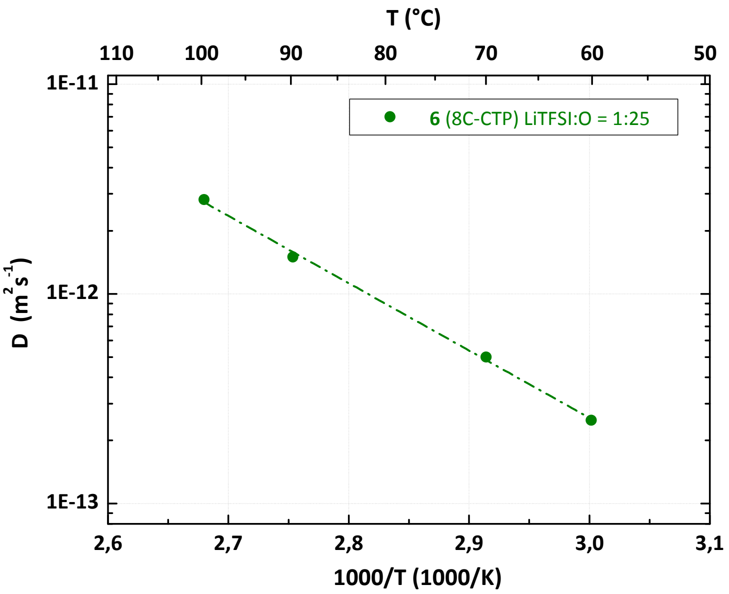

Figure 5.29. Diffusion coefficient of ^{7}Li in the blend of ***6*** with LiTFSI in a molar ratio of Li:O equal to 1:25.

This is underlined by the long-range activation energy. Figure 5.29 shows the diffusion coefficients of blended ***6*** as a function of temperature. In the investigated temperature window the temperature dependence of the diffusion coefficient follows Arrhenius law.

According to

$$D = D_0 \, exp\left(\frac{-E_a}{RT}\right) \quad \textbf{eq. 5.20}$$

an activation energy of 61 kJ/mol for the long-range lithium diffusion is obtained.[5.11] This value is comparable to the average value of the E_a calculated from the ionic conductivity data in the regarding temperature range (compare Figure 5.16). Notably, these values are clearly higher than the respective values for EO based electrolytes (PEO-LiTf: 40 kJ/mol) or oligo(ethylene oxide)-grafted polysiloxanes (30 kJ/mol).[5.11]

In contrast, the activation energies obtained for rather local motional processes are markedly lower (compare *SLR* results), leading to the suggestion that the activation of short-range dynamics is solely not sufficient to enable macroscopic transport in the μm-range. For the latter, it is crucial to overcome further energy barriers.

Up to 100 °C the hexaphenylbenzene model substance ***21*** (8C-HPB) blended with LiTFSI (Li:O = 1:25) did not show adequate dynamics in order to measure diffusion coefficients, pointing out to a value of D below the detection limit of around 10^{-14} $m^2 \cdot s^{-1}$, consistent with the reduced ionic conductivity in comparison to ***6***.

Finally, ^{19}F diffusion was observed to be faster for model substance ***6*** (8C-CTP) (70 °C, Δ = 350 ms, δ = 2 ms, D^{19F} = 9.48 x 10^{-13} $m^2 \cdot s^{-1}$) blended with LiTFSI in a molar Li:O ratio of 1:25, indicating a tighter coordination of the cations to the matrix in comparison to the anions, in agreement with a rather independent anion dynamic.

The author gratefully acknowledges Prof. M. Schönhoff for the opportunity to measure PFG NMR in her laboratory at the University of Münster, as well as S. Jeremias for assistance in performing the actual experiments.

5.4 Bibliography

[5.1] J. Keeler, *Understanding NMR Spectroscopy*, University of Cambridge, Dept. of Chemistry, **2002** & **2004**.

[5.2] (a) Hore, P. J.; Jones, J. A.; Wimperis, S. *NMR: The Toolkit*, Oxford University Press Inc., New York, **2000**. (b) A. Abragam*, The Principles of Nuclear Magnetism*, Oxford University Press, Oxford, **1993**. (c) M. Munowitz, *Coherence and NMR*, Wiley-Interscience, New York, **1988**. (d) M. J. Duer, *Introduction to Solid-State NMR Spectroscopy*, Blackwell Science Ltd, Oxford, **2004**.

[5.3] Christoph Kins, Diploma Thesis, Mainz, **2009**.

[5.4] Andrew, E. R.; Bradbury, A.; Eades, R. G. *Nature* (London, U. K.) **1958**, 182, 1659.

[5.5] Lowe, I. J. *Phys. Rev. Lett.* **1959**, 2, 285.

[5.6] Laws, D. D.; Bitter, H.-M. L.; Jerschow, A. *Angew. Chem. Int. Ed.* **2002**, 41, 3096.

[5.7] Waugh, J. S.; Huber, L. M.; Haeberlen, U. *Phys. Rev. Lett.* **1968**, 20, 180.

[5.8] Lee, M.; Goldburg, W. I. *Phys. Rev.* **1965**, 140, 1261.

[5.9] Bennett, A. E.; Rienstra, C. M.; Auger, M.; Lakshmi, K. V.; Griffin, R. G. *J. Chem. Phys.* **1995**, 103, 6951.

[5.10] Böhmer, R.; Jeffrey, K. R.; Vogel, M. *Progress in Nuclear Magnetic Resonance Spectroscopy* **2007**, 50, 87.

[5.11] Kunze, M.; Karatas, Y.; Wiemhöfer, H.-D.; Eckert, H.; Schönhoff, M. *Phys. Chem. Chem. Phys.* **2010**, 12, 6844.

[5.12] Bensch, W.; Bredow, T.; Ebert, H.; Heitjans, P.; Indris, S.; Mankovsky, S.; Wilkening, M *Progress in Solid State Chemistry* **2009**, 37, 206.

[5.13] Heitjans, P.; Schirmer, A.; Indris, S. in *Diffusion in Condensed Matter – Methods, Materials, Models*, Eds.: Heitjans, P.; Kärger, J. (Springer, Berlin, **2005**), 367.

[5.14] Heitjans, P.; Indris, S., Wilkening, M. *Diffusion Fundamentals II* **2005**, 45, 1.

[5.15] Heitjans, P.; Wilkening, M. *MRS Bulletin* **2009**, 34, 915.

[5.16] Bunde, A.; Dieterich, W.; Maass, P.; Meyer, M. in *Diffusion in Condensed Matter – Methods, Materials, Models*, Eds.: Heitjans, P.; Kärger, J. (Springer, Berlin, **2005**), 813.

[5.17] Wilkening, M.; Heitjans, P.; *Phys. Rev. B* **2008**, 77, 024311.

[5.18] Wilkening, M.; Heitjans, P. *J. Phys.: Condens. Matter* **2006**, 18, 9849.

[5.19] Spiess, H. W. *J. Chem. Phys.* **1980**, 72, 6755.

[5.20] Fujara, F.; Wefing, S.; Spiess, H. W. *J. Chem. Phys.* **1986**, 84, 4579.

[5.21] Dries, T.; Fujara, F.; Kiebel, M.; Rössler, E.; Silescu, H. *J. Chem. Phys.* **1988**, 88, 2139.

[5.22] (a) Qi, F.; Jörg, T.; Böhmer, R. *Solid State Nucl. Magn. Reson.* **2002**, 22, 484.
(b) Böhmer, R.; Jörg, T.; Qi, F.; Titzen, A. *Chem. Phys. Lett.* **2000**, 316, 419.

[5.23] Bowden, G. D.; Hutchison, W. D.; Khachan, J. *J. Magn. Reson.* **1986**, 67, 415.

[5.24] Jeener, J.; Broekaert, P. *Phys. Rev.* **1967**, 157, 232.

[5.25] Tang. X.-P.; Wu, Y. *Magn. Reson*. **1998**, 133, 155.

[5.26] Tang, X.-P.; Geyer, U.; Busch, R.; Johnson, W.; Wu, Y. *Nature* **1999**, 402, 160.

[5.27] Böhmer, R.; *J. Magn. Reson.* **2000**, 147, 78.

[5.28] Wilkening, M.; Heine, J.; Lyness, C.; Armstrong, A. R.; Bruce, P. G. *Phys. Rev. B* **2009**, 80, 064302.

[5.29] Price, W. S. *Concepts Magn. Reson*. **1997**, 9, 299.

[5.30] Claridge, T. D. W. *High Resolution NMR Techniques in Organic Chemistry* **1999**, Elsevier-Pergamon, Amsterdam.

[5.31] (a) Kärger, J., Stallmach, F., Chap. 10 in [5.13].

(b) Kärger, J.; Pfeifer, H.; Heink, W. in: J. S. Waugh (Ed.), *Advances in Magnetic Resonance*, Vol. 12, Academic Press, New York, **1988**, 1.

[5.32] Tanner, J. E. *J. Chem. Phys*. **1970**, 52, 2523.

[5.33] Price, W. S. *Concepts Magn. Reson.* **1998**, 10, 197.

[5.34] Liang, Y.-H.; Wang, C.-C.; Chen, C.-Y. *Electrochimica Acta* **2006**, 52, 527.

[5.35] Levitt, H. M. in Spin Dynamics: *Basic of Nuclear Magnetic Resonance*, John Wiley & Sons, New York, **2001**.

[5.36] Vogel, M.; Torbrügge, T. *J. Chem. Phys.* **2006**, 125, 054905.

[5.37] Kao, H.-M.; Hung, T.-T., Fey, G. T. K. *Macromolecules* **2007**, 40, 8673.

[5.38] Waugh, J. S.; Fedin, E. I.; *Sov. Phys. Solid State 4* **1963**, 1633.

[5.39] Murugavel, S.; Roling, B. *Phys. Rev. B* **2007**, 76, 180202(R).

[5.40] Grüne, M.; Müller-Warmuth, W.; zum Hebel, P.; Krebs, B. *Solid State Ionics* **1993**, 66, 165.

[5.41] Faske, S.; Eckert, H.; Vogel. M. *Phys. Rev. B* **2008**, 77, 104301.

[5.42] Bloembergen, N.; Purcell, E. M.; Pound, R. V. *Phys. Rev.* **1948**, 73, 679.

[5.43] Chung, S. H.; Jeffrey, K. R.; Stevens, J. R. *J. Chem. Phys.* **1991**, 94, 1803.

[5.44] Kao, H.-M.; Chao, S.-W.; Chang, P.-C. *Macromolecules* **2006**, 39, 1029.

[5.45] H. W. Spiess, NMR, *Basic Principles and Progress, Dynamic NMR Spectroscopy*, Springer, Berlin, **1978**.

[5.46] Jeon, J.-D.; Kwak, S.-Y. *Macromolecules* **2006**, 39, 8027.

[5.47] Pechner, O.; Kong, S.-T.; Goebel, T.; Nickel, V.; Weichert, K.; Reiner, C.; Deiseroth, H.-J.; Maier, J.; Haarmann, F.; Zahn, D. *Chem. Eur. J.* **2010**, 16, 8347.

[5.48] Hayamizu, K.; Aihara, Y.; Price, W. S. *J. Chem. Phys.* **2000**, 113, 11, 4785.

[5.49] Hubbard, P. S. *Phys. Rev.* **1963**, 131, 1155.

[5.50] Wilkening, M.; Heitjans, P. *Solid State Ionics* **2006**, 177, 3031.

[5.51] Ruprecht, B.; Billetter, H.; Ruschewitz, U.; Wilkening, M. *J. Phys. Condens. Matter* **2010**, 22, 245901.

[5.52] Karatas, Y.; Kaskhedikar, N.; Burjanadze, M.; Wiemhöfer, H.-D. *Macromol. Chem. Phys.* **2006**, 20.

[5.53] Bloch, F. *Phys. Rev.* **1958**, 111, 841.

CHAPTER VI

6. Conclusions & Outlook

In the present work, based on the concept of immobilizing ion solvating moieties, well-defined model compounds with tethered lithium ion solvents were successfully synthesized. Those model compounds were fully characterized and studied in terms of their ionic conductivity influenced by the spacer length and the type of solvating moieties. Those model compounds were further employed for systematic studies of the molecular ion transport and the complex matrix dynamics, where the latter constitutes an essential prerequisite for a more tailored optimization of future electrolytes.

The three investigated series of model compounds were based on cyclotriphosphazene (CTP), hexaphenylbenzene (HPB) and tetramethylcyclotetrasiloxane (TMS) scaffolds, respectively, covering the requested broad range of glass transition temperatures. Cyclic carbonates were identified as preferred solvating moieties, since ethylene carbonate and propylene carbonate as electrolyte components have proven to fulfill safety and market concerns in commercial lithium ion batteries.

The CTP based derivatives were obtained upon reaction of $N_3P_3Cl_6$ with the appropriate alkenoles, followed by epoxidation with MCPBA and catalytic CO_2 insertion. It turned out that epoxidation requires *equimolar* amounts of antioxidant BHT to successfully prevent degradation of the CTP core. Remarkably, the CO_2 insertion step into the terminal epoxide containing HPB based intermediates warranted high partial pressures of more than 80 bar in order to achieve full conversion. Furthermore, a rather rarely reported full conversion of a CO_2 insertion into an internal epoxide was achieved for one of the model compounds.

All obtained compounds were found to be good solvents for LiTFSI and revealed sufficient heat resistance up to 235 °C. The cyclotriphosphazenes turned out to rearrange over time at elevated temperatures, which questions the general stability of alkyl alkoxide related (poly)phosphazenes.

Beside any evidence of core stacking for neither the CTP nor the HPB derivatives, also no significant differences in the observable bulk ionic conductivity of the CTP blends were observed applying either LiBETI, LiBOB or $LiClO_4$, indicating a comparable salt dissociation and rather independent motion of cations and anions.

Furthermore, all blends exhibit *William-Landel-Ferry* (*WLF*) type behavior for the observable bulk lithium ion conductivity with the highest value of $6 \times 10^{-6}\ S{\cdot}cm^{-1}$ at ambient temperatures. Notably, modifications of the alkyl spacer length separating the cyclic carbonate moieties and the cores were shown to influence dc ion conductivities only in addition to changes in glass transition temperatures, thus leading to substantially reduced ionic conductivities in case of the rather low T_g HPB analogues.

The observed bulk conductivities of the low glass transition models strongly suggest rather tight coordination of the lithium ions to the solvating 2-oxo-1,3-dioxolane moieties. Additional evidence stems from increased DC ion conductivity values of the EO references and unfavorable values of the TMS model compound bearing 1-oxo-4-methoxy-2,6,7-trioxa-1-phosphabicyclo[2,2,2]-octane side groups.

Further insights into the molecular mechanism of lithium ion dynamics were derived from ^{7}Li, ^{19}F and ^{13}C Solid-State NMR investigations. While localized ion motion identified from spin-lattice relaxation measurements in the laboratory frame yielded apparent activation energies of circa 15-20 kJ/mol, short range diffusion was probed by ^{7}Li line width analysis with increased apparent activation energies of around 40 kJ/mol. In contrast, long-range macroscopic transport was monitored by Pulsed-Field Gradient NMR, leading to activation energies of 61 kJ/mol, which is in good agreement with the average values determined from bulk conductivity data at elevated temperatures. Thus, the major contribution to bulk ion transport is only detected by PFG NMR.

Nevertheless, the observable μm-range diffusion in the present model compounds is rather slow compared to reported EO based polymers, emphasizing the impact of strong lithium ion coordination to the carbonyl oxygens of the cyclic carbonates moieties, which hampers sufficient ionic conductivities.

Outlook

Apart from required improvements of both cathode and anode materials (compare Chapter I) applied in lithium ion batteries, the obtained results suggest to explore '*softer*' solvating moieties in future electrolytes, while maintaining a good balance between the competing demands of an adequate degree of salt dissociation and elevated ion dynamics due to fairly weak lithium coordination to its solvating moieties.

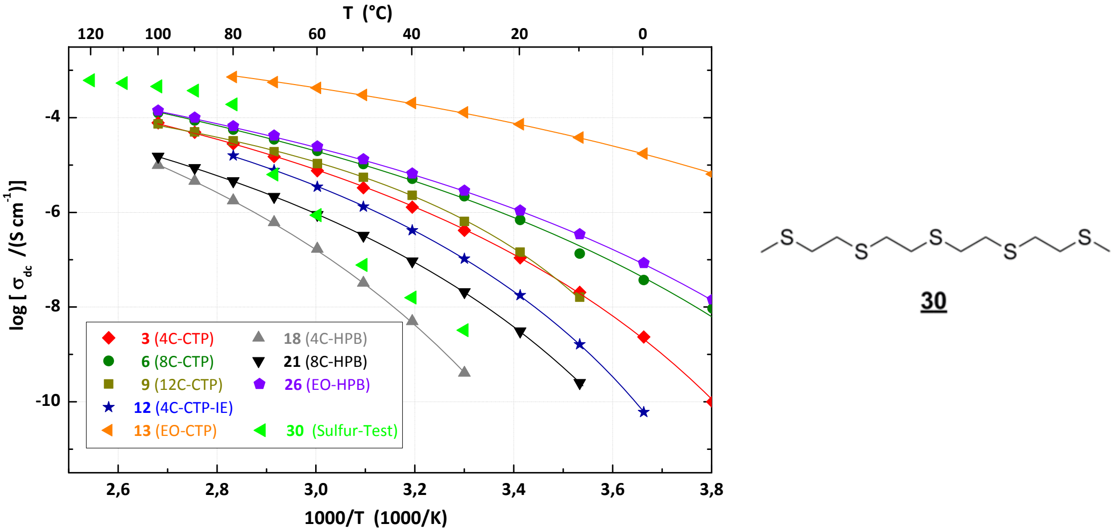

Figure 6.1. Ionic conductivity of the sulfur test compound in comparison to the various model compounds. In all cases the molar Li:O ratio is equal to 1:25 (see Figure 2.13 for sample numbering).

Therefore, as a first proof of principle, a sulfur model compound was prepared and blended with LiTFSI in a molar Li:O ratio of 1:25. Above the melting transition of ***30*** the observed lithium ionic conductivity (Figure 6.1) indeed exceeds the one of the cyclic carbonate based model compounds as well as the oligo(ethylene oxide) functionalized HPB derivative. Despite potentially reduced long-term stability (e.g. due to oxidation), this approach appears rather promising and future efforts along those lines may yield compounds with appreciably improved lithium ion conductivities.

CHAPTER VII

7. Experimental Section

7.1 Materials

5-hexen-1-ol, 5-cis-octen-1-ol, 9-decen-1-ol, tetraethylene glycol monomethyl ether and triethylamine were dried over calcium hydride and distilled under argon before use. Tetrahydrofuran (THF, 99.9%, *Acros*) and dioxane (99.9%, *Acros*) were dried over sodium and also distilled under argon before use. Acetonitrile and methylene chloride were dried with activated molecular sieves (4 Å). Hexachlorocyclotriphosphazene (99.99%, resublimed, *Aldrich*) and all other chemicals were used as received without further purification unless indicated otherwise. Air or moisture-sensitive reactions were performed in thoroughly flame dried glass vessels in an inert atmosphere of dry argon using standard *Schlenk* techniques. Analytical thin layer chromatography (TLC) was carried out on *Alugramm® F-254* percoated silica gel plates (*Machery Nagel*). Visualization was performed with UV light (254 nm), potassium permanganate solution or iodine staining. Column Chromatography on all compounds was conducted with silica gel 60 from *Fluka* (0.063-0.2 mm pore size). The final products were dried at a Schlenk line under high vaccum (2 x 10^{-3} mbar) at temperatures between 50 °C and 120 °C.

7.2 Measurements

^{1}H and ^{13}C NMR spectra were recorded either on a *Bruker* AC 300 MHz or a *Bruker Avance III* 250 MHz spectrometer; ^{31}P NMR spectra were measured with either a *Bruker Avance III* 500 MHz or a *Bruker Avance III* 700 MHz spectrometer. ^{1}H and ^{13}C chemical shifts are quoted on the δ-scale in units of parts per million (ppm) using the residual solvent protons as internal standard: ^{1}H-Spectra: DMSO-d$_6$, $\delta = 2.51$ ppm; $CDCl_3$, $\delta = 7.24$ ppm. ^{13}C-Spectra: DMSO-d$_6$ $\delta = 39.51$ ppm; $CDCl_3$ $\delta = 77.23$ ppm. ^{31}P NMR signal shifts were referred to triphenylphosphine (TPP) ($\delta = -6.00$ ppm) as external reference.

Coupling constants (J) are reported in Hertz (Hz), and splitting patterns are designated as s (singlet), d (doublet), dd (double doublet), t (triplet), m (multiplet), and br (broad).

MALDI mass spectra were obtained on a *Bruker*-Daltonics Reflex-Tof by using a N_2-Laser (337 nm, 3-5 ns pulse) and applying an acceleration voltage between 15 kV and 35 kV. As matrix served dithranol (1,8-Dihydroxy-10*H*-anthracen-9-on).

Thermogravimetric analysis (TGA) was measured under nitrogen at a heating rate of 10 $K \cdot min^{-1}$ using a TGA/SDTA-851 (*Mettler-Toledo*). For each measurement about 10 mg of the sample were heated in an atmosphere of dry nitrogen at a heating rate of 10 $K \cdot min^{-1}$.

Differentical scanning calorimetry (DSC) was carried out on a *Mettler-Toledo* DSC-30 under nitrogen at a heating rate of 10 $K \cdot min^{-1}$. Each sample was subjected to three successive heating and cooling circles.

Impedance Spectroscopy was recorded as a function of temperature using a *Solartron SI 1260* impedance / gain phase analyzer with a high resolution dielectric converter (Alpha high-resolution dielectric analyzer, *Novocontrol*) in the range from 10^{-2}-10^{7} Hz. The measurements were performed using plain, polished stainless steel or platinum electrodes with a temperature controlled cryostat (accuracy ±0.2 K) under N_2 (*Novocontrol*). DC conductivities were usually obtained from the lower-frequency plateau values of the real part of the AC conductivities (*Bode* plot).

Sample preparation was dependent on the consistency of the probe. In most of the cases a homogenous mixture of the sample and the lithium salt was accomplished by dissolving both in an appropriate solvent and subsequent removing of the solvent in high vacuum over several days. In all cases, the absence of any remaining moisture/solvent was verified by ^{1}H NMR spectroscopy.

Elemental analyses were performed by the *Institute for Inorganic Chemistry* at the *Johannes Gutenberg University* in Mainz.

7.3 Synthesis

7.3.1 Polyphosphazenes

Polydichlorphosphazene [7.1]

(***A***)

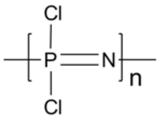

Commercial lithium bis(trimethylsilyl)amide ($LiN(SiMe_3)_2$) (7.00 g, 41.42 mmol) was weighed out in a nitrogen-filled glove box into a flame-dried 250 mL three-neck *Schlenk* flask equipped with an inner thermometer. The flask is channeled out of the glove box and the amount of $LiN(SiMe_3)_2$ is checked by comparing the overall weight to the net-weight of the flask. Afterwards, 150 mL of dry toluene (H_2O < 50 ppm) are transferred by cannulating technique into the flask. The resulting solution is cooled to -12 °C followed by a dropwise addition of freshly distilled PCl_3 (3.65 mL, 41.80 mmol) under vigorous stirring over a period of 30 minutes. The temperature should thereby not exceed -10 °C. Subsequent, the mixture was stirred for further 30 minutes at 0 °C before it was allowed to warm up slowly to ambient temperature. After additional 2 hours the slightly yellow suspension was cooled down again to -12 °C before freshly distilled sulfuryl chloride (3.34 mL, 41.79 mmol) was added dropwise within 15 minutes. The polymerization of the yielded monomer (phosphoranimine $Cl_3P=NSiMe_3$) is initiated after one hour at room temperature by a solution of PCl_5 (16.2 mg, 0.04 mmol) in 0.6 mL of dry toluene. The mixture is sucked through fritted glass under argon after 36 hours. The yellow filtrate is concentrated under high vacuum in order to remove the volatiles (i.e. $ClSiMe_3$, excess PCl3 or SO_2Cl_2). Finally, the remaining slightly yellow and viscous polymer ***A*** (3.48 g, 30.0 mmol, 72.5% yield) is re-dissolved in 25 mL of dry toluene. In this way it can be stored in a freezer (-18 °C) under inert gas for several weeks.

^{31}P NMR (Toluene-d_8, 500 MHz): δ -19.05 (s, polymer), +19.1 (s, side product $N_3P_3Cl_6$).

Poly[bis(5-hexenyl-1-oxy)phosphazene]

(***B***)

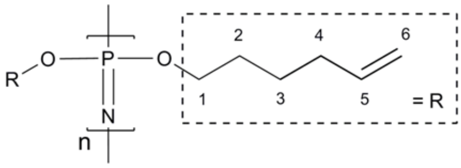

12 g (120.0 mmol) 5-hexen-1-ol were added under argon atmosphere to a mixture of 2.70 g (117.0 mmol) metallic sodium in 80 mL dry dioxane (H_2O < 50 ppm). The mixture was stirred under reflux until the metallic sodium vanished. Afterwards, PDCP (2.02 g, 17.41 mmol) dissolved in 15 mL dry toluene was added dropwise to the alkoxide suspension. The reaction was stopped after vigorous stirring for 48 hours at 65 °C. Filtering the mixture through fritted glass, evaporating the volatiles and precipitation in dry methanol lead to polymer ***B*** (2.83 g, 67% yield).

^{1}H NMR ($CDCl_3$, 250 MHz): δ 1.45-1.20 (m, 8H, 2-C*H*$_2$, 3-C*H*$_2$, -OCH$_2$C*H*$_2$ C*H*$_2$-), 1.90 (m, 4H, 4-C*H*$_2$, -C*H*$_2$-CH=), 3.50 (t, 4H, 1-C*H*$_2$, -OC*H*$_2$-), 4.83 (m, 4H, 6-C*H*$_2$, =C*H*$_2$), 5.65 (m, 2H, 5-C*H,* -C*H*=CH$_2$).

^{13}C NMR ($CDCl_3$, 250 MHz): δ 25.67 (C-3), 33.62 (C-2), 33.98 (C-4), 63.01 (C-1), 114.98 (C-6), 138.4 (C-6).

^{31}P NMR (Dioxane-THF-d$_8$, 700 MHz): δ -8.29 (s).

7.3.2 Cyclotriphosphazene based Model Compounds

Hexakis-(5-hexenyl-1-oxy)-cyclotriphosphazene

(***1***)

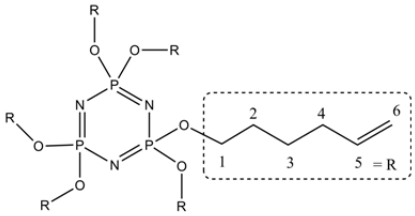

5-Hexen-1-ol (4.61 g, 46.02 mmol) was added to a suspension of NaH (95%, 1.16 g, 45.97 mmol) in 20 mL of dioxane. The mixture was stirred at 50 °C for 24 h under argon atmosphere to form the corresponding alkoxide. $N_3P_3Cl_6$ (1.32 g, 3.80 mmol) was dissolved in 60 mL freshly distilled dioxane and added dropwise to the alkoxide suspension. The resultant mixture was stirred at 60 °C for 48 h under an atmosphere of dry argon. Completion of the reaction was checked by ^{31}P NMR. The mixture was then filtrated and the solvent evaporated in vacuum. The crude product was purified by column chromatography ($CHCl_3$/MeOH, 100/1, v/v, retardation factor R_f = 0.80) leading to a colorless, viscous liquid ***1*** (2.13 g, 2.92 mmol, 77% yield).

^{1}H NMR (DMSO-d_6, 250 MHz): δ 1.33-1.44 (m, 12H, 2-CH_2, -OCH_2CH_2-), 1.53-1.63 (m, 12H, 3-CH_2, -CH_2CH_2CH=), 1.96-2.05 (m, 12H, 4-CH_2, -CH_2-CH=), 3.77-3.85 (m, 12H, 1-CH_2, -OCH_2-), 4.91-5.04 (m, 12H, 6-CH_2, =CH_2), 5.69-5.86 (m, 6H, 5-CH, -CH=CH_2).

^{13}C NMR (DMSO, 250 MHz): δ 24.4 (C-3), 29.1 (C-2), 32.7 (C-4), 64.9 (C-1), 114.9 (C-5), 138.4 (C-6).

^{31}P NMR (DMSO-d_6, 700 MHz): δ 18.03 (s).

MALDI-TOF m/z (%): 729.9 (100).

Hexakis-(4-(oxiran-2-yl)-but-1-oxy)-cyclotriphosphazene

(***2***)

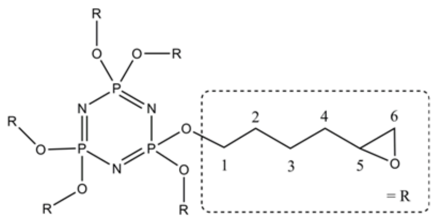

2,6-di-tert-butyl-4-methylphenol (BHT) (7.67 g, 34.81 mmol) and ***1*** (1.50 g, 2.06 mmol) were dissolved in 50 mL methylene chloride. The solution was cooled to 0 °C and metachloroperoxybenzoic acid (MCPBA) (77%, 7.81 g, 34.85 mmol) was added portion wise. The mixture was stirred vigorously for 48 h. After complete epoxidation, the mixture was washed three times with 10 wt% sodium hydroxide solution and water. The organic phase was dried over $MgSO_4$ and then concentrated to dryness. After purification by column chromatography (gradient, *n*-hexane/ethyl acetate, 5/1, v/v, passing over to ethyl acetate and finally MeOH, $R_{f,n\text{-hexane/ethyl acetate},5/1}$ = 0.11) compound ***2*** was obtained as a slightly orange, viscous oil (1.34 g, 1.62 mmol, 79% yield).

^{1}H NMR ($CDCl_3$, 250 MHz): δ 1.35-1.80 (m, 36H, 2-CH_2, 3-CH_2, 4-CH_2, OCH$_2$-(CH_2)$_3$-), 2.42 (dd, 6H, ^2J = 4.9, ^3J = 2.7, 6'-CH_2, -CH-(-O-)-CH_2), 2.70 (dd, 6H, ^2J = 4.8, ^3J = 3.6, 6-CH_2, -CH-(-O-)-CH_2), 2.80-2.92 (m, 6H, 5-CH, -CH-(-O-)-CH$_2$), 3.80-3.95 (m, 12H, 1-CH_2, -OCH_2-).

^{13}C NMR ($CDCl_3$, 250 MHz): δ 22.5 (C-3), 30.1 (C-2), 32.2 (C-4), 47.1 (C-6), 52.3 (C-5), 65.7 (C-1).

^{31}P NMR (DMSO-d$_6$, 700 MHz): δ 17.24 (s).

MALDI-TOF m/z (%): 825.9 (100).

Hexakis-(4-(4-butoxy)-1,3-dioxolan-2-one)-cyclotriphosphazene

(***3***)

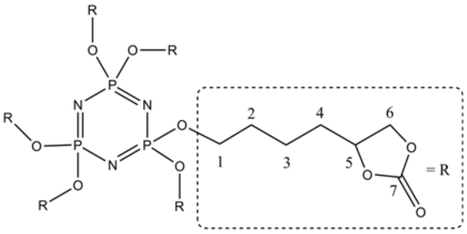

Tetrabutylammonium iodide (0.18 g, 0.49 mmol), tributyltin iodide (0.20 g, 0.49 mmol), and ***2*** (1.34 g, 1.62 mmol), were homogenously mixed in 25 mL of THF. Under N_2 atmosphere CO_2 was passed continuously through the clear solution for 24 h at 50 °C. The mixture was then concentrated and the crude product was purified by column chromatography (ethyl acetate/THF, 2/1, v/v, R_f = 0.48). Product ***3*** was obtained as colorless, highly viscous oil (1.01 g, 0.93 mmol, 57% yield).

^{1}H NMR (DMSO-d$_6$, 250 MHz): δ 1.23-1.51 (m, 12H, 3-CH_2, -OCH$_2$CH$_2$CH_2-), 1.52-1.83 (m, 24H, 2-CH_2, 4-CH_2, -OCH$_2$CH_2-, -CH_2CH-(O(C=O)O)-CH$_2$), 3.84 (m, 12H, -OCH_2-), 4.11 (dd, 6H, ^2J = 8.0, ^3J = 7.2, 6-CH_2, -CH-(O(C=O)O)-CH_2), 4.56 (dd, 6H, ^2J = 8.1, ^3J = 7.2, 6'-CH_2, -CH-(O(C=O)O)-CH_2), 4.73-4.84 (m, 6H, 5-CH, -CH-(O(C=O)O)-CH$_2$).

^{13}C NMR (DMSO, 250 MHz): δ 20.5 (C-3), 29.2 (C-2), 32.4 (C-3), 64.9 (C-1), 69.2 (C-6), 76.9 (C-5), 154.9 (C-7).

^{31}P NMR (DMSO-d$_6$, 500 MHz): δ 17.21 (s).

MALDI-TOF m/z (%): 1090 (100).

Hexakis-(9-decenyl-1-oxy)-cyclotriphosphazene

(***4***)

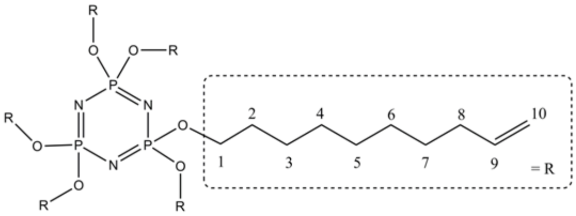

Synthetic procedure followed that for compound ***1*** but with 7-octen-1-ol to afford ***4*** as colorless liquid (column chromatography, *n*-hexane/ethyl acetate, 4/1, v/v, $R_f = 0.88$, 82% yield).

^{1}H NMR ($CDCl_3$, 250 MHz): δ 1.17-1.44 (m, 60H, 3-CH_2, 4-CH_2, 5-CH_2, 6-CH_2, 7-CH_2, -OCH$_2$CH$_2$-(CH_2)$_5$-), 1.52-1.70 (m, 12H, 2-CH_2, -OCH$_2$CH_2-), 1.94-2.06 (m, 12H, 8-CH_2, -CH_2-CH=), 3.82-3.92 (m, 12H, 1-CH_2, -OCH_2-), 4.85-5.01 (m, 12H, 10-CH_2, =CH_2), 5.69-5.85 (m, 6H, 9-CH, -CH=CH$_2$).

^{13}C NMR ($CDCl_3$, 250 MHz): δ 25.9 (C-5), 29.1 (C-4), 29.3 (C-6), 29.5 (C-7), 29.6 (C-3), 30.5 (C-2), 34.0 (C-8), 66.0 (C-1), 114.4 (C-10), 139.3 (C-9).

^{31}P NMR ($CDCl_3$, 700 MHz): δ 17.85 (s).

MALDI-TOF m/z (%): 1067 (100).

Hexakis-(8-(oxiran-2-yl)-oct-1-oxy)-cyclotriphosphazene

(***5***)

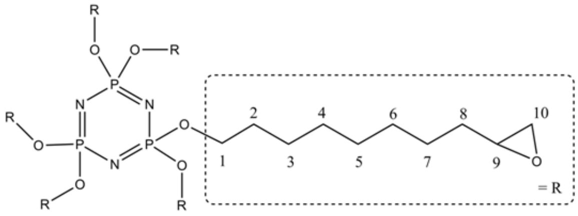

Synthetic procedure followed that for compound ***2*** to afford ***5*** out of ***4*** as slightly orange, viscous oil in 78% yield (column chromatography, *n*-hexane/ethyl acetate, 10/1, v/v, passing over to pure ethyl acetate, $R_{f,\ n\text{-hexane/ethyl acetate},\ 5/1} = 0.2$).

^{1}H NMR ($CDCl_3$, 250 MHz): δ 1.18-1.71 (m, 84H, 2-CH_2, 3-CH_2, 4-CH_2, 5-CH_2, 6-CH_2, 7-CH_2, 8-CH_2, -OCH$_2$-(CH_2)$_7$-), 2.44 (dd, 6H, $^2J = 5.2$, $^3J = 2.6$, 10-CH_2, -CH-(-O-)-CH_2), 2.73 (dd, 6H, $^2J = 5.1$, $^3J = 4.0$, 10'-CH_2, -CH-(-O-)-CH_2), 2.82-2.92 (m, 6H, 9-CH, -CH-(-O-)-CH$_2$), 3.79-3.95 (m, 12H, 1-CH_2, -OCH_2-).

^{13}C NMR ($CDCl_3$, 250 MHz): δ 25.9 (C-5), 26.2 (C-6), 29.4 (C-4), 29.6 (C-7), 29.7 (C-3), 30.5 (C-2), 32.7 (C-8), 47.3 (C-10), 52.6 (C-9), 66.0 (C-1).

^{31}P NMR (DMSO-d$_6$, 700 MHz): δ 17.25 (s).

Hexakis-(4-(8-octoxy)-1,3-dioxolan-2-one)-cyclotriphosphazene

(***6***)

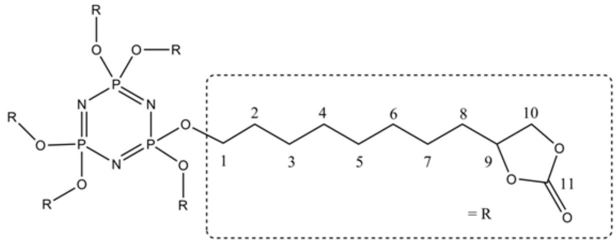

Synthetic procedure followed that for compound ***3*** to afford ***6*** out of epoxide ***5*** as slightly yellow, viscous oil (column chromatography, *n*-hexane/ethyl acetate, 4/1, v/v, R_f = 0.55, 75% yield).

^{1}H NMR ($CDCl_3$, 250 MHz): δ 1.17-1.53 (m, 60H, 3-C*H*$_2$, 4-C*H*$_2$, 5-C*H*$_2$, 6-C*H*$_2$, 7-C*H*$_2$, -OCH$_2$CH$_2$-(C*H*$_2$)$_5$-), 1.54-1.82 (m, 24H, 2-C*H*$_2$, 8-C*H*$_2$, -OCH$_2$C*H*$_2$-, -C*H*$_2$CH-(O(C=O)O)-CH$_2$), 3.87 (m, 12H, 1-C*H*$_2$, -OC*H*$_2$-), 4.05 (dd, 6H, ^2J = 8.3, ^3J = 7.1, 10-C*H*$_2$, -CH-(O(C=O)O)-C*H*$_2$), 4.52 (dd, 6H, ^2J = 8.2, ^3J = 7.1, 10'-C*H*$_2$, -CH-(O(C=O)O)-C*H*$_2$), 4.64-4.75 (m, 6H, 9-C*H*, -C*H*-(O(C=O)O)-CH$_2$).

^{13}C NMR ($CDCl_3$, 250 MHz): δ 24.6 (C-5), 25.9 (C-6), 29.3 (C-4, C-7), 29.5 (C-3), 30.4 (C-2), 34.1 (C-8), 66.0 (C-1), 69.6 (C-10), 77.3 (C-9), 155.4 (C-11).

^{31}P NMR ($CDCl_3$, 700 MHz): δ 17.22 (s).

MALDI-TOF m/z (%): 1426 (100).

Hexakis-(13-tetradecenyl-1-oxy)-cyclotriphosphazene

(***7***)

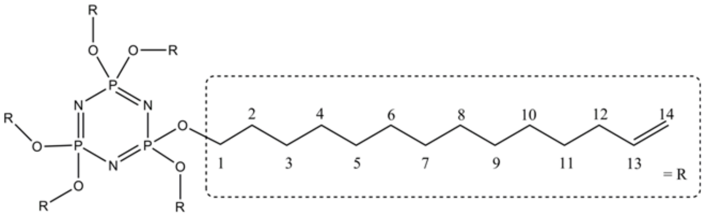

13-tetradecen-1-ol was synthesized following a reported literature procedure.[7.2][7.3] Synthetic procedure for compound ***7*** followed that for compound ***1*** but with 13-tetradecen-1-ol to afford ***7*** as white solid (column chromatography, *n*-hexane/ethyl acetate, 15/1, v/v, R_f = 0.51, 66% yield).

^{1}H NMR ($CDCl_3$, 250 MHz): δ 1.13-1.44 (m, 108H, 3-C*H*$_2$, 4-C*H*$_2$, 5-C*H*$_2$, 6-C*H*$_2$, 7-C*H*$_2$, 8-C*H*$_2$, 9-C*H*$_2$, 10-C*H*$_2$, 11-C*H*$_2$, -OCH$_2$CH$_2$-(C*H*$_2$)$_9$-), 1.55-1.70 (m, 12H, 2-C*H*$_2$, -OCH$_2$C*H*$_2$-), 1.95-2.08 (m, 12H, 12-CH_2, -CH_2-CH=), 3.81-3.94 (m, 12H, 1-CH_2, -OCH_2-), 4.85-5.02 (m, 12H, 14-CH_2, =CH_2), 5.69-5.88 (m, 6H, 13-CH, -CH=CH_2).

^{13}C NMR ($CDCl_3$, 250 MHz): 25.96, 29.17, 29.39, 29.56, 29.76, 29.87 (C-3 - C-10), 29.91 (C-11), 30.47 (C-2), 34.04 (C-12), 66.06 (C-1), 114.30 (C-14), 139.43 (C-13).

^{31}P NMR ($CDCl_3$, 500 MHz): δ 17.03 (s).

Hexakis-(12-(oxiran-2-yl)-dodecan-1-oxy)-cyclotriphosphazene

(***8***)

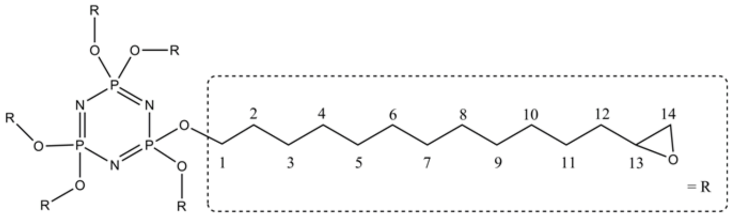

Synthetic procedure followed that for compound **2** to afford ***8*** out of epoxide ***7*** as a white powder in 45% yield (column chromatography, *n*-hexane/ethyl acetate, 5/1, v/v, passing over to pure ethyl acetate, $R_{f,\ n\text{-hexane/ethyl acetate},\ 5/1}$ = 0.3).

^{1}H NMR ($CDCl_3$, 250 MHz): δ 1.11-1.68 (m, 132H, 2-CH_2, 3-CH_2, 4-CH_2, 5-CH_2, 6-CH_2, 7-CH_2, 8-CH_2, 9-CH_2, 10-CH_2, 11-CH_2, -OCH$_2$-(CH_2)$_{10}$-), 2.42 (dd, 6H, ^2J = 5.0, ^3J = 2.7, 14-CH_2, -CH-(-O-)-CH_2), 2.71 (dd, 6H, ^2J = 4.9, ^3J = 4.0, 14'-CH_2, -CH-(-O-)-CH_2), 2.79-2.91 (m, 6H, 13-CH, -CH-(-O-)-CH_2), 3.79-3.93 (m, 12H, 1-CH_2, -OCH_2-).

^{13}C NMR ($CDCl_3$, 250 MHz): δ 25.90, 26.15, 26.62, 29.50, 29.63, 29.75, 29.79 (C-3 - C-10), 29.81 (C-11), 30.46 (C-2), 32.66 (C-12), 47.27 (C-14), 52.54 (C-13), 65.98 (C-1).

^{31}P NMR (DMSO-d_6, 700 MHz): δ 17.86 (s).

Hexakis-(4-(12-dodecyloxy)-1,3-dioxolan-2-one)-cyclotriphosphazene

(***9***)

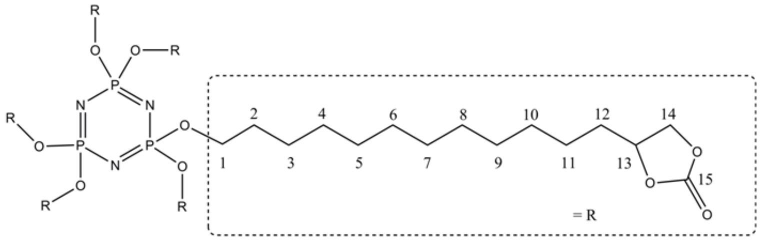

A stainless steel autoclave (250 mL) was charged with a solution of ***8*** (0.56 g, 0.37 mmol), tetrabutylammonium iodide (82.8 mg, 0.22 mmol), tributyltin iodide (93.4 mg, 0.22 mmol) in 40 mL THF. After purging with nitrogen, the reaction was started by pressurization of the solution with CO_2 up to 55 bar. The mixture was then heated to 75 °C accompanied by a pressure increase to 90 bar and stirred for 120 h at this temperature. The autoclave was allowed to cool to room temperature and excess CO_2 was discharged. The mixture was concentrated and the crude product dispersed in hexane, filtered and washed several times with hexane and methanol. Product ***9*** was obtained as white powder (0.42 g, 2.24 mmol, 65% yield).

^1H NMR ($CDCl_3$, 250 MHz): δ 1.10-1.52 (m, 108H, 3-CH_2, 4-CH_2, 5-CH_2, 6-CH_2, 7-CH_2, 8-CH_2, 9-CH_2, 10-CH_2, 11-CH_2, OCH_2CH_2-$(CH_2)_9$-), 1.53-1.87 (m, 24H, 2-CH_2, 12-CH_2, -OCH_2CH_2-, -CH_2CH-(O(C=O)O)-CH_2), 3.88 (m, 12H, 1-CH_2, -OCH_2-), 4.04 (dd, 6H, ^2J = 8.2, ^3J = 7.9, 14-CH_2, -CH-(O(C=O)O)-CH_2), 4.52 (dd, 6H, ^2J = 8.2, ^3J = 7.9, 14'-CH_2, -CH-(O(C=O)O)-CH_2), 4.59-4.78 (m, 6H, 13-CH, -CH-(O(C=O)O)-CH_2).

^{13}C NMR ($CDCl_3$, 250 MHz): δ 24.60, 25.94, 29.37, 29.54, 29.59, 29.69, 29.81 (C-3 - C-11), 30.46 (C-2), 34.11 (C-12), 66.03 (C-1), 69.60 (C-14), 77.3 (C-13), 155.29 (C-15).

^{31}P NMR ($CDCl_3$, 700 MHz): δ 17.85 (s).

MALDI-TOF m/z (%): 1763 (100).

Hexakis-(cis-5-octenyl-1-oxy)-cyclotriphosphazene

(***10***)

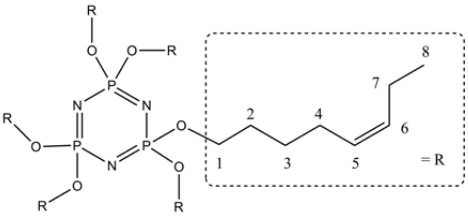

Synthetic procedure followed that for compound ***1*** but with 5-cis-octen-1-ol to afford ***10*** as colorless, viscous liquid (column chromatography, methylene chloride, R_f = 0.85, 89% yield).

^1H NMR ($CDCl_3$, 250 MHz): δ 0.91 (t, 18H, ^3J = 7.3, 8-CH_3, -CH_3), 1.31-1.46 (m, 12H, 2-CH_2, -OCH_2CH_2-), 1.54-1.70 (m, 12H, 3-CH_2, -$OCH_2CH_2CH_2$-), 1.92-2.06 (m, 24H, 4-CH_2, 7-CH_2, -CH_2-CH=CH-CH_2-), 3.83-3.92 (m, 12H, 1-CH_2,-OCH_2-), 5.20-5.40 (m, 12H, 5-CH, 6-CH, -CH_2-C*H*=C*H*-CH_2-).

^{13}C NMR ($CDCl_3$, 250 MHz): δ 14.5 (C-8), 20.7 (C-7), 26.0 (C-3), 26.8 (C-4), 30.0 (C-2), 65.8 (C-1), 128.8 (C-5), 132.2 (C-6).

^{31}P NMR ($CDCl_3$, 700 MHz): δ 18.56 (s).

MALDI-TOF m/z (%) 898 (100).

Hexakis-(4-(3-ethyloxiran-2-yl)-but-1-oxy)-cyclotriphosphazene

(***11***)

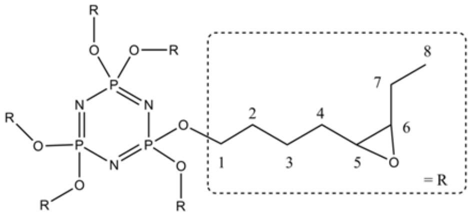

Synthetic procedure followed that for compound ***2*** to afford ***11*** out of epoxide ***10.*** After column chromatography (methylene chloride/ethyl acetate, $R_f = 0.85$) ***11*** was obtained as slightly yellow, highly viscous oil in 82% yield.

^{1}H NMR (DMSO-d_6, 250 MHz): δ 0.89-1.02 (t, 18H, ^{3}J = 7.3, 8-CH_3, -C*H*$_3$), 1.35-1.73 (m, 48H, 2-CH_2, 3-CH_2, 4-CH_2, 7-CH_2, -C*H*$_2$$CH_3$, -$OCH_2$-(C*H*$_2$)$_3$-), 2.74-2.90 (m, 12H, 5-CH, 6-CH, -C*H*-(-O-)-C*H*-C_2H_5), 3.74-3.90 (m, 12H, 1-CH_2, -OC*H*$_2$-).

^{13}C NMR (DMSO, 250 MHz): δ 10.5 (C-8), 20.6 (C-7), 22.5 (C-3), 26.6 (C-4), 29.5 (C-2), 56.0 (C-5), 57.1 (C-6), 64.9 (C-1).

^{31}P NMR (DMSO-d_6, 700 MHz): δ 18.81 (s).

MALDI-TOF m/z (%): 994 (32), 1016 (Na^+-Peak, 32), 1032 (K^+-Peak, 100).

Hexakis-(4-ethyl-5-(4-butoxy)-1,3-dioxolan-2-one)-cyclotriphosphazene

(***12***)

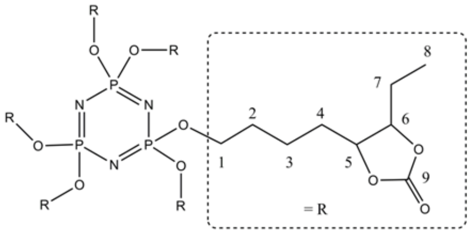

Chlorocobalt tetraphenylporphyrin ((TTP)Co^{III}Cl) catalyst was synthesized following a reported procedure.[7.4-7.6] A stainless steel autoclave (250 mL) was charged with a solution of ***11*** (0.50 g, 0.50 mmol), (TPP)Co^{III}Cl (2 mol%) and *N,N*-Dimethylaminopyridine (DMAP, 4 mol%) in 15 mL methylene chloride. After purging with nitrogen, the reaction was started by pressurization of the solution with CO_2 up to 50 bar. The mixture was then heated to 100 °C accompanied by a pressure increase to 80 bar and stirred for 72 h at this temperature. The autoclave was allowed to cool to room temperature and excess CO_2 was discharged. The mixture was concentrated and the crude product was purified by column chromatography (ethyl acetate/*n*-hexane, 5/1, v/v, R_f = 0.25). Product ***12*** was obtained as slightly orange, highly viscous oil (0.42 g, 3.34 mmol, 67% yield).

^{1}H NMR ($CDCl_3$, 250 MHz): δ 1.03 (t, 18H, ^3J = 7.3, 8-CH_3, -C*H*$_3$), 1.36-1.83 (m, 48H, 2-CH_2, 3-CH_2, 4-CH_2, 7-CH_2, -C*H*$_2$$CH_3$, -$OCH_2$(C*H*$_2$)$_3$-), 3.90 (br, 12H, , 1-$CH_2$, -OC*H*$_2$-), 4.13-4.30 (m, 0.72 H, 5-CH, 6-CH, *trans*-CH_2-C*H*-(O(C=O)O)-C*H*-C_2H_5), 4.48-4.72 (m, 11.28 H, 5-CH, 6-CH, *cis*-CH_2-C*H*-(O(C=O)O)-C*H*-C_2H_5).

^{13}C NMR ($CDCl_3$, 250 MHz): δ 10.3 (C-8), 22.4 (C-3), 22.5 (C-7), 28.7 (C-2), 29.9 (C-4), 65.7 (C-1), 80.0 (C-5), 81.5 (C-6), 154.9 (C-9).

^{31}P NMR ($CDCl_3$, 700 MHz): δ 18.57 (s).

MALDI-TOF m/z (%): 1258 (100).

Hexakis-(2-(2-(2-(2-methoxyethoxy)ethoxy)ethoxy)ethoxy)-cyclotriphosphazene [7.7]

(***13***)

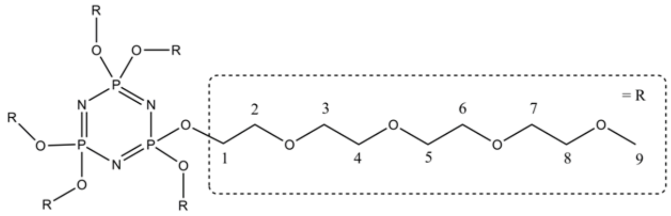

Synthetic procedure followed that for compound ***1*** to afford ***13*** out of the reaction between $N_3P_3Cl_6$ and the alkoxide of tetraethyleneglycol monomethyl ether as a colorless oil (column chromatography, *n*-hexane/THF, 1/3, v/v, R_f = 0.28, 90% yield).

^{1}H-NMR ($CDCl_3$, 250 MHz): δ 3.34 (s, 18H, 9-CH_3, -C*H*$_3$), 3.48-3.54 (m, 12H, 2-CH_2, P-OCH_2C*H*$_2$-), 3.55-3.68 (m, 72H, 3-CH_2, 4-CH_2, 5-CH_2, 6-CH_2, 7-CH_2, 8-CH_2, O-(C*H*$_2$C*H*$_2$O)$_3$-CH_3), 4.00 (br, 12H, 1-CH_2, P-OC*H*$_2$-).

^{13}C-NMR ($CDCl_3$, 250 MHz): δ 59.3 (C-9), 65.2 (C-1), 70.2 (C-7), 70.7 (C-3, C-4, C-5, C-6), 70.8 (C-2), 72.1 (C-8).

^{31}P-NMR ($CDCl_3$, 700 MHz): δ 17.11 (s).

MALDI-TOF m/z (%) 1379 (100).

7.3.3 Hexaphenylbenzene based Model Compounds

Hexakis-(4-hydroxyphenyl)-benzene

(***14***)

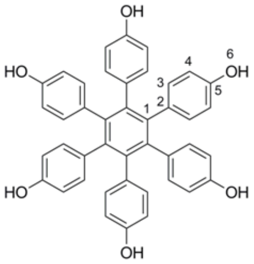

Synthesis of ***14*** followed a reported literature procedure (59% overall yield).[7.8]

^{1}H NMR (CD$_3$OD, 250 MHz): *δ* 6.30 (d, 12H, ^{3}J = 8.6, *4-Aryl*-H), 6.57 (d, 12H, ^{3}J = 8.6, *3-Aryl*-H).

^{13}C NMR (CD$_3$OD, 250 MHz): *δ* 114.7 (C-4), 133.9 (C-3), 134.5 (C-2), 141.9 (C-1), 155.5 (C-5).

MALDI-TOF m/z (%): 630 (100).

Hexakis-(4-(2-oxiran-2-yl)-phenyl)-benzene

(***15***)

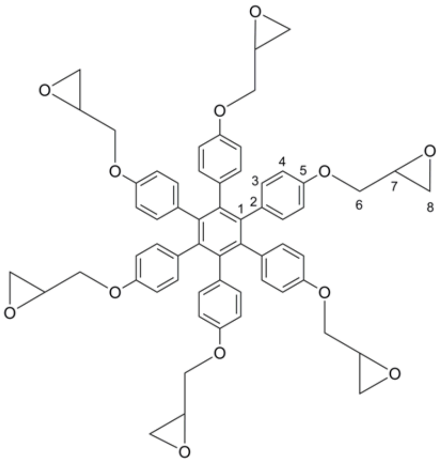

Hexakis-(4-hydroxyphenyl)-benzene ***14*** (0.20 g, 0.32 mmol) was dissolved in 4 mL methanol. After addition of freshly grounded potassium hydroxide (0.13 g, 2.32 mmol) the mixture was stirred at 45 °C for 1 h. Three quarters of the methanol were removed under argon atmosphere at 70 °C oil bath temperature resulting in a clear orange solution. After cooling down to 45 °C, epichlorhydrin (20 mL, 23.60 g, 0.255 mol) was added. The white reaction mixture was then stirred for 48 h at 45 °C. Epichlorhydrin was removed by distillation under argon followed by addition of 50 mL toluene and concentrating the mixture to dryness. The residue was washed with a mixture of water/acetone (1/1, v/v) and dried under high vacuum to obtain **15** as white powder (0.248 mmol, 78% yield).[7.9]

^{1}H NMR (DMSO-d_6, 250 MHz): *insoluble.*

MALDI-TOF m/z (%) 966 (100), 989 (Na^+-Peak, 12), 1005 (K^+-Peak, 5).

EA (%): Calc.: C 74.51 H 5.63; Found: C 74.22 H 5.75.

Hexakis-(4-(hept-4-enoate)-phenyl)-benzene

(***16***)

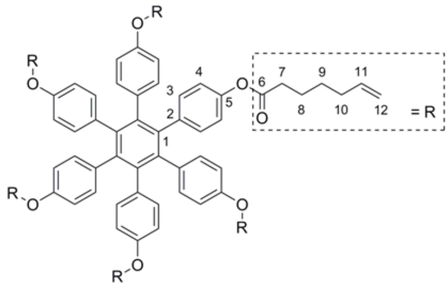

6-heptenoyl chloride was synthesized following a reported procedure.[7.10] Hexakis-(4-hydroxyphenyl)-benzene ***14*** (0.20 g, 0.32 mmol) and dry pyridine (125 mL) were mixed at 60 °C in a *Schlenk* flask. Under N_2 atmosphere a solution of 6-heptenoyl chloride (0.56 g, 3.81 mmol) in 5 mL dry acetonitrile was added dropwise at 60 °C under stirring. The temperature was increased to 85 °C and the mixture was stirred at this temperature for 24 h. Subsequently, 15 mL acetonitrile, 15 mL ethyl acetate and 15 mL of water were added and the organic phase was washed three times with 10 mL of 15 wt% aqueous sodium carbonate and once with 15 mL water. The combined organic layer was dried over $MgSO_4$, concentrated and the residue was subjected to column chromatography with *n*-hexane/ethyl acetate (3/1, v/v, R_f = 0.65) as eluent. Product ***16*** was obtained as white powder (0.35 g, 0.27 mmol, 84% yield).

^{1}H NMR ($CDCl_3$, 250 MHz): δ 1.35-1.51 (m, 12H, 9-CH_2, -CH_2CH_2-$CH=CH_2$), 1.57-1.75 (m, 12H, 8-CH_2, -O-C(=O)-CH_2CH_2-), 1.96-2.13 (m, 12H, 10-CH_2, -CH_2-$CH=CH_2$), 2.42 (t, 12H, ^3J = 7.4, 7-CH_2, -O-C(=O)-CH_2-), 4.88-5.06 (m, 12H, 12-CH_2, -CH_2-$CH=CH_2$), 5.67-5.88 (m, 6H, 11-CH_2, -CH_2-$CH=CH_2$), 6.63 (d, 12H, ^3J = 8.7, 4-*Aryl*-H, *ortho*-Ar*H*), 6.74 (d, 12H, ^3J = 8.7, 3-*Aryl*-H, *meta*-Ar*H*).

^{13}C NMR ($CDCl_3$, 250 MHz): δ 24.5 (C-8), 28.5 (C-9), 33.6 (C-10), 34.4 (C-7), 115.0 (C-12), 120.3 (C-4), 132.4 (C-3), 137.7 (C-2), 138.6 (C-11), 140.2 (C-1), 148.8 (C-5), 171.8 (C-6).

MALDI-TOF m/z (%) 1315 (Na^+-Peak, 100).

Hexakis-(4-(5-oxiran-2-yl-pentanoate)-phenyl)-benzene

(***17***)

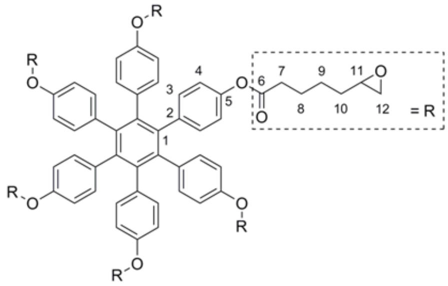

16 (0.35 g, 0.27 mmol) was dissolved in 80 mL methylene chloride. The solution was cooled to 0 °C and MCPBA (77%, 0.61 g, 2.72 mmol) was added portion wise. The mixture was stirred vigorously at room temperature for 96 h. After complete epoxydation, the mixture was washed three times with 2 wt% sodium hydroxide solution and water. The organic phase was dried over $MgSO_4$ and then concentrated to dryness. The crude product ***17*** was obtained as white powder and used without further purification (0.36 g, 0.26 mmol, 96% yield).

^1H NMR ($CDCl_3$, 250 MHz): δ 1.40-1.80 (m, 36H, 8-CH_2, 9-CH_2, 10-CH_2, -O-C(=O)-CH_2-(CH_2)$_3$-), 2.36-2.50 (m, 18H, 7-CH_2, -O-C(=O)-C*H*$_2$-, 12-CH_2, -CH-(-O-)-C*H*$_2$), 2.72 (dd, 6H, ^2J = 5.0, ^3J = 4.0, 12'-CH_2, -CH-(-O-)-C*H*$_2$), 2.83-2.96 (m, 6H, 11-CH_2, -C*H*-(-O-)-CH_2), 6.63 (d, 12H, ^3J = 8.6, 4-Aryl-H, *ortho*-Ar*H*), 6.74 (d, 12H, ^3J = 8.6, 3-Aryl-H, *meta*-Ar*H*).

^{13}C NMR ($CDCl_3$, 250 MHz): δ 24.8 (C-8), 25.7 (C-9), 32.3 (C-10), 34.4 (C-7), 47.9 (C-12), 54.3 (C-11), 120.3 (C-4), 132.4 (C-3), 137.7 (C-2), 140.2 (C-1), 148.7 (C-5), 171.6 (C-6).

Hexakis-(4-(5-(2-oxo-1,3-dioxolan-4-yl)-pentanoate)-phenyl)-benzene

(***18***)

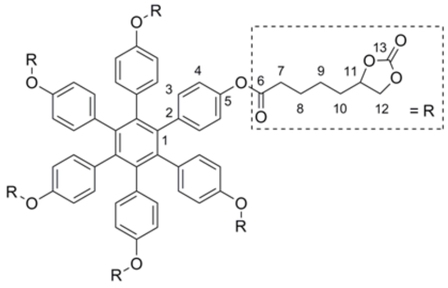

A stainless steel autoclave (250 mL) was charged with a solution of ***17*** (0.36 g, 0.26 mmol), tetrabutylammonium iodide (0.06 g, 0.16 mmol) and tributyltin iodide (0.07 g, 0.16 mmol) in 50 mL of freshly distilled THF. After purging with nitrogen, the reaction was started by pressurization of the solution with CO_2 up to 50 bar. The mixture was then heated to 80 °C accompanied by a pressure increase to 80 bar and stirred for 120 h at this temperature. The autoclave was allowed to cool to room temperature and excess CO_2 was discharged. The product was precipitated in a minimum amount of ethyl acetate, filtered and washed with 100 mL chilled methanol, 100 mL chilled hexane and a small amount of chilled acetone to obtain ***18*** as a white powder (0.34 g, 0.21 mmol, 79% yield).

^{1}H NMR (DMSO-d_6, 250 MHz): δ 1.23-1.81 (m, 36H, 8-CH_2, 9-CH_2, 10-CH_2, -O-C(=O)-CH_2-(CH_2)$_3$-), 2.41-2.53 (m, 12H, 7-CH_2, -O-C(=O)-CH_2-), 4.11 (dd, 6H, ^2J = 8.0, ^3J = 7.3, 12-CH_2, -CH-(O(C=O)O)-CH_2), 4.55 (dd, 6H, ^2J = 8.0, ^3J = 7.2, 12'-CH_2, -CH-(O(C=O)O)-CH_2), 4.68-4.88 (m, 6H, 11-CH_2, -CH-(O(C=O)O)-CH_2), 6.66 (d, 12H, ^3J = 8.3, 4-Aryl-H, *ortho*-Ar*H*), 6.87 (d, 12H, ^3J = 8.3, 3-Aryl-H, *meta*-Ar*H*).

^{13}C NMR (DMSO-d_6, 250 MHz): δ 23.6 (C-8), 23.8 (C-9), 32.5 (C-7), 33.2 (C-10), 69.2 (C-12), 76.9 (C-11), 120.0 (C-4), 131.8 (C-3), 137.1 (C-2), 139.7 (C-1), 148.1 (C-5), 154.9 (C-13), 171.0 (C-6).

Hexakis-(4-(undec-10-enoate)-phenyl)-benzene

(***19***)

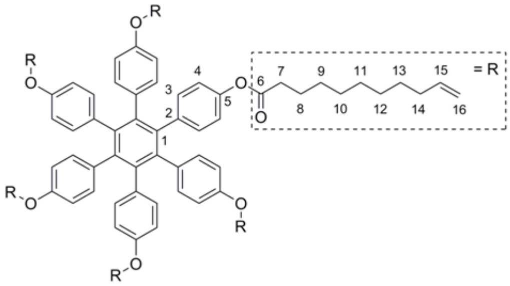

Synthetic procedure followed that for compound ***16*** but with 10-undecenoyl chloride to afford product ***19*** as colorless oil (column chromatography, *n*-hexane/THF, 4/1, v/v, R_f = 0.53, 78% yield).

^{1}H NMR ($CDCl_3$, 250 MHz): δ 1.18-1.41 (m, 60H, 9-CH_2, 10-CH_2, -O-C(=O)-(CH_2)$_2$-(CH_2)$_2$-, 11-CH_2, 12-CH_2, 13-CH_2, -(CH_2)$_3$-CH_2-CH=CH_2), 1.56-1.72 (m, 12H, 8-CH_2,

-O-C(=O)-CH$_2$C*H*$_2$-), 1.97-2.05 (m, 12H, 14-CH$_2$, -C*H*$_2$-CH=CH$_2$), 2.40 (t, 12H, ^3J = 7.1, 7-CH$_2$, -O-C(=O)-C*H*$_2$-), 4.86-5.03 (m, 12H, 16-CH$_2$, -CH$_2$-CH=C*H*$_2$), 5.70-5.87 (m, 6H, 15-CH$_2$, -CH$_2$-C*H*=CH$_2$), 6.63 (d, 12H, ^3J = 8.7, 4-Aryl-H, *ortho*-Ar*H*), 6.74 (d, 12H, ^3J = 8.7, 3-Aryl-H, *meta*-Ar*H*).

^{13}C NMR (CDCl$_3$, 250 MHz): δ 25.0 (C-8), 29.1, 29.3, 29.4 (C-9 – C-12), 29.5 (C-13), 34.0 (C-7), 34.6 (C-14), 114.4 (C-16), 120.3 (C-4), 132.4 (C-3), 137.7 (C-2), 139.4 (C-15), 140.2 (C-1), 148.8 (C-5), 172.0 (C-6).

MALDI-TOF m/z (%): 1628 (10), 1651 (Na$^+$-Peak, 100).

Hexakis-(4-(9-oxiran-2-yl-nonanoate)-phenyl)-benzene

(***20***)

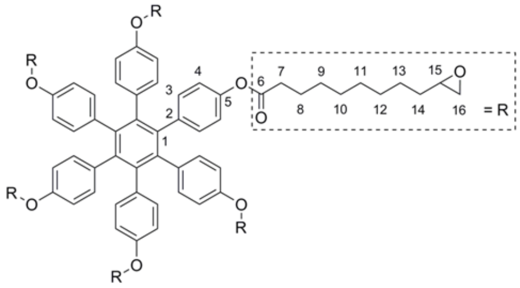

Synthetic procedure followed that for compound ***17*** to afford product ***20*** out of ***19*** as white powder (95% yield).

^{1}H NMR (CDCl$_3$, 250 MHz): δ 1.18-1.71 (m, 84H, 8-CH$_2$, 9-CH$_2$, 10-CH$_2$, 11-CH$_2$, 12-CH$_2$, 13-CH$_2$, -O-C(=O)-CH$_2$-(C*H*$_2$)$_7$-), 2.35-2.45 (m, 18H, 7-CH$_2$, -O-C(=O)-C*H*$_2$-, 16-CH$_2$, -CH-(-O-)-C*H*$_2$), 2.68-2.74 (dd, 6H, ^2J = 5.1, ^3J = 3.9, 16'-CH$_2$, -CH-(-O-)-C*H*$_2$), 2.82-2.91 (m, 6H, 15-CH$_2$, -C*H*-(-O-)-CH$_2$), 6.61 (d, 12H, ^3J = 8.6, 4-Aryl-H, *ortho*-Ar*H*), 6.73 (d, 12H, ^3J = 8.6, 3-Aryl-H, *meta*-Ar*H*).

^{13}C NMR (CDCl$_3$, 250 MHz): δ 25.0 (C-8), 26.1 (C-9), 29.3, 29.4, 29.5, 29.6 (C-10 – C-13), 32.7 (C-14), 34.5 (C-7), 47.3 (C-16), 52.7 (C-15), 120.3 (C-4), 132.4 (C-3), 137.7 (C-2), 140.2 (C-1), 148.8 (C-5), 172.0 (C-6).

MALDI-TOF m/z (%) 1746 (Na$^+$-Peak, 100), 1762 (K$^+$-Peak, 60), 1786 (Na$^+$/K$^+$-Peak, 33).

Hexakis-(4-(9-(2-oxo-1,3-dioxolan-4-yl)nonanoate)-phenyl)-benzene

(***21***)

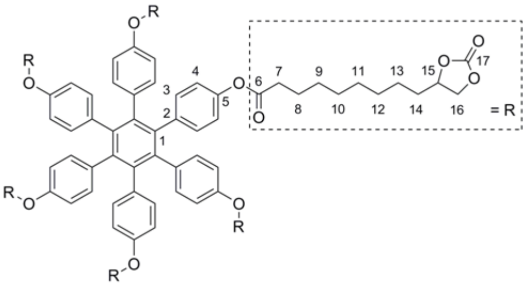

Synthetic procedure followed that for compound ***18*** to afford product ***21*** out of epoxide ***20*** as white powder (77% yield).

^{1}H NMR (CDCl$_3$, 250 MHz): δ 1.21-1.86 (m, 84H, 8-CH$_2$, 9-CH$_2$, 10-CH$_2$, 11-CH$_2$, 12-CH$_2$, 13-CH$_2$, 14-CH$_2$, 15-CH$_2$, -O-C(=O)-CH$_2$-(C*H*$_2$)$_7$-), 2.41 (t, 12H, ^3J = 7.4, 7-CH$_2$, -O-C(=O)-C*H*$_2$-), 4.05 (dd, 6H, ^2J = 8.0, ^3J = 7.2, 16-CH$_2$, -CH-(O(C=O)O)-C*H*$_2$), 4.50 (dd, 6H, ^2J = 8.1, ^3J = 7.2, 16'-CH$_2$, -CH-(O(C=O)O)-C*H*$_2$), 4.60-4.75 (m, 6H, 15-CH$_2$, -C*H*-(O(C=O)O)-CH$_2$), 6.62 (d, 12H, ^3J = 8.6, 4-Aryl-H, *ortho*-Ar*H*), 6.74 (d, 12H, ^3J = 8.6, 3-Aryl-H, *meta*-Ar*H*).

^{13}C NMR (CDCl$_3$, 250 MHz): δ 24.6 (C-8) , 24.9 (C-9), 29.1, 29.2, 29.3 (C-10 – C-13), 34.1 (C-7), 34.5 (C-14), 69.6 (C-16), 77.4 (C-15), 120.3 (C-4), 132.4 (C-3), 137.8 (C-2), 140.4 (C-1), 148.8 (C-5), 155.3 (C-17), 171.9 (C-6).

EA (%): Calc.: C 68.86 H 6.99; Found: C 68.78 H 6.91.

Hexakis-(4-(pent-4-enoate)-phenyl)-benzene

(***22***)

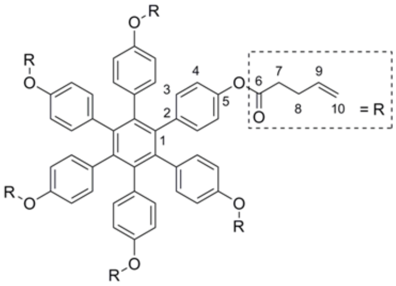

Synthetic procedure followed that for compound ***16*** but with 4-pentenoyl chloride to afford product ***22*** as white powder (column chromatography, *n*-hexane/THF, 1/1, v/v, R_f = 0.4, 59% yield).

^{1}H NMR (CDCl$_3$, 250 MHz): δ 2.32-2.58 (m, 24H, 7-C*H*$_2$, 8-C*H*$_2$, -O-C(=O)-(C*H*$_2$)$_2$-), 4.96-5.12 (m, 12H, 10-C*H*$_2$, -CH$_2$-CH=C*H*$_2$), 5.73-5.91 (m, 6H, 9-C*H*$_2$, -CH$_2$-C*H*=CH$_2$), 6.63 (d, 12H, ^{3}J = 8.7, 4-Aryl-H, *ortho*-Ar*H*), 6.74 (d, 12H, ^{3}J = 8.7, 3-Aryl-H, *meta*-Ar*H*).

^{13}C NMR (CDCl$_3$, 250 MHz): δ 28.9 (C-8), 33.81 (C-7), 116.0 (C-10), 120.3 (C-4), 132.4 (C-3), 136.6 (C-2), 137.7 (C-9), 140.2 (C-1), 148.8 (C-5), 171.2 (C-6).

MALDI-TOF m/z (%): 1146 (Na$^+$-Peak, 100).

Hexakis-(4-(3-oxiran-2-yl-propanoate)-phenyl)-benzene

(***23***)

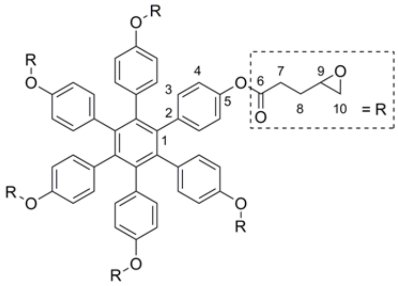

Synthetic procedure followed that for compound ***17*** to afford product ***23*** out of ***22*** as white powder (76% yield).

^{1}H NMR (CDCl$_3$, 250 MHz): δ 1.70-2.09 (m, 12H, 8-CH$_2$, -O-C(=O)-CH$_2$-C*H*$_2$-), 2.50 (dd, 6H, 10-CH$_2$, ^{2}J = 4.9, ^{3}J = 2.7, -CH-(-O-)-C*H*$_2$), 2.58 (t, 12H, 7-CH$_2$, ^{3}J = 7.3, -O-C(=O)-C*H*$_2$-), 2.75 (dd, 6H, ^{2}J = 5.0, ^{3}J = 4.7, 10'-CH$_2$, -CH-(-O-)-C*H*$_2$), 2.95-3.03 (m, 6H, 9-CH$_2$, -C*H*-(-O-)-CH$_2$), 6.65 (d, 12H, ^{3}J = 8.7, 4-Aryl-H, *ortho*-Ar*H*), 6.75 (d, 12H, ^{3}J = 8.7, 3-Aryl-H, *meta*-Ar*H*).

^{13}C NMR (CDCl$_3$, 250 MHz): δ 27.7 (C-8), 30.8 (C-7), 47.3 (C-10), 51.3 (C-9), 120.2 (C-4), 132.4 (C-3), 137.8 (C-2), 140.2 (C-1), 148.7 (C-5), 171.0 (C-6).

Hexakis-(4-(2-(2-(2-(2-methoxyethoxy)ethoxy)ethoxy)ethoxy)-phenyl)-benzene

(***26***)

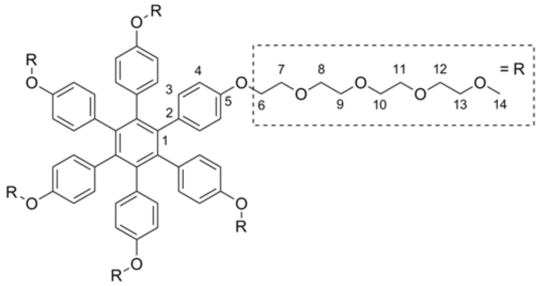

Compound ***26*** was prepared by the following steps: 1-(2-(2-(2-(2-methoxyethoxy)-ethoxy)ethoxy)ethoxy)-4-bromobenzene (***24***) is formed by reacting 2-(2-(2-(2-methoxyethoxy)ethoxy)ethoxy)ethyl-4-methylbenzensulfonate with 4-bromo-phenol in presence of anhydrous K_2CO_3 in DMF.[7.11][7.12] A one-pot *Sonogashira* reaction of ***24*** provides 1,2-Bis(4-(2-(2-(2-methoxyethoxy)-ethoxy)ethoxy)-ethoxy)phenyl)ethyne (***25***).[7.13] After subsequent one-pot cyclotrimerization of ***25*** product ***26*** is obtained as colorless oil (overall yield 32%).[7.8][7.11]

^{1}H NMR ($CDCl_3$, 300 MHz): δ 3.33 (s, 18H, 14-CH_3, -CH_3), 3.49-3.55 (m, 12H, 13-CH_2, CH_2-OCH_3), 3.58-3.68 (m, 60H, 8-CH_2, 9-CH_2, 10-CH_2, 11-CH_2, 12-CH_2, -O(CH_2CH_2O)$_2$-OC$H_2$$CH_2$-$OCH_3$), 3.69-3.75 (m, 12H, 7-$CH_2$, Ar-O-$CH_2CH_2$-), 3.86-3.93 (m, 12H, 6-CH_2, Ar-O-CH_2-), 6.37 (d, 12H, ^3J = 8.7, 4-Aryl-H, *ortho*-Ar*H*), 6.60 (d, 12H, ^3J = 8.7, 3-Aryl-H, *meta*-Ar*H*).

^{13}C NMR ($CDCl_3$, 300 MHz): δ 59.2, 67.1, 70.0, 70.7, 70.9, 113.1, 132.5, 133.8, 140.4, 156.1.

MALDI-TOF m/z (%): 1171 (100), 1793 (Na^+-Peak, 14), 1809 (K^+-Peak, 14).

7.3.4 Tetramethylcyclotetrasiloxane based Models

4,4',4'',4'''-[(2,4,6,8-tetramethylcyclotetrasiloxane-2,4,6,8-tetrayl)tetrakis(butane-4,1-diyl)]tetrakis(1,3-dioxolan-2-one)

(***27***)

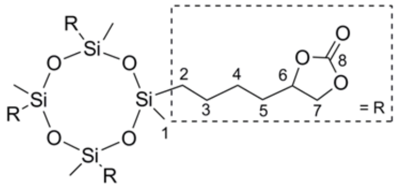

A 50 mL flask was charged with a solution of 2,4,6,8-tetramethylcyclotetrasiloxane (0.91 g, 3.78 mmol) in 10 mL dry toluene and degased. 4-(3-buten-1-yl)-1,3-dioxolan-2-one (2.80 g, 19.7 mmol)[7.12] was added drop wise followed by the addition of 2 drops of *Karstedt's catalyst* ($Pt_2\{[(CH_2{=}CH]Me_2Si]_2O\}_3$). Complete conversion was achieved after stirring for 24 hours at 45 °C. Next, the solution was filtered through *Celite* in order to remove the platinum catalyst and the filtrate was concentrated. At a temperature of 60 °C and high vacuum of 2 x 10^{-3} mbar for about two days removed the excess of 4-(3-buten-1-yl)-1,3-dioxolan-2-one and ***27*** was obtained as a colorless, slightly viscous oil (1.83 g, 2.26 mmol, 59% yield).

^{1}H NMR (CDCl$_3$, 250 MHz): δ 0.10 (s, 12H, 1-CH$_3$, -C*H*$_3$), 0.41-0.63 (m, 8 H, 2-CH$_2$, Si-C*H*$_2$-), 1.24-1.47 (m, 16H, 3-CH$_2$, 4-CH$_2$, Si-CH$_2$-(C*H*$_2$)$_2$-), 1.56-1.78 (m, 8H, 4-C*H*$_2$, -C*H*$_2$-CH-(O(C=O)O)-C*H*$_2$), 4.10 (dd, 4H, ^2J = 15.2, ^3J = 7.8, 7-CH$_2$, -CH-(O(C=O)O)-C*H*$_2$), 4.56 (dd, 4H, ^2J = 8.0, ^3J = 7.0, 7’-CH$_2$, -CH-(O(C=O)O)-C*H*$_2$), 4.66-4.84 (m, 4H, 6-CH, -C*H*-(O(C=O)O)-CH$_2$).

^{13}C NMR (CDCl$_3$, 250 MHz): δ -0.5 (C-1), 17.1 (C-3), 22.8 (C-2), 27.8 (C-4), 33.8 (C-5), 69.6 (C-7), 76.7 (C-6), 155.3 (C-8).

FD m/z (%): 809.2 (100).

(1-oxido-2,6,7-trioxa-1-phosphabicyclo[2.2.2]octan-4-yl)methyl undec-10-enoate [7.15]

(***28***)

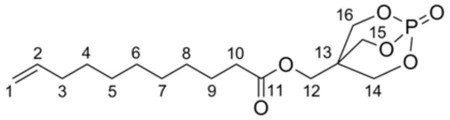

A two-neck flask (250 mL) equipped with a dropping funnel and a *Dimroth* condenser was fed with 1-oxo-4-methoxy-2,6,7-trioxa-1-phosphabicyclo[2.2.2]octane (10 g, 55.5 mmol)[7.16] and 25 g (0.316 mol) of pyridine. The reaction mixture was stirred at 60 °C under an atmosphere of dry argon. A solution of 10-undecenoyl chloride (13.6 g, 67.2 mmol) in 100 mL of dry acetonitrile was added dropwise and the reaction was effected at 85 °C for 10 hours. Subsequently, the reaction mixture was cooled to room temperature and 150 mL of ethyl acetate and 150 mL of water were added. The organic phase was washed three times with 150 mL of 15 wt% of aqueous sodium carbonate and once with 150 mL of water. The combined organic layer was dried over MgSO$_4$, concentrated and the residue was subjected to column chromatography with *n*-hexane/ethyl acetate (1/2, v/v, R_f = 0.69) as eluent. Product ***28*** was obtained as colorless liquid which crystallized over time (16.76 g, 48.4 mmol, 87% yield).

^{1}H NMR (DMSO-d$_6$, 250 MHz): δ 1.17-1.62 (m, 12H, 4-C*H*$_2$, 5-C*H*$_2$, 6-C*H*$_2$, 7-C*H*$_2$, 8-C*H*$_2$, 9-C*H*$_2$), 1.95-2.08 (m, 2H, 3-C*H*$_2$), 2.34 (t, 2H, 10-C*H*$_2$, ^3J = 7.4), 3.96 (s, 2H, 12-C*H*$_2$), 4.66 (d, J = 6.5, 6H, 14-CH$_2$, 15-CH$_2$, 16-CH$_2$), 4.89-5.06 (m, 2H, 2-CH$_2$), 5.70-5.90 (m, 1H, 2-CH).

^{13}C NMR (DMSO-d$_6$, 250 MHz): δ 172.5 (C-11), 138.8 (C-2), 114.7 (C-1), 75.5 (d, ^3J = 5.9, C-14, C-15, C-16), 59.4 (d, *J* = 2.5, C-12), 37.5 (d, *J* = 37.3, C-13), 33.2 (C-3), 33.0 (C-10), 28.7 (C-4), 28.6 (C-5), 28.5 (C-6), 28.4 (C-7), 28.2 (C-8), 24.2 (C-9).

^{31}P NMR (DMSO-d$_6$, 700 MHz): δ -6.83 (s).

FD m/z (%): 346.2 (100).

11,11',11'',11'''-[(2,4,6,8-tetramethylcyclotetrasiloxane-2,4,6,8-tetrayl)tetrakis(1-oxido-2,6,7-trioxa-1-phosphabicyclo[2.2.2]octan-4-yl)methyl]tetrakisundecanoate

(***29***)

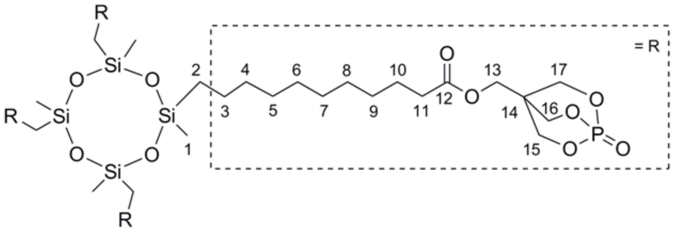

Synthetic procedure followed that for compound ***27*** but with to afford product ***29*** as colorless gel (60% yield).

^{1}H NMR (DMSO-d$_6$, 250 MHz): δ 0.04 (s, 12H, 1-CH_3, -CH_3), 0.50 (m, 8H, 2-CH_2, Si-CH_2-), 1.20-1.60 (m, 56H, 3-CH_2, 4-CH_2, 5-CH_2, 6-CH_2, 7-CH_2, 8-CH_2, 9-CH_2), 2.34 (m, 8H, 11-CH_2), 3.96 (s, 8H, 13-CH_2), 4.66 (d, 24H, 15-CH_2, 16-CH_2, 17-CH_2).

^{31}P NMR (DMSO-d$_6$, 700 MHz): δ -6.87.

MALDI-TOF m/z (%): 1626 (100).

7.3.5 Sulfur Approach

2,5,8,11,14-pentathiapentadecane [7.17]

(***30***)

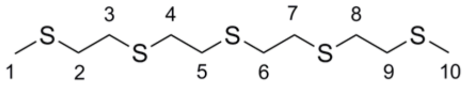

Freshly distilled 2,2'-thiodiethanethiol (22.9 mL, 167.5 mmol) is added dropwise to a solution of NaOEt (29.1 g, 427.6 mmol) in 300 mL absolute ethanol (H_2O < 50 ppm). After stirring for 3 h at room temperature, 2-chloromethyl ethyl sulfide (21.0 mL, 210.7 mmol) was added dropwise within 1 h. The mixture was subsequently stirred overnight at 100 °C and concentrated afterwards. Subjecting the residue to column chromatography with *n*-hexane/ethyl acetate (1/5, v/v, $R_f = 0.65$) as eluent yielded Product ***30*** as a white powder (8.51 g, 28.1 mmol, 17% yield).

^{1}H NMR (DMSO-d$_6$, 250 MHz): δ 2.17 (s, 6H, 1-CH_3, 10-CH_3, -SCH_3), 2.66-2.90 (m, 16H, 2-CH_2, 3-CH_2, 4-CH_2, 5-CH_2, 6-CH_2, 7-CH_2, 8-CH_2, 9-CH_2, H_3C-S(CH_2CH_2S)$_4$-CH$_3$).

^{13}C NMR (DMSO-d$_6$, 700 MHz): δ 14.6 (C-1, C-10), 30.8 (C-3, C-8), 31.3 (C-4, C-5, C-6, C-7), 33.2 (C-2, C-9).

FD m/z (%): 302 (100).

7.4 Bibliography

[7.1] B. Wang, *Macromolecules* **2005***,* 38, 643.

[7.2] Gebauer, J.; Blechert, S. *J. Org. Chem.* **2006**, 71, No 5, 2021.

[7.3] Zou, Y.; Millar, G. J. *Tetrahedron Letters* **2010**, 51, 1336.

[7.4] Sugimoto, H.; Kuroda, K. *Macromolecules* **2008**, *41*, 312.

[7.5] Sakurai, T.; Yamamoto, K.; Naito, H.; Nakamoto, N. *Bull. Chem. Soc. Jpn.* **1976**, *49*, 3042.

[7.6] Paddock, R. L.; Hiyama, Y.; McKay, J. M.; Nguyen, S. T. *Tetrahedron Letters* **2004**, *45*, 2023.

[7.7] Allcock, H. R.; Ravikiran, R.; O'Connor, S. J. M. *Macromolecules* **1997**, *30*, 3184.

[7.8] Kobayashi, K.; Shirasaka, T.; Sato, A.; Horn, E.; Furukawa, N. *Angew. Chem. Int. Ed.* **1999**, 38, 3483

[7.9] Regla, I.; Luviano-Jardon, A.; Demare, P.; Hong, E.; Torres-Gavilan, A.; Lopez-Munguia, A.; Castillo, E. *Tetrahedron Asymmetry* **2008***,* 19, 2439.

[7.10] Gaul, C.; Njardarson, J. T.; Shan,D.; Dorn, D. C.; Wu, K.; Tong, W. P.; Huang, X.-Y.; Moore, M. A. S.; Danishefsky, S. J. *J. Am. Chem. Soc.* **2004**, 126, 11326.

[7.11] Lu, Y.; Suzuki, T.; Zhang, W.; Moore, J. S.; Marinas, B. *J. Chem. Mater.* **2007**, 19, 3194.

[7.12] Buizide, A.; LeBerre, N.; Sauve, G. *Tetrahedron Lett.* **2001**, 42, 8781.

[7.13] Tohda, Y.; Sonogashira, K.; Hagihara, N. J. C. S. *Chem. Commun.* **1975**, 2, 54.

[7.14] Zhu, Z.; Einset, A. G.; Yang, C.-Y.; Chen, W.-X.; Wnek, G. E. *Macromolecules* **1994**, Vol. 27, 15, 4076.

[7.15] US-Patent 6,794,528 B2.

[7.16] Xing, W.; Song, L.; Lu, H.; Hu, Y.; Zhou, S. *Polym. Adv. Technol.* **2009***,* 20, 696.

[7.17] Fushimi, T.; Allcock, H. R. *Dalton Trans.* **2009**, 2477.

Appendix

List of Symbols and Abbreviations

Abbreviations

4C-CTP	Hexakis-(4-(4-butoxy)-1,3-dioxolan-2-one)-cyclotriphosphazene
4C-CTP-IC	Hexakis-(4-ethyl-5-(4-butoxy)-1,3-dioxolan-2-one)-cyclotriphosphazene
4C-HPB	Hexakis-(4-(5-(2-oxo-1,3-dioxolan-4-yl)-pentanoate)-phenyl)-benzene
4C-TMS	4,4',4'',4'''-[(2,4,6,8-tetramethylcyclotetrasiloxane-2,4,6,8-tetrayl)tetrakis(butane-4,1-diyl)]-tetrakis(1,3-dioxolan-2-one)
8C-CTP	Hexakis-(4-(8-octoxy)-1,3-dioxolan-2-one)-cyclotriphosphazene
8C-HPB	Hexakis-(4-(9-(2-oxo-1,3-dioxolan-4-yl)nonanoate)-phenyl)-benzene
8C-P-TMS	11,11',11'',11'''-[(2,4,6,8-tetramethylcyclotetrasiloxane-2,4,6,8-tetrayl)tetrakis(1-oxido-2,6,7-trioxa-1-phosphabicyclo[2.2.2]octan-4-yl)methyl]tetrakisundecanoate
12C-CTP	Hexakis-(4-(12-dodecyloxy)-1,3-dioxolan-2-one) cyclotriphosphazene
A	Area
AC	Alternating current
AcN	Acetonitrile
BHT	2,6-di-tert-butyl-4-methylphenol
BPP	Bloembergen-Purcell-Pound
COSY	Correlated spectroscopy
CP	Cross polarization
CSA	Chemical shift anisotropy
CW	Continuous wave
CTP	Cyclotriphosphazene
d	Days
DBU	1,8-Diazabicyclo[5.4.0]undec-7-ene
DC	Direct current
DCM	Dichloromethane
DEC	Diethyl carbonate
DFT	Density functional theory
DHP	Dihydropuran
DMC	Dimethyl carbonate

DMAP	Dimethylaminopyridine
DMF	N,N-Dimethylformamide
DMSO	Dimethyl sulfoxide
DSC	Differential scanning calorimetry
EA	Elemental analysis
EC	Ethylene carbonate
EFG	Electric field gradient
EO	Ethylene oxide
EO-CTP	2,2,4,4,6,6-Hexakis-(2-(2-(2-(2-methoxyethoxy)ethoxy)ethoxy)ethoxy)-cyclotriphosphazene
EO-HPB	Hexakis-(4-(2-(2-(2-(2-methoxyethoxy)ethoxy)ethoxy)ethoxy)phenyl)-benzene
eq	Equivalent
FD	Field desorption
FID	Free induction decay
FTIR	Fourier transformed infrared spectroscopy
FWHM	Full width at half maximum
HPB	Hexaphenylbenzene
IL	Ionic liquid
JB	Jeener-Broekaert
KWW	Kohlrausch-Williams-Watts
LiBETI	Lithium bis(pentafluoroethanesulfonyl)imide
LiBOB	Lithium bis(oxalate)borate
$LiPF_6$	Lithium hexafluorphosphate
LiTFSI	Lithium bis(trifluoromethanesulfonyl)imide
MALDI-TOF	Matrix-assisted laser desorption/ionization time of flight
MAS	Magic angle spinning
MCBA	3-chlorobenzoic acid
MCPBA	3-chloroperoxybenzoic acid
MEEEP	Poly[bis(methoxyethoxyethoxyethoxy)phosphazene]
MEEP	Poly[bis(methoxy-ethoxy-ethoxy)phosphazene]
MN	Motional narrowing
p-6PA-HPB	Hexakis(*p*-phosphonatophenyl)benzene
PAN	Poly(acrylonitrile)
PC	Propylene carbonate
PDCP	Polydichlorophosphazene
PDOA	Poly(2-oxo-[1,3]-dioxolan-4-yl)methacrylate)
PDOBMA	Poly(2-oxo-[1,3]-dioxolan-4-yl)butylmethacrylate)
PEO	Poly(ethylene oxide)
PFG	Pulsed-field gradient

ppm	parts per million
PPP(EO)	Poly(*p*-phenylene) with oligo(ethylene oxide) side chains
PVdF	Poly(vinylidene fluoride)
*p*TsOH	*p*-Toluenesulfonic acid
RT	Room temperature
SEI	Solid/electrolyte interphase
SAE	Spin-alignment echo
SLR	Spin-lattice relaxation
SPE	Solid polymer electrolyte
STE	Stimulated echo
TGA	Thermal gravimetric analysis
TFSI	Bis(trifluormethanesulfonyl)imide
THF	Tetrahydrofuran
THP	Tetrahydropuran
TMS	Tetramethylcyclotetrasiloxane
TOF	Turnover frequency
TON	Turnover number
TPP	Tetraphenylporphyrin
VTF	Vogel-Tamman-Fulcher
W.F.	Waugh-Fedin
WLF	William-Landel-Ferry

Symbols

a	Expansion coefficient
A, B	VTF fit parameter
B	Magnetic field
C	Capacitance
C_1, C_2	WLF fit parameter
C_e	Capacitance of the electrode
c_i	Concentration of species i
C_p	Heat capacity
C_{pr}	Capacitance of the electrolyte
D_i	Diffusion coefficient of species i
Δ_0	Rigid-lattice line width
σ	Ionic conductivity
E_a	Activation energy
ε_0	Vacuum permittivity

ε_{pr}	Dielectric constant of the electrolyte
η	Viscosity
h	Planck's constant
H	Enthalpy
I	Current
$J(\omega)$	Spectral density function
k	Cell constant
k_B	Boltzmann's constant
M	Magnetization
q_i	Electric charge of species i
R	Resistance
R^2	Correlation coefficient
r_i	Hydrodynamic radius of species i
t	Transport number
t_m	Mixing time
t_p	Preparation time
T_+	Cation transference number
T_1^{-1}	Spin-lattice relaxation rate in the laboratory frame
$T_{1,\rho}^{-1}$	Spin-lattice relaxation rate in the rotating frame
T_0	Critical temperature
T_g	Glass transition temperature
T_m	Melting transition
T_ref	Reference temperature
V	Voltage
V_0	Van der Waals volume
V_f	Free volume
Y	Admittance
Z	Impedance
ω_Q	Angular quadrupolar frequency
$\omega_{(L)}$	Larmor frequency
ω_0	Zeeman frequency

Acknowledgements

An dieser Stelle möchte ich mich herzlich bei allen bedanken, die in jeglicher Form zum Gelingen dieser Arbeit beigetragen haben.

An erster Stelle gilt mein aufrichtiger Dank meinem Doktorvater Herrn Prof. … für die Möglichkeit, diese Arbeit in seinem Arbeitskreis am Max-Planck-Institut für Polymerforschung durchführen zu können, ebenso für die hilfreichen Diskussionen.

Meinem Projektleiter Herrn Dr. … möchte ich für die sehr angenehme fachliche, wie menschliche Betreuung ganz herzlich danken. Neben den zahlreichen mir zugestandenen Freiheiten beim Arbeiten, den vielen Feedbacks, der Motivation und den aufbauenden Worten, wenn sie nötig waren, hätte die Unterstützung meiner Arbeit in jeglicher Hinsicht nicht besser sein können. Danke für alles, … .

Herrn Prof. … von der Universität Mainz möchte ich für seine Bereitschaft die Funktion des Zweitbetreuers zu übernehmen herzlich danken.

Des Weiteren danke ich Herrn Dr. …. für die Betreuung der Festkörper-NMR-Experimente und die angeregten Diskussionen. Außerdem …. für die Einarbeitung am Spektrometer und die Hilfe bei auftretenden Problemen während der zahlreichen Messungen.

Frau Prof. … danke ich für die reibungslose Übernahme in ihren Arbeitskreis nach der Emeritierung von Herrn Prof. … und die optimalen Bedingungen in Ihren Laboren.

Besonders herzlich bedanken möchte ich mich weiterhin bei … für die exzellente Unterstützung bei größeren und kleineren Problemen, speziell während der Synthesen aber auch im alltäglichen Laborbetrieb. Ebenso bei … für die ausgezeichnete Hilfe bei den zahlreichen Impedanzmessungen, sowie bei … für die physikalischen Erläuterungen.

Frau Prof. … und ihrer Arbeitsgruppe an der Universität Münster, insbesondere … , danke ich für das Ermöglichen der PFG-NMR Messungen. Gleiches gilt für Herrn Prof. … an der University of St. Andrews und dessen Postdoc … , die sich bereit erklärten die Transferzahlen der Modellelektrolyte zu bestimmen.

Für die Durchführung der vielen weiteren Messungen bedanke ich mich herzlich bei … (DSC/TGA), …, …, … (NMR), und … (X-Ray), sowie allen weiteren Mitarbeitern, mit denen ich in Kontakt war, für die exzellente Zusammenarbeit.

All meinen Kollegen im AK … und AK … danke ich sehr für das lockere Arbeitsklima und die schöne Zeit am Institut. Vielen Dank dabei speziell an alle mit denen ich das Labor 1.304 und das Büro 1.316 geteilt habe – Es war nie langweilig. Insbesondere danke ich ganz herzlich …, … und … für die zahlreichen (nichtchemischen) Gespräche, Laufrunden und sonstigen Erlebnisse. Ich hoffe sehr, dass wir in Kontakt bleiben.

Für die Finanzierung dieser Arbeit und das Ermöglichen des Besuches mehrerer internationaler Konferenzen, den '*Summer Schools*' und '*Softskill*'-Kursen bzw. Seminaren danke ich der IMPRS und Frau Dr. … für die perfekte Koordination. Die internationale Atmosphäre war eine große Bereicherung meiner Zeit am MPIP und auch der Vortrag auf dem *XII International Symposium on Polymer Electrolytes* in Padua/Italien war eine inspirierende Erfahrung, wissenschaftlich wie persönlich.

Schließlich möchte ich ganz besonders meinen Eltern und meiner Schwester … für die beständigste und uneingeschränkte Unterstützung nicht nur während des gesamten Studiums danken. Speziell in den stressigen und schwierigeren Zeiten während des Verlaufes dieser Arbeit waren sie immer für mich da und ein großer Rückhalt, ohne den ich nicht so weit gekommen wäre. Vielen Dank!